Technical University of Denmark

DTU

Electronically Steerable Antennas for Satellite Communications

Larsen, Niels Vesterdal; Breinbjerg, Olav; Gothelf, Ulrich

Publication date:
2007

Document Version
Publisher's PDF, also known as Version of record

Link back to DTU Orbit

DTU Library
Technical Information Center of Denmark

ELECTRONICALLY STEERABLE ANTENNAS FOR SATELLITE COMMUNICATIONS

PhD Thesis

Niels Vesterdal Larsen

May 2007

ABSTRACT

ELECTRONICALLY STEERABLE ANTENNAS FOR SATELLITE COMMUNICATIONS

A study of phased array antennas for application to mobile satellite communications has been conducted. The study is focused on small 7-element arrays but it also includes investigations of mutual coupling, influence of finite ground planes, and application of sequential rotation.

Three types of phased arrays are devoted particular attention. The antenna elements of these arrays are cavity-backed annular slot antennas, printed drooping dipole antennas, and dielectric resonator antennas. The three arrays are analysed with a three-stage model which includes numerical simulations of the arrays, the impacts of finite ground planes, and inclusion of the receiver and feed network characteristics. This allows for an assessment of the G/T of the array. It is concluded, that the dipole array offers the best performance among the three arrays, in particular due to its superior coverage at low elevation angles. The investigations have led to the construction of a prototype of the dipole array on which measurements have been conducted. The measurements agree well with the numerical simulations.

The mutual coupling between the antenna elements is investigated with emphasis on the impact of the element radiation pattern, array size, ground plane, and parasitic structures. Some means of reducing the mutual coupling and, thereby the array scan loss, are identified. One of these means is the use of parasitic monopoles positioned between the elements of the array, and such monopoles are employed in the dipole array.

The influence of finite ground planes on the array radiation is investigated in several respects. The investigations are conducted using a numerical Method of Auxiliary Sources model of the ground plane. With this ground plane model, the impacts of the ground plane size, shape, and curvature are analysed as well as the consequences of raising the array slightly above the surface of the ground plane. It is concluded, that these ground plane properties have significant influence on the array radiation and hence the overall performance.

The application of sequential rotation to phased arrays is investigated using two different models. An analytical spherical wave expansion model has been derived and can be employed for general antenna elements, planar array geometries, and scan angles. This model is based on the assumption of identical element patterns and it does not include the mutual coupling. The other model, a numerical Method of Auxiliary Sources model, includes the entire array without making the above assumptions. The two models demonstrate the significant improvement of the polarisation purity that can be obtained with the sequential rotation for arrays whose elements have poor polarisation purity. It is further concluded, that the improvement of the polarisation purity does not necessarily guarantee an improvement of the main-beam circularly-polarised directivity.

Resumé

Elektronisk styrbare antennesystemer til satellitkommunikation

Et studium af fasestyrede antennegrupper til anvendelse for mobil satellitkommunikation er blevet udført. Studiet er fokuseret på små 7-element antennegrupper, men det indbefatter også undersøgelser af gensidig kobling, indflydelse af endelige jordplan og anvendelse af sekventiel rotation.

Opmærksomheden er specielt rettet mod tre typer af fasestyrede antennegrupper. Elementerne i disse antennegrupper er kavitetsantenner med cirkulære slidser, printede skrå dipolantenner og dielektriske resonatorantenner. De tre antennegrupper undersøges med en tretrins model, som inkluderer numeriske simuleringer af antennegrupperne, påvirkningerne fra endelige jordplan og inklusion af karakteristika for modtager og fødenetværk. Dette muliggør en vurdering af antennegruppens G/T. Det konkluderes, at dipolantennegruppen fungerer bedst blandt de tre antennegrupper, specielt pga. en overlegen dækningsgrad ved lave elevationsvinkler. Undersøgelserne har ført til en fremstilling af en prototype af dipolantennegruppen, på hvilken der er blevet udført målinger. Målingerne stemmer godt overens med de numeriske simuleringer.

Den gensidige kobling mellem antenneelementerne undersøges med særlig vægt på påvirkninger fra elementernes udstrålingsmønstre, antennegruppens størrelse, jordplan og parasitiske strukturer. Enkelte virkemidler, til at nedbringe den gensidige kobling og dermed antennegruppens skan-tab, identificeres. En af disse er brugen af parasitiske monopoler placeret mellem antennegruppens elementer, og sådanne monopoler anvendes i dipolantennegruppen.

Påvirkningen fra endelige jordplan på antennegruppens udstråling undersøges i flere sammenhænge. Undersøgelserne udføres med en numerisk "Method of Auxiliary Sources"-model af jordplanet. Med denne jordplansmodel analyseres påvirkningerne fra jordplanets størrelse, facon og krumning samt konsekvenserne af at løfte antennegruppen en anelse over jordplanets overflade. Det konkluderes, at disse karakteristika for jordplaner har en signifikant indvirkning på antennegruppens udstråling og dermed den samlede virkningsgrad.

Anvendelsen af sekventiel rotation til fasestyrede antennegrupper undersøges med to forskellige modeller. En analytisk, sfærisk bølgeudviklingsmodel er blevet udledt og kan anvendes for generelle antenneelementer, plane antennegruppegeometrier og skanvinkler. I denne model antages det, at antenneelementerne har samme udstrålingsdiagram, og den gensidige kobling inkluderes ikke. Den anden model, en numerisk "Method of Auxiliary Sources"-model, inkluderer hele antennegruppen uden at gøre ovennævnte antagelser. De to modeller demonstrerer den signifikante forbedring af polarisationsrenheden, som kan opnås vha. sekventiel rotation af antennegrupper, bestående af elementer med dårlig polarisationsrenhed. Det konkluderes endvidere, at forbedringen af polarisationsrenheden ikke nødvendigvis garanterer en forbedring af den cirkulært polariserede direktivitet i antennegruppens hovedsløjfe.

PREFACE

The work presented in this thesis has been carried out at Thrane & Thrane A/S and ElectroScience, Ørsted·DTU, Technical University of Denmark (DTU). The study was initiated June 2004 and ended May 2007. It has been financed primarily by Thrane & Thrane A/S with support from the Industrial PhD initiative. From May 2006, I spent 6 months as a visiting scholar at the Jet Propulsion Laboratory (JPL), Pasadena, California.

There are many people to whom I would like to extend my gratitude. Especially my two supervisors, from Thrane & Thrane and DTU, Ulrich V. Gothelf and Olav Breinbjerg. With their extensive experience and knowledge of experimental and theoretical topics, they have formed an invaluable team. This is indeed essential for Industrial PhD projects such as this, where theory and application are equally important. I furthermore thank my friends and colleagues at Thrane & Thrane and DTU for many interesting discussions and suggestions. Particularly, Tonny Rubæk and Samel Arslanagić are acknowledged for reading and commenting many of the chapters of the present thesis.

Many people have been helpful in making my visit at JPL, and California in general, a great experience. I particularly thank John Huang for accepting me at JPL and generously sharing his immense knowledge on antennas and phased arrays. I also thank the Boyd and Poulsen families for accepting me into their homes, providing much help and advice, and introducing me to the Californian culture and society in general.

Kgs. Lyngby, May, 2007

Niels Vesterdal Larsen

The present version of the thesis was revised in October 2007 after the thesis defense. This was with the purpose of correcting misprints that occurred in the original version. In addition, the status of the publications has been updated.

TABLE OF CONTENTS

LIST OF PUBLICATIONS

As a part of the study, the following publications have been prepared, divided into journal papers [J1- J6], conference papers [C1, C2], technical reports [R1- R3], and a business report [R4]. The journal papers are included in the latter half of this thesis in pages 61-112.

Journal Publications

[J1] N.V. Larsen and O. Breinbjerg, "An L-band, Circularly Polarised, Dual-Feed, Cavity-Backed Annular Slot Antenna for Phased Array Applications", *Microwave and Optical Technology Letters*, Vol. 48, No. 5, 2005, pp. 873-878, (included, pp. 61-68).

[J2] N.V. Larsen and O. Breinbjerg, "Modelling the Impact of Ground Planes on Antenna Radiation Using the Method of Auxiliary Sources", *IET Microwave, Antennas and Propagation*, Vol. 1, No. 2, 2007, pp. 472-479. (included, pp. 69-78).

[J3] N.V. Larsen and O. Breinbjerg, "Analysis of Circularly Polarised Hemispheroidal Dielectric Resonator Antenna Phased Arrays Using the Method of Auxiliary Sources", accepted for publication in *IEEE Transactions on Antennas and Propagation*[*], March, 2007, (included, pp. 79-93).

[J4] N.V. Larsen and O. Breinbjerg, "A Two-Stage MAS Technique for Analysing DRA Elements and Arrays on Finite Ground Planes", accepted for publication in *Electronic Letters*[†], May, 2007, (included, pp. 95-99).

[J5] N.V. Larsen and O. Breinbjerg, "Single-Feed Circularly Polarised Hemi-Ellipsoidal Dielectric Resonator Antenna", May, 2007, (included, pp. 101-104).

[J6] N.V. Larsen and O. Breinbjerg, "A Spherical Wave Expansion Model of Sequentially Rotated Phased Arrays with Arbitrary Elements", in submission[‡], May, 2007, (included, pp. 105-112).

Conference Publications

[C1] N.V. Larsen and O. Breinbjerg, "An L-band, Circularly Polarized, Dual-Feed, Cavity-Backed Annular Slot Antenna with Wide-Angle Coverage", *Proceedings of the IEEE Antennas and Propagation Symposium Digest*, Albuquerque, New Mexico, 2006, pp. 1549-1552.

[C2] N.V. Larsen and O. Breinbjerg, "A Method of Auxiliary Sources Approach for Modelling the Impact of Ground Planes on Antenna Radiation", *Proceedings of The European Conference on Antennas and Propagation, EuCAP*, Nice, France, 2006.

Reports

[R1] N.V. Larsen, "Implementation and Applications of the Method of Auxiliary Sources for Smooth Scatterers and Wires", Report, R 731, *Ørsted·DTU, Technical University of Denmark*, April, 2007.

[R2] N.V. Larsen "Design of Circularly-Polarised, Crossed Drooping Dipole, Phased Array Antenna Using Genetic Algorithm Optimisation", Internal Report, IR 792, *Ørsted·DTU, Technical University of Denmark*, April, 2007.

[R3] N.V. Larsen, "Investigation of the Sequential Rotation Technique and its Application for Phased Arrays", Report, R 732, *Ørsted·DTU, Technical University of Denmark*, April, 2007.

---

[*] [J3] later appeared in *IEEE Transactions on Antennas and Propagation*, Vol. 55, No. 8, 2007, pp. 2163-2173.
[†] [J4] later appeared in *Electronic Letters*, Vol. 43, No. 12, 2007, pp. 657-659.
[‡] [J6] later appeared in *Microwave and Optical Technology Letters*, Vol. 49, No. 12, 2007, pp. 3148-3154.

[R4] N.V. Larsen, "Business Report - in the Framework of the Industrial PhD-project Electronically Steerable Antennas for Satellite Communication", Prepared for the *Ministry of Science, Technology, and Innovation*, December, 2006.

LIST OF ACRONYMS

Several acronyms are employed in this thesis. Some are used generally in the main text whereas others are only used in figures and tables. They are all are listed below. In addition to this list, the acronyms are defined at first use in each of the chapters.

ACeS   Asia Cellular Satellite, a mobile satellite communications provider.
AEP   Active Element Pattern.
AMSC   American Mobile Satellite Corporation, a mobile satellite communications provider.
AR   Axial Ratio.
AWAS   Analysis of Wire Antennas and Scatterers, simulation software.

BGAN   Broadband Global Area Network.

C-   C-Band. Designation for the frequency band from 4 GHz to 8 GHz.
CBASA   Cavity-Backed Annular Slot Antenna.
CDA   Crossed Dipole Antenna.
CPA   Conventional Phased Array, as opposed to SRPA.
CST-MS   CST Microwave-Studio, simulation software.

DBF   Digital Beam Forming.
DL   Delay Line.
DRA   Dielectric Resonator Antenna.
DTU   Technical University of Denmark.

EBG   Electromagnetic Band Gap.
EIRP   Effective Isotropic Radiated Power.
EMSS   Experimental Mobile Satellite System.

FAS   Finite Array Scheme.
FDM   Finite Difference Method.
FEM   Finite Element Method.
FGP   Finite Ground Plane.

GA   Genetic Algorithm.
GEO   Geostationary Earth Orbit.
GTD   Geometrical Theory of Diffraction.

HAPDAR   Hard Point Demonstration Array Radar, a phased array radar.
HEO   Highly Elliptical Orbit.
HFSS   High-Frequency Structure Simulator, simulation software.
HOPES   Higher-Order Parallel Electromagnetic Simulator, simulation software.
HWD   Half-Wave Dipole.

I-   Inmarsat-, prefix for the Inmarsat satellite fleet, e.g., I-2.
IAS   Infinite Array Scheme.
IES   Isolated Element Scheme.
IGP   Infinite Ground Plane.
INES   INexpensive Earth Station, a switched-beam array.

JPL   Jet Propulsion Laboratory.

Ka-   Ka-Band. Designation for the frequency band from 26 GHz to 40 GHz.

L-   L-Band. Designation for the frequency band from 1 GHz to 2 GHz.
LCGP   Large Circular Ground Plane.
LEO   Low Earth Orbit.

LHCP	Left-Hand Circular Polarisation.
LNA	Low-Noise Amplifier.
LSGP	Large Square Ground Plane.
MAS	Method of Auxiliary Sources.
MEO	Medium Earth Orbit.
MoM	Method of Moments.
MSAT-X	Mobile Satellite Experiment.
MSS	Mobile Satellite Service.
PDDA	Printed Drooping Dipole Antenna.
PEC	Perfect Electric Conductor.
PMC	Perfect Magnetic Conductor.
PO	Physical Optics.
QWM	Quarter-Wave Monopole.
RHCP	Right-Hand Circular Polarisation.
SANTANA	Smart ANTennA termiNAl, a phased array employing DBF technology.
SCGP	Small Circular Ground Plane.
SIBC	Standard Impedance Boundary Condition.
SR	Sequential Rotation.
SRPA	Sequentially Rotated Phased Array.
SSGP	Small Square Ground Plane.
SWE	Spherical Wave Expansion.
TE	Transverse Electric.
TM	Transverse Magnetic.
WAIM	Wide Angle Impedance Matching.
WPD	Wilkinson Power Divider.

CHAPTER 1

INTRODUCTION

Electronically steerable antennas, also known as phased arrays, have been a research topic during more than 60 years with the analysis of linear arrays by Schelkunoff in 1943 [1] being one of the pioneering works. Following the 2nd World War, the interest in phased arrays received a boost as the necessity of improving the existing radar technology became apparent [2]. Thus it was realised that the phased array antennas enable very fast scanning compared to the bulky mechanical radars, prevalent in the air defense systems of that time. The phased array antennas remained an important research topic for military applications during the "Cold War" era. In the 1960s and 1970s the increasing armament with ballistic missiles spurred the development of more advanced air defense systems, including ground-based missile tracking radars [3] as well as radars for ships and aircraft [4, 5]. An example is the so-called Hard Point Demonstration Array Radar (HAPDAR), shown in Figure 1.1, built at the White Sands Missile Range in New Mexico, USA, with the purpose of tracking multiple airborne targets [6].

While the early applications of phased arrays were almost exclusively military, the technology slowly permeated into civilian applications during the late 1980s and early 1990s. It remained a very expensive technology, employed mostly for specialised applications such as air traffic control in airports [3, 7], as well as various space-borne applications [8]. During the 1980s and 1990s early experiments with mobile satellite communications systems were conducted. In the Mobile Satellite Experiment (MSAT-X) in the USA [9] and the Experimental Mobile Satellite System (EMSS) in Japan [10], a number of phased array antennas were developed for land-vehicular and aeronautical applications [11–14]. With the continued breakthroughs and cost reductions of electronic components, phased array technology is no longer prohibitively expensive. Furthermore, the development of modern-day mobile satellite communications and the increased demands hereof, imply that phased arrays are now of interest for such applications, also from a commercial perspective.

In the following, a brief review of mobile satellite communications systems is given with specific emphasis on Inmarsat. This is followed by an overview of different types of antennas used for the mobile user terminals and a discussion of the challenges of phased array design. Finally, the topics of the present study and the contents of the remaining chapters are outlined.

Figure 1.1: *The HAPDAR is a phased array radar for tracking multiple airborne targets. The picture is from [6].*

1.1 Overview of Mobile Satellite Communication Systems

Mobile satellite communications systems, or Mobile Satellite Services (MSSs), enable people to communicate from almost anywhere on the surface of the Earth without the need for fixed communications infrastructure, e.g., traditional land-line and cellular phone services. Important areas of application are ships (maritime), aircraft (aeronautical), and ground use (land-mobile). In case of the latter, disaster areas, where the fixed communications systems have broken down, as well as remote areas that completely lack this infrastructure, are examples.

The MSSs consist of three main parts; the satellite fleet or satellite repeaters, the fixed Earth stations which are connected to the terrestrial communications networks, and the mobile user terminals. The satellite repeaters relay the communication from the mobile user terminals to the fixed Earth stations (up-link) and vice versa (down-link).

MSSs typically employ circular polarisation in order to avoid signal degradation due to the atmospheric effect known as Faraday rotation [15]. This effect is predominant for low frequencies and is not negligible, for instance, for the L-band frequency range that is employed in many MSSs, including Inmarsat.

1.1.1   Brief Historical Outline

The 1960s saw the initial development of experimental communication satellites and in 1965 the first commercial, INTELSAT I, entered operation. At that time, satellite communications merely provided links between fixed Earth stations to which the users were connected via terrestrial networks. The demand for corresponding services for mobile use arose, primarily among maritime nations, and resulted in the formation of the International Maritime Satellite Organisation, also known as Inmarsat, in 1979 [16]. Inmarsat launched the first commercially based global satellite communications service in 1982 with the initial launches of the Inmarsat-2 (I-2) fleet [16, 17]. Since then, the demand for MSS has expanded into the land-mobile and aeronautical user segments.

Typical for the early communications satellites were low capacity and high cost. As the technology progressed, larger and more powerful satellites were developed and this translated into higher capacity, lower requirements for the user terminals, and thereby an overall reduction of the cost passed on to the user. Over the years, several other MSS operators have entered the market and today both global and regional MSSs are in operation [18]. Inmarsat, however, remains in the leading role, being by far the largest, and is considered to be the most important [19].

1.1.2   Some Existing Mobile Satellite Communication Systems

Present-day MSSs primarily operate with satellite constellations in the Geostationary Earth Orbit (GEO) and Low Earth Orbit (LEO). The LEO is located at an altitude of about 700-1500 km, while the GEO is at about 35600 km, above the Equator [18].

The early MSSs, including the globally operating Inmarsat, were all based on GEO constellations. Advantages of the GEO are that the entire Earth, except the polar regions, can be covered with 3 satellites and that the satellite positions remain fixed relative to the Earth. Disadvantages are the high altitude which implies a large signal path loss, lack of coverage at the polar regions, and the very costly process of inserting satellites in the high-altitude GEO [20]. Today, several regional MSSs operate from the GEO, e.g., the American Mobile Satellite Corporation (AMSC) in North America, Thuraya in the Middle East, Asia Cellular Satellite (ACeS) in Southeast Asia, and the Optus MobileSat in Australia [18].

In the late 1980s it was concluded that LEO constellations were no longer infeasible for commercial MSSs [18] and some of the attention shifted from GEO to LEO. Within a relatively short time a number of LEO services sprang to life. In practice, however, many have yet to enter commercial operation. Advantages of the LEO are that the satellites are much cheaper to put in orbit. Furthermore, the path loss is much smaller and thus the requirements for the antenna gain of the user terminals are not so severe [20]. The low altitude of the LEO implies that many satellites are necessary in order to provide global coverage. Furthermore, the LEO satellites are not fixed with respect to the Earth and this requires complicated hand-over procedures between the satellites as they traverse the sky. MSSs based on LEO constellations include Iridium [21] and GlobalStar [22].

The Medium Earth Orbit (MEO) and Highly Elliptical Orbit (HEO) are examples of other satellite constellations. MEO constellations are located at altitudes of about 10000-12000 km [18] with the ICO Global Communications MSS being an example. For further details of satellite constellations, used for fixed as well as mobile satellite communications, excellent overviews can be found in [15, 18].

1.1.3   The Inmarsat Satellite Fleet and Services

Inmarsat is an international MSS provider offering global coverage with a GEO-based satellite fleet. As mentioned earlier, Inmarsat was the first provider to inaugurate a commercial MSS, and presently the satellite fleet comprises 3 generations of satellites, I-2, I-3, and I-4. The I-3 are still in use while the I-2 are primarily functioning as back-up capacity [23]. The I-4 satellites, with two launched in 2005 and a third planned for 2007, host the new Broadband Global Area Network (BGAN) service [24] as well as the older existing services and

Figure 1.2:   (a) *Quadrifilar helix antenna developed by Thrane & Thrane [25] for the Inmarsat mini-C service. The picture is from [26].* (b) *The WorldSpace Boat Antenna developed by JAST [27]. The picture is from [27].*

(a)   (b)

will, with the third satellite, cover the entire Earth except for the polar regions. The Inmarsat services extend to maritime, aeronautical, and land-mobile applications, including a number of emergency and security services.

The Inmarsat system operates with circularly polarised radio signals at L- and C-band , on the mobile terminal side and Earth station side, respectively [18]. With respect to the mobile terminals the frequency bands are 1525 MHz - 1559 MHz for the receiving case (down-link) and 1626.5 MHz - 1660.5 MHz for the transmitting case (up-link).

1.2   Antenna Types for Mobile User Terminals

The various satellite communications systems set very different requirements for the user terminals. Depending on the distance to the satellite, data rate, and the satellite repeater gain, the user terminals must comply with certain requirements for the Effective Isotropic Radiated Power (EIRP) and receiver G/T, (ratio of antenna gain to system noise temperature) in the transmit and receive cases, respectively. Hence, a range of different antenna types are employed in user terminals in order to comply with these requirements.

1.2.1   Omnidirectional Antennas

For applications where the requirement of the user terminal antenna gain is sufficiently low, omnidirectional antennas are well suited. In particular for LEO constellations, such as employed by Iridium, the path loss is relatively small. Since the LEO satellites are not geostationary, the omnidirectional antennas are even more advantageous because there is no need to direct an antenna main beam towards the satellite.

Omnidirectional antennas are also used with GEO constellations, an example being the low data rate Inmarsat mini-C service [23]. Examples are quadrifilar helix antennas [26, 28], drooping dipole antenna [29], and small omnidirectional arrays [30]. In Figure 1.2a an example of a quadrifilar helix antenna for the Inmarsat mini-C service is shown. In order to increase the directivity at low elevation angles, some omnidirectional antennas are designed with a null in the radiation pattern in the antenna bore-sight direction*. An example of such an antenna is the JAST WorldSpace Boat Antenna in Figure 1.2b [27].

In applications where the gain requirements are larger, the omnidirectional antennas are not feasible choices. In such cases the antenna must have a distinct main beam, directed towards the satellite either by mechanical or electronic means.

1.2.2   Manually and Mechanically Steerable Antennas

The manually and mechanically steerable antennas have distinct main beams that are directed towards the satellite. They may consist of a single antenna element or a fixed-beam antenna array. For stationary applications, the main beam can be steered manually towards the satellite by simply orienting an antenna panel appropriately. In Figure 1.3a, an example of a manually steered antenna array is shown in virtue of the Explorer^TM 700 antenna [31] developed by Thrane & Thrane A/S.

---

*In principle, an antenna with such a null is not omnidirectional. However, in the case of the antenna in Figure 1.2b, this term is nevertheless used, and probably denotes that steering of the antenna is unnecessary.
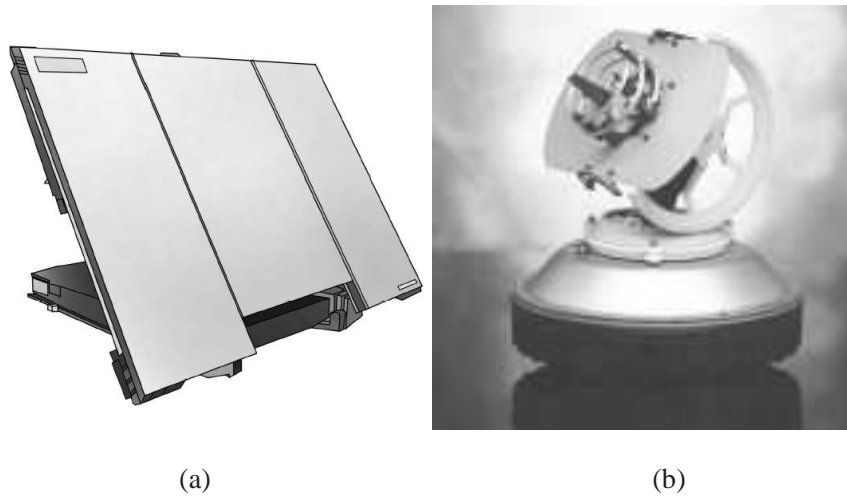
(a)   (b)

Figure 1.3:   (a) *A manually steerable antenna, Explorer^{TM} 700, developed by Thrane & Thrane [25]. The picture is from [31]. (b) A mechanically steerable antenna with a single helix antenna element developed by Omnipless [32]. The picture is from [32].*

For mobile applications, where the direction to the satellite changes, the proper orientation of the antenna is maintained automatically by a satellite tracking system and positioning motors which mechanically steer the antenna [15]. Examples of applications are the Inmarsat Fleet 33, 55, and 77 services [23]. Typical antenna types, used either as single antennas or as elements of fixed-beam arrays, are microstrip and helix antennas. In Figure 1.3b, a mechanically steered helix antenna, developed by Omnipless [32], is shown.

From an electrical point of view, the mechanically and manually steerable arrays are relatively simple. However, the mechanical steering is disadvantageous for some applications for a number of reasons. First, it requires complicated machinery which is susceptible to break down if the antenna is operated in a rough environment such as on a vehicle crossing over uneven terrain. Second, it is a relatively slow process to direct the antenna towards the satellite. The high-gain antennas, which are needed for high data rates, are furthermore quite large, and must be enclosed by large bulky radomes. For these reasons the mechanically steerable antennas are best suited for maritime applications where ample space is available on the ship whose orientation changes slowly. For aeronautical and land-vehicular applications the large radomes and fragile

Figure 1.4:   *Switched-beam array with 8 slanted microstrip patches [33] developed for the Optus MobileSat programme. The patches are operated as 8 two-element phased arrays, providing a total of 24 beam settings. The picture is from [33].*

mechanical components may very well be incompatible with the aerodynamic design requirements as well as the vibration and shaking that may occur in these environments.
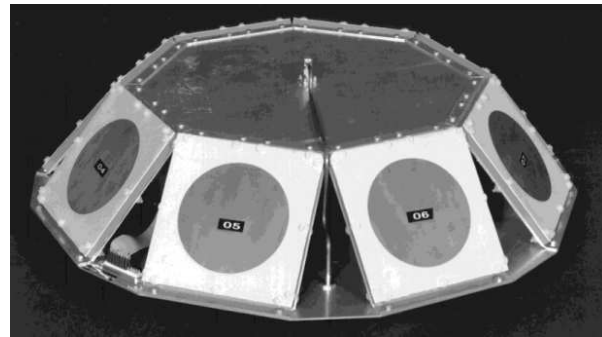
1.2.3   Switched-Beam Arrays

The switched-beam array is a type of electronically steerable antenna in which a single element or subset of elements cover a certain angular portion of the hemisphere. Depending on the direction to the satellite, the relevant subset of elements is turned on while the remaining elements are left inactive.

A switched-beam array, where a single element is used at a time, is developed in [34] with 4 microstrip patches arranged on the 4 lateral sides of a cube. In [33] an 8-element circularly polarised microstrip switched-beam array is constructed for use with the Australian Optus MobileSat programme. In this case 2 of the 8 elements are excited at a time. Furthermore, a phase delay of 50° can be introduced in either of the two active elements. Thus the array consists of 8 different two-element phased arrays and a total of 24 different beams can be formed. This switched-beam array is shown in Figure 1.4. It is noted that a very similar design has been described in [35].

The so-called INexpensive Earth Station (INES) [36] is another example. It has been developed for used with the Inmarsat BGAN service. The INES array consists of 8 microstrip patches arranged with one horizontal
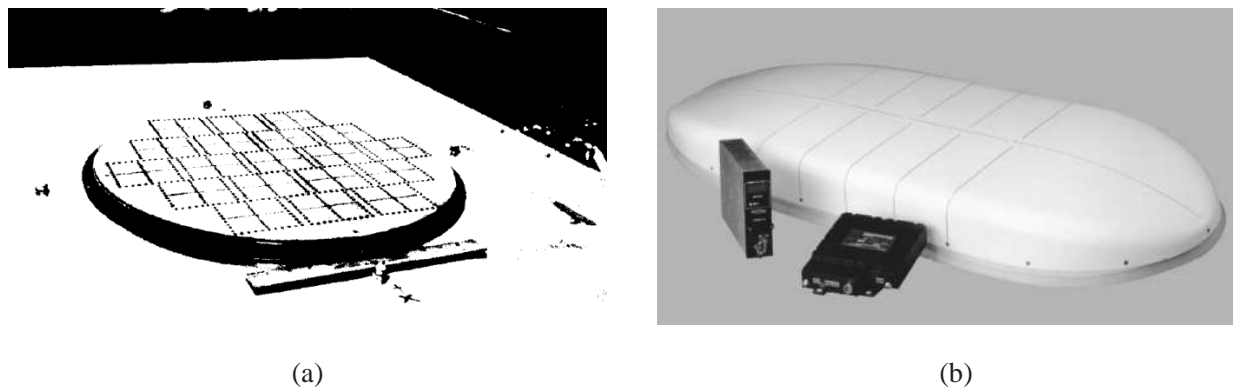
<div align="center">(a)   (b)</div>

Figure 1.5: (a) *A 19-element phased array of crossed-slot elements developed for the* MSAT-X *project by Teledyne Ryan Electronics. The picture is from [37].* (b) *The T-4000 Inmarsat High-Gain Antenna developed by TECOM Industries. The picture is from [38].*

element on the top and 7 slanted patches on the sides of a pyramid-like structure. The patches can be excited individually or in pairs consisting of the top patch and one of the 7 slanted patches.

The non-horizontal alignment necessary for most of the elements implies that switched-beam arrays have a relatively high profile. The electronic switching inherent in the switch-beam arrays results in a certain complexity of the design. Furthermore, the switches will contribute with some loss that will have detrimental effects on the antenna G/T.

1.2.4 Phased Arrays

In phased arrays all the antenna elements are excited simultaneously and the main beam of the array is steered by applying a progressive phase shift across the array aperture. Thereby higher gain can be achieved than for switched-beam arrays where only a small number of the elements are turned on at a time. Some of the first applications to satellite communications were developed for land-vehicular use under the MSAT-X programme in the 1980s. Two different 19-element phased arrays were constructed, a cavity-baked crossed-slot array by Teledyne Ryan Electronics [11, 37] and a microstrip patch array by Ball Aerospace [12], both in co-operation with Jet Propulsion Laboratory (JPL). The former of the two is shown in Figure 1.5a. In the late 1980s, planar [13] and trigonal shaped [14] phased arrays were developed in Japan, consisting of microstrip and crossed-slot elements. Both were aimed at the Inmarsat aeronautical services which received much interest in the wake of the EMSS project. For the maritime Inmarsat-M service, a 12-element spiral antenna array was developed in [39] and more recently a 19-element patch array [40]. A further example is the 12-element stacked-patch array for use with the Optus MobileSat service, developed in [41]. An examples of a modern, commercially available phased array antenna is shown in Figure 1.5b in virtue of the T-4000 Inmarsat High-Gain Antenna developed by TECOM Industries for aeronautical applications.

The simultaneous excitation of all elements with different phase shifts constitutes a significant complexity compared to the switched-beam array. Due to the mutual coupling, the phased arrays are subject to scan-dependent input impedances which ultimately result in some of the input power being reflected at the element terminals. This leads to the so-called scan loss which is one of the most challenging problems in phased array design.

1.2.5 Smart Antennas and Digital Beam Forming

The so-called Digital Beam Forming (DBF) represents a further step in complexity compared to the phased array. Instead of combining the element patterns directly as is done in ordinary phased arrays, the signals received by the elements are converted to digital form individually. Once the signals are available they can be combined using digital signal processing. This allows for much more advanced signal processing than the simple addition in the standard phased array. Thus spacial filtering of the received signals is obtained by weighting these with general complex coefficients. The purpose of this is not necessarily to obtain a main beam in a certain direction but to maximise the signal quality. In environments where multi-path signals occur, such as cities with high buildings, the direct and multi-path signals can be combined in-phase by adjusting the element excitations, or weights, dynamically such as done in [42].

Antennas employing DBF technology are typically referred to as adaptive arrays or smart antennas. They do not necessarily have a single main beam but, depending on the number and directions of multi-path signals, several smaller beams may be formed. An example is the so-called Smart ANTennA termiNAl (SANTANA), shown in Figure 1.6, intended for Ka- band operation in future mobile satellite communications [36]. For a detailed treatment of DBF and smart antennas in general, the reader is referred to [43].
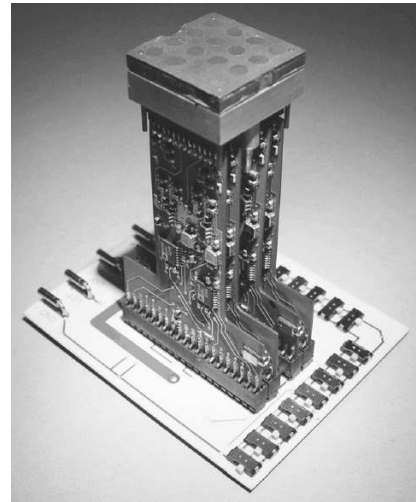
1.3   Challenges of Phased Array Antenna Design

A number of challenges must be overcome in order to arrive at a well-working phased array design. These concern the actual performance of the array as well as simulations and numerical models necessary for predicting of the array performance.

Figure 1.6:   *Prototype of the SANTANA developed by EADS/Astrium and others. The picture is from [36].*

1.3.1   Array Height

As mentioned earlier, the height of the antenna array is of some importance. This is particularly the case for aeronautical applications where the antenna should not compromise the aerodynamic shape of the aircraft. However, the height is also important for land-mobile applications. In this case the visual impression of the antenna is very important from a commercial perspective. If customers can choose between two different antennas they are likely to choose a flat, smooth antenna rather than a high-profile bulky one.

1.3.2   Array Performance

A critical parameter of the antenna performance is the G/T which is the ratio between the gain of the antenna and the system noise temperature. This number is also known as the Figure of Merit [15] and it is of interest because it is directly proportional to the ratio of the received carrier power to the noise power spectral density. The antenna loss plays an important role in the G/T in that it diminishes the gain as well as increases the system noise temperature. For further details, see Section 2.2. Another important antenna property is the EIRP which relates to the transmit mode of the antenna and is the product of the gain and input power. Typically, the requirements for the G/T are the most difficult to fulfill since both the antenna gain and loss must be considered.

For MSS applications where geostationary satellites are employed, e.g., the Inmarsat system, it may be necessary to scan the beam to low elevation angles, especially if the user terminal is positioned in the northern or southern regions of the Earth. Therefore, sufficient G/T must be obtained for a wide range of scan angles. In order to ensure this, the elements must have wide element patterns. They must be located close to each other to avoid the occurrence of grating lobes, and generally the antenna loss and system noise temperature must be kept as small as possible.

One of the most problematic issues of phased array design is the mutual coupling occurring between the elements of the array. The mutual coupling results in non-identical active element patterns and non-ideal element excitations which have detrimental effects on the polarisation purity of the array. Furthermore, the element excitations become interdependent since the excitation of one element is affected by that of the surrounding elements. This implies that the input impedance of the elements becomes scan-dependent, resulting in impedance mismatch. Depending on the feed network, the reflected signals may enter the input terminals of the surrounding elements which causes further excitation errors. Alternatively, resistors may be inserted in the feed network in which case the reflected signals are dissipated and do not contribute to the excitation errors. However, in this case the antenna loss will increase accordingly.

Since the mutual coupling is generally larger for small element separations than for large, wide element separations may seem preferable. However, it is also well known that a small element separation has the effect of reducing the impedance variation with scan angle [44]. From the above it is clear that a number of challenges exist and that the successful design of a phased array antenna for wide-angle scanning applications

is not a trivial task.

1.3.3 Array Modelling

From a simple investigation of a single isolated element it is difficult, if not impossible, to ascertain the overall array performance. While application of simple array theory, i.e., the "array factor", may provide an approximate assessment of radiation properties, such as main beam directivity, side lobes, and grating lobes, it basically disregards all the challenging issues [44]. It is therefore important to be able to model the array with sufficient accuracy, that is, to predict the mutual coupling, the active element patterns, the resulting array scan loss, and ultimately the array G/T.

In many cases, a numerical simulation of an entire array is difficult to conduct and requires large computational resources. In order to avoid this problem it may be preferable to model the elements of the array individually or in pairs of two to assess the mutual coupling. Alternatively, the array may be modelled as an infinite array. In the case of a large or moderate-sized array, both approximate models may imply significant reductions of the computational complexity. However, these approximations may yield unacceptably inaccurate results.

A further aspect of the array performance is how the radiation is affected by surrounding structures such as a finite ground plane which vary in shapes, curvatures, etc.

1.4 The Present Study

1.4.1 Purpose and Main Topics of the Study

The overall purpose of this study is to acquire knowledge of a range of topics relevant to phased arrays. In particular, small phased arrays suited for application within the Inmarsat MSS are of interest since this is an important business area for Thrane & Thrane. The arrays considered in this study must not necessarily comply with strict requirements of the Inmarsat specifications but provide a general idea of the obtainable performance[†]. The investigations require the use, and where necessary, development of a range of mathematical models as well as the construction of an array prototype and measurements hereof. More specifically, the following investigations should be conducted:

- A prototype of the phased array should be constructed, based on initial investigations using simulation models. In this respect, the focus is on 7-element phased arrays with the elements arranged in a hexagonal lattice, designed for a frequency of 1.6 GHz.

- The mutual coupling between the antenna elements in the array is to be analysed and, if possible, suggestions on how to minimise it should be given.

- Application of the sequential rotation principle for phased arrays and the possible benefits that can be achieved, must be clarified.

- The impact of finite ground planes on the array performance must be investigated.

The investigations relate primarily to the radiating parts of the array and not so much the feed network and receiver which are also important parts of the phased array antenna system. The feed network and receiver are, however, included in a theoretical manner in the investigations, which is necessary in order to assess the array performance.

1.4.2 Outline of the Remaining Chapters

The present thesis is intended to give an overview of the most important results of the study. In addition to the thesis a number of papers and technical reports have been prepared. Included in the last parts of the thesis

---

[†]It may be noted here that Inmarsat specifications for the mobile terminals and services naturally exist. However, these are confidential and will not be discussed in this thesis. It will thus not be concluded whether these requirements are fulfilled or not for the investigated phased arrays.

are 6 papers [J1 - J6], which have been submitted to scientific journals. At the time of writing four of these have either been published or accepted for publication, and the remaining two await the review. In addition, 2 conference papers [C1, C2], and 4 reports [R1 - R4]‡ have been prepared but are not included in this thesis. A list of these works can be found in page ix.

The thesis is organised in 7 chapters. Following this introduction in Chapter 1, Chapter 2 gives an overview of the various mathematical models that have been employed in the study. The mathematical details of the methods are generally not discussed here but can be found in the referenced literature. In Chapter 3, selected results from investigations of the mutual coupling and related topics are presented. Examples of the impacts from a range of different configurations are presented and some means of reducing the coupling are discussed. In Chapter 4, the three different phased arrays, which were chosen for detailed investigations, are presented. The arrays are the Cavity-Backed Annular Slot Antenna (CBASA) array, Printed Drooping Dipole Antenna (PDDA) array, and Dielectric Resonator Antenna (DRA) array. The array performance is presented in term of directivity, scan loss, and G/T. In Chapter 5, the impact of finite ground planes is addressed. The CBASA and PDDA arrays are investigated with ground planes of different sizes, shapes, and curvatures. Also the consequences of raising the arrays above the ground planes are investigated. Chapter 6 presents results from an investigation of the use of sequential rotation of the phased array elements. Finally, the conclusions are drawn in Chapter 7 where also recommendations and suggestions for further work are given.

---

‡The Business Report [R4] is a mandatory report supplemental to the PhD thesis and is an integral part of the Industrial PhD Programme. From the home page of the Industrial PhD Initiative [45]: "The Business report must present the Industrial PhD project from the commercial perspective of the enterprise. The business report thereby documents the fellow's understanding of commercial aspects of the Industrial PhD project in a theoretical and enterprise context". The Business Report is confidential and is not discussed further in this thesis.

CHAPTER 2

MATHEMATICAL MODELS FOR PHASED ARRAY ANALYSIS

In this chapter, an overview of the mathematical methods, which have been employed for the analyses of the phased arrays, is given. The topics cover specific analytical derivations and numerical computations, conceptual phased array models, as well as incorporation of antenna feed network and receiver models. Before addressing these issues further, it is emphasised that the mathematical formulations in the remainder of this thesis are based on an assumed harmonic time dependence $e^{j\omega t}$, where t is the time and ω is the angular frequency. This time dependence is suppressed throughout.

2.1 Electromagnetic Field Analysis

In this section, the different mathematical techniques used in the study are briefly presented. Some of the methods are developed and implemented during the study and others are used via existing software.

2.1.1 Spherical Wave Expansion

For configurations with spherical symmetry the Spherical Wave Expansion (SWE) of the electromagnetic field can be employed. In this study the SWE formulations in [46] are used. Based on this SWE, the field from electric or magnetic sources can be expressed using dyadic Green's functions, as described in [47]. The dyadic Green's functions, thus derived, are valid for infinite homogenous media and configurations with dielectric and impedance spheres, and are given in [J3, R1]. With the use of the image source principle these configurations can be extended to those of an infinite half-space with an Infinite Ground Plane (IGP), with the spheres being substituted by hemispheres. Following the principles in [48], this method has been used in [J3, R1] to model probe-fed hemispherical Dielectric Resonator Antennas (DRAs).

2.1.2 Method of Moments

The Method of Moments (MoM) [49] is essentially a method for solving integral equations and it is the underlying technique in a number of simulations tools. For electromagnetic problems the unknown integrand, to be solved for, is the electric or magnetic current.

In this study, the commercially available simulation tool AWAS 2.0 (Analysis of Wire Antennas and Scatterers) [50] has been used in the design of the Printed Drooping Dipole Antenna (PDDA) array which is presented in Chapter 4. AWAS is based on the so-called "thin wire approximation", in which it is assumed that the current is confined to the wire surface and uniformly distributed, and that it has only axially directed components. In AWAS the wire current is expanded in polynomial basis functions which, combined with the thin wire approximation, results in fast calculations. Due to the low computational cost of AWAS it was feasible to optimise the PDDA array using the Genetic Algorithm (GA) which is discussed further in Section 2.5.

A more complex MoM programme that has been used to some extent, is the HOPES (Higher-Order Parallel Electromagnetic Simulator), developed by Erik Jørgensen during his PhD project at the Technical University of Denmark (DTU) [51]. HOPES employs higher-order hierarchical Legendre basis functions and this implies that the convergence rate is significantly faster than for MoM implementations based on more simple basis functions. The HOPES programme was used in [J2] for validation purposes.

Last, an implementation of the method developed in [52] for analysis of infinite phased arrays has been employed. It is based on the so-called Floquet-mode formulation, which is discussed briefly in Section 2.3.2.

2.1.3 *Method of Auxiliary Sources*

In contrast to the MoM, the Method of Auxiliary Sources (MAS) does not aim at recovering the currents on the structure. Instead the scattered field, due to the presence of the structure, is expanded in weighted contributions from so-called auxiliary sources. These weights are found by enforcing the boundary conditions of the total field which is the sum of the incident field and the scattered field.

Since the MAS is not based on integrations of the current but on simple summations of field contributions from the auxiliary sources, it is much simpler to implement than the MoM. This is particularly the case for the so-called Standard MAS [53] where infinitesimal current elements such as Hertzian dipoles are used as auxiliary sources. This simplicity comes with the cost that rapidly varying fields along the boundaries are difficult to recover accurately. Such difficulties typically occur for thin structures or structures with sharp edges and for closely positioned illuminating sources. Both problems can be solved by employing a localised MoM solution at the corners and near closely positioned sources as suggested in [54, 55]. This will, however, be at the expense of increased computational complexity. Alternatively, the positions and density of the auxiliary sources can be varied to improve the accuracy for such configurations. This was done in [56] for scatterers with corners and in [J2] for closely positioned illuminating sources. An alternative approach is rounding of the sharp edges as employed in [57, J2] and this is also used in the investigations of the Finite Ground Plane (FGP) influence in Chapter 5. The so-called Modified MAS [58] is an alternative to the Standard MAS and has been shown to be effective for thin structures, e.g., microstrip and dipole antennas. An investigation of the computational complexity between the MAS, Modified MAS, and the MoM is given in [59], and concludes that the MAS and the Modified MAS are preferable to the MoM in many cases.

In this study, a MAS formulation for smooth scatterers, closely resembling the Standard MAS, has been applied to analysis of FGPs [J2] as well as modelling of probe-fed DRA arrays [J3]. The MAS has previously proved useful for such large-scale problems, e.g., as in [60] where an antenna mounted on a car is analysed. The MAS has also been employed in the analysis of dielectric antennas in [61] where an infinite waveguide array with protruding dielectric elements is modelled.

Another variety of the MAS, which is particularly useful for wires, is that developed in [62]. Here auxiliary sources with finite lengths and sinusoidal currents are used, distributed more densely than is typically the case for the Standard MAS. This allows the auxiliary sources to be positioned much closer to the surface of the scatterer, and as a consequence it is well suited for modelling of wires. This type of MAS model has been used for the the analysis of mutual coupling in Chapter 3 as well as for analysis of sequentially rotated phased arrays in [R3, J6] and Chapter 6. For the details of this MAS formulation, reference is made to [62, R1].

2.1.4 *Finite Element and Finite Difference Methods*

The Finite Element Method (FEM) and Finite Difference Method (FDM) are fundamentally different from the MoM and MAS since the entire surrounding volume is discretised and not only the antennas and scatterers. For radiation problems such as antenna analysis the discretised volume can be bounded by so-called radiation boundaries or perfectly matched layers. Two commercially available programmes have been used which are based on the FEM and FDM, namely HFSS (High-Frequency Structure Simulator) [63], which employs a frequency-domain formulation, and CST-MS (CST Microwave-Studio) [64] which is based on FDM and uses both frequency and time-domain formulations. In [J1] HFSS was used for the modelling of a Cavity-Backed Annular Slot Antenna (CBASA) element, and in [J3] CST-MS was used for validation purposes.

2.1.5 *Examples of Application*

An example of application of some of the numerical methods, mentioned in this section, are given in virtue of the hemispherical DRA fed with a single probe. The physical configuration of the antenna is depicted in Figure 2.1a and Figure 2.1b shows the input impedance Z_{11}. The DRA has been modelled with the MAS, FDM (via CST-MS), and the analytical SWE technique. The MAS and SWE model are based on a probe current model in which it is assumed that the current is sinusoidal. This model is, however, not used in the CST-MS analysis and this leads to a deviation of about 2 % in the resonance frequency and about 20 % in the resistance at this resonance. The good agreement between the SWE and MAS results demonstrates that the MAS can accurately recover the field inside the DRA. Further discussions of the DRA array models can be found in [J3] where
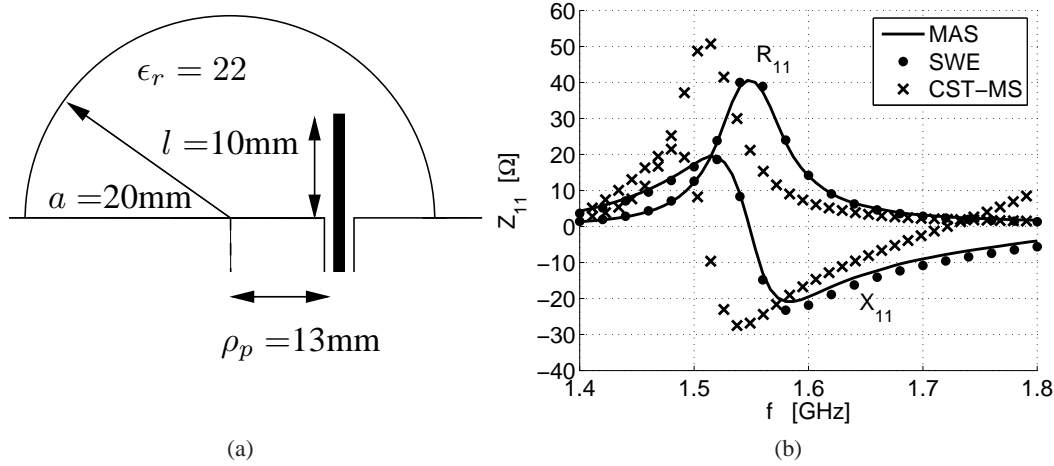
Figure 2.1: (a) *Hemispherical DRA with a single probe.* (b) *Impedance calculated with MAS, SWE, and FDM (CST-MS).*

similar examples are given.

2.2   Models of the Feed Network and Receiver Chain

In addition to the electromagnetic models of the radiating elements, the influences of the feed network and receiver chain must also be considered before the array performance can be accurately assessed. The feed network constitutes an important part of any antenna or array model, and it is necessary in order to evaluate the antenna excitations and reflection coefficients. By including a model of the receiver chain, some clarification can be obtained, as to whether the phased array G/T fulfills the requirements. It is noted here, that the quantities of actual interest when calculating the G/T is the main-beam realised gain G_{MB} and the system noise temperature T_{sys} which are defined in this section. The two subscripts MB and sys will be omitted in the following and G/T will be used instead of the more precise, but cumbersome, G_{MB}/T_{sys}.

2.2.1   Feed Network Models

The feed network is incorporated in the array model by combining known or assumed scattering matrices, that represent the various feed network components, with those of the array, as described in [65]. It allows calculation of the forward and reflected voltage waves at all ports of the components in the network as well as to represent a certain subset of the feed network by a single scattering matrix. An example of this is given in Figure 2.2 where an array of dual-feed antenna elements is fed via Wilkinson Power Dividers (WPDs), delay lines (DLs), and matching circuits. Here the scattering matrix $\overline{\overline{\mathbf{S}}}^{N}$ represents the network consisting of the antenna array, delay lines, and matching circuits.

The power reflected at the input of this combined network is assumed to be dissipated in loads in the WPDs. For a certain set of forward voltage waves $\mathbf{V}^{N+}(\theta_0, \phi_0)$ from the WPDs output, corresponding to specific scan angles (θ_0, ϕ_0), the reflected voltage waves of the combined network can be calculated

$$\mathbf{V}^{N-}(\theta_0, \phi_0) = \overline{\overline{\mathbf{S}}}^{N} \mathbf{V}^{N+}(\theta_0, \phi_0). \tag{2.1}$$

The input reflection coefficient of the i'th input terminal of the combined network is then

$$\Gamma_{in,i}^{N}(\theta_0, \phi_0) = \frac{V_i^{N-}}{V_i^{N+}} = S_{ii}^{N} + \frac{1}{V_i^{N+}} \sum_{j \neq i} S_{ij}^{N} V_j^{N+}. \tag{2.2}$$

Due to the mutual coupling terms S_{ij}^{N}, which are generally non-zero, the $\Gamma_{in,i}^{N}$ depend on the forward voltage waves fed to the other input terminals. These are selected in accordance with the desired scan angles and hence the $\Gamma_{in,i}^{N}$ are generally functions of the scan angles. The term scan loss is used here to signify the apparent loss resulting from this scan-dependent impedance mismatch. It is defined as

$$L_{scan}(\theta_0, \phi_0) = \left(1 - |\Gamma_{ant}(\theta_0, \phi_0)|^2\right)^{-1}, \tag{2.3}$$

where $|\Gamma_{ant}(\theta_0, \phi_0)|$ is defined as

$$|\Gamma_{ant}(\theta_0, \phi_0)| = \sqrt{\frac{\sum_i |V_i^{N-}(\theta_0, \phi_0)|^2}{\sum_i |V_i^{N+}(\theta_0, \phi_0)|^2}}. \tag{2.4}$$

$|\Gamma_{ant}(\theta_0, \phi_0)|^2$ is the ratio between the total reflected power, which is assumed to be dissipated in the loads of the WPDs in Figure 2.2, and the total input power. For a lossless array, $|\Gamma_{ant}|$ is similar to the so-called Total Active Reflection Coefficient defined in [66], which also includes conductor and dielectric losses.

The current excitations of the array elements can be calculated from the forward and reflected voltage waves at the terminals of the antenna elements

$$\mathbf{I}^A = \frac{1}{Z_0}(\mathbf{V}^{A+} - \mathbf{V}^{A-}), \tag{2.5}$$

where Z_0 is the characteristic impedance of the transmission lines. With these current excitations the array directivity can be calculated from the Active Element Patterns (AEPs) of the array. For notational convenience the main-beam co-polar directivity, D_{MB}, will be used repeatedly in the following chapters. It is defined by[*]

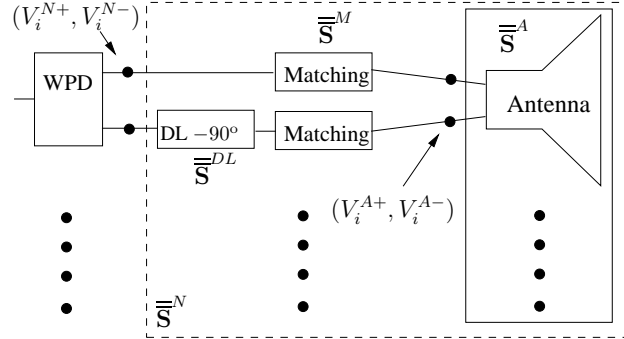$$D_{MB}(\theta_0, \phi_0) = D_{co}(\theta_0, \phi_0; \theta_0, \phi_0), \tag{2.6}$$

Figure 2.2: *Feed network for an array of dual-feed antenna elements. The scattering matrices for the array, matching circuits, and delay lines (DL) are combined in $\overline{\overline{\mathbf{S}}}^N$.*

i.e., it equals the co-polar directivity evaluated at observation angles (θ, ϕ) coinciding with the scan angles (θ_0, ϕ_0). In this work, the co-polar component is defined as the Right-Hand Circular Polarisation (RHCP) component and thus the Left-Hand Circular Polarisation (LHCP) is the cross-polar component. It is noted that some authors, e.g., [44], define the scan loss to include the variation of the D_{MB} with scan angle. This is, however, not the case in this text, as is also evident from (2.3).

2.2.2   Assumed Configurations of the Receiver Chain

In order to model the receiver chain, the system shown in the block diagram of Figure 2.3 has been assumed. It consists of a several parts which influence T_{sys}. After the antenna elements are filters, characterised by a loss L_{filter}, and Low-Noise Amplifiers (LNAs), with noise figure F_{LNA} and gain G_{LNA}. Following the LNAs are phase shifters with loss L_{PS}. The 7 circuits are combined in a combiner with loss L_{comb}. Following this, the signal is converted and demodulated, however, this is not included in the model.

The system noise temperature T_{sys} is the noise temperature just after the antenna elements as indicated in Figure 2.3. Different expressions of T_{sys} exist in the literature and differ with respect to the level of generality. To the knowledge of the author, the expression given in [67] is the most general and it specifically takes the scan-dependent impedance variation into account. The expression used here is a special case of the very general one of [67]. At the antenna input, see Figure 2.3, the system noise temperature is given by

$$T_{sys} = \eta_{ant} T_{ant}(1 - |\Gamma_{ant}|^2) + T_0(1 - \eta_{ant}) + T_0|\Gamma_{ant}|^2 + T_{RX}. \tag{2.7}$$

Here η_{ant} is the antenna efficiency which includes the losses in the feed network, L_{FN}, and antenna elements, L_{ele}, and T_{ant} is the antenna noise temperature. The expression in (2.7) deviates from that in [67] in that the thermodynamic temperature T_0 is assumed to apply for all components. Furthermore, all the receiver characteristics are included in the receiver noise temperature T_{RX}. For the configuration in Figure 2.3

$$T_{RX} = T_0\left(F_{LNA}L_{filter} - 1 + \frac{L_{filter}(L_{PS}L_{comb} - 1)}{G_{LNA}}\right). \tag{2.8}$$

---

[*]With this definition, it is assumed that the scan angles (θ_0, ϕ_0) can be chosen arbitrarily. In practice, however, this is not the case since the phase shifters only allow a discrete set of possible scan angles. Generally, that particular scan angle, among the finite set of possible scan angles, which maximises the G/T at the desired observation angle should be selected. However, for simplicity, the definition in 2.6 will be used in the following.
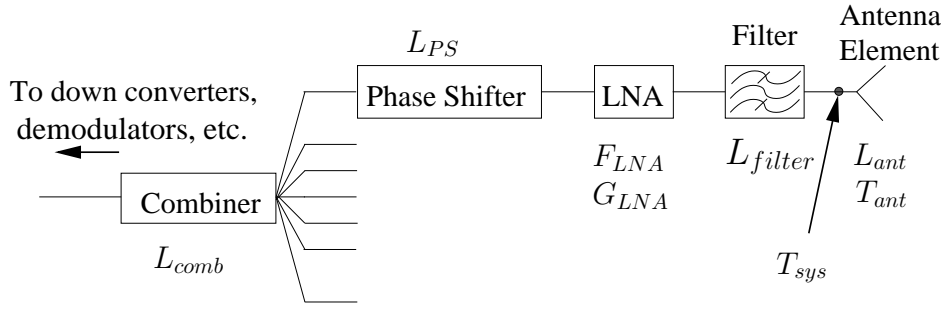
Figure 2.3:   *Block diagram of the assumed receiver configuration. L, G, T, and F denote loss, gain, noise temperature, and noise figure, respectively.*

Here L, G, and F with their respective subscripts denote the loss, gain, and noise figure, respectively, of the receiver components. The presence of Γ_{ant} in (2.7) implies that T_{sys} is in fact a function of the scan angle. The design of the receiver is, as mentioned, not within the scope of this study and the values assumed for the receiver are based on investigations in [68]. Further details of the receiver model are given in Chapter 4 where the three phased arrays of primary interest are presented.

With respect to the array gain, the mismatch due to reflections at the input terminals as well as the requirement of circular polarisation are included. It is, therefore, a function of scan angles (θ_0, ϕ_0) and reads

$$G_{co}(\theta_0, \phi_0; \theta, \phi) = \eta_{ant}(1 - |\Gamma_{ant}|^2)D_{co}(\theta_0, \phi_0; \theta, \phi). \tag{2.9}$$

By including the mismatch in this way, the gain G_{co} is usually referred to as the realised gain [44]. Similar to D_{MB}, the main-beam realised gain G_{MB} is defined as G_{co}, evaluated at observation angles coinciding with the scan angles. Expressed in terms of the losses, G_{MB} and T_{sys} can be expressed as [†]

$$G_{MB}(\theta_0, \phi_0) = \frac{D_{MB}(\theta_0, \phi_0)}{L_{FN}L_{ele}L_{scan}(\theta_0, \phi_0)}, \tag{2.10}$$

$$T_{sys}(\theta_0, \phi_0) = \frac{T_{ant}}{L_{FN}L_{ele}L_{scan}(\theta_0, \phi_0)} + T_0\left(2 - \frac{L_{FN}L_{ele} + L_{scan}(\theta_0, \phi_0)}{L_{FN}L_{ele}L_{scan}(\theta_0, \phi_0)}\right) + T_{RX}. \tag{2.11}$$

From (2.10) and (2.11) it follows that the impact of the array scan loss L_{scan} is significant since it reduces the G/T both by reducing the realised gain as well as by increasing the system noise temperature.

2.3   *Models of the Array Environment*

Three conceptually different schemes, which can be employed in phased array modelling, are presented in this section. The three schemes are presently denoted the Isolated Element Scheme (IES)[‡], the Infinite Array Scheme (IAS), and the Finite Array Scheme (FAS) and they differ in regard to how the array environment, surrounding the individual elements, is modelled. Which scheme is preferable depends on the array size, the available computational resources, and the desired accuracy. The three schemes are discussed in the following from a general perspective. Examples of applications are deferred to Chapter 3 where they are employed in investigations of the mutual coupling.

2.3.1   *Isolated Element Scheme (IES)*

In the IES, only the antenna elements of direct interest are included in the analysis. For instance, for calculation of the impedance properties, an isolated element, i, is modelled to obtain the self-impedance Z_{ii} whereas a two-element model, with elements i and j, is analysed for each combination of elements in order to obtain the entire set of mutual impedances Z_{ij}. This procedure can of course be used for the admittances Y_{ij} or scattering parameters S_{ij} also. Correspondingly, the AEPs are taken as the pattern of the isolated element. Thus the self impedances and AEPs are identical for all elements as are the mutual impedances between

---

[†]The antenna noise temperature, T_{ant}, is generally a function of the antenna directivity, i.e., scan angles, and the brightness temperature of the surroundings [15]. However, in this work it is approximated by a constant.

[‡]The IES is sometimes denoted the "Element-by-Element Approach" [69].

elements with the same relative separation. It is thus clear that in the IES, the antenna elements are analysed without the surrounding array environment being taken into account at all. Nevertheless, the knowledge of the mutual coupling, although calculated approximately, ensures that the element current excitations (2.5), and thereby the array radiation patterns, as well as the input reflection coefficients (2.2) can be calculated with some accuracy. Thus the influence from the surrounding elements is included to some extent, even-though the neighbouring elements are excluded for the initial calculation of the mutual coupling and AEPs.

The IES is the computationally least demanding of the three schemes but the lack of information on the array environment may lead to inaccurate results, in particular for large arrays. For array analysis, applications of the simple IES does not seem to be widespread, however, in [70] the IES is used to derive the mutual impedances between crossed dipoles in an array. A discussion of the accuracy of the method is, however, not given. The IES has been used in this study for investigating the mutual coupling for a range of different configurations and some of these results are discussed in Chapter 3.

2.3.2 *Infinite Array Scheme (IAS)*

In the IAS the array is modelled as an infinite periodic array with a progressive phase shift, corresponding to the desired scan angle. The Floquet modal formulation [69] can be used to calculate the input impedance of the elements for a specific scan angle. The input impedance resulting from this analysis is known as the Floquet impedance $Z^{\mathrm{FL}}(\theta_0, \phi_0)$. It is a function of the scan angle (θ_0, ϕ_0) and is identical for all elements.

Different approaches exist with which to derive the impedance properties and AEPs of a finite array from this analysis of the infinite array. These methods are characterised by varying levels of accuracy and complexity. An overview and discussion of the methods can be found in [71]. A simple approach for extracting the impedance characteristics is to perform a two-dimensional Fourier transform, as described in [69]. In this way the self and mutual impedances of the elements can be calculated, however, the resulting Z_{ij} are identical for elements with the same relative separation. Thus the influence of the element positions in the array, e.g., being near or far from the array edge, is not taken into account.

The advantages of the IAS are that the computation is done for a single element, or "unit cell" instead of many elements and that the array environment, i.e., the interaction between the elements, is taken into account at the same time. The disadvantages are that this interaction, being calculated for an infinite array, is not necessarily accurate for a finite array. Also, the computation must be performed for each scan angle, which implies that the method is much more computationally expensive than the IES. This is especially the case if the self and mutual impedances are desired, since the Floquet impedances must be sampled with a reasonable density in the scan angles (θ_0, ϕ_0) in order for the Fourier transformation to be accurate. The technique is very useful for large arrays where each element is surrounded by several others, however, for small arrays or for elements near the array edge, the results are inaccurate [69]. The IAS has found wide-spread use for analysis of microstrip patch arrays with one or more layers of dielectric substrate as well as printed dipole antennas [72]. It is particularly useful for the prediction of scan blindness which may be caused either by grating lobes or surface waves in dielectric substrates [73, 74]. In Chapter 3, an example of this is given.

2.3.3 *Finite Array Scheme (FAS)*

By modelling the entire finite array, all elements are included in the model. The advantages of the FAS are that the interactions between the elements are taken fully into account and thus the individual element positions in the array are correctly modelled. Hence the self- and mutual impedances are not simple periodic repetitions as is the case for the IES and IAS, and also the AEPs are generally different. The disadvantages of the FAS are that for large arrays it is seldom possible to model the entire array without extensive computational resources and even for small arrays it may be difficult.

The FAS has been used for most of the array investigations in this study. In particular, the three 7-element arrays investigated in Chapter 4 are sufficiently small as to be modelled with the FAS. However, for certain simple element types larger arrays have also been investigated with the FAS. In Chapter 3, the method is thus applied to arrays of up to 91 elements.

2.4 Three-Stage Model of Arrays on Finite Ground Planes

The mathematical models discussed above will be employed in Chapter 4 for investigations of the three different phased arrays. This is done in three stages, described in the following. The purpose is to assess the array performance including the impact of an FGP, the receiver, and feed network. In [J2, J4], two-stage models were employed for analysis of antennas and arrays positioned on large or moderate-sized FGPs. These models do not include the receiver and feed networks, and therefore, the third stage is added in the present analysis.

The first-stage analysis focuses on modelling the radiating elements of the array. Since the ground plane is not of particular importance at this stage, it can be chosen as either a small FGP or an IGP, and hence it does not represent an excessive computational cost. The antenna can, therefore, readily be analysed with the methods discussed in the Section 2.1. From this analysis the antenna characteristics, such as currents on wires, fields in apertures, as well as impedance

Stage	Task
1	Analysis of array on small FGP or IGP
2	Influence of large or moderate-sized FGP
3	Inclusion of feed network and receiver

Table 2.1: *The three stage of array analysis.*

characteristics, can be obtained [J2]. Similarly in [J4], the auxiliary sources from a first-stage MAS model is used to characterise DRAs. These characteristics can be used to represent the antenna in the second stage of the analysis which focuses on the FGP.

In the second-stage analysis, the antenna characteristics from the first-stage analysis are employed to form a scattering problem in which the calculated currents, aperture fields, or auxiliary sources, illuminate the FGP. The second-stage model takes outset in the assumption that the antenna characteristics are not affected by replacing the IGP with the FGP, which is a reasonable assumption for large and moderate-sized FGPs. Indeed, for low-profile antennas, such as microstrip and slot antennas, investigations [75, 76] have shown that the input impedance is largely unaffected by the FGP size, even for small FGPs. However, other investigations [77, 78] conclude that for high-profile antennas such as monopoles and helix antennas, some variation with the FGP size may be expected for small FGPs. Further details of the implementations of the first and second stages are given in [J2, J4, R2]. An example of a second-stage analysis is given in Figure 2.4. The investigated configuration is that of a pair of crossed magnetic Hertzian dipoles, excited in phase quadrature, centred $0.03 \lambda_0$ above a $2 \lambda_0$ radius circular FGP, where λ_0 is the free-space wavelength. The configuration has been modelled in [J2] with the MAS and the HOPES programme, mentioned in Section 2.1.2. The results are very similar, except for a slight deviation in the cross-polar component. This deviation is a consequence of the FGP edges being rounded in the MAS model. For a further discussion of this, see [J2].

In the third-stage analysis, the feed network and receiver are included, as discussed in Section 2.2, leading to the assessment of the array G/T. The three stages of the analysis have been employed for the arrays discussed in Chapter 4, as summarised in Table 2.1. However, the order in which the three stages are applied is not rigidly followed in all cases. The CBASA and DRA arrays are analysed in the order 1-2-3 whereas the PDDA array analysis is done in the order 1-3-2. The reason is that a GA optimisation, described in Section 2.5, is employed and this requires a fast evaluation of the array performance. In this case the G/T is calculated for the IGP case, which can be done relatively fast with AWAS, and the FGP analysis is then deferred to later.

2.5 Genetic Algorithm Optimisation

The GA optimisation technique belongs to the class of global optimisation techniques. The object to be optimised is represented by an object function which must be either maximised or minimised and which has a number of parameters that can be adjusted. Global optimisation techniques are in many ways preferable to local optimisation techniques, in particular when large parameter spaces are analysed, since the local techniques are likely to find a local optimum instead of the global optimum [79].

During the last decade, the GA has become increasingly popular in the electromagnetic community due to its suitability to complex problems, and [79] gives an overview of electromagnetic applications of the technique. Besides its suitability to problems with large parameters spaces, other favourable features are the abilities to deal with discontinuous solution domains and non-differentiable object functions. This last feature separates the GA from gradient methods which do not handle these challenges well. A weakness of GA is the
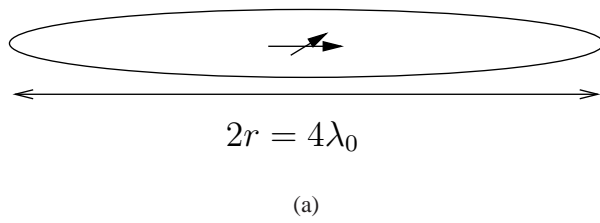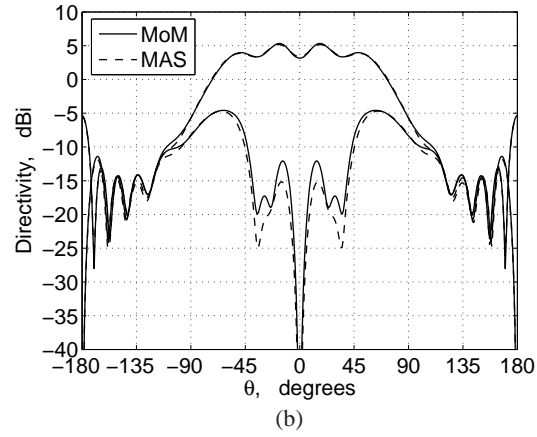
$$2r = 4\lambda_0$$

(a)

(b)

Figure 2.4:   (a) *Crossed magnetic Hertzian dipoles in phase quadrature above a circular FGP modelled with MAS.* (b) *Directivity of this configuration. The figure is taken from [J2].*

convergence rate which is not as fast as for many local optimisation techniques. The object function must be evaluated many times before an optimum is obtained and this implies that, even though the GA may in principle provide the true global maximum it is not always a feasible approach. Clearly, the suitability and practicability of using GA is highly dependent on the time it takes to perform a single evaluation.

The GA has been used in combination with the MoM programme AWAS 2.0 to analyse the PDDA array. The computationally inexpensive nature of AWAS makes the problem well suited for GA optimisation. The programme developed for this purpose was based on the C++ GA package "GAlib" [80] which is freely available from the Internet. The object function of the GA algorithm consists of the output from AWAS with additional post processing which comprises calculation of array directivity, gain, G/T as function of scan angles and frequency as described in Section 2.2. Additional details of these calculations can be found in [R2].

2.6   Summary

In this chapter, different mathematical models have been presented. The models were divided into specific techniques for solving electromagnetic problems, incorporation of the array feed network and receiver chain, and overall conceptual array models. Last, a discussion on the GA used for optimisation was given.

The different analytical and numerical methods employed for the electromagnetic simulations were initially discussed. The numerical techniques are used both via existing software and programmes developed in the course of this study and comprise the MoM, MAS, FEM, and FDM. Particular attention was devoted to the MAS since this is the method used most frequently.

The calculation of the G/T requires incorporation of the antenna feed network and receiver chain. Based on assumed characteristics, these are incorporated in the array analysis. This allows calculation of the array scan loss and realised gain which, together with other factors, determine the array G/T.

Three conceptually different array modelling schemes, the IES, IAS, and FAS were subsequently discussed, and the advantages and disadvantages were pointed out. Examples of the methods are given in Chapter 3.

By combining the electromagnetic analysis tools and the receiver and feed network models, a three-stage model for analysis of phased arrays on FGPs has been established. The method is based on a first-stage analysis in which the radiating elements are positioned on a small FGP or on the IGP. The results from this analysis is used in the second-stage analysis which incorporates large or moderate-sized FGPs. Last, the feed network and receiver is taken into account in the third stage. Examples of results, using the first- and second-stage models, were given in virtue of a probe-fed DRA and a pair of crossed Hertzian dipoles above an FGP. In both cases, the results agreed well with reference solutions. For the DRA, different probe models resulted in minor deviations for the antenna input impedance.

Last, the GA used for the optimisation of the PDDA array was discussed and both the electromagnetic simulations, feed network and receiver models were incorporated to evaluate the performance of each array design. The GA is computationally expensive since the convergence rate is quite slow. However, if used in combination with computationally inexpensive simulation tools, such as AWAS, the GA optimisation can be a very useful tool.

CHAPTER 3

MUTUAL COUPLING

As discussed in Section 2.2.1, the mutual coupling between the antenna elements is responsible for a scan-dependent impedance mismatch leading to scan loss. Furthermore, the coupling introduces errors in the current excitations of the element input terminals which may lead to an increase in the cross-polarisation as well as inaccuracy in the beam scanning. Investigations of the mutual coupling have been reported for many types of antennas, representative examples being microstrip antennas [81], Dielectric Resonator Antennas (DRAs) [82], dipole antennas [83], and slot antennas [84].

In this chapter, the impact on the mutual coupling, due to different array environments, is discussed and some means of reducing the mutual coupling are pointed out. The investigations focus on the impact of the antenna elements, the array size, different ground planes, and parasitic structures in the array. The implications on the array scan loss are also addressed for some of the configurations. The topic is related to Wide Angle Impedance Matching (WAIM) which denotes techniques that aim at decreasing the scan loss in general [85]. Such techniques are, however, very general and span beyond a reduction of the mutual coupling. A brief overview of different WAIM techniques is given in the last section of the chapter.

3.1 Crossed Dipole Antenna Element and Array

For demonstration purposes, many of the points discussed in this chapter are illustrated with examples. To this end, a hexagonal array consisting of circularly polarised Crossed Dipole Antenna (CDA) elements is employed and investigated for a range of different configurations. A single CDA element is depicted in Figure 3.1a. The two crossed dipoles are parallel to the x and y-axes, respectively, which is indicated with subscripts x and y in the following. The dipoles have lengths L, widths w, and are each fed at an input terminal between the dipole arms. They are positioned above an Infinite Ground Plane (IGP) at a height h. In some cases, parasitic monopoles with height h_{mp} and width w are introduced near the ends of the dipole arms. The CDA elements are separated by the distance d as shown in Figure 3.1b. The particular CDA designs vary somewhat depending on the investigation, albeit, L and w are fixed at $L = 0.4\lambda_0$ and $w = 0.01\lambda_0$. The circular polarisation is achieved by exciting the two dipoles in the CDA element with forward voltage waves, V_x^+ and V_y^+, in phase quadrature such that $V_y^+ = -jV_x^+$.

An example of a hexagonal array of CDA elements is shown in Figure 3.1b with elements arranged in concentric hexagonal "rings" around the centre element. This example shows a 19-element array with 2 rings. The number of elements N and the number of rings R are related by

$$N = 1 + 3R(R + 1). \tag{3.1}$$

The CDA array is modelled using the three array models, discussed in Section 2.3, the Isolated Element Scheme (IES), Finite Array Scheme (FAS), and the Infinite Array Scheme (IAS), which are implemented using two different numerical models. For the IES and FAS, the Method of Auxiliary Sources (MAS) technique derived in [86] is used, while for the IAS case, the Floquet-mode/MoM derived in [73, 74] is used.

3.2 Influence of the Element Radiation Pattern

The amount of coupling between two elements is strongly related to the element radiation patterns. This is intuitively reasonable since antennas with wide beams will radiate more toward the neighbouring elements than antennas with narrow beams. Examples of elements which have a relatively large coupling are thus dipoles in free space, monopoles, DRAs and slot antennas which all have wide elements patterns, whereas microstrip antennas and dipoles above ground planes typically exhibit less coupling due to their more narrow
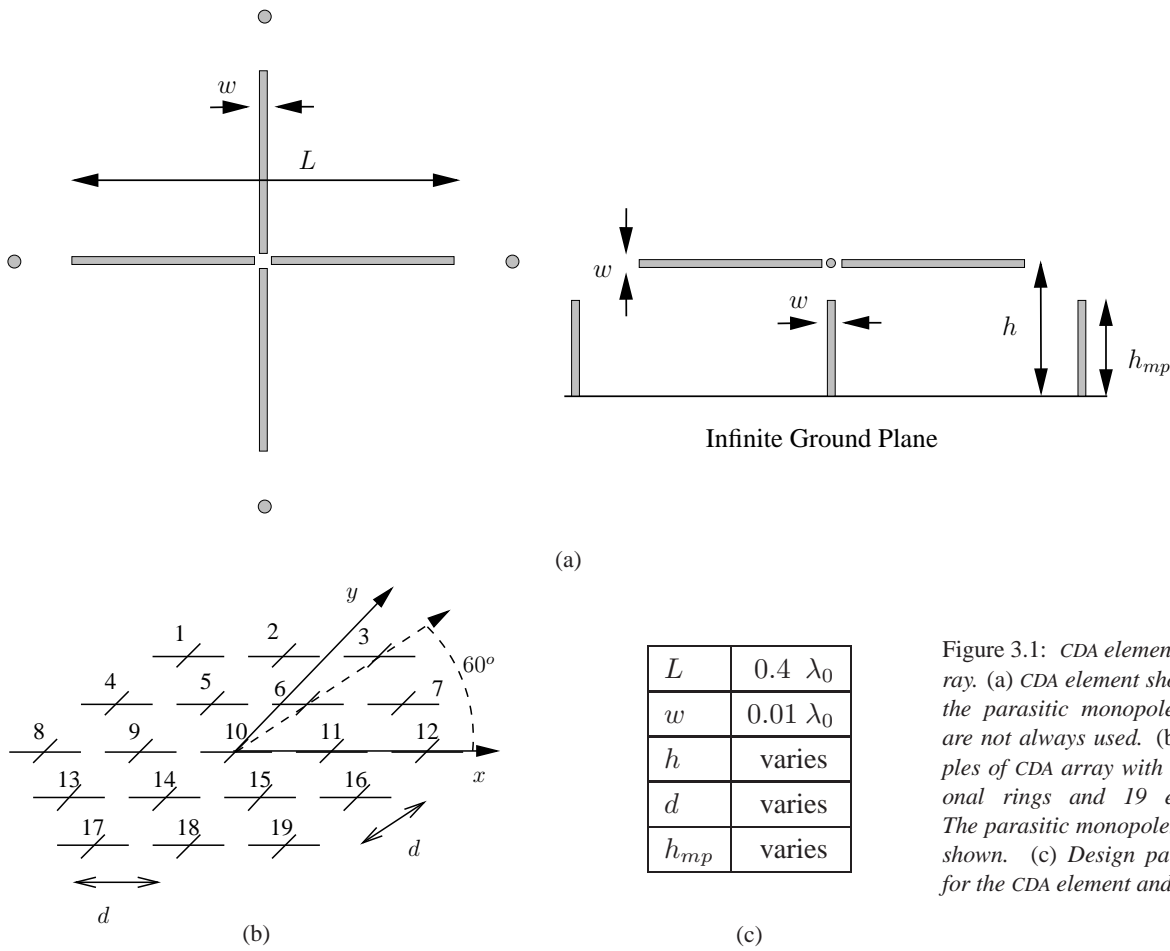
(a)

(b)

L	$0.4\ \lambda_0$
w	$0.01\ \lambda_0$
h	varies
d	varies
h_{mp}	varies

(c)

Figure 3.1: *CDA element and array.* (a) *CDA element shown with the parasitic monopoles which are not always used.* (b) *Examples of CDA array with 2 hexagonal rings and 19 elements. The parasitic monopoles are not shown.* (c) *Design parameters for the CDA element and array.*

patterns, as demonstrated in [82].

A simple way to illustrate the influence of the radiation patterns is to consider a configuration of two CDAs without parasitic monopoles ($h_{mp} = 0$). The relative positions of the two CDAs are similar to those of elements 1 and 2 in Figure 3.1b. Four different heights h above the ground plane as well as a free-space case, indicated by $h = \infty$, are investigated. It is well known that a change in h will affect the radiation pattern, and thus when the antenna is close to the ground plane the radiation pattern will be relatively narrow but will become more broad as h is increased. The co-polar directivity D_{co} of an isolated CDA element and the mutual coupling between the two y-directed dipoles, S_{12}^{yy}, are shown in Figure 3.2a,b, respectively. From this example it is clearly seen that the coupling is larger for the configurations having the broad beams, particularly for the wide separations. For separations of $d = 0.5\ \lambda_0$ the difference is, however, not very large, and S_{12}^{yy} varies between -15 dB and -20 dB.

3.3   *Influence of the Array Size*

The self- and mutual impedances will to some extent be influenced by the surrounding elements due to scattering within the array. The extent to which this happens depends on the number of surrounding elements, i.e., the array size. Even more so, the input reflection coefficients $\Gamma_{in,i}$ are influenced since they depend directly on the excitations of the surrounding elements, as seen from (2.2). In this section, the impact off the array size on the mutual coupling and input reflection coefficient is investigated.

The CDA arrays are now modelled using the IES, FAS, and IAS. For the FAS, an array with 91 elements, arranged in 5 hexagonal rings constitute the practical limitation due to the available computational resources. For the IES, very large arrays can be investigated since the only practical limitation comes from the size of the scattering matrices. Arrays consisting of up to $R = 25$ rings ($N = 1951$ elements) have thus been modelled with the IES.
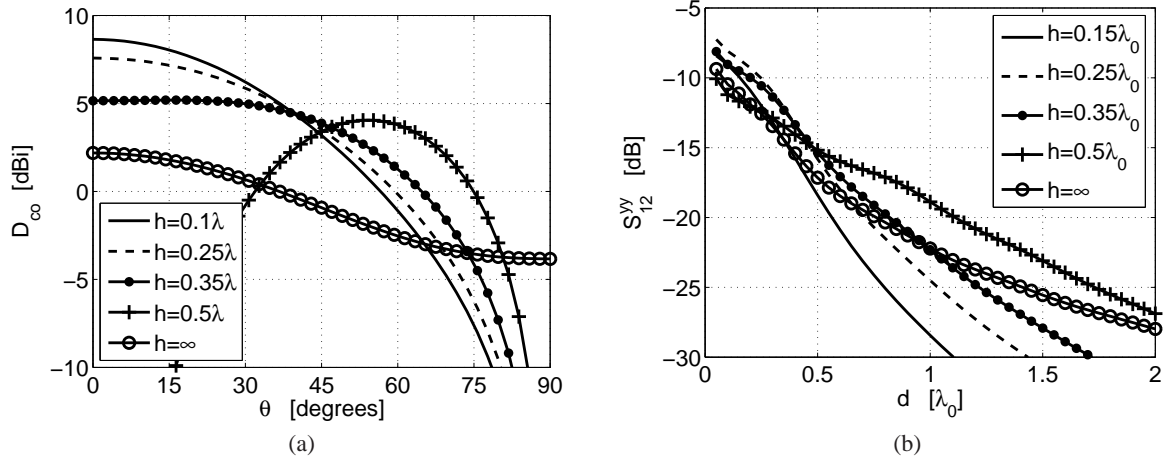
Figure 3.2: *Radiation patterns and mutual coupling for CDA elements at different heights without monopoles, $h_{mp} = 0$. (a) Co-polar directivity D_{co} of CDA element for different heights h. (b) Mutual coupling between the two y-directed dipoles as function of h and separation d.*
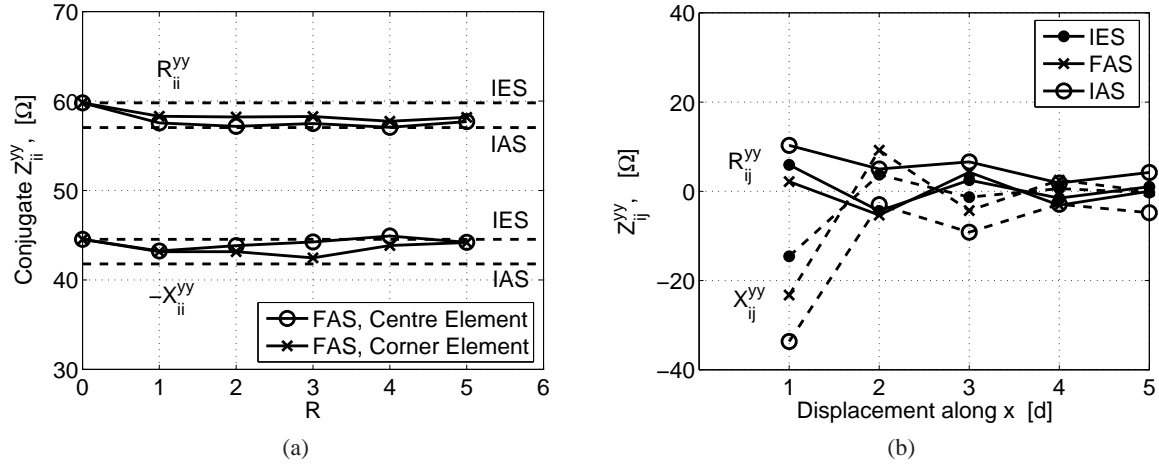

Figure 3.3: *Self- and mutual impedances for y-directed dipoles of the CDA elements for $h = 0.25 \lambda_0$, $d = 0.5 \lambda_0$, and $h_{mp} = 0$. (a) Self impedance (conjugate value is shown for graphical convenience) as function of array size (number of rings, R). (b) Mutual impedance between the centre element and neighbouring elements towards increasing x.*

A few examples of the self- and mutual impedances, calculated with the three methods, are shown in Figure 3.3a,b. This is done for $h = 0.25 \lambda_0$, $d = 0.5 \lambda_0$, and $h_{mp} = 0$. The self impedances of the y-directed dipoles Z_{ii}^{yy} are shown in Figure 3.3a, for the corner and centre elements, corresponding to element 1 and 10 of the 19-element array in Figure 3.1b. For graphical convenience the complex conjugate value of Z_{ii}^{yy} is shown. For the FAS, Z_{ii}^{yy} is shown as function of the number of element rings R. The corresponding values for the IES and IAS are shown as horizontal broken lines. It is seen that the FAS results are almost constant and generally they are within the bounds set by the IES and IAS results. However, the FAS results do not necessarily converge to the IAS results as R increases. This is particularly the case for the reactance X_{ii}^{yy}.

In Figure 3.3b, the mutual impedance Z_{ij}^{yy} between the y-directed dipoles of the centre element and the neighbouring elements along the positive x-axis is shown. This corresponds to elements 10, 11, and 12 in Figure 3.1b. For the FAS this is calculated for a 5-ring array (91 elements). The results are generally quite similar. It is seen, however, that the IAS results deviate somewhat from the FAS results, particularly for the large element separations, corresponding to the case where one element is near the edge of the array. Thus the mutual impedances calculated with the IAS are generally higher than that calculated with the more accurate FAS. In conclusion, the impacts of the array size, and which calculation scheme is used do not influence the self impedance results very much. However, some difference exists for the mutual impedance, particularly for large element separations.

Although the self- and mutual impedances are almost constant with array size, the input impedance and input reflection coefficient are not. From (2.2) it is clear that the number of neighbouring elements and their
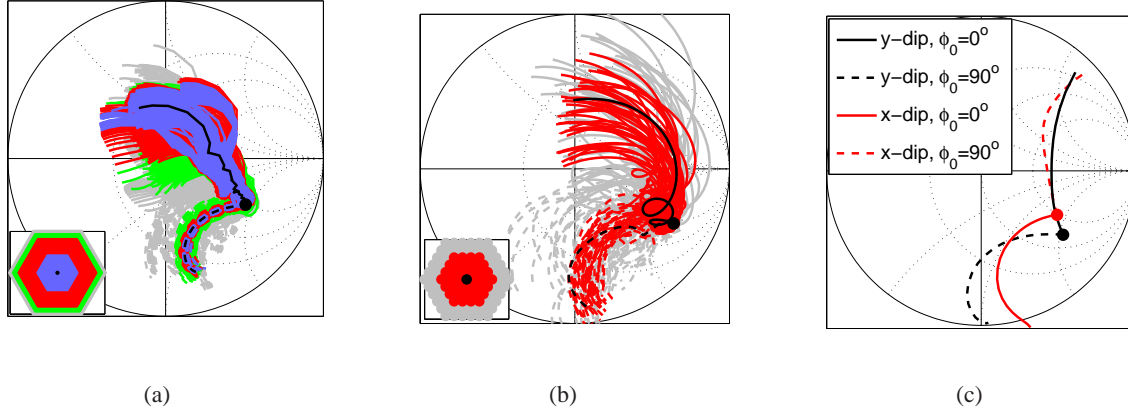
(a)   (b)   (c)

Figure 3.4:   *Input reflection coefficient of CDA elements shown in Smith charts for a characteristic impedance of* $50\ \Omega$. *The configuration is the same as in Figure 3.3.* (a) *1951-element array calculated with the IES (using MAS), only* $\Gamma^y_{in,i}$ *is shown.* (b) *91-element array calculated with the FAS scheme (using MAS), only* $\Gamma^y_{in,i}$ *is shown.* (c) *Infinite array calculated with the IAS (using MoM), both* $\Gamma^y_{in,i}$ *and* $\Gamma^x_{in,i}$ *are shown.*

excitations have direct influence on this. This implies that the element position in the array, the size of the array, and also which calculation scheme is used have some impact on the final result. In Figure 3.4a-c, the input reflection coefficients $\Gamma_{in,i}(\theta_0,\phi_0)$ of the dipoles are shown as function of scan angles (θ_0,ϕ_0). Each dipole is represented by two lines, a solid line indicating $\Gamma_{in,i}(\theta_0,0^\circ)$ for scanning in the $\phi=0^\circ$ plane and a dashed line indicating $\Gamma_{in,i}(\theta_0,90^\circ)$ for scanning in the $\phi=90^\circ$ plane. The big dots indicate $\theta_0=0^\circ$ and the ends of the lines indicate $\theta_0=90^\circ$. The purpose of the plots is to show the variation of the element reflection coefficients due to the different positions in the array and not to distinguish between particular curves.

Figure 3.4a shows the case of a 25-ring array (1951 elements) calculated with the IES. Only the results for the y-directed dipoles, $\Gamma^y_{in,i}$ are shown. The elements are indicated by different colours corresponding to the proximity to the array edge. The significance of the element position in the array is clearly seen from this figure. There is a significant spread among the curves even for the elements close to the centre, shown in blue. This spread increases for the elements closer to the edges, and the two outer rings, shown with grey, behave very differently from the rest, as well as from each other. Figure 3.4b shows the corresponding results for a 5-ring array (91 elements) calculated by the FAS. Again the elements behave differently according to their positions. In Figure 3.4c the results for the IAS are shown and $\Gamma^x_{in,i}$ for the x-directed dipoles is also shown. In this case the elements behave the same by definition, and thus only a single curve results for each dipole orientation and scan plane. From a comparison of

Figure 3.5:   *Scan loss CDA array with* $N = 7, 19, 91$ *(FAS), and* ∞ *(IAS). The configuration is the same as in Figure 3.3*

the 3 plots in Figure 3.4a-c, it is clear that the IES does not yield similar high values of the reflection coefficients as the FAS, nor does it resemble the IAS results very much. For the IAS the reflection coefficients are very large for $\theta_0=90^\circ$ and they generally deviate significantly from the FAS results. In Figure 3.5, the corresponding scan loss, calculated using (2.3), is shown for different array sizes when the dipoles are matched to their self impedances Z^{xx}_{ii} and Z^{yy}_{ii}. The calculations are based on the FAS for the finite arrays and the IAS for the infinite array. It is obvious that the scan loss of the finite arrays generally grows with the array size and comes closer to that of the infinite array as the array size increases. It is furthermore clear, that for small arrays the approximate IAS is not accurate and it does not recover the scan loss results of the FAS.
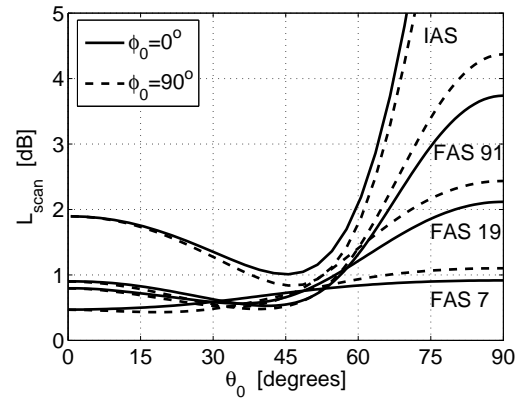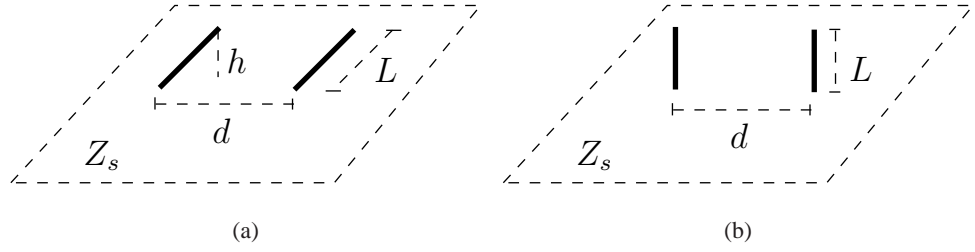
Figure 3.6: *Configurations of simple antennas on an impedance ground plane of infinite extent.* (a) *HWD.* (b) *QWM.*

3.4 Influence of the Ground Plane

The ground plane beneath the antenna elements may influence the mutual coupling in a number of ways. The presence of a dielectric coating or surface corrugations directly affect the electrical properties of the ground plane and thus its ability to support surface waves [87]. Such surface waves are generally undesired, in particular for phased array applications, since they tend to increase the mutual coupling between the elements. Surface waves are bound to the ground plane and, as opposed to waves travelling in free space, they propagate in a 2-dimensional domain. Thus the coupling between two antennas due to surface waves will only decrease slowly with the distance. Surface waves can be separated into Transverse Electric (TE) waves, where the electric field is parallel to the ground plane, and Transverse Magnetic (TM) waves, where the magnetic field is parallel to the ground plane.

3.4.1 Impedance Ground Planes

In many cases it is convenient to represent surface corrugations and thin dielectric coatings by assigning an effective surface impedance Z_s to the ground plane [88]. For moderate values of Z_s, the ability of the ground plane to support or suppress surface waves depends on whether the surface impedance is capacitive or inductive. Ground planes with inductive surface impedances support TM waves whereas capacitive ground planes support TE waves [88].

Two simple antenna configurations are used for illustrating the coupling via surface waves. They are modelled under the assumption of an impedance ground plane of infinite extent. For such a configuration the fields radiated by the antennas can be evaluated using the mathematical results derived in [89]. Due to the complexity of these calculations it has not been practical to employ the MAS model to these problems and for this reason the CDA elements are not used here. Instead the antenna configurations consist of two Quarter-Wave Monopoles (QWMs) of length $L = 0.25\,\lambda_0$ and two Half-Wave Dipoles (HWDs)

Figure 3.7: *Mutual coupling between the HWD and QWM on an infinite impedance ground plane. The configurations are $L = 0.5\,\lambda_0$, $w = 0.02\,\lambda_0$, $h = 0.05\,\lambda_0$ for the HWD and $L = 0.25\,\lambda_0$, $w = 0.02\,\lambda_0$, $h = 0\,\lambda_0$ for the QWM.*

of length $L = 0.5\,\lambda_0$, located $h = 0.05\,\lambda_0$ above the ground plane. The wire width is $w = 0.02\,\lambda_0$ in both cases. The configurations are shown in Figure 3.6a,b. The shape of the currents on the QWMs and HWDs are assumed to be sinusoidal and given by

$$I_{HWD}(y') = I_0 \sin(k_0[L/2 - |y'|]), \quad y' \in [-L/2, L/2], \tag{3.2a}$$
$$I_{QWM}(z') = I_0 \sin(k_0[L - z']), \quad z' \in [0, L], \tag{3.2b}$$

respectively. I_0 is a constant and k_0 is the free-space wave number. From these currents and the electric field, calculated from the expressions in [89], the self and mutual impedances have been calculated using the reaction theorem [90]. Since the antennas extend above the ground plane, the mutual coupling can not be attributed exclusively to the surface waves. This is particularly the case for the QWMs which extend $0.25\,\lambda_0$ above ground plane, however, a significant impact of the surface impedance is still evident.
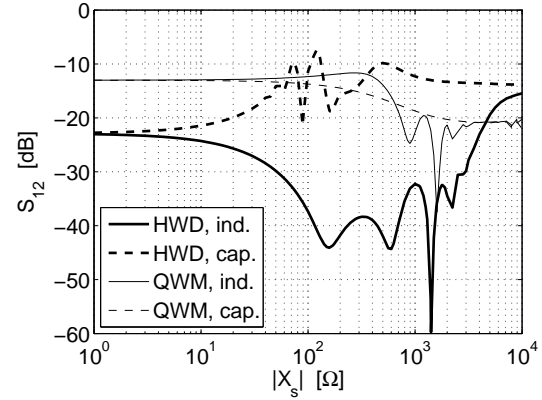
In Figure 3.7 the coupling coefficient S_{12} for the HWD and QWM configurations is shown as function of a purely reactive surface impedance $Z_s = jX_s$. For negative X_s the ground plane is capacitive and for positive X_s it is inductive.

For the HWD case, the coupling is relatively small when $|X_s|$ is small. This is expected since the ground plane is almost a Perfect Electric Conductor (PEC) which suppresses the TE surface waves. For medium-range values of $|X_s|$ the coupling is larger in the capacitive case illustrating that the TE surface waves are not suppressed as much, whereas the coupling is smaller in the inductive case illustrating that they are suppressed even more.

In the QWM case, the opposite behaviour is, to some extent, visible. The relatively large coupling from the PEC case remains, even for large $|X_s|$, but for $|X_s| \simeq 500\,\Omega$ the difference between the capacitive and inductive impedances becomes evident. Thus the TM surface waves are suppressed slightly more by the capacitive ground plane leading to a decrease of the coupling, while for the inductive one the coupling increases.

For large value of about $|X_s| \simeq 10^3\,\Omega$ the coupling diminishes for the QWM and increases for the HWD configurations, for both the inductive and capacitive ground planes. An explanation for this can be gained from the so-called Standard Impedance Boundary Condition (SIBC) [91] which is an approximate model of impedance surfaces. The SIBC reads

$$\hat{\mathbf{n}} \times \mathbf{E} = Z_s \hat{\mathbf{n}} \times (\hat{\mathbf{n}} \times \mathbf{H}), \tag{3.3}$$

where $\hat{\mathbf{n}}$ is the normal vector to the ground plane, and $\mathbf{E}$ and $\mathbf{H}$ are the electric and magnetic fields, respectively. In the PEC case ($Z_s = 0$), it is clear that the tangential component of the electric field will vanish since (3.3) reduces to $\hat{\mathbf{n}} \times \mathbf{E} = 0$. Thus the TE surface waves vanish and do not contribute to the coupling. In the case of a large value of $|Z_s|$ this is not the case, and as Z_s approaches infinity (3.3) reduces to $\hat{\mathbf{n}} \times \mathbf{H} = 0$, i.e., the TM surface waves vanish and do not contribute to the coupling. Such a surface is equivalent to a Perfect Magnetic Conductor (PMC) [90].

3.4.2   Grounded Dielectric Substrates

In the case where the dielectric substrate, which covers the ground plane, is thin it can be represented by an impedance surface [88], thus justifying the analysis of the previous section. In cases where the substrate is thick, this simple representation is not accurate and both TE and TM surface waves of different modes can propagate depending on the thickness and dielectric constant of the substrate. In these cases, the dielectric coating can instead be modelled as a waveguide and the analysis becomes considerably more complicated. It should be noted that for these cases, the term "surface wave" is still used by many authors, for instance [88]. Here the term "guided wave" is adopted.

With regard to phased arrays the excitation of these guided waves can have severe consequences and cause significant scan loss. In practical cases where the substrate is reasonably thin, it is typically only the zero-order TM mode, TM_0, that can propagate. Higher-order TM and TE modes may also propagate, however, only if the substrate thickness and dielectric constant are sufficiently large [88].

Figure 3.8:   *Input reflection coefficient for infinite CDA array with dielectric material beneath the dipoles. The configuration is the same as in Figure 3.3 except for the $\epsilon_r = 2.5$ substrate below the dipoles. The dots indicate $\theta_0 = 0°$ and the circles $\theta_0 = 67°$.*

The antenna elements, such as slots or microstrip patches, will thus excite the TM_0 mode regardless of the substrate thickness and in special cases higher-order modes may also be excited. A significant amount of the power fed to the phased array may thus become trapped as a guided wave inside the substrate and couple to the neighbouring elements, leading to a high scan loss. The excitation of guided waves and the criteria for scan blindness have been widely investigated in the literature. Depending on the substrate, element locations, and scan angle, the guided waves may couple strongly to other elements [69]. In particular it can be shown
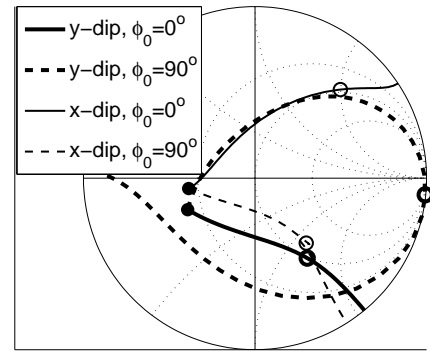
[72], that for infinite arrays total scan blindness may occur. In general an increase in the element separation and widening of the scan angle will increase the possibility of guided waves to cause scan loss.

As an example, the infinite CDA array discussed in Section 3.3 is revisited, this time with the volume below the dipoles filled with a dielectric material with $\epsilon_r = 2.5$ but with all other parameters retained. It can be theoretically predicted [72], that for this combination of substrate thickness and permittivity, scan blindness occurs for the y-directed dipole for a scan angle of approximately $(\theta_0 = 67^{\mathrm{o}}, \phi_0 = 90^{\mathrm{o}})$. In Figure 3.8 the input reflection coefficient for this configuration is shown. Since the configuration is identical to the one investigated in Section 3.3, except for the dielectric constant of the region below the dipoles, the results can be compared with those in Figure 3.4c. This example clearly demonstrates the scan blindness that may occur due to guided waves in the substrate. It is noted that the occurrence of scan blindness, such as shown in this example, does not happen for finite arrays [92] where only partial scan blindness, or scan loss, occurs. Another aspect, which is not obvious from the present example, is that in all practical cases the dielectric substrate is of finite extent. This implies that at the substrate edges some of the guided wave power will radiate out of the substrate and some will be reflected back into the substrate. The latter will cause standing waves in the substrate which will affect the mutual coupling.

3.4.3   *Artificial High-Impedance Surfaces*

In Figure 3.7 it was seen that neither the capacitive nor inductive impedance ground planes suppress both the TE and TM surface waves. For very high surface impedances the TM surface waves are attenuated, however, at the same time the TE waves are allowed to propagate. A useful surface for reducing the mutual coupling must therefore suppress both TE and TM surface waves. Such surfaces are denoted soft surfaces, while surfaces that support both TE and TM waves are denoted hard surfaces [93].

Just as a high-impedance or PMC surfaces do not exist naturally, neither do hard and soft surfaces. However, various designs have been proposed which simulate soft surfaces in some frequency bands. Surfaces which behave in this way are generally referred to as Electromagnetic Band Gap (EBG) surfaces [94] since they prevent the propagation of surface wave in certain frequency bands.

One of the simplest examples of a soft surface is the corrugated ground plane which is essentially a PEC ground plane with parallel grooves. For grooves with a depth of $\lambda_0/4$ such a corrugated ground plane can be considered as a grid of alternating PEC and PMC strips and, depending on whether the surface wave propagates parallel or perpendicular to the grooves, it exhibits hard or soft properties [93]. Thus, an arrangement of concentric grooves surrounding an antenna will suppress both the TM and TE surface waves propagating away from the antenna. This idea has been pursued in [95] where surface corrugations are applied parallel to radiating slots to suppresses the TM surface wave propagation across the grooves. Clearly, an EBG ground plane which is soft regardless of the direction of propagation would be useful, and surfaces which come close to this behaviour have been constructed in various forms. In [96] an EBG ground plane consisting of vertical metallic pins embedded in a substrate is investigated theoretically with the aim of suppressing the TM surface wave coupling between magnetic dipoles. More recently, another such surface, shown in Figure 3.9 and sometimes denoted the Sievenpiper surface [97], has been developed in [87]. It should be noted, however, that compared to a conventional PEC ground plane the TE surface waves

Figure 3.9:   *Examples of an artificial high-impedance ground plane, sometimes denoted a Sievenpiper surface.* (a) *Side view.* (b) *Top view. The figures are taken from [87].*

are suppressed to a lesser extent [98]. The ability to reduce the mutual coupling by suppressing both TE and TM surface waves has been experimentally verified in [87, 97]. In [99] a similar EBG ground plane is applied between the elements of a microstrip patch array. From a theoretical investigation of an infinite array it is found that a significant decrease of scan loss can be achieved.

Another consequence of employing such artificial surfaces is that the E- and H-plane of the antenna radia-
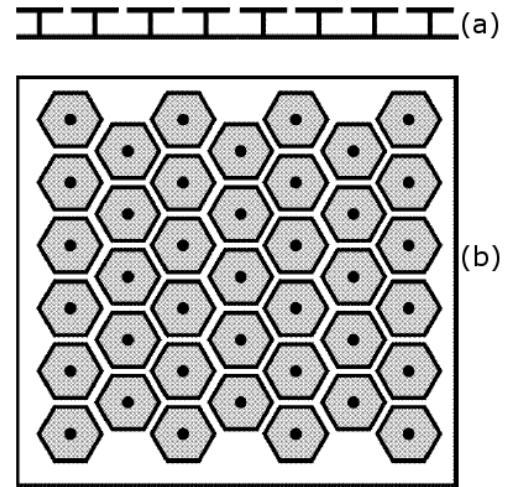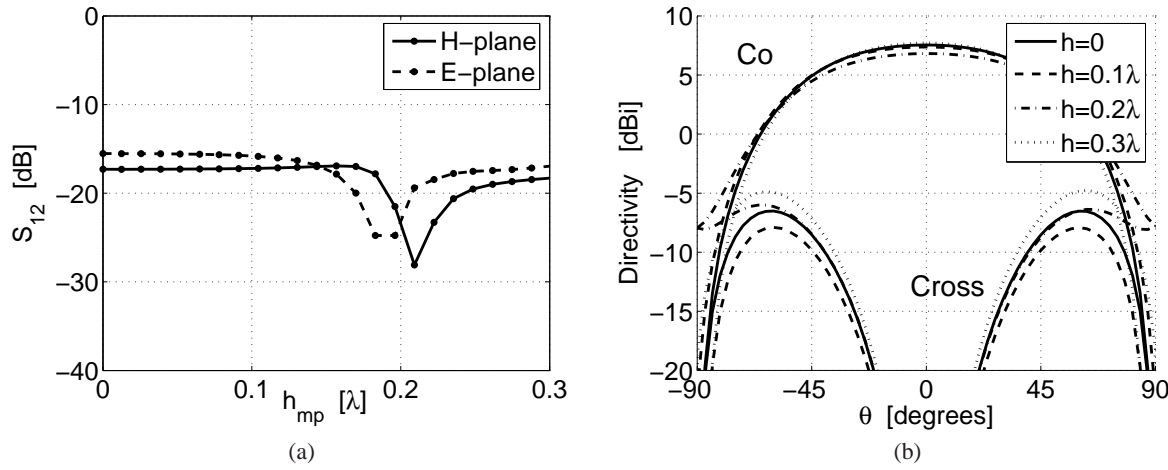
Figure 3.10:   (a) *Mutual coupling between 2 CDA elements as function of h_{mp}.* (b) *Co- and cross-polar directivity of an isolated CDA element with parasitic monopoles for different values of h_{mp}. The configuration is $L = 0.4\,\lambda_0$, $w = 0.01\,\lambda_0$, $h = 0.25\,\lambda_0$, $d = 0.5\,\lambda_0$, and for* (b)*, $h_{mp} = 0.2\,\lambda_0$.*

tion pattern become similar in shape, whereas for the PEC case either the E- or H-plane vanishes at the horizon, depending on the type of antenna. This can be exploited to improve the uniformity of the axial ratio of the antennas as shown in [100, 101].

3.5   Influence of Parasitic Structures

The introduction of parasitic structures above or between the antenna elements is another way of improving the performance of phased arrays. Depending on the purpose and array configuration, different types of structures have been used. The parasitic monopole is widely acknowledged for reducing mutual coupling between certain types of antenna elements and simultaneously making the element radiation pattern more uniform. Such improvements have been obtained for slot antennas in [102, 103] and for dipole antennas in [104–107].

Investigations in [107, 108] confirm, that for phased arrays of horizontal or drooping dipole antennas, the insertion of parasitic monopoles results in an overall reduction of scan loss. In addition, the axial ratio can be improved at low elevation angles. The parasitic monopoles have also been shown to improve the array scan performance for the theoretical case of an infinite array [109].

Similar to placing parasitic monopoles around the elements, conductive walls have also been employed. This is proposed in [110] for a cavity-backed slot antenna array. In [111] parasitic microstrip patches, positioned between driven patch antennas, have been shown to eliminate scan blindness. However, for phased array applications it is clear that the necessity of small element separation puts some limitations on which types of parasitic elements that can be used. Among the techniques discussed above only the parasitic monopoles and conducting walls are realistic choices, whereas the parasitic patches take up too much room.

As an example, the CDA array in Figure 3.1 is now equipped with parasitic monopoles with height h_{mp}. The monopoles are positioned at the end of the dipole arms at a distance $d/2$ from the centre of each CDA element. A two-element CDA configuration is considered with the elements positioned in the same way as elements 1 and 2 in Figure 3.1b. For this configuration, the coupling between the x-directed dipoles, S_{12}^{xx}, and the y-directed dipoles, S_{12}^{yy}, constitute E- and H-plane coupling, respectively, and the monopoles are thus located in both the E- and H-plane of the respective dipoles. The resulting mutual coupling is calculated as function of the height of the monopoles h_{mp} and is shown in Figure 3.10a. As can be seen, both the E- and H-plane coupling are reduced for a monopole height of about $h_{mp} = 0.2\,\lambda_0$. Such reductions in the E-plane coupling are well known and expected [106, 107] whereas only marginal reductions in the H-plane coupling are reported [106]. However, in [106] the monopoles were located in the E-plane of the dipoles only. The reported optimal monopole height varies somewhat depending on the configuration and values of about $h_{mp} = 0.14\,\lambda_0$ to $0.3\,\lambda_0$ have been reported [107, 108]. The optimal $h_{mp} = 0.2\lambda_0$, resulting from the present analysis, is thus within the range of these values.

The element radiation patterns for different values of h_{mp} are shown in Figure 3.10b. It is seen that the pattern becomes slightly uniform for $h_{mp} = 0.2 \lambda_0$ which is in agreement with the expectations. In Figure 3.11, the scan loss for arrays of 7 and 19 CDA elements with $h_{mp} = 0.2 \lambda_0$ is shown. From a comparison with Figure 3.5, it is clear that the reduction in mutual coupling obtained with the parasitic monopoles leads to a significant decrease in the scan loss (note the different ordinate axes in Figure 3.5 and Figure 3.11).

3.6 Wide-Angle Impedance Matching

Figure 3.11: *Scan loss for 7- and 19-element CDA array with parasitic monopoles. The elements are matched to the self impedance. The configuration is the same as in Figure 3.10.*

Many different techniques have been proposed for reducing the scan loss of phased arrays. Since the scan loss is often most severe for wide scan angles, close to the horizon, these techniques are typically referred to as Wide Angle Impedance Matching (WAIM) techniques. WAIM techniques have been the topic of much research through the years and a general overview can be found in [85]. WAIM techniques can be divided into two classes depending on the "region" in which they are employed. The term "free-space WAIM" denotes specific designs involving the radiating elements or the array, whereas the "transmission-line WAIM" relates to feed network designs which attempt to cancel the impact of the scan-dependent impedance.

Many of the topics discussed in this chapter can be considered free-space WAIM techniques. The high-impedance ground planes, used in [99], and the conducting walls between elements proposed in [110] are examples of WAIM techniques [85]. The employment of dielectric layers above the array is yet another technique which has been employed for waveguide arrays [112]. A very similar approach has been used in a microstrip patch array [113] where a reduction of the mutual coupling was reported. In principle, the choice of smaller element separation is also a free-space WAIM technique since it is instrumental in eliminating the scan blindness for infinite arrays [44, 85]. However, in this case it is clearly not a reduction of the mutual coupling that causes the decrease in scan loss.

Generally, the transmission-line WAIM techniques do not attempt to reduce the mutual coupling. Rather the impact of the input impedance variations are sought ameliorated by designing special feed networks. For large arrays, the matching circuits are typically designed to favour scanning towards $\theta = 0°$ [85]. In contrast, a matching circuit designed for wide scan angles can be considered a transmission-line WAIM approach, e.g., by matching the average value of $\Gamma_{in,i}(\theta_0, \phi_0)$ among the azimuthal scan angles ϕ_0 but for a fixed polar scan angle θ_0. In practice, however, this approach is not very useful since the variation with ϕ_0 is typically quite large. Another approach is to disregard the element coupling all together and match the average value of the element input impedance. This approach was found to be preferable for the DRA array investigated in [J3].

A number of more complicated WAIM schemes, employing scan-dependent matching circuits that always match the input impedance, have been proposed. In [85] the principle of electronically tunable matching circuits is proposed but not elaborated further. In [114] a design with interconnecting circuits inserted between the transmission lines, feeding the elements of an infinite array of dipoles, is treated theoretically. This provides a scan-dependent matching which to some degree cancels the impedance variation with the scan angle. It is noted, however, that a practical implementation of this design has not been found.

3.7 Summary

In this chapter, the mutual coupling and its dependence on different parameters of the element and array configurations have been investigated. In order to illustrate some of the main points, the CDA array was introduced and employed for different configurations. The CDA array was modelled using the IES, FAS, and IAS in combination with the MAS and MoM. In addition, two-element configurations of dipoles and monopoles
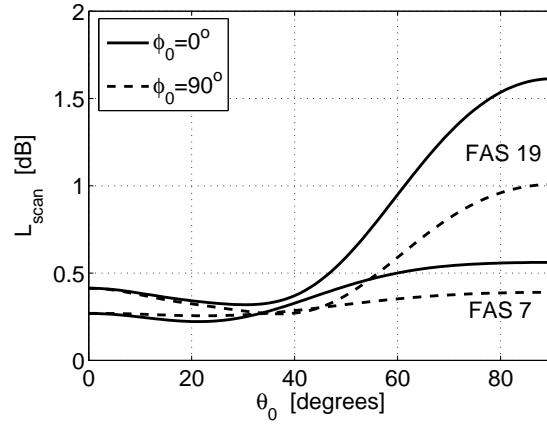
on an impedance ground plane were also investigated.

By varying the height of the dipoles of the CDA elements the element pattern can be changed. Thereby it was seen, that the element radiation pattern has a significant impact on the mutual coupling and thus it was found that the wide-beam elements generally couple more than narrow-beam elements. However, for close distances, relevant for phased-array applications, the differences were not large.

The CDA array was modelled for different sizes and by employing the three modelling schemes. The impacts on the calculated self impedances from both the array size and choice of modelling scheme were quite small. For the mutual impedances, however, it was found that the IAS deviated increasingly from the FAS as the element distance was increased. For the input reflection coefficient it was seen that the array size and element location in the array have significant impact even for elements close to the centre of large arrays. Generally, the scan loss increases with array size and total scan blindness occurred for the infinite array.

An investigation of the influence of the ground planes on the coupling via surface waves was then undertaken. For thin dielectric coatings, the ground plane can be modelled by an effective surface impedance. It was verified, by example, that moderate values of capacitive and inductive surface impedances will either suppress or increase the coupling via TM or TE surface waves, respectively, but not both. For large values, a general suppression of TM surface waves occur. For thicker dielectric coatings this impedance surface model is not sufficient. Instead the dielectric can be considered as a waveguide in which different guided wave modes can propagate. From an IAS analysis these guided waves and their ability to cause scan blindness can be investigated. The occurrence of scan blindness was exemplified with the CDA array on a thick dielectric substrate.

Different artificial high-impedance surfaces exist which may improve the array performance. These surfaces are denoted EBG surfaces and can suppress both the TE and TM surface waves in certain frequency bands, and thus reduce the mutual coupling due to the surface waves. In addition, these surfaces may also ensure more uniform E- and H-plane radiation patterns which, in turn, result in an improved axial ratio.

Last, an overview of the so-called WAIM techniques was given. Many of the aforementioned means to influence and reduce the mutual coupling belong to the specific class of "free-space WAIM" techniques. Additionally, specific designs of feed networks and matching circuits, denoted "transmission-line WAIM", can in principle be employed to achieve a reduction of the scan loss. Practical implementation of these techniques have, however, not been found.

CHAPTER 4

THREE ARRAY TYPES

In this chapter, the three different phased array designs, which were chosen for further investigations, are presented. The three arrays consist of Cavity-Backed Annular Slot Antenna (CBASA), Printed Drooping Dipole Antenna (PDDA), and Dielectric Resonator Antenna (DRA) elements. These element types were chosen because of the requirement of wide-angle coverage of the array. They all have nearly omnidirectional radiation patterns within the hemisphere and can be designed for circular polarisation. In this chapter, brief discussions and key results for the three arrays will be presented which allow comparison of the performance. For more detailed descriptions of the work, reference is made to the three publications [J1, R2, J3].

4.1   General Remarks on the Investigations

The array designs are based on numerical simulations, using combinations of the mathematical methods discussed in Chapter 2. They are all simulated using the Finite Array Scheme (FAS) scheme, either using commercially available software or programmes developed during the study. The simulations are done in the three stages listed in Table 2.1. In the first-stage model, the arrays are positioned on either the Infinite Ground Plane (IGP) or a small Finite Ground Plane (FGP), depending on the simulation tool and array type. From these simulations the antenna scattering matrices are obtained together with an array representation, as described in the following sections. The second-stage model takes the influence of the FGP into account. This is done using the Method of Auxiliary Sources (MAS) models described in [J2, J4]. A circular FGP with a diameter of 1.0 m was chosen for this purpose, and thus the three arrays are equipped with similar ground planes. In the third-stage model the assumed feed network and receiver characteristics are incorporated in the simulation as discussed in Section 2.2 and thus the array G/T can be calculated.

Quantity	Symbol	Assumption
Element loss	L_{ele}	0 dB
Feed network loss	L_{FN}	0.3 dB
Antenna noise temp.	T_{ant}	80 K
Filter loss	L_{filter}	1.0 dB
LNA noise figure	F_{LNA}	0.5 dB
LNA Gain	G_{LNA}	15 dB
Phase shifter loss	L_{PS}	2.5 dB
Combiner loss	L_{comb}	0.5 dB

Table 4.1: *Assumptions on loss and noise temperatures in the receiver chain, from [68].*

The element feed networks assumed during the simulations are depicted in Figure 4.1, for the cases of dual-feed elements and quadruple-feed elements. They consists of Wilkinson Power Dividers (WPDs), delay lines (DLs), and matching networks as discussed in Section 2.2.1. The delay lines are frequency dependent and only provide the desired phase shift at the design frequency $f_0 = 1.6$ GHz. The matching networks are designed
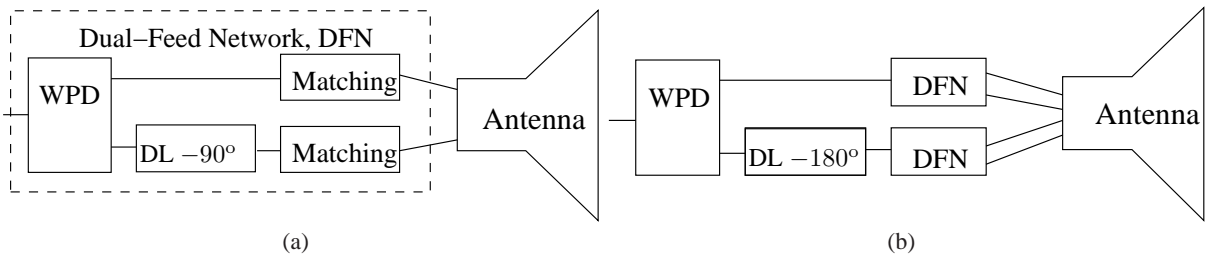

Figure 4.1: *The antenna element feed networks assumed in simulations.* (a) *Dual-feed element (for CBASA).* (b) *Quadruple-feed element (for PDDA, DRA).*
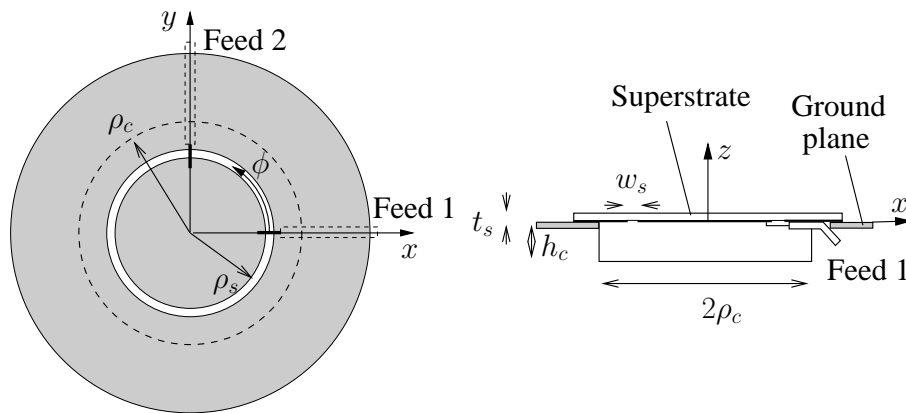
Figure 4.2: *Geometry of the CBASA element. For simplicity the dielectric superstrate is not shown in the top view. The figures are taken from [J1].*

to match the average of the isolated element input reflection coefficients at f_0. Mathematically, this reflection coefficient is calculated from (2.2) using the scattering parameters of the un-matched array. Furthermore, the mutual coupling coefficients S_{ij} are set to zero for input terminals, i and j, of different elements. This omission of the element-to-element coupling ensures that the matching network does not favour certain scan angles, which would be the case if this coupling were included in the design of the matching network.

The antenna elements (excluding feed networks) are assumed to be lossless with no dielectric or conductor losses. The power reflected at the element terminals, i.e., the scan loss L_{scan}, is furthermore assumed to be dissipated in loads in the WPDs and thus the signals do not re-enter the array via multiple reflections in the feed network. In addition to the scan loss, the element feed networks are assumed to introduce a loss $L_{FN} = 0.3$ dB. This assumption is based on measurements of a feed network prototype developed for the PDDA array, see [R2].

In order to calculate the array G/T, the receiver chain is assumed to be that of Figure 2.3. The properties of the constituent components are based on investigations in [68] and are given in Table 4.1. The antenna noise temperature, T_{ant}, is generally a function of the antenna directivity, i.e., scan angle, and the brightness temperature of the surroundings [15]. However, in this work it is approximated by a constant.

4.2   Cavity-Backed Annular Slot Array

A variety of circularly polarised cavity-backed slot antennas have been reported in the literature and, depending on the desired polarisation purity, single-feed [115–120], dual-feed [121, 122, J1], and quadruple-feed [37, 123, 124] excitation schemes have been employed. In particular, the crossed-slots [37, 120, 123, 124] and annular slots [115–117, 121, 122, J1] have been widely used. The inherent low profile and wide-beam element pattern qualify the cavity-backed slot antennas for phased array applications.

The CBASA is based on the design in [122, J1] and is shown in Figure 4.2. It consists of a circular cavity in which an annular slot is cut. On top of this slot a dielectric superstrate is placed. A prototype of a single CBASA element was constructed during the study in [122] and is shown in Figure 4.3 where also the design parameters and performance of the isolated element are given. Here the resonance frequency, f_{res}, defined at zero input reactance, the impedance bandwidth BW, defined for $|\Gamma_{in}| < -10$ dB, the co-polar directivity at $\theta = 0°$, $D_{co}(\theta = 0°)$, and the 3 dB beam width BeW are given. In [J1] it was found that the bandwidth of the CBASA can be increased by using larger cavities, wider slots, or thinner superstrate and lower permittivity. The resonance frequency increases for smaller cavity dimensions, slot radius, and superstrate thickness and permittivity. Among the three arrays, the CBASA array has the least wide-beam elements with $BeW = 90°$.

In the array configuration, the 7 CBASA elements are positioned in a hexagonal configuration as exemplified by the 7 central elements in Figure 3.1b. The element separation is $d = 90.0$ mm. During the initial simulations, which were conducted with the programme HFSS [63], the array was positioned on a small circular ground plane with a diameter of 0.4 m. From this model the array scattering matrix was determined and by including the assumed feed network, the scan loss and element excitations were calculated. In order to model the 1.0 m circular ground plane, the CBASA elements were represented by the electric field in the annular slots which, in turn, were modelled as magnetic ring currents, illuminating the ground plane. For further details of

(a)
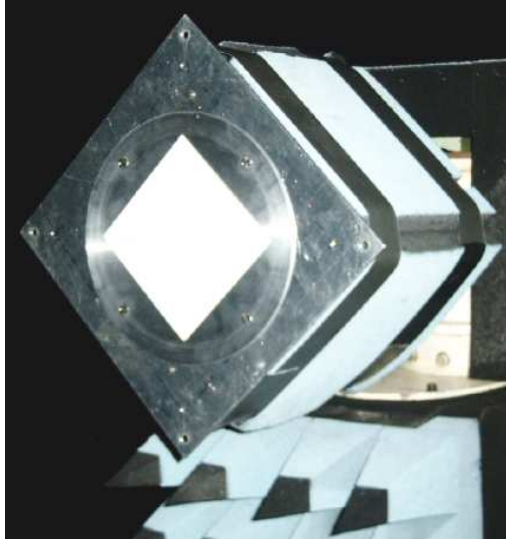
Design		Performance	
ρ_c	40.00 mm	f_{res}	1.59 GHz
ρ_s	32.00 mm	BW	6 %
h_c	20.00 mm	$D_{co}(\theta = 0^\circ)$	7 dBi
w_s	2.00 mm	BeW	90°
t_s	0.79 mm		
ϵ_r	3.38		

(b)

Figure 4.3:   (a) *Prototype of the* CBASA *prototype, developed in [122], mounted on a small square ground plane.* (b) *Design parameters and measured performance of the* CBASA *element.* D_{co} *and* BeW *are for the square ground plane in* (a).

the ground plane model, see [J1, J2].

The simulated array performance is shown in Figure 4.4a-d. In Figure 4.4a, the D_{MB} is shown as function of the polar scan angle θ_0 for 5 frequencies where the average values among the azimuthal scan angles ϕ_0 are shown. It is seen that the D_{MB} varies between 12.5 dBi and 14 dBi for $\theta_0 = 0^\circ$. However, at lower elevation angles it decreases significantly and at $\theta_0 = 60^\circ$ and $\theta_0 = 75^\circ$ approximately 11 dBi and 7 dBi are achieved, respectively. In Figure 4.4b, the scan loss is shown as function of frequency for $\theta_0 = 0^\circ$ and $\theta_0 = 60^\circ$. It is clear that the array is quite narrow-band with respect to the scan loss, especially when the array is scanned away from the $\theta = 0^\circ$ direction. In Figure 4.4c, the G/T is shown, calculated using (2.8) and (2.11) under the assumptions stated in Table 4.1. The low D_{MB} combined with the large scan loss result in very poor G/T, and only for frequencies close to the centre frequency of $f_0 = 1.6$ GHz does the CBASA array perform well. Last, in Figure 4.4d, the D_{MB} and scan loss are shown for $\theta_0 = 60^\circ$ as function of ϕ_0. It is seen that the azimuthal variation is quite dramatic and does not follow a periodically repeating pattern for every 60° as should be expected from the hexagonal array topology. As will be clear from the following sections, this behaviour is not typical. It is believed that the cause is two-fold. First, the locations of the two feeds of the CBASA elements are far from being rotationally symmetric, and second, surface waves, or guided waves, are excited in the dielectric superstrate above the slot. As discussed in Chapter 3, the impact of these guided waves depend on the scan angles and type of superstrate. Since the superstrate is finite, standing waves will form inside the superstrate which, in combination with the asymmetrical feed points, affect the mutual coupling in a complicated way.

With regard to the practical implementations, different designs of the CBASA arrays can be imagined. The crossed-slot array in [37] was composed of different layers forming the ground plane with slots, the cavity material, the cavity bottom, and feed networks, etc. The cavity walls were implemented with rows of plated through-holes. For the present design where the cavities are air-filled this approach is probably not practical. Nor is it practical to fasten individual circular cavities to a ground plane such as done with the single element prototype in [J1]. Instead, the cavities can be cut out of a thick aluminium plate and the top or bottom conducting layers can be fastened with screws. This may, however, be too expensive a procedure for a large-scale commercial production. Another approach is to construct the array of a lighter material, e.g., plastic, with a conducting metallic material added to the inner cavity surface. Whether this is a feasible approach will depend on the conductivity of the metallic coating and its durability and performance under possibly harsh environmental conditions with large variations in humidity and temperature.
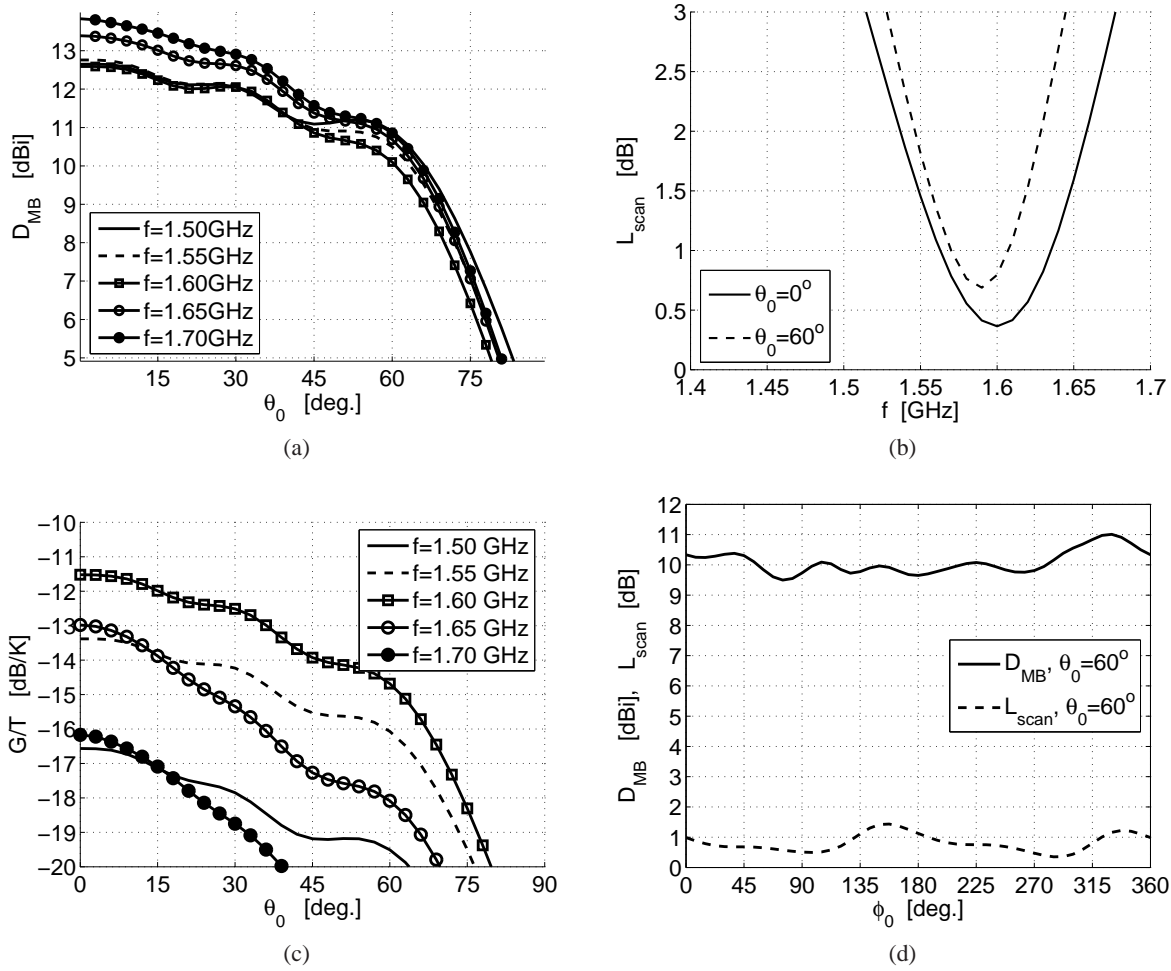
Figure 4.4: *Simulated performance of* CBASA *array.* (a) D_{MB} *as function of* θ_0, *averaged in* ϕ_0. (b) *Scan loss as function of frequency for* $\theta_0 = 0^{\circ}$ *and* $\theta_0 = 60^{\circ}$, *averaged in* ϕ_0. (c) G/T *as function of* θ_0, *averaged in* ϕ_0. (d) *Azimuth variation of* D_{MB} *and scan loss for* $f = 1.6\,GHz$ *and* $\theta_0 = 60^{\circ}$.

4.3   *Printed Drooping Dipole Array*

The dipole antennas have, in various shapes, been used as phased array elements in a number of works [105–108, 125–128]. For the horizontal dipole, the element radiation pattern falls off at low elevation angles since the electric field is parallel to the ground plane. This implies that the beam width is much more narrow than for the crossed slot antenna. In order to alleviate this, a vertical current component must be introduced. The simplest way to do this is by slanting or bending the dipole arms downwards creating a drooping dipole. The beam width can be further widened by increasing the height of the dipole above the ground plane, as exemplified in Figure 3.2 for the Crossed Dipole Antenna (CDA) elements.

Several types of drooping dipoles exist with simple straight dipole arms [125, 128–130], bent dipole arms [126], or curved arms [131]. More complicated shapes with split and twisted dipole arms are reported to have increased bandwidth [132]. Instead of designing the dipoles as wires positioned in air, printed dipoles are also widely used [106, 125, 127, 130, 133, 134].

Introduction of parasitic monopoles near the end of the dipole arms have been found to widen the element radiation pattern as well as to have the positive feature of reducing the mutual coupling [104, 107]. A simple example of this was shown in Section 3.5 with the CDA elements and arrays. These features have rendered the drooping dipole element, with or without parasitic monopoles, a popular choice for phased array applications, especially for configurations in which the constraints on the element height are not too severe. Examples of parasitic monopoles, being used with dipole arrays, have been reported in [107] for horizontal and in [105, 106, 108] for drooping dipoles.

This PDDA design is the result of an extensive optimisation process of the entire PDDA array based on
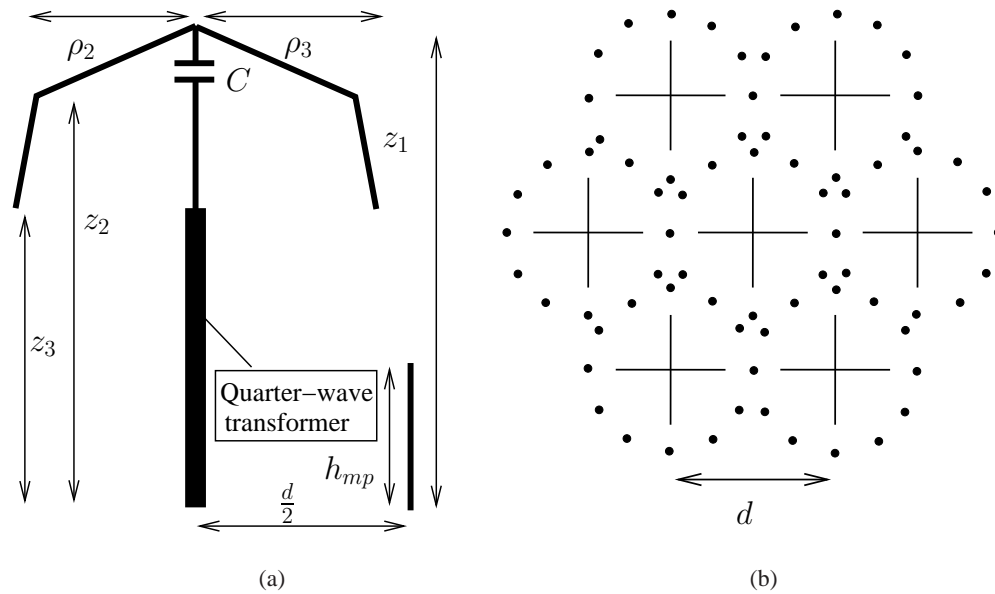
Figure 4.5: *Geometry of the PDDA array. (a) Cross section of a single element. The matching network is included in the central stem and consists of a quarter-wave transformer and a capacitor. (b) Top view of the PDDA array. Each element is surrounded by 12 parasitic monopoles.*

the Genetic Algorithm (GA) using the GAlib package [80] and the simulation programme AWAS 2.0 [50] in combination. This allowed a range of different dipole shapes and configurations of the monopoles to be investigated, and due to the very low computation time of AWAS the necessary time for the optimisation process was within practical limits. The goal of the optimisation was to maximise the array G/T within the solid angle $\theta_0 \leq 75^\circ$, and this requires knowledge of the array directivity and scan loss. With respect to the three-stage model of Table 2.1, the GA optimisation only considered the first and third stages. The second stage, where the FGP is taken into account, was performed subsequently for the optimised PDDA design. This was done by representing the array by the wire currents obtained with AWAS as discussed in [J2].

The PDDA design resulting from the simulations is shown in Figure 4.5 and the constructed prototype[*] is shown in Figure 4.6, where also the design parameters are given. Each PDDA element consists of a pair of crossed drooping dipoles whose arms are bent further downwards at approximately the middle of the arms. The 7 elements are positioned in the hexagonal lattice and are each surrounded by 12 parasitic monopoles, totalling 72 monopoles. The elements are matched using quarter-wave transformers embedded in the central stems. The element height thus influences both the matching and radiation pattern, and therefore capacitors were added between the dipole arms and the stems to provide an extra degree of freedom in the design. Since the entire PDDA array was simulated at once, the isolated element has not been considered in detail and its performance is not given in Figure 4.6. It should be noted, however, that a single element of the shape in Figure 4.5 has a very wide radiation pattern characterised by $D_{co}(\theta = 0^\circ) = 4.1$ dBi and $BeW = 174^\circ$ when mounted on an IGP.

The constructed prototype deviates somewhat from the simulation model. One of the most significant differences is that the simulation model employs circular wires in free space for the dipoles and monopoles, whereas the prototype consists of printed wires and bras screws. The dipoles were printed on a Rogers RO 5870 substrate with $\epsilon_r = 2.33$ and thickness 0.787 mm [135]. Further details of the simulation and prototype designs as well as the optimisation procedure are given in [R2].

The performance of the PDDA array is shown in Figure 4.7a-d with the same quantities as for the CBASA array in Figure 4.4a-d. In this case, the simulation results calculated with AWAS and the MAS ground plane model, as well as measurements of the prototype mounted on a similar ground plane, are shown. The MAS ground plane model and the ground plane used for the measurements have a small hole beneath the PDDA array. This is necessary for connecting cables to the feed network. The radiation pattern measurements were conducted at the ESA/DTU Spherical Near-Field Test Facility [136] in two steps. First, the Active Element Patterns (AEPs) were measured and from these, the scanned-beam radiation patterns were calculated. Second, the elements were fed with coaxial cables of specific lengths to obtain the phase fronts corresponding to certain scan angles. For these configurations the realised gain and the antenna loss were measured. In order

---

[*]The work done by the author, in relation to the prototype, primarily concerns the design and optimisation process. The actual construction was done primarily by Ulrich V. Gothelf from Thrane and Thrane.

(a)
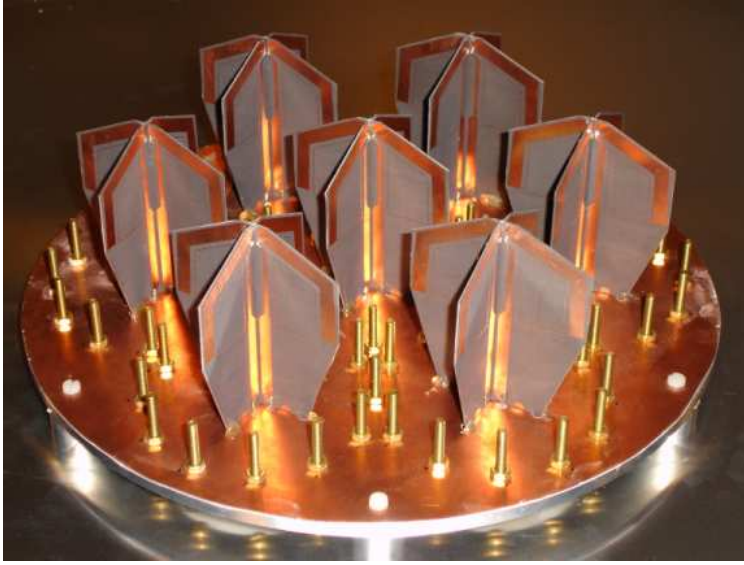
ρ_2	31.50 mm
ρ_3	32.75 mm
z_1	78.50 mm
z_2	66.00 mm
z_3	41.25 mm
d	91.20 mm
h_{mp}	21.75 mm
C	4.3 pF

(b)

Figure 4.6: (a) *Prototype of the PDDA array.* (b) *Optimum design parameters for the PDDA array in Figure 4.5 found with the GA.*

to calculate the array scan loss, the estimated loss in the cables and feed network was subtracted from the measured loss. However, since the printed dipole material (RO 5870) is not lossless, as is assumed in the simulation model, some difference remains.

The fact that the PDDA array has been optimised for maximum G/T has implied that both the radiation and impedance results are significantly better than for the CBASA array. With respect to the D_{MB}, the PDDA array has a significantly better coverage at the low elevation angles than the CBASA array, and the D_{MB} is nearly constant within $\theta_0 \leq 65^\circ$. At $\theta_0 = 75^\circ$ about 10 dBi is obtained. It should be noted that the ripples present in the D_{MB} depend on the ground plane size and different ripples will occur if other ground plane sizes are employed. This is discussed further in Chapter 5. The uniformity of the D_{MB} is primarily due to the element height which diminishes the D_{MB} for scanning near $\theta = 0^\circ$ and increases it for low elevation scan angles. The wider beam widths of the isolated PDDA element is also indicative of this. With regard to the scan loss, the simulation and measurement results agree reasonably well within the simulated frequency range of 1.5 GHz to 1.8 GHz (note that the depicted spectrum is different than for the CBASA case in Figure 4.4b). The deviations are thus below 0.4 dB in most of this spectrum. It is seen that the scan loss is lower for the low elevation angles than for the high which is not the case for the other arrays investigated in this study. The improvement of the D_{MB} and scan loss, as compared to the CBASA array, leads to much better G/T. Last, the azimuthal variations are seen to follow the expected 60° periodicity, and there is generally a larger degree of uniformity than for the CBASA array.

The PDDA array prototype has been constructed without regard for the production costs. The capacitors and the monopole screws were fixed by hand, and in its present form the PDDA array is thus very time-consuming to assemble. For a large-scale production such time-consuming work is too expensive. Alternatively, the capacitors can be implemented as interdigital capacitors printed directly onto the circuit board [137]. The 72 parasitic monopoles might conceivably be replaced with 7 conducting rings or walls around the elements in a way similar to that proposed in [110]. However, at present, investigations into this have not been conducted. In its present form the PDDA elements are not very robust and the substrate used for the printed dipoles is somewhat fragile. This may be improved by using thicker substrates or by placing blocks of foam between the dipoles.

4.4   Dielectric Resonator Array

The DRA has been in the focus of much research in recent years, due to its many favourable features such as low loss, compact size, structural simplicity, and simple feeding schemes [138]. Thus from the early work of Long et al. [139] applications of DRAs has been reported for a wide range of specialised shapes and configurations.
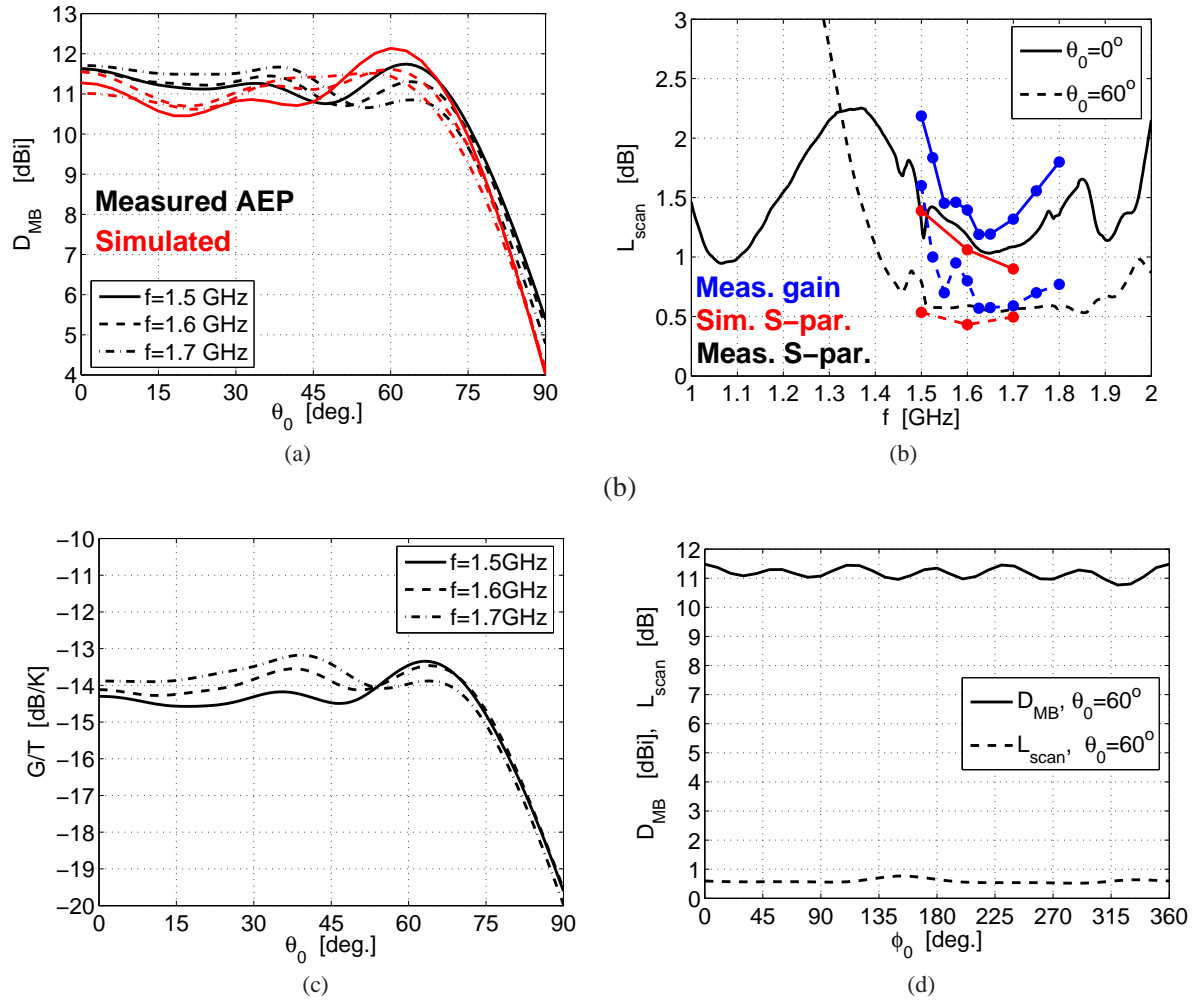
Figure 4.7: *Measured and simulated performance of PDDA array.* (a) D_{MB} *as function of θ_0, averaged in ϕ_0.* (b) *Scan loss as function of frequency for $\theta_0 = 0°$ and $\theta_0 = 60°$, averaged in ϕ_0.* (c) *G/T as function of θ_0, averaged in ϕ_0, from measured AEP.* (d) *Azimuth variation of D_{MB} and scan loss for $f = 1.6\ GHz$ and $\theta_0 = 60°$, from measured AEP and S-parameters.*

Overviews of different DRA configurations can be found in [138, 140].

The resonance frequency and bandwidth of the DRA are basically determined by the permittivity and size of the DRA [138]. The shape of the DRA is of less importance since the fundamental broadside mode [48] of the DRA can be excited almost regardless of the shape. Inclusions of air-gaps and combinations of different dielectrics may, however, be employed to increase the bandwidth or obtain multi-band operation [138].

The compact size of the DRA is important when considering candidate elements for phased arrays since it allows for a smaller element separation than is the case for many other types of elements. Thus the DRA may be advantageous for wide-angle scanning array applications, wherein a small element separation is beneficial for reducing scan loss [44]. Planar, linearly polarised phased arrays have previously been examined in [141, 142] where the elements are fed using probes and microstrip feed lines. Circularly polarised arrays have also been constructed using sequentially rotated single-feed DRAs [143, 144].

The investigations conducted in this study are focused on probe-fed DRA elements. To this end, cylindrical and rectangular DRAs have been simulated with HFSS [63] and CST-MS [64], and hemispherical DRAs have been analysed with an analytical Spherical Wave Expansion (SWE) model. The analytical model is based on the dyadic Green's functions for a dielectric sphere similar to the work in [48], and it allows modelling of a single hemispherical DRA.

For array investigations, the SWE model is not applicable since the spherical symmetry is not present. Furthermore, the numerical investigations with HFSS and CST-MS may become impractical due to the high computational cost and limited available computer resources. Instead, the 7-element array was modelled using a MAS model developed for this purpose [J3, R1]. DRA arrays have previously been investigated with the MAS
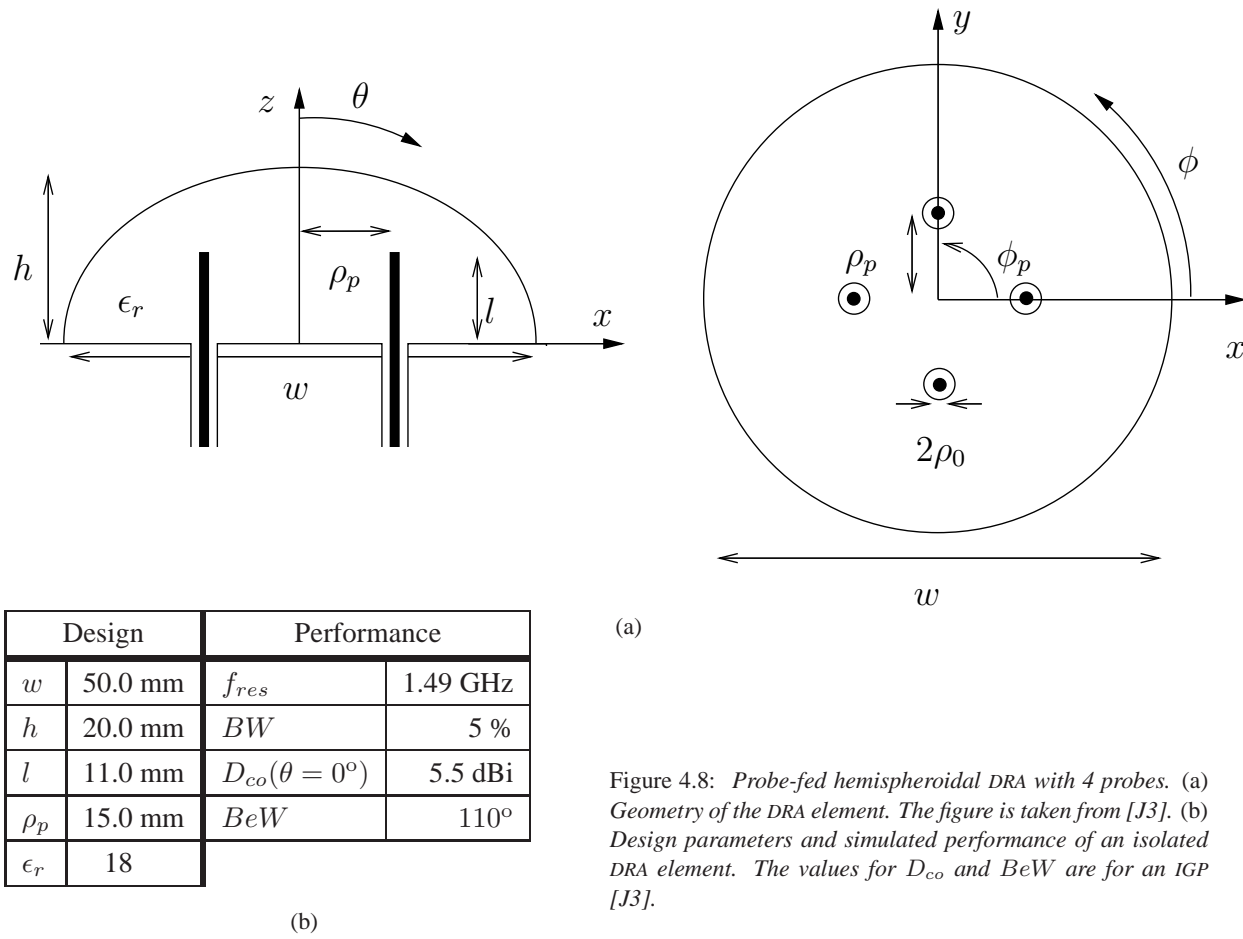
(a)

Design		Performance	
w	50.0 mm	f_{res}	1.49 GHz
h	20.0 mm	BW	5 %
l	11.0 mm	$D_{co}(\theta = 0^\circ)$	5.5 dBi
ρ_p	15.0 mm	BeW	110°
ϵ_r	18		

(b)

Figure 4.8: *Probe-fed hemispheroidal DRA with 4 probes. (a) Geometry of the DRA element. The figure is taken from [J3]. (b) Design parameters and simulated performance of an isolated DRA element. The values for D_{co} and BeW are for an IGP [J3].*

in [61] where an infinite periodic waveguide array with protruding dielectric elements was investigated. As is discussed in Chapter 2, the MAS is not well suited for structures with sharp corners. The shape of the DRA elements was therefore chosen as hemispheroidal. This allows use of the so-called Standard MAS which is particularly simple and computationally cheap [53]. The MAS model will not be discussed in detail here, and it is merely noted that the DRA probes are modelled under an assumptions of an IGP and a sinusoidal shape of the probe currents. This probe model leads to slightly different results for the impedance as compared to more accurate simulation tools, e.g., CST-MS. Thus the resonance frequency typically varies with 2 % and the resistance at the resonance is about 20 % lower, as exemplified in Figure 2.1. The details of the SWE and the MAS models can be found in [J3, R1]. The second-stage model of the FGP is based on the obtained MAS solution from the first-stage IGP model. The details of this are given in [J4] and will not be elaborated here.

A single hemispheroidal DRA element is depicted in Figure 4.8 where also the details of the design and performance are given. The investigations of the DRA array were based on an initial analysis of isolated DRA elements. The elements were designed to obtain a resonance frequency somewhat below 1.6 GHz. By lowering the relative permittivity ϵ_r and increasing the width w, the impedance bandwidth can be increased while the height h and resonance frequency f_{res} can be kept constant. Several examples of this are given in [J3]. An advantage of the DRA element is that its relatively small size allows the elements to be positioned closer to each other than, for instance, is the case for the CBASA elements due to the space-consuming cavities. In the examples given here, two different element separations of $d = 70.0$ mm and $d = 90.0$ mm are used.

In Figure 4.9a-d, the performance of the DRA array is shown for $d = 70.0$ mm (shown with thick lines) and $d = 90.0$ mm (shown with thin lines). The different element separations are seen to have a significant influence on the array D_{MB}. For the small separation, the D_{MB} is quite uniform but not very high. For the larger element separation it is significantly higher but also falls off more rapidly with scan angle and for $\theta_0 > 70^\circ$, the D_{MB} curves converge. In terms of the D_{MB}, the large element separation of $d = 90.0$ mm is clearly preferable.
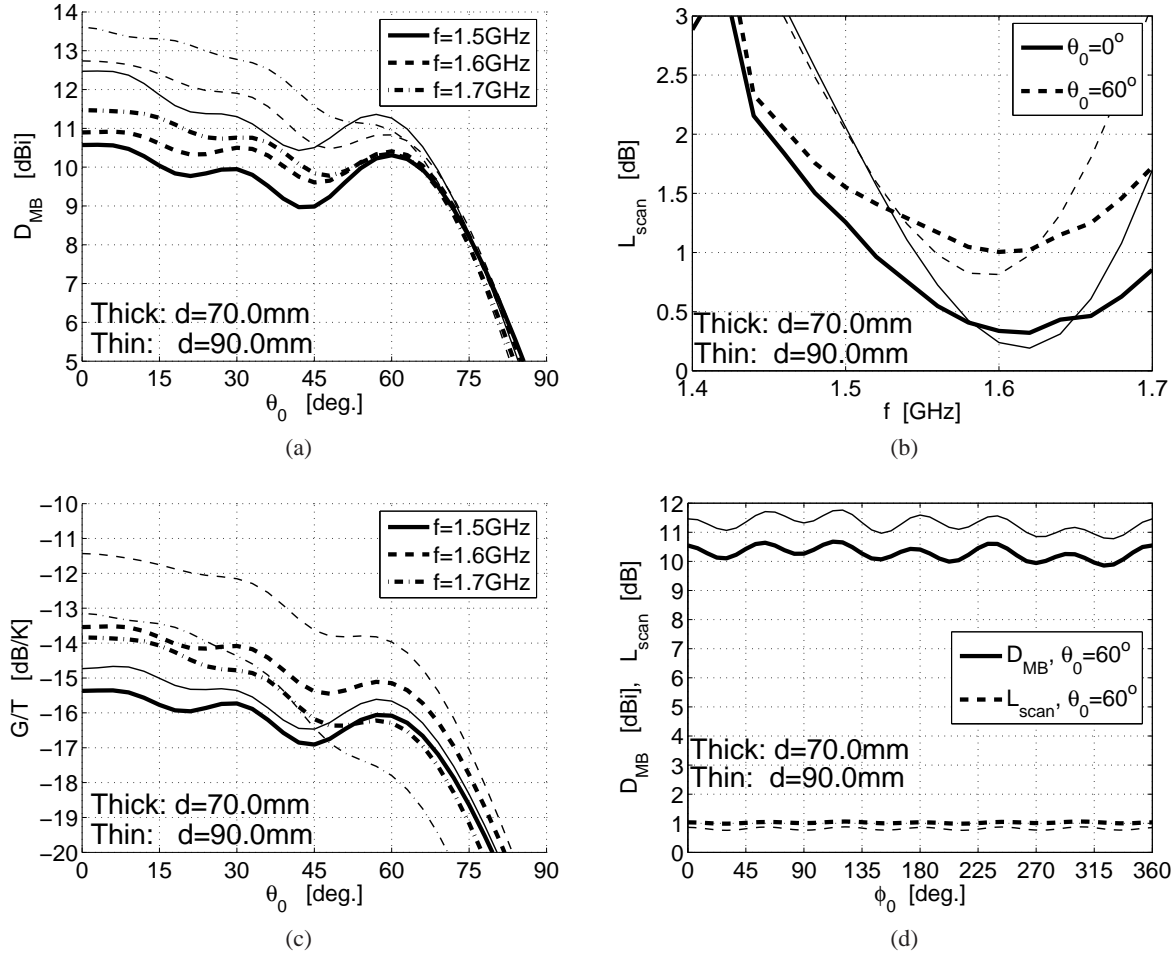
Figure 4.9: *Simulated performance of DRA array. Thick lines are for $d = 70.0$ mm and thin lines for $d = 90.0$ mm. (a) D_{MB} as function of θ_0, averaged in ϕ_0. (b) Scan loss as function of frequency for $\theta_0 = 0°$ and $\theta_0 = 60°$, averaged in ϕ_0. (c) G/T as function of θ_0, averaged in ϕ_0. (d) Azimuth variation of D_{MB} and scan loss for $f = 1.6\ GHz$ and $\theta_0 = 60°$.*

For both element separations, the scan loss is better than that of the CBASA array, see Figure 4.4, in spite of the fact that the element bandwidth is slightly more narrow. This improvement is believed to be due to a lesser degree of mutual coupling in the absence of the dielectric superstrate, in which guided waves are excited for the CBASA array. For the small element separation of $d = 70.0$ mm, the scan loss is low in a wider frequency band than for $d = 90.0$ mm. However, the scan loss is still inferior to that of the PDDA array. This illustrates the benefits of using a small element separation which is possible for small elements, such as this DRA design. It is noted that the inherent element bandwidth is also important in this respect. Wide-band elements will cause an increase in the bandwidth with respect to the scan loss, whereas, the larger element separation, which simultaneously becomes necessary, will have the opposite effect. From the G/T results, it is seen that the DRA array performance is better than that of the CBASA array but worse than that of the PDDA array as expected from the D_{MB} and scan loss results. The azimuthal variation of the D_{MB} and scan loss exhibit the expected rotational symmetry as was also the case for the PDDA array.

Typical materials used for DRA elements can be found in [140] with relative permittivities ranging from about $\epsilon_r = 3$ to more than 100. However, inquiries into the price of pre-fabricated DRA elements showed that this was too high to warrant fabrication of a prototype. A further aspect of practical importance is that the high-permittivity materials typically require special tools for processing [145]. On the other hand, DRA elements are quite durable and can be excited in many different ways, such as coupling via slots, microstrip lines, or probes positioned inside, outside, or on the DRA surface [138] and it is therefore not necessary to drill holes for internal probe feeding and this may ease the production somewhat. Nevertheless, the price of the DRA elements is probably too high for commercial production to be feasible.

4.5   *Summary*

In this chapter, the three different phased arrays, which have been of primary interest in the study, were presented. The arrays consist of 7 elements positioned in a hexagonal lattice, however, with different elements, namely the CBASA, the PDDA, and the DRA.

Prior to the discussions of the individual array designs, a number of common features were pointed out. The process of simulating the arrays, based on the three stage discussed in Section 2.4, was outlined. Also the details of the assumed feed networks and receiver chains, which are important for assessing the array G/T, were given.

The CBASA element generally has the poorest performance of the three. It is quite narrow-band, which implies that the scan loss is high, both for the extreme parts of the frequency band and for low elevation scan angles. Even though the isolated element has a beam width of about 90°, this is insufficient for the array to provide good coverage at the low elevation angles. This is further worsened by the wide element separation of $d = 90.0$ mm, which implies a relatively large amount of scan loss and grating lobes. The scan loss may be improved by designing more wide-band elements. This will, however, require larger cavities and hence either an increase in the element height or width. The latter will require an increased element separation which is not desirable as it will exacerbate the scan loss. Compared to the other arrays, the CBASA array has a large azimuthal variation of both D_{MB} and scan loss. This is believed to be the consequence of guided waves which are excited in the superstrate and lead to significant mutual coupling. The attractive features of the CBASA array are its low profile and robust mechanical features.

The PDDA array is the best of the 3 arrays in terms of performance. The fact that the GA optimisation was possible for this array has resulted in a particularly good performance for low elevation angles. This is a result of the high element profile which yields a very wide element pattern and thus an increased array D_{MB} at low elevation angles. Another advantage is that the scan loss is lower for low elevation angles than for high. Thus the D_{MB} and G/T are close to being uniform within most of the hemisphere. The obvious disadvantage of the PDDA array is its height of about 8 cm. Also, further work must be done to ensure a more rugged design which should also be less time-consuming to assemble.

The DRA array exhibit some of the favourable as well as the unfavourable properties of the CBASA and PDDA arrays. The bandwidth of the DRA element can easily be tuned by selecting the DRA size and permittivity appropriately, and thus larger bandwidth than that of the CBASA element can be achieved. This increase in bandwidth is, however, achieved at the expense of larger element size and hence larger element separation. The large element separation implies a high D_{MB} at high elevation scan angles which, in turn, falls off for low elevations. At the same time, the scan loss is increased at the extreme parts of the investigated frequency band. The large element separation does, however, allow for wider elements which, due to their inherent wide bandwidth, will have a positive impact on the scan loss. Overall the DRA performs better than the CBASA array but generally poorer than the PDDA array. Positive features of the DRA are its relatively low height and high degree of robustness. Its negative features are that the dielectric material is expensive and generally difficult to process mechanically.

INFLUENCE OF FINITE GROUND PLANES

The influence of Finite Ground Planes (FGPs) is of importance in any practical application of antennas, including phased arrays. For mobile satellite communications, such FGPs may often take the form of a vehicle, such as a car or an airplane, and it has significant impact on the radiation pattern and hence the overall array performance [146]. Typically, the location of the antenna on the vehicle is a compromise between competing design requirements of the vehicle, and many other engineering issues, than those related to the communications, may often be prioritised higher [147]. Therefore, the antenna must perform sufficiently well regardless of the particular shape of the FGP employed and it is, therefore, of importance to be able to ascertain this performance for different FGPs.

The influence of FGPs on the radiation from antennas and phased arrays has been devoted some attention in this study, and as a consequence the Method of Auxiliary Sources (MAS) model given in [J2] has been developed. As discussed in Section 2.4 and Chapter 4, the FGP is taken into account as an inherent part of the array analyses via the 3-stage model in Table 2.1. In this context, the present investigations can be considered as the second stage, this time with a range of different FGPs being investigated. For the three phased arrays discussed in Chapter 4, the directivity was shown for a flat circular FGP with a diameter of 1.0 m. This served the purpose of enabling direct comparison of the main-beam co-polar directivity, D_{MB} and the G/T. The impact on the radiation from the FGP is now addressed in a broader sense. The investigations in this chapter cover the FGP size, shape, and curvature, as well as the impact of raising the array slightly above the FGP. Specifically, the D_{MB}, and the main-beam Axial Ratio (AR), AR_{MB}, are considered. The investigations presented here, have been conducted for the Cavity-Backed Annular Slot Antenna (CBASA) and Printed Drooping Dipole Antenna (PDDA) arrays.

5.1 Methods for Analysing the Influence of Finite Ground Planes

Many different techniques have been employed for analysing the impact of FGPs on the antenna radiation. In recent years, the advances of computer technology has enabled very large and complex structures to be accurately modelled. A typical example of practical relevance is that of an antenna mounted on a car. In [148] a Method of Moments (MoM) model is used to model a car with an antenna at a frequency of 90 MHz and in [149] a similar problem is considered for 1.52 GHz, using the Finite Difference Method (FDM). A phased array on flat, square FGPs is modelled in [150] with FGP sizes exceeding $12 \lambda_0^2$, using both Finite Element Method (FEM) and MoM models. Common to these investigations are that the associated computational cost is high and several hours of computation time on powerful computers were required [148–150].

Figure 5.1: *Simulation model of CBASA array mounted on a square FGP. The black rings represent the annular slots.*

In situations where the available computational resources are modest, these approaches are often unfeasible. For this reason different hybrid methods have been derived and are still valuable tools. They rely on representing the antenna accurately, using for instance the MoM combined with approximate methods, such as the Physical Optics (PO) [151] or the Geometrical Theory of Diffraction (GTD) [152–154]. Also curved FGPs have been analysed in [155] with a hybrid PO/MoM technique. Further examples can be found in the reference lists in [151, 154].

The computationally inexpensive nature of MAS qualifies it for modelling of large structures such as FGPs,
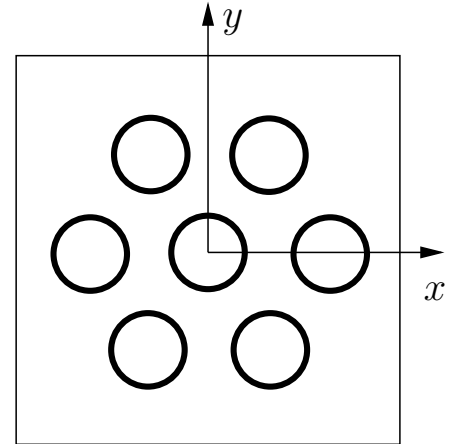
and MAS has indeed previously been employed to this end. Thus a wire antenna mounted on a car is analysed in [60] where results are reported for up to 2 GHz. The MAS model developed in this study is discussed in more detail in [J2], and it has been applied for investigations of circular FGPs of sizes up to $49\,\lambda_0^2$.

5.2   *Impact of Ground Plane Size and Shape*

It is well known that ripples occur in the radiation patterns of antenna, when they are mounted on large or moderate-sized FGPs, for instance as shown in [J2] for the CBASA element and the PDDA array. In the following, some results for the CBASA array mounted on 4 different flat FGPs are presented. The FGPs used for these examples comprise small and large, square and circular FGPs as summarised in Table 5.1. In Figure 5.1, a top view of a configuration with the CBASA and a small, square FGP is shown.

FGP Shape	Size	
Small circular FGP	0.196 m^2	(5.6 λ_0^2)
Large circular FGP	0.785 m^2	(22.3 λ_0^2)
Small square FGP	0.250 m^2	(7.1 λ_0^2)
Large square FGP	1.000 m^2	(28.4 λ_0^2)

Table 5.1: *The flat FGPs used in the examples. The sizes in λ_0^2 are given for 1.6 GHz.*

The results for the 4 FGP and the Infinite Ground Plane (IGP) are given in Figure 5.2a-c. In Figure 5.2a, the D_{MB}, averaged in the azimuthal scan angles ϕ_0, is shown. For the small square and small circular FGPs (SSGP and SCGP shown in red) the D_{MB} decreases monotonically with the polar scan angle θ_0 without notable ripples. For the large square and large circular FGPs (LSGP and LCGP shown in blue) the rippling effect is clearly seen and the decrease with scan angle is not monotonous. For the IGP (shown in black) the ripples are not occurring. For the large FGP the coverage at low elevation angles is almost as good as for the IGP case. However, for the small FGPs it is clearly reduced.

In Figure 5.2b, the D_{MB} is shown as function of polar scan angle θ_0 for 3 azimuthal scan angles $\phi_0 = 0°$, $45°$, and $90°$, for the large circular and square FGPs. In both cases, an azimuthal variation occurs, caused by the rotationally asymmetric hexagonal array topology. For the large circular FGP this constitutes the only asymmetry. It is seen that for the circular and square FGPs, the D_{MB} is similar for $\phi_0 = 0°$ (black) and $\phi_0 = 90°$ (red). In these azimuth planes the two FGPs both have widths of 1 m. However, for $\phi_0 = 45°$ (blue), along the diagonal of the square FGP, this is not the case and differences are clearly notable between the square and circular FGPs. It is thus clear that an additional azimuthal asymmetry is introduced by the square FGP.

In Figure 5.2c, the AR_{MB} is shown for the IGP (black), small square (red) and large square (blue) FGPs, for the azimuth scan angles $\phi_0 = 0°$, $45°$. The AR_{MB} is seen to be very different for the two azimuthal directions, even in the IGP case. This latter result demonstrates the impact of the array hexagonal topology. However, additional differences occur for the FGP results. For $\theta_0 \geq 60°$ it is thus seen that the AR is lower for the small FGPs. However, a general increase or decrease of the AR_{MB}, specifically caused by the FGP size or shape, can not be identified.

In conclusion, the impact from the FGP size and shape is clearly visible and causes ripples in the radiation pattern. This is especially the case for the low and medium-range elevation scan angles whereas for high elevations the FGPs have a minor impact only. In addition, the rotational asymmetry of the hexagonal array has some impact on the D_{MB} and in particular on the AR_{MB}. The results shown here only include the CBASA array. Corresponding investigations of the PDDA array, mounted on circular FGPs of different sizes, can be found in [R2] where also measurement results are presented.

5.3   *Influence of a Vertical Gap between the Array and Ground Plane*

In special cases, such as for satellite applications, the antenna position is typically carefully considered during the satellite design phase. For instance, the Danish "Rømer" satellite was intended* to be equipped with flush-mounted, crossed-slot antennas embedded into the satellite surface at optimal positions [156, 157]. In contrast, if an antenna is to be mounted on a car, it is likely to be placed on top of the existing car roof thus introducing a vertical gap between the antenna ground plane and the surrounding ground plane formed by the car roof. If the electronic components, such as receiver and transmitter, are located below the antenna, this will further
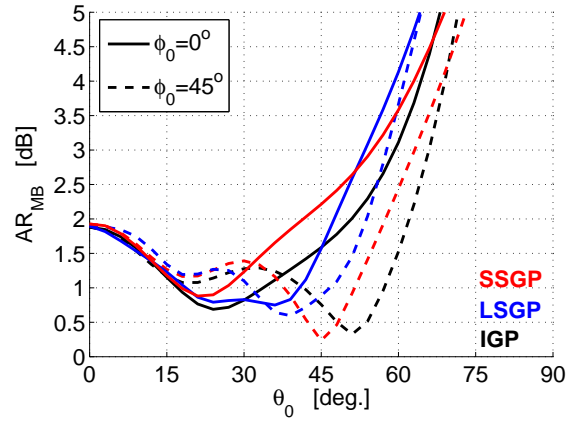
---

*Regrettably, the mission for which this satellite was intended, was aborted.
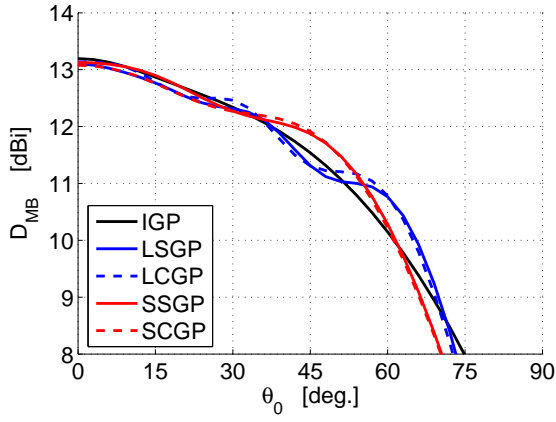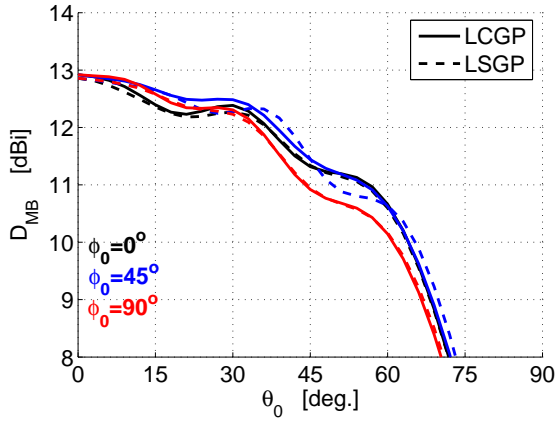
Figure 5.2: D_{MB} and AR_{MB} for CBASA mounted on different ground planes. For brevity: LS=large square, LC=large circular, SS=small square, and SC=small circular. (a) D_{MB} for IGP and the 4 FGPs in Table 5.1, averaged in ϕ_0. (b) D_{MB} for large circular FGP and large square FGP for $\phi_0 = 0°, 45°, 90°$. (c) AR_{MB} for small square FGP, large square FGP, and IGP for $\phi_0 = 0°$ and 45°.

increase the gap height. As an example, the aperture plane of the crossed-slot phased array described in [37], see Figure 1.5a, was raised about 1.4 cm above the surrounding FGP. The CBASA and Dielectric Resonator Antenna (DRA) arrays, discussed in Chapter 4, were simulated when mounted directly on the FGP, whereas the PDDA was raised 2 cm above as can be seen in Figure 4.6.

In this section, the impact of a vertical gap or step between the array and the surrounding FGP is investigated. As was seen in Section 3.2, the height above the ground plane significantly changes the radiation pattern, and it is thus of interest to investigate to which extend such a gap will influence the directivity.

In order to ascertain the impact of such vertical gaps, the PDDA array has been simulated when mounted on a large circular FGP with different gap heights from $h = 0$ to $h = 3$ cm. The PDDA array,

Figure 5.3: *Simulation model of PDDA array mounted on a flat FGP with a vertical gap with height h.*

including its small circular FGP is positioned above the large circular FGP with a hole cut directly below, as discussed in Section 4.3. A cross-section of this configuration is shown in Figure 5.3. The diameter of the small FGP of the PDDA is 30 cm diameter, whereas the hole in the large FGP has a diameter 28 cm, except for the $h = 0$ case where it is 33 cm, to allow for the presence of the small FGP.

In Figure 5.4a,b the radiation patterns for the cases of $h = 0$ and $h = 3$ cm for scan angles $\theta_0 = 0°$ and $\theta_0 = 60°, \phi_0 = 0°$ are shown, respectively. It is seen that the main beam changes slightly and that the cross-polarisation is higher for the large gap. In Figure 5.4c,d, the D_{MB} and AR_{MB}, averaged in ϕ_0, are shown, respectively, as function of the polar scan angle θ_0 for different values of h. It is clear that the D_{MB} increases with h for high elevation angles $\theta_0 \leq 20°$, with a maximum increase of almost 1 dB. For medium-range
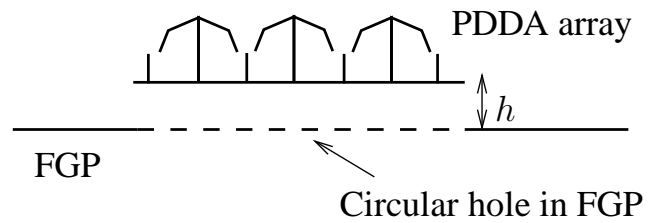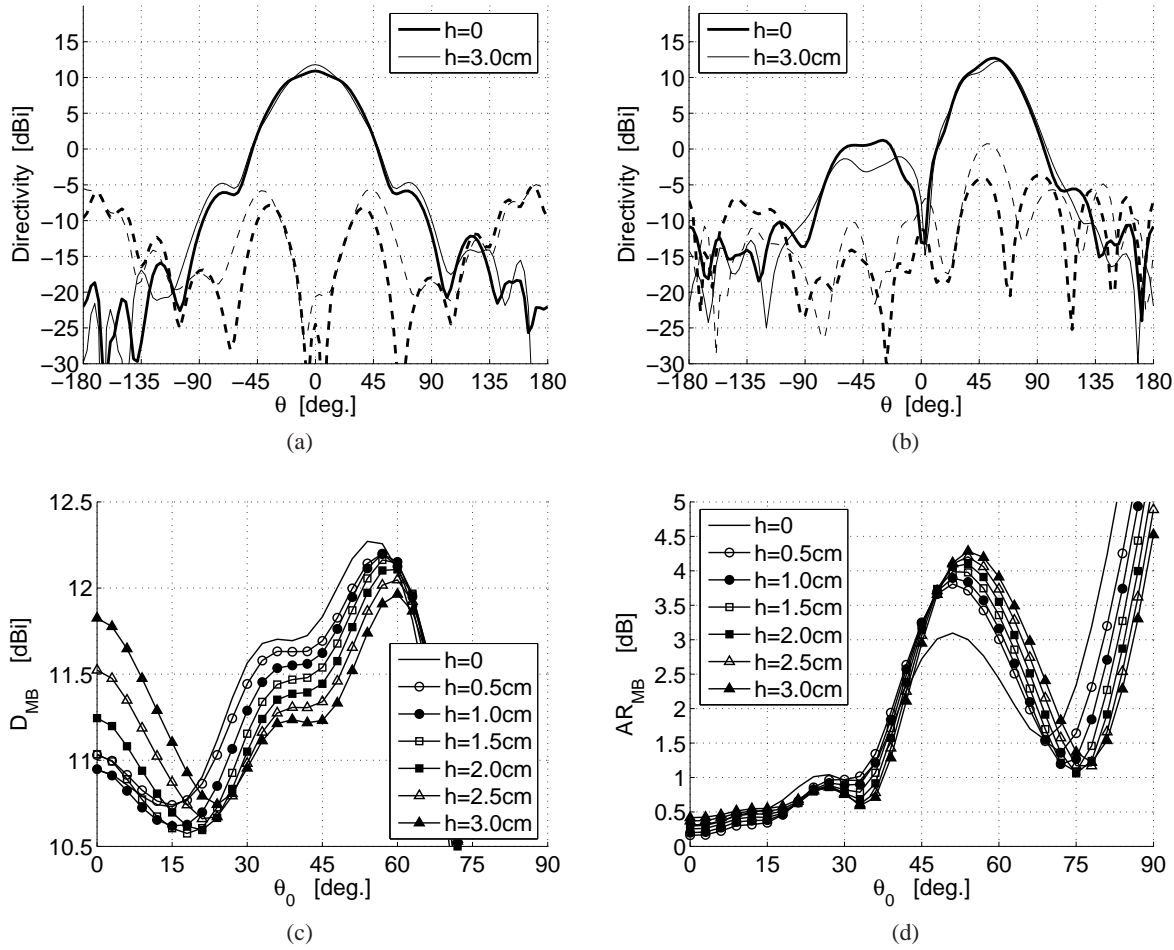
Figure 5.4: *Directivity and AR of the PDDA array on the large circular FGP with a gap. The frequency is $f = 1.6$ GHz. (a-b) Radiation patterns for gap heights $h = 0 - 3$ cm. (a) $\theta = 0°$, (b) $\theta_0 = 60°, \phi_0 = 0°$. (c-d) D_{MB} and AR_{MB}, as function of θ_0, averaged in ϕ_0, for different gap heights.*

elevation angles $25° \leq \theta_0 \leq 60°$ it decreases with a maximum decrease of about 0.5 dB. At lower elevation angles the dependence on h is negligible. The AR_{MB} increases with h for medium-range elevation angles, whereas it decreases for low values. The large difference that occur between the $h = 0$ and the $h = 0.5$ cm cases for the AR_{MB} are not believed to be caused exclusively by the gap size. The differences in the size of the hole, which is slightly larger for the $h = 0$ case, is also believed to cause some of the difference.

The results illustrate the impact of introducing a small gap between the antenna and the FGP below. Since the PDDA was optimised under the assumption of $h = 0$, the performance achieved under these conditions is compromised by the increase of the gap height. It must therefore be anticipated that the array performance will deviate somewhat from this optimum when a small gap is introduced and, depending on the elevation angle, this change may be for the worse.

5.4   *Influence of Ground Plane Curvature*

In this section, the influence of ground plane curvature is investigated. Such curved ground planes may be encountered, for instance, in aeronautical applications, where an antenna is mounted on an airplane.

The shape of the curved FGP is defined by bending the large, square and circular FGPs from Table 5.1 as shown in Figure 5.5. The central square part of 30 cm by 30 cm is maintained flat. The exterior parts are curving downwards such that the FGP follows downward arcs, with certain curvature radii C_x and C_y, for increasing x and y values. Figure 5.5 shows the cross section in the (x, z)-plane of an FGP which curves in the x-direction with the curvature radius C_x. The C_x and C_y used in these investigations are chosen as 2 m, 5 m, and ∞, where the latter signifies that the FGP is not curved along the particular direction.

In the first investigation the PDDA is positioned on a large square FGP which curves in the x direction but not in the y direction, that is $C_y = \infty$. In Figure 5.6a,b the D_{MB} and AR_{MB} are shown, respectively, as function of polar scan angles θ_0 for scanning in the $\phi = 0°$ (solid curve) and $\phi = 90°$ (broken curve) planes. The curvature is seen to significantly reduce the ripple occurring for $\theta_0 = 60°$ in the $\phi = 0°$ plane, and thus cause a decrease in the D_{MB} of 0.5 dB compared to the flat, large, square FGP case ($C_x = \infty$, black). The AR_{MB} is slightly affected in the case of the sharp curvature of $C_x = 2$ m but not for $C_x = 5$ m. For scanning in the $\phi = 90°$ plane, where the large square FGP is not curving, there are no notable changes.

Figure 5.5: *Cross section in the (x, z)-plane of an FGP curved in the x-direction. The middle part below the array remains flat.*

A similar investigation is done for the CBASA array and is shown in Figure 5.6c. In this case, the large, circular FGP curves along both the x and y directions with equal curvature radii $C_x = C_y = C$. It is seen that for polar scan angles $\theta_0 = 30°$ and $50° \leq \theta_0 \leq 65°$, the D_{MB} decreases approximately 0.5 dB to 1.0 dB relative to the flat case ($C = \infty$), while for $35° \leq \theta_0 \leq 45°$ it increases slightly. The changes occur in both scan planes in this case since the FGP curves in both the x and y directions.

It is thus clear that the curvature also influences the coverage, especially at low elevation angles, where it is reduced.

5.5   Summary

In this chapter, the impact of the FGP on the radiation from phased arrays has been investigated. The first part of the investigations focused on the influence of the size and shape of flat FGPs. Two circular and two square FGPs with the CBASA and PDDA arrays were simulated. It was seen that the D_{MB} is influenced significantly by both the size and shape of the FGP. For the large FGPs, the coverage at the low elevation angles was improved relative to the small FGP cases, where the D_{MB} decreases more rapidly with the polar scan angle θ_0. However, the performance for the large FGPs was not as good as for the theoretical IGP case. Significant ripples were introduced by the large FGPs and this led to considerable variation in the D_{MB}. In total, a variation of about 0.7 dB was seen to occur in the D_{MB} for the different FGPs.

The next investigation focused on the introduction of small vertical gaps between the array and the surrounding ground plane. For the PDDA array, gaps from 0 to 3 cm were investigated. It was found that an increase of the gap height will cause an increase in the D_{MB} for high elevation scan angles whereas a decrease occurs for low elevation angles. Within the investigated span of 3 cm it was found that the D_{MB} may vary with up to 1.0 dB for $\theta = 0°$ and up to 0.5 dB for $\theta = 45°$. The AR_{MB} was also found to be affected for medium and low elevation angles.

The final investigation dealt with the influence of FGP curvature. FGPs with curvature radii of 2 m and 5 m were investigated. It was found that the curvature significantly affects the D_{MB} in the planes where the FGP is curved. The impact of the curvature is particularly noteworthy for low elevation angles. In cases where the FGP is flat in one plane, the impact on the D_{MB} in that plane is negligible.

In conclusion, the different FGPs have been found to affect the D_{MB} to a significant extent. It is advisable to take these effects into account during the design phase. For instance, by insisting on a minimum size or curvature radius of the antenna ground plane before guaranteeing the performance. Also, the design should aim at introducing only a minimum gap between the array and surrounding ground plane when the antenna is mounted. Alternatively, this gap should be taken into account when designing and optimising the array. If the final mounting procedure and ground plane are unknown during the antenna design phase, the degradation of the performance, due to the various ground plane effects, may be taken into consideration by designing for a sufficient performance margin. For instance by designing for a D_{MB} about 1 dB above the requirements.

The results presented in this section are not validated by measurements. It is noted, however, that the accuracy of the employed MAS model has been validated in [J2] for flat FGPs.
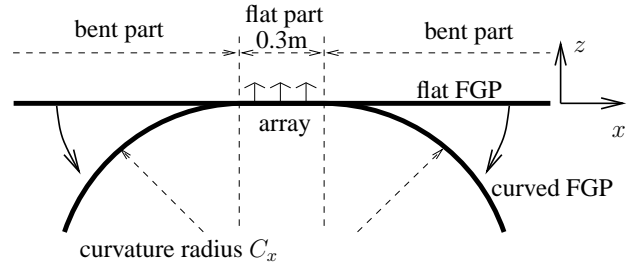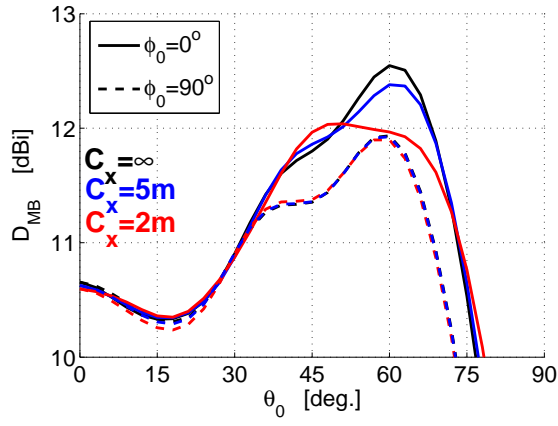
(a)
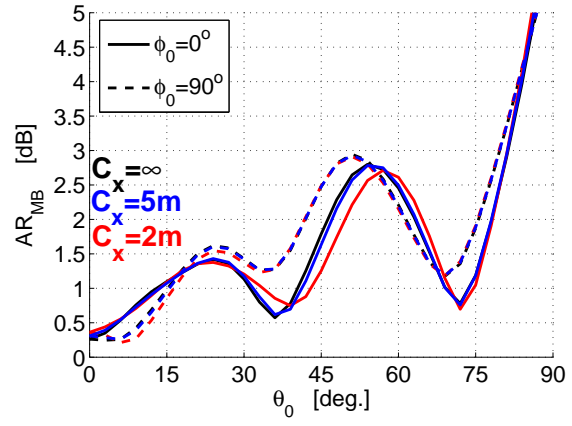
(b)
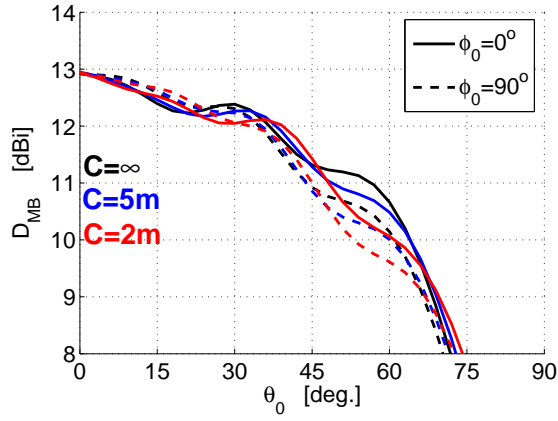
(c)

Figure 5.6:   *Influence of FGP curvature on the D_{MB} and AR_{MB} for the PDDA and CBASA arrays for $\phi_0 = 0°$ and $\phi_0 = 90°$ at 1.6 GHz. (a) D_{MB}, and (b) AR_{MB} as function of θ_0 for the PDDA array on the large square FGP, with different C_x and $C_y = \infty$. (c) D_{MB} of CBASA array on the large circular FGP with $C_x = C_y = C$.*

SEQUENTIALLY ROTATED PHASED ARRAYS

The Sequential Rotation (SR) is a well-known technique for improving the circular polarisation purity of an antenna array. In a Conventional Phased Array (CPA) the lack of polarisation purity of the antenna elements and mutual coupling will impair the circular polarisation of the array, leading to high Axial Ratio (AR) or narrow AR bandwidth. Early applications of the SR include [158, 159] and theoretical descriptions of the technique have been presented in [160–162]. It is well known that the polarisation purity of a sequentially rotated array, in the absence of mutual coupling effects, is independent of the polarisation of the antenna elements [160, 161]. The SR has primarily been used with fixed-beam arrays where significant improvement of the AR can be obtained. Fixed-beam applications include arrays of microstrip antenna elements [158, 160–164] and Dielectric Resonator Antenna (DRA) elements [165, 166]. The SR has also been employed for phased arrays, however, to a lesser extent. In [167, 168] sequentially rotated linear phased arrays of circularly polarised elements are investigated theoretically and experimentally, and in [159, 169–171] planar microstrip phased arrays are investigated. In these works, it is established that the SR indeed yields improvements, also for the case of phased arrays. However, general theoretical expressions are not provided.

In this study, an investigation of the performance of Sequentially Rotated Phased Arrays (SRPAs) have been undertaken. The results from this work are described in detail in [J6, R3], and in this chapter, examples of the possible improvements that can be obtained, compared to the CPA case, will be given. This is done by employing two different mathematical models, a theoretical model based on the analytical Spherical Wave Expansion (SWE) of the element far field and a full-wave Method of Auxiliary Sources (MAS) numerical simulation.

6.1 Sequential Rotation Principle

The general principles of the SR are well known from the abundant literature on the subject, see the aforementioned references. The principle is illustrated conceptually in Figure 6.1a where K antenna elements are located in an array in the (x, y)-plane. The element positions are indicated by the cylindrical coordinates (d_k, ϕ_k). The elements are furthermore rotated by angles ϕ_{pk}, and simultaneously, a phase shift ϕ_{ek} is introduced as shown in the figure. The beam scanning is accomplished in the usual manner by applying a progressive phase shift across the array aperture, indicated symbolically by ψ_k.

Figure 6.1: (a) *Illustration of the SR principle for phased arrays.* (b) *4-element SRPA.* (c) *7-element SRPA.*

The term "sequential" refers to the rotation of the elements only, and the element positions are not restricted. Therefore, a given set of rotation angles ϕ_{pk} does not uniquely characterise the SR, as employed in
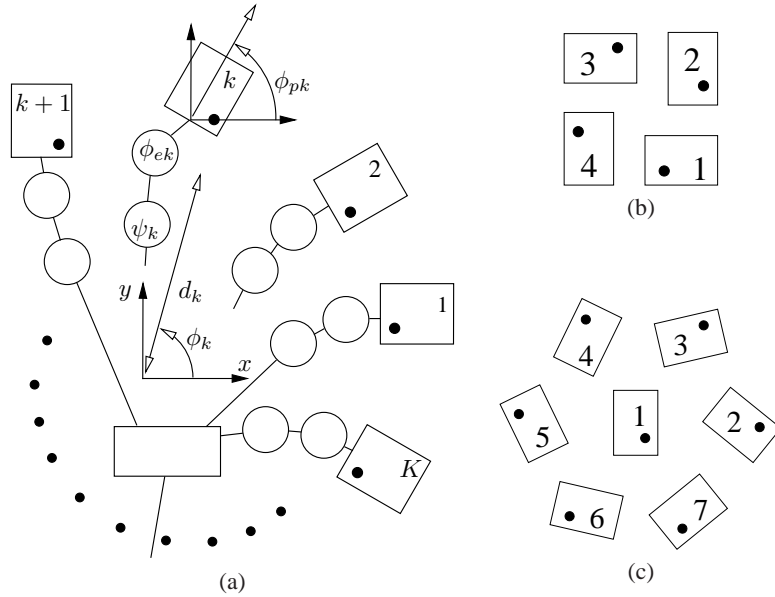
the array. Furthermore, the physical rotations ϕ_{pk} and electric phase shift ϕ_{ek} can be chosen in many ways and thus different implementations of the SR are possible. A general discussion of these issues is given in [J6, R3] where the different choices of SRPA configuration and their consequences are discussed in detail.

The results presented here focus on configurations where the elements are rotated such that they cover the full 360° in equiangular steps. Two examples of such SRPAs are shown in Figure 6.1b,c for $K = 4$ and 7. Moreover, for the configurations considered in the following, it is chosen that the physical rotation and the electric phase shift are related as $\phi_{ek} = -\phi_{pk}$. In the case where the Active Element Patterns (AEPs) are identical and in the absence mutual coupling, this configuration will ensure Right-Hand Circular Polarisation (RHCP) with an AR of 0 dB in the $\theta = 0^\circ$ direction, regardless of the element positions. In practice, however, the element positions affect the performance of the SRPA and may introduce errors via the mutual coupling and non-identical AEPs. Also, the ϕ_{ek} may be difficult to realise exactly since some frequency variation may occur, and this will introduce additional errors and degrade the performance of the SRPA.

6.2   *SWE Model and Application to a CDA Array*

Based on the general SWE [46], analytical expressions for the far field of SRPAs have been derived [J6]. These expressions are in some respects similar to those derived in [161] for fixed-beam arrays in that they are based on the assumption of identical AEPs and in that the mutual coupling is not taken into account. However, those derived in this study are general in the sense that arbitrary antenna elements can readily be employed in the model by directly inserting the far-field SWE. Furthermore, the model allows for general choices of element positions (d_k, ϕ_k), element rotations (ϕ_{pk}), SR phase shifts (ϕ_{ek}), and array scan angles (θ_0, ϕ_0). It is noted that general scan angles have also been considered theoretically in other works [167, 171].

(a)
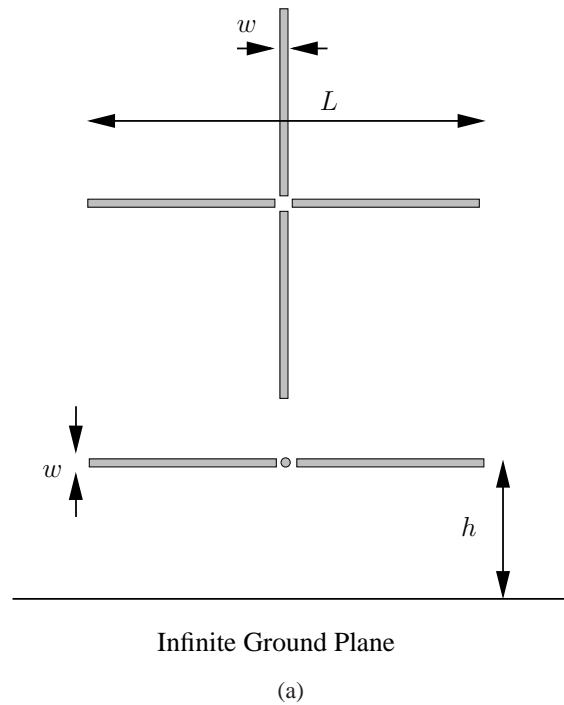
CDA Design		Performance	
L	75.0 mm	f_{AR}	1.6 GHz
w	2.0 mm	AR BW	3.1 %
h	47.0 mm	min. AR	0.87 dB
d	112.5 mm		
h_{mp}	0 mm		
α	16		
β	0.1		

(b)

Figure 6.2: (a) *CDA element used for the 7-element arrays.* (b) *Design parameters and simulated performance of CDA element. The performance is calculated for an IGP.*

In the following, an example of application of the SR is given. The purpose of this example is two-fold. First, the improvements obtainable with the SR will be illustrated, and second, the validity and limitations of the SWE model will be demonstrated. To this end, the Crossed Dipole Antenna (CDA) element introduced in Section 3.1 is revisited. It is now employed in the 7-element SRPA of Figure 6.1c as well as the corresponding CPA. The element and its AR characteristics are shown in Figure 6.2. For a frequency of 1.6 GHz, the lengths of the dipoles equal $0.4\,\lambda_0$ thus resembling the CDA of Figure 3.1a. For the purpose of illustrating the benefits of the SR, the CDA element has been defined to have a narrow-band AR. This is accomplished by exciting the two crossed dipoles with an imperfect phase quadrature between the forward voltage waves, $V_{x,0}^+$, $V_{y,0}^+$, such
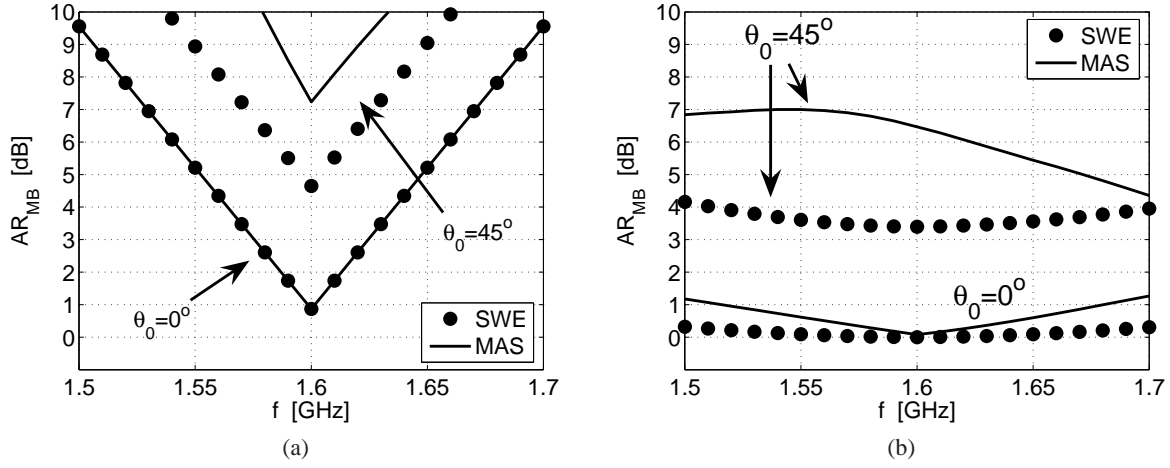
Figure 6.3: AR_{MB} for 7-element CDA array for $\theta_0 = 0°$ and $\theta_0 = 45°$ as function of frequency. The worst case in ϕ_0 is shown. (a) CPA. (b) SRPA.

that

$$V_{x,0}^+ = e^{-\left(\alpha \frac{|f - f_{AR}|}{f_{AR}} + \beta\right)}, \tag{6.1a}$$

$$V_{y,0}^+ = -j, \tag{6.1b}$$

where α and β are positive constants. These excitations imply a frequency-dependent AR of the CDA array with a minimum AR at the frequency f_{AR}. For increasing α and β, more narrow-band AR and larger minimum AR result, respectively. Presently, $\alpha = 16$, $\beta = 0.1$, and $f_{AR} = 1.6$ GHz are chosen and imply a 3 dB AR bandwidth at $\theta = 0°$ of about 3.1 % and a minimum AR of 0.87 dB at f_{AR}.

The SR is typically designed for a particular design frequency and the electric phase shifts ϕ_{ek} will not be exactly obtained at other frequencies. In order to incorporate this practical aspect, a linear frequency dependence is introduced in the electric phase shifts

$$\phi_{ek} = -\phi_{pk} \frac{f}{f_0}, \tag{6.2}$$

where f_0 is the frequency for which the SR is designed. This models an implementation of the ϕ_{ek} using fixed-length transmission lines. In this example, $f_0 = 1.6$ GHz is chosen which coincides with the frequency of minimum AR, f_{AR}, of the CDA element.

Two different simulation models are employed to model the CDA arrays, the SWE model described in detail in [J6] and a MAS model in which the entire array is included. In the SWE model, a single CDA element, with a known far field given by an SWE, is employed[*]. That is, the AEPs are assumed to be identical, and equal to the isolated element pattern[†]. Furthermore, the mutual coupling is not included in this model. In the second model, the entire SRPA is modelled with MAS and the different AEPs as well as the mutual coupling is included.

In Figure 6.3, the AR_{MB} is shown for the CPA and SRPA using both the SWE and MAS models. This is done for the cases of $\theta_0 = 0°$ and $\theta_0 = 45°$ and it is noted that the worst case in ϕ_0 is shown. In Figure 6.3a, the CPA case is shown and it is obvious that the polarisation purity is poor at the extreme parts of the investigated frequency band, as expected from (6.1a,b). The SWE and MAS models are in good agreement for the case of $\theta_0 = 0°$. However, for $\theta_0 = 45°$ the more realistic MAS model reveals that the low AR_{MB}, predicted by the SWE, is too optimistic. In Figure 6.3b, the SRPA case is shown. The improvement in the AR, due to the SR, is quite dramatic. For the SWE model, an AR of 0 dB is obtained for $\theta_0 = 0°$ at the design frequency $f_0 = 1.6$ GHz. For the other frequencies the frequency variation of ϕ_{ek}, given by (6.2), results in larger AR at $\theta = 0°$. Still, the AR has become much better than for the CPA array, both for $\theta_0 = 0°$ and $\theta_0 = 45°$. For the

---

[*]This single CDA element is, in fact, modelled using a MAS model from which the SWE of the isolated element far field has been calculated. The details of calculating the SWE from a MAS solution are given in [R1].

[†]Note that, in principle, only the assumption of *identical* AEPs is necessary in the SWE model. The AEPs need not generally be assumed to equal the isolated element pattern. However, in many practical cases this further assumption is an obvious choice since the actual AEPs are typically unknown.

MAS model, the improvements are less impressive and for $\theta_0 = 0^\circ$ the AR is 0.1 dB at f_0. This increase is a consequence of the mutual coupling and non-identical AEPs, which are included in the MAS model but not in the SWE model. The occurrence of these undesired phenomena can be explained from Figure 6.1.

The 4-element SRPA in Figure 6.1b is rotationally symmetric in the sense that all elements have exactly the same surroundings. Therefore, the AEPs are identical, although they are different from the isolated element pattern. The rotational symmetry also affects the mutual coupling which becomes similarly symmetric. Mathematically, this means that scattering matrix of the array, $\overline{\overline{\mathbf{S}}}$, is a symmetric Toeplitz matrix [J6]. In this case it can be shown that, if the forward voltage wave excitations, $\mathbf{V}^+$, are in ideal phase quadrature, the resulting current excitations, $\mathbf{I}$, will also be in ideal phase quadrature for $\theta_0 = 0^\circ$ and this happens in spite of the mutual coupling. It is noted that the identical AEPs and ideal phase quadrature of the current excitation, thus obtained, in fact renders the assumptions of the SWE model unimportant. The SWE is, therefore, in principle exact if the actual identical AEPs are employed instead of the isolated element patterns.

For the 7-element SRPA in Figure 6.1c, this rotational symmetry is not present. Thus the AEPs are not identical and $\overline{\overline{\mathbf{S}}}$ is not a symmetric Toeplitz matrix. In this case, the mutual coupling will introduce errors resulting in an AR larger than 0 dB for the $\theta_0 = 0^\circ$ case, and the SWE can not accurately recover the true far field of the SRPA. In the following section, these aspects are illustrated further from an investigation of 4- and 7-element SRPAs consisting of circularly polarised DRA elements.
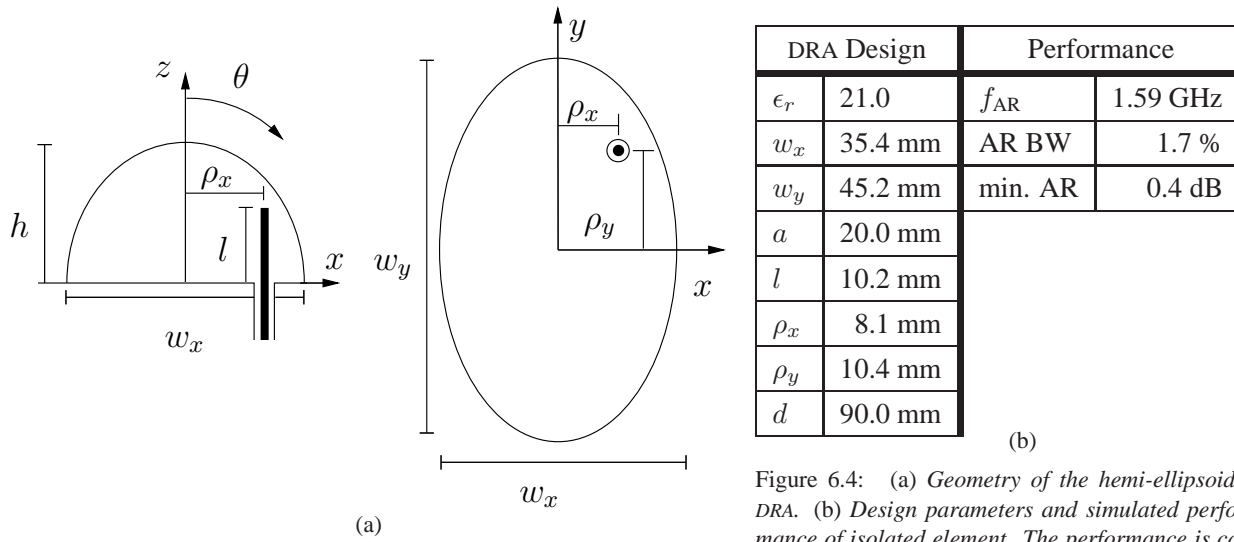

DRA Design		Performance	
ϵ_r	21.0	f_{AR}	1.59 GHz
w_x	35.4 mm	AR BW	1.7 %
w_y	45.2 mm	min. AR	0.4 dB
a	20.0 mm		
l	10.2 mm		
ρ_x	8.1 mm		
ρ_y	10.4 mm		
d	90.0 mm		

(a)

(b)

Figure 6.4:   (a) *Geometry of the hemi-ellipsoidal DRA.* (b) *Design parameters and simulated performance of isolated element. The performance is calculated for an IGP.*

6.3   *Application to a DRA Array*

The SR is now applied to a more realistic antenna model in virtue of DRA elements. This has been done for single-feed and dual-feed DRA element in 4- and 7-element SRPAs. In this section, the results for the single-feed DRA element are presented. Brief discussions on the dual-feed DRA element will also be given, however, for the details of this investigation, reference is made to [R3]. The emphasis is on the impact of the rotational symmetry of the SRPA, as exemplified by the 4- and 7-element SRPAs in Figure 6.1b,c.

The single-feed DRA element has been investigated theoretically in [J5], and it has a more realistic narrowband AR than the CDA element of the previous section. It has a hemi-ellipsoidal shape as shown in Figure 6.4, and it is similar to the hemispheroidal elements of the DRA array in Section 4.4 except that the two lateral axes may be of different lengths. It is fed by a single probe only, and due to the hemi-ellipsoidal shape, it is possible to obtain circular polarisation in a narrow frequency band. The single element and the SRPA are modelled with the MAS model employed for the DRA array. The design parameters and the AR characteristics are also included in Figure 6.4. The DRA element is now used in the 4- and 7-element SRPAs of Figure 6.1b,c as well as in the corresponding CPAs. The SRPAs are designed for $f_0 = 1.6$ GHz, i.e., the ϕ_{ek} are exact for this frequency only.
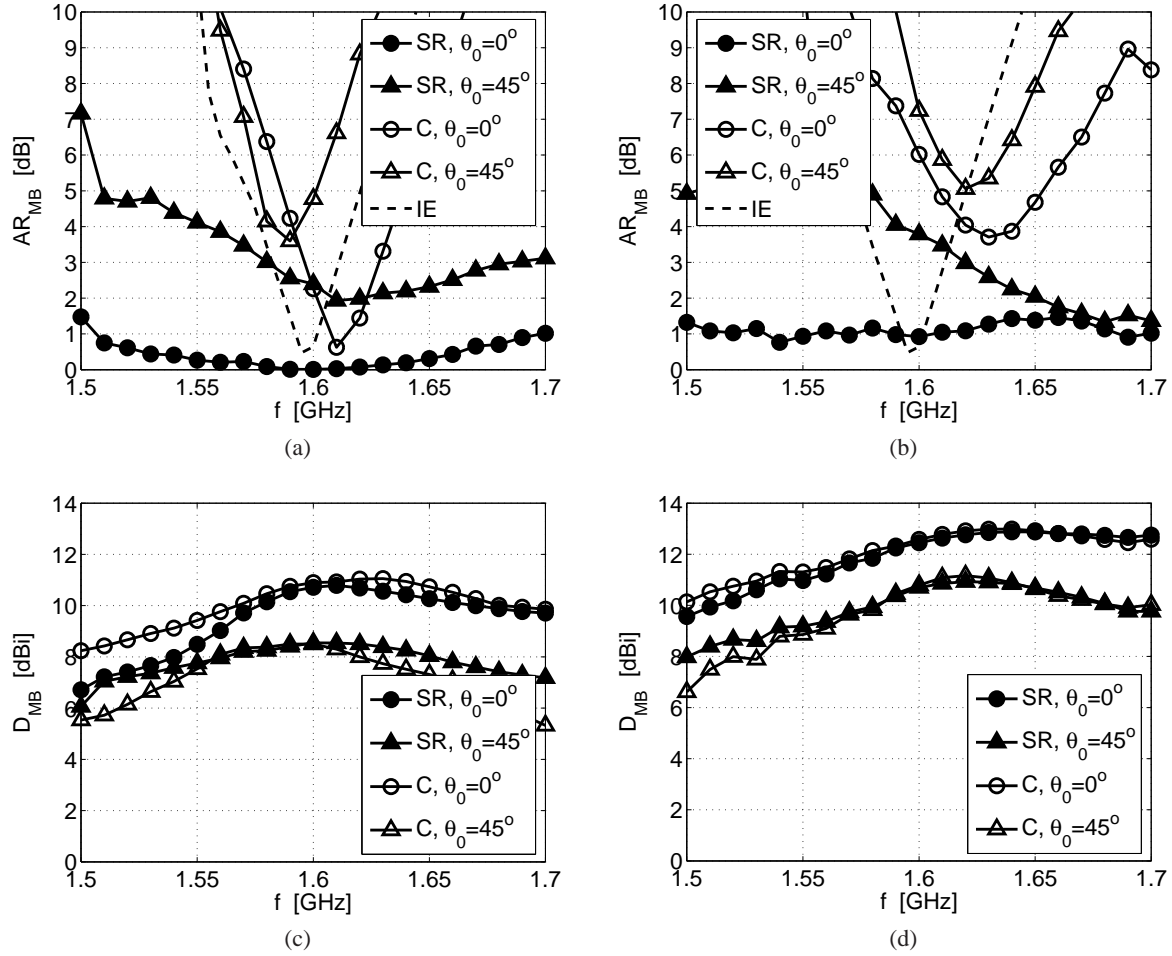
Figure 6.5: *Results for single-feed hemi-ellipsoidal DRA elements in CPAs and SRPAs.* (a) AR_{MB} *for 4-element arrays.* (b) AR_{MB} *for 7-element arrays.* (c) D_{MB} *for 4-element arrays.* (d) D_{MB} *for 7-element arrays. The AR for the isolated element (IE) is also shown in the* AR_{MB} *plots. For brevity: SR=SRPA, C=CPA, IE=isolated element.*

Figure 6.5a,b show the MB_{AR} of the CPAs and SRPAs with 4 and 7 elements, respectively. The worst case among the azimuthal scan angles ϕ_0 is shown for the polar scan angles $\theta_0 = 0°$ and $\theta_0 = 45°$. Also the AR of the isolated element is shown for $\theta = 0°$. The minimum AR of the isolated element is 0.4 dB at $f_{AR} = 1.59$ GHz and it has a 3 dB AR bandwidth of about 1.7 %. It is seen that for the CPA cases the AR_{MB} is similarly narrow-band. Furthermore, the minimum AR does not not occur for f_{AR} but varies with θ_0. For the 7-element array, the results are particularly poor with high AR_{MB} at f_{AR} for both polar scan angles. For both the 4- and 7-element SRPAs, significant improvements are evident. In particular, for the rotationally symmetric 4-element SRPA, the AR_{MB} of only 0.01 dB for $\theta = 0°$ and f_0 is very low. For the 7-element SRPA, which is not rotationally symmetric, a similar improvement is not obtained, and the AR_{MB} is generally around 1 dB. This further illustrates, that the mutual coupling and non-identical AEPs may compromise the performance of the SR for SRPAs that are not rotationally symmetric.

In Figure 6.5c,d, the corresponding D_{MB} is shown. Generally the D_{MB} peaks near f_0 and decreases for other frequencies. For the CPA case, this can be explained by the fact that the elements are almost linearly polarised for the extreme parts of the frequency band, which is also evident from the high AR_{MB}. In such cases of nearly linearly polarised elements, the horizontal far field will, for some azimuthal angles, be tangential to the ground plane, and consequently the worst case D_{MB} will be low. Interestingly, a similar decrease is seen for the SRPAs, but in this case the AR_{MB} is relatively low due to the improvements obtained with the SR. That is, the decrease in the D_{MB} can not be explained as a consequence of poor polarisation purity in the main beam. Instead, the decrease can be explained by the formation of cross-polarised side lobes. The formation of these cross-polarised side lobes are not shown here, but can be found in [R3]. Similar observations have previously been reported in [169] where linearly polarised elements are used in a 4-element SRPA. It is thus clear, that the SR does not necessarily improve the D_{MB} even though it does improve the AR_{MB}. It should

be noted that the decrease of the D_{MB} is not as severe in cases where larger SRPAs are used, e.g., with 7, 16, or more elements [169]. In these cases, the cross-polar side lobes are less prominent, and consequently the improvement of the D_{MB} from the SR is not compromised this severely. This is also evident from the D_{MB} of the 7-element SRPA. Some reduction of the D_{MB} still occurs for the frequencies where the elements are linearly polarised, but it is not as prominent as for the 4-element SRPA. For further details on this, the reader is referred to [R3].

In the case of the dual-feed circularly polarised DRA elements, where the feeds are excited in phase quadrature, much more wide-band AR is obtained for the elements. In [R3] the application of SR to arrays of such elements has been investigated. It is found that the SR will indeed improve the AR for the case of rotationally symmetric SRPA. However, for the asymmetric SRPA, the errors introduced by the mutual coupling and non-identical AEPs render the improvements of the AR quite small. Thus the advantages of using SR for dual-feed circularly polarised elements are minor, compared to the case of the narrow-band single-feed elements. The SR was in fact found to degrade the D_{MB} for 4-element arrays, however, for the 7-element case no notable impact occurred. For further details, the reader is referred to [R3].

6.4   Summary

The SR has been investigated for application to phased arrays using two mathematical models, a theoretical model based on an analytical SWE of the element far field and a full-wave MAS numerical model.

The analytical SWE model allows for arbitrary antenna elements with arbitrary positions, rotations, and array scan angles. It is assumed that the AEPs are identical and the mutual coupling between the elements is not included. In order to model limitations in a practical implementation, a linear frequency variation of the SR phase shifts is introduced, which implies that they are only exact for a certain design frequency. In the MAS model, the entire SRPA is modelled and thus both the mutual coupling and the possibly non-identical AEPs are included.

The two models were employed to model a 7-element array of CDA elements with known element far field and with poor polarisation purity. From both models it was concluded that the AR_{MB} can be significantly improved compared to the CPA case. In particular, for scanning in the $\theta = 0^{\circ}$ direction, the SWE shows a resulting AR_{MB} of 0 dB whereas the MAS model yields a slightly larger AR_{MB}. These deviations are due to the omission of the mutual coupling and non-identical AEPs in the SWE model, which as a consequence yields too optimistic results. For certain array topologies, where the elements are arranged rotationally symmetric, the mutual coupling will also be symmetric and the AEPs will be identical. In this case, the SR is not subject to these unwanted effects and it works well in spite of the mutual coupling. Moreover, the SWE is in fact accurate in these cases since the assumption of identical AEPs is justified, and also the phase quadrature of the current excitations is accurate in spite of the mutual coupling.

This point was further demonstrated by a MAS model of two SRPAs with 4 and 7 DRA elements. It was confirmed that the improvement of the AR due to the SR is very good when the SRPA is symmetric. For the opposite case, a minimum AR of 1 dB was obtained which is still an improvement. The CDA and DRA models employed for these results were positioned on an Infinite Ground Plane (IGP). For a Finite Ground Plane (FGP) additional asymmetries may be introduced, in particular if the SRPA is not centred on the FGP. This will result in non-identical AEPs even when the SRPA is rotationally symmetric.

The frequency dependence of the SR phase shifts was found to increase the AR slightly. However, in cases where narrow-band, single-feed, circularly polarised elements are used, the AR bandwidth is still much better than without the SR.

The resulting D_{MB} of the SRPAs was also investigated. It was found that even though the AR can be optimised, the resulting D_{MB} may be poor. Thus for linearly polarised elements the resulting cross-polar radiation in directions away from the main beam caused a decrease of the D_{MB} which is in agreement with the observations in [169]. The effect of this phenomenon decreases as the array becomes larger and for the 7-element array the degradation was already found to be less prominent.

The case of dual-feed, circularly polarised elements, where the AR bandwidth is wider, was also briefly mentioned. In this case the improvements due to the SR are minor, compared to the single-feed case, where significant improvements can be obtained. Furthermore, the D_{MB} may be worse than for the CPA cases.

CHAPTER 7

CONCLUSION

In this study, the electronically steerable antennas, known as phased arrays, as well as a range of related topics have been investigated. The emphasis is primarily on small 7-element phased arrays for application in mobile satellite communications. The other topics comprise investigations of various aspects relating to mutual coupling, influence of Finite Ground Planes (FGPs), as well as application of Sequential Rotation (SR). In the course of the study, a phased array prototype has been designed and constructed, and several publications [J1 - J6, C1, C2, R1 - R4] have resulted from the work. In this concluding chapter, the investigations and main results of the study are briefly summarised. Following this, recommendations and suggestions for further work are given.

7.1 Summary of the Study

In Chapter 2, the different mathematical methods and phased array models, employed in the investigations, were presented. The mathematical methods comprise analytical Spherical Wave Expansion (SWE) solutions and numerical computations. The latter include commercially available software as well as methods derived in the literature and during the study. The phased array models comprise three different array modelling schemes, the Isolated Element Scheme (IES), the Infinite Array Scheme (IAS), and the Finite Array Scheme (FAS), as well as models of the array feed network and receiver. Many of the methods were employed in combination, forming a three-stage model with which the investigations of the phased arrays were conducted. The three stages focus on the array, the surrounding FGP, and the array feed network and receiver chain and ultimately lead to an assessment of the main-beam co-polar directivity D_{MB}, scan loss, and the Receiver Figure of Merit, G/T, of the phased arrays.

In Chapter 3, the impacts of different types of element and array configurations on the mutual coupling and array scan loss were investigated. The investigations covered the influence of the array size, element radiation patterns, ground planes, as well as the use of parasitic structures. Two means of reducing the mutual coupling, and thereby also the scan loss, were identified. The application of artificial high-impedance or Electromagnetic Band Gap (EBG) ground planes is one such means, and it has been employed successfully in several designs [87, 97, 99]. The EBG ground planes suppress both the Transverse Magnetic (TM) and Transverse Electric (TE) surface waves which, compared to a regular Perfect Electric Conductor (PEC) ground plane implies a significant reduction of the mutual coupling, ordinarily occurring due to TM surface waves. Another consequence of applying EBG ground planes is that the E- and H-plane radiation patterns become alike. This can be used to improve the Axial Ratio (AR) for low elevation angles, however, at the same time it is apparent that the radiation at these low elevation angles is reduced. Another means of reducing the scan loss is by applying parasitic monopoles between the elements such as demonstrated in [104–107, 109]. For an array of crossed dipoles, a reduction of S_{ij} of almost 10 dB was thus obtained. Coincidentally, the parasitic monopoles also serve to give a slightly more uniform element pattern. Such parasitic monopoles were employed in the constructed array prototype.

In Chapter 4, the three different phased arrays, which have been of primary interest in the study, were presented. The arrays all consist of 7 elements positioned in a hexagonal lattice with different element types, namely the Cavity-Backed Annular Slot Antenna (CBASA), the Printed Drooping Dipole Antenna (PDDA), and the Dielectric Resonator Antenna (DRA). The investigations of the CBASA and DRA were based on initial optimisation of the isolated elements, whereas the entire PDDA array was optimised using the Genetic Algorithm (GA).

The CBASA array has the poorest performance of the three. The CBASA element is relatively narrow-band and it also has the most narrow beam width of the three element types. This implies that the array coverage at low elevation angles is poor, both due to low D_{MB}, as well as high scan loss, resulting in poor G/T.

Additionally, significant azimuthal variation occurs for both D_{MB} and scan loss and this is believed to be the consequence of guided waves, or surface waves, which are excited in the superstrate and increase the mutual coupling. The attractive features of the CBASA array are its low profile and robust mechanical features, which are desirable from a commercial perspective.

The PDDA array is the best of the three arrays in terms of performance and exhibits a particularly good performance for low elevation scan angles. It is a results of a GA optimisation aimed at maximising the G/T. This has resulted in a high element profile which yields a very wide element pattern. Thus the D_{MB} does not decrease as rapidly as for the CBASA array at low elevation angles. A further advantage is that the scan loss is lower for low elevations than for high. Therefore, the G/T is almost uniform within most of the hemisphere. The obvious disadvantage of the PDDA array is the high element profile of about 8 cm which is undesirable from a commercial perspective.

The DRA array performs better than the CBASA array but generally poorer than the PDDA array. The possibility of a small element size enables a smaller element separation which is instrumental in reducing the scan loss. At the same time it yields a more uniform D_{MB}. Since, the element pattern is almost as narrow as that of the CBASA element, sufficient coverage is still difficult to obtain at low elevation angles. Positive features of the DRA array are its relatively low height and high degree of robustness. Its negative features are that the dielectric material is expensive and generally difficult to process mechanically.

In Chapter 5, the impact of the size, shape, and curvature of the FGP on the array radiation was investigated. Furthermore, the impact of raising the array above the surrounding FGP was addressed. The D_{MB} is influenced significantly by both the size and shape of the FGP and generally the coverage is poorer for small FGPs than for large. For the large FGPs, ripples are introduced in the radiation pattern, leading to considerable variation in the D_{MB}. For a fixed polar scan angle, the D_{MB} may thus change with up to 0.7 dB due to the FGP size. For the PDDA array, the impact of small vertical gaps from 0 to 3 cm between the array and ground plane was investigated. It was found that an increase of the gap height will cause an increase in the D_{MB} for high elevation scan angles, whereas a decrease will occur for low elevation angles. Within the investigated span of gap heights it was found that the D_{MB} may vary with up to 1.0 dB depending on the scan angle. It was further found, that the curvature of the FGP significantly affects the D_{MB} in the planes where the FGP is curved, but not in the plane where it is flat. Curvature radii of 2 m and 5 m were investigated with the most significant impact occurring for 2 m. The impact was particularly noteworthy at low elevation angles.

In Chapter 6, the application of the SR principle for phased arrays was investigated. To this end, an analytical SWE model and a full-wave Method of Auxiliary Sources (MAS) numerical model were developed. The two models differ in that the SWE model assumes that the Active Element Patterns (AEPs) are identical and the mutual coupling is not included. This is not the case for the MAS model. The two models were employed in 4- and 7-element arrays of Crossed Dipole Antenna (CDA) and hemi-ellipsoidal DRA elements. It was concluded that for arrays with poor polarisation purity or low AR bandwidth, the AR can be significantly improved by applying the SR. Due to the approximations in the SWE model, it yields slightly optimistic results, particularly in the case where the elements are not positioned in a rotationally symmetric way. In this case, the effects of the mutual coupling imply a slight degradation of the SR performance, which is clearly seen from the full-wave MAS model. However, in the case of rotationally symmetric arrays, this degradation does not occur and the SWE model is essentially accurate if the true identical AEPs are used. An investigation into the D_{MB} revealed that this may be poor in spite of a general improvement of the AR, particularly for small arrays of elements with poor polarisation purity. This observation is in agreement with the observations in [169]. For elements that do not have a poor polarisation purity, the improvements obtainable with the SR are less significant. In the case of dual feed DRA elements, it was found that the SR improved the AR somewhat, but coincidentally the D_{MB} was typically degraded.

7.2   *Recommendations and Suggestions for Further Work*

7.2.1   *The Three Arrays*

Among the three phased arrays investigated in the study, further investigations will be particularly useful for the CBASA and PDDA arrays. They both exhibit very positive but also negative features and improvements may be obtainable. Furthermore, they are not impaired by high material costs and difficulty of mechanical

processing, which is the case for the DRA array.

The CBASA array is attractive due to its low profile and rugged mechanical features. However, the investigations concluded that the performance is poor. It may be possible to improve the performance by using an element with larger bandwidth. Some means to achieve this for the CBASA element are given in [J1] but also other types of cavity-backed slot antennas may be used, e.g., with crossed slots [37, 123, 124]. It is apparent, however, that the element separation should not be increased as a consequence hereof. Another problem evident for the CBASA array is the large azimuthal variations in the D_{MB} and scan loss which are believed to be caused by excitation of surface waves in the superstrate covering the slot. A slot antenna without this superstrate will not exhibit this problem, however, a removal of the superstrate will simultaneously increase the resonance frequency considerably [J1]. The application of parasitic structures has not been employed for the CBASA array. This has, however, been suggested in [110] and the possibilities of improving the coverage of slot arrays in this way should be investigated.

Although the PDDA array is the best among the three in terms of performance, it is clear that its height is problematic from a commercial perspective. The height is a consequence of the GA optimisation in which the array performance was the only goal. By limiting the allowed element height in the GA optimisation, a useful compromise between the element height and performance requirements might be found. A practical aspect of the PDDA array is that it is too time-consuming to assemble in its present form. Further work with this array should, therefore, focus on obtaining a less complicated design, e.g., by replacing the soldered capacitors with printed interdigital capacitors [137]. Also the use of circular walls instead of the 72 parasitic monopoles should be investigated as this may offer similar performance but less complexity of the design.

7.2.2   Other Investigations

In addition to the investigation directly concerned with the phased arrays, a number of different mathematical and computational topics have been considered. In this respect, the MAS models have been widely used, both for smooth structures, such as the DRA arrays and FGPs with the Standard MAS [53], and also for the CDA arrays using the MAS formulation for wires [62]. With regard to the former, it is clear that the inability to model structures with sharp edges limits the possible investigations considerably. It would indeed be of interest to improve the MAS models, either by augmenting the Standard MAS with localised Method of Moments (MoM) patches [54, 55], or by using the so-called Modified MAS [58], which can handle sharp edges. Alternatively, a full MoM formulation could be implemented. These improvements will allow for FGP investigations without using rounded corners. Also the DRA investigations may then encompass more general shapes such as cylindrical and box-shaped DRAs. These can easily be analysed with commercially available simulation tools, e.g., HFSS or CST-MS, however, for a 7-element array the computational cost has rendered this impractical. In its present form, the MAS model can model such arrays. It is possible, however, that the computational inexpensive nature of MAS will be compromised by the above improvements, and in this case the purpose of such improvements will be defeated.

The feed network and receiver has not been of primary interest in this work. Therefore, the receiver was incorporated via a simple model based on assumed receiver characteristics. As already emphasised, the employed receiver model is meant to give a rough idea of the performance, however, a detailed analysis will require more accurate receiver models. Furthermore, a more accurate model of the antenna noise temperature could be included, such that its dependence on the array directivity is taken into account.

BIBLIOGRAPHY

For the papers and reports prepared during the project work, [J1- J6, C1, C2, R1- R4], see the List of Publications in page ix.

[1] S. A. Schelkunoff, "A Mathematical Theory of Linear Arrays," *Bell Syst. Techn. J.*, vol. 22, pp. 80–107, 1943.

[2] W. H. von Aulock, "Properties of Phased Arrays," *Proc. IRE*, vol. 48, no. 10, pp. 1715–1727, 1960.

[3] A. C. Schell, "Survey of Ground Based Phased Array Antennas," in *Phased Array Antennas*, A. A. Oliner and G. H. Knittel, Eds.   Artech House, Inc., Dedham, 1972, ch. 2, pp. 9–14.

[4] M. I. Skolnik, "Survey of Phased Array Accomplishments and Requirements for Navy Ships," in *Phased Array Antennas*, A. A. Oliner and G. H. Knittel, Eds.   Artech House, Inc., Dedham, 1972, ch. 2, pp. 15–20.

[5] J. F. Rippin, Jr., "Survey of Airborne Phased Array Antennas," in *Phased Array Antennas*, A. A. Oliner and G. H. Knittel, Eds.   Artech House, Inc., Dedham, 1972, ch. 2, pp. 21–29.

[6] P. J. Kahrilas, "HAPDAR - An Operational Phased Array Radar," *Proc. IEEE*, vol. 56, no. 11, pp. 1967–1975, 1968.

[7] A. K. Kamal, "Airport Surveillance Radar Design for Increased Air Traffic," *Int. Conf. Radar 92*, pp. 151–154, 1992.

[8] W. H. Kummer, "Phased Array Antennas for Applications on Spacecraft," in *Phased Array Antennas*, A. A. Oliner and G. H. Knittel, Eds.   Artech House, Inc., Dedham, 1972, ch. 2, pp. 30–42.

[9] W. Rafferty, K. Dessouky, and M. K. Sue, "Current Developments in NASA's Mobile Satellite Program," *Int. Conf. Satellite Systems for Mobile Communications and Navigation*, pp. 33–37, 1988.

[10] Y. Hase, S. Ohmori, and K. Kosaka, "Experimental Mobile Satellite System (EMSS) Using ETS-V," *Denshi Tokyo*, vol. 25, pp. 10–12, 1986.

[11] Teledyne Ryan Electronic, "Report No.TRE/SD105665-3B, Vehicle Antenna for the Mobile Satellite Experiment, Final Report," Jet Propulsion Laboratory, Pasadena, California, Tech. Rep., March 1988.

[12] Ball Aerospace Systems Division, "MSAT Final Report," Jet Propulsion Laboratory, Pasadena, California, Tech. Rep., December 1987.

[13] M. Yasunaga, *et al.*, "Phased Array Antennas for Aeronautical Satellite Communications," *Int. Conf. Antennas Propag.*, vol. 7, pp. 47–50, 1987.

[14] T. Hirata, "Develoment Status of Aeronautical Satellite Communication System at TOYOCOM Japan," *Elsevier Space Communications*, vol. 7, pp. 119–131, 1990.

[15] G. Maral and M. Bousquet, *Satellite Communications Systems - Systems, Techniques and Technology*, 4th ed.   John Wiley & Sons, New York, 2003.

[16] O. Lundberg, "Mobile Communications via Satellite in the 1990s," *Phil. Trans. R. Soc. Lond., A*, vol. 312, no. 1519, pp. 41–54, 1984.

[17] F. Ananasso and F. D. Priscoli, "The Role of Satellites in Personal Communication Services," *IEEE J. Sel. Areas Commun.*, vol. 13, no. 2, pp. 180–196, 1995.

[18] M. Richharia, *Mobile Satellite Communications - Principles and Trends*.   Addison-Wesley, London, 2001.

[19] Thrane & Thrane A/S, *Thrane & Thrane Annual Report*, Thrane & Thrane A/S, 2005.

[20] R. Sorace, "Overview of Multiple Satellite Communication Networks," *IEEE Trans. Aero. Elect. Sys.*, vol. 35, no. 4, pp. 1362–1368, 1999.

[21] C. E. Fossa, *et al.*, "An Overview of the IRIDIUM® Low Earth orbit (LEO) Satellite System," *Proc. IEEE National Aerospace and Electronics Conference*, pp. 152–159, 1998.

[22] F. J. Dietrich, "The Globalstar Cellular Satellite System," *IEEE Trans. Antennas Propag.*, vol. 46, no. 6,

pp. 935–942, 1998.

[23] Inmarsat. (2007, March) Inmarsat Web Page. [Online]. Available: http://www.inmarsat.com

[24] A. Franchi, A. Howell, and J. Sengupta, "Broadband Mobile via Satellite: Inmarsat BGAN," *IEE Seminar on Broadband Satellite: The Critical Success Factors - Technology, Services and Markets*, pp. 23/1–7, 2000.

[25] Thrane & Thrane A/S. (2007, May) Thrane & Thrane Web Page. [Online]. Available: http://www.thrane.com/

[26] ——, *Thrane & Thrane Mini-C Solutions*.

[27] JAST. (2007, May) JAST Web Page. [Online]. Available: http://www.jast.ch/JJ_site_1/

[28] N. Terada, K. Satoh, and F. Yamazaki, "Compact Mobile Antennas for Mobile Satellite Communications," *IEEE Vehic. Tech. Conf.*, pp. 104–112, 1987.

[29] P. Estabrook and W. Rafferty, "Mobile Satellite Vehicle Antennas: Noise Temperature and Receiver G/T," *IEEE Vehic. Tech. Conf.*, pp. 757–762, 1989.

[30] R. E. Munson, "Microstrip Patch Array for the Mobile Terminal Antenna of a Mobile Communication System," *Europ. Microwave Conf.*, pp. 579–583, 1997.

[31] Thrane & Thrane A/S, *Explorer 700^{TM} User Manual*, 2007.

[32] Omnipless. (2007, April) Omnipless Web Page. [Online]. Available: http://www.omnipless.com

[33] N. C. Karmakar and M. E. Bialkowski, "A Compact Switched-Beam Array Antenna for Mobile Satellite Communications," *Microwave Opt. Technol. Lett.*, pp. 186–191, 1999.

[34] X. Lan and B. Foo, "A Novel Low-Cost Switched-Beam Microstrip Smart Antenna," *IEEE Antennas Propag. Soc. Int. Symp. Dig.*, pp. 477–480, 2002.

[35] H. Ashoka, D. de Jager, and J. Logan, "ALPES: A Low Profile Electronically Steered Antenna for MobileSat® Applications," *Asia-Pacific Microwave Conference Proceedings*, pp. 637–640, 1997.

[36] L. Baggen, *et al.*, "Advances in Phased Array Technology," *3rd European Radar Conference*, pp. 88–91, 2006.

[37] H. H. Chung, W. Foy, and S. Y. Peng, "Printed Crossed Slot Phased Array Antenna System for Mobile Satellite Communication," *IEEE Antennas Propag. Soc. Int. Symp. Dig.*, vol. 1, pp. 204–207, 1988.

[38] TECOM Industries, Inc. (2007, April) TECOM Industries Web Page. [Online]. Available: http://www.tecom-ind.com

[39] Y. Kazama, *et al.*, "12-Element Printed Array Antenna for Inmarsat-M Maritime Communications," *Int. Conf. Antennas Propag.*, pp. 368–371, 1993.

[40] A. P. Ansbro, "A Phased Array Antenna for Mobile-Satellite Communications in L-Band," *CSELT Technical Reports*, vol. 24, no. 4, pp. 695–707, 1996.

[41] N. C. Karmakar and M. E. Bialkowski, "Development and Performance of an L-Band Phased Array Antenna for Mobile Satellite Communications," *IEEE Antennas Propag. Soc. Int. Symp. Dig.*, pp. 158–161, 1999.

[42] R. Miura, *et al.*, "A DBF Self-Beam Steering Array Antenna for Mobile Satellite Applications Using Beam-Space Maximal-Ratio Combination," *IEEE Trans. Vehic. Tech.*, vol. 48, no. 3, pp. 665–675, 1999.

[43] L. C. Godara, *Smart Antennas*. CRC Press, 2004.

[44] R. J. Mailloux, *Phased Array Antenna Handbook*. Artech House, Boston, 1994.

[45] Ministry of Science, Technology, and Innovation. (2007, April) Industrial PhD Initiative. [Online]. Available: http://www.erhvervsphd.dk

[46] J. E. Hansen, *Spherical Near-Field Antenna Measurements*. Peter Peregrinus Ltd., London, 1998.

[47] C.-T. Tai, *Dyadic Green Functions in Electromagnetic Theory*. IEEE Press, New York, 1994.

[48] K. W. Leung, *et al.*, "Theory and Experiment of a Coaxial Probe Fed Hemispherical Dielectric Resonator Antenna," *IEEE Trans. Antennas Propag.*, vol. 41, no. 10, pp. 1390–1398, 1993.

[49] R. F. Harrington, *Field Computation by Moment Methods*. The Macmillan Company, New York, 1968.

[50] A. R. Djordjević, *et al.*, *AWAS for Windows, Version 2.0, Analysis of Wire Antennas and Scatterers, Software and User Manual.* Artech House Inc., Boston, 2002.

[51] E. Jørgensen, "Higher-Order Integral Equation Methods in Computational Electromagnetics," Ph.D. dissertation, Ørsted·DTU, Technical University of Denmark, DTU, Lyngby, Denmark, 2003.

[52] D. M. Pozar and D. H. Schaubert, "Analysis of an Infinite Array of Rectangular Microstrip Patches with Idealized Probe Feeds," *IEEE Trans. Antennas Propag.*, vol. 32, no. 10, pp. 1101–1107, 1984.

[53] D. I. Kaklamani and H. T. Anastassiu, "Aspects of the Method of Auxiliary Sources in Computational Electromagnetics," *IEEE Antennas Propag. Mag.*, vol. 44, no. 3, pp. 48–64, 2002.

[54] S. Eisler and Y. Leviatan, "Analysis of Electromagnetic Scattering From Metallic and Penetrable Cylinders with Edges Using Multifilament Current Model," *IEE Proc., Pt. H*, vol. 136, no. 6, pp. 431–438, 1989.

[55] N. V. Larsen and O. Breinbjerg, "A Hybrid MAS/MoM Technique for 2D Impedance Scatterers Illuminated by Closely Positioned Sources," *Microwave Opt. Technol. Lett.*, vol. 44, no. 2, pp. 112–114, 2005.

[56] M. Karamehmedovic and O. Breinbjerg, "A Convergent Method of Auxiliary Sources for Two Dimensional Impedance Scatterers With Edges," *Proc. 16th. Int. Conf. Applied Electromagnetics and Communications, ICECOM'01*, pp. 46–49, 2001.

[57] H. T. Anastassiu, *et al.*, "Electromagnetic Scattering Analysis of Coated Conductors With Edges Using the Method of Auxiliary Sources (MAS) in Conjunction With the Standard Impedance Boundary Condition (SIBC)," *IEEE Trans. Antennas Propag.*, vol. 50, no. 1, pp. 59–66, 2002.

[58] F. Shubitidze, H. T. Anastassiu, and D. I. Kaklamani, "An Improved Accuracy Version of the Method of Auxiliary Sources for Computational Electromagnetics," *IEEE Antennas Propag. Mag.*, vol. 52, no. 1, pp. 302–309, 2004.

[59] G. K. Avdikos and H. T. Anastassiu, "Computational Cost Estimation and Comparison for Three Methods of Applied Electromagnetics (MoM, MAS, MMAS)," *IEEE Antennas Propag. Mag.*, vol. 47, no. 1, pp. 121–129, 2005.

[60] R. S. Zaridze, *et al.*, "Electromagnetic Analysis for Vehicle Antenna Development Using Method of Auxiliary Sources," *IEEE Antennas Propag. Soc. Int. Symp. Dig.*, pp. 185–188, 2003.

[61] S. P. Skobelev, "Algorithm of the Method of Auxiliary Sources for Analysis of Arrays of Circular Waveguides with Protruding Dielectric Rods," *IEEE Int. Symp. Phased Array Systems and Technology*, pp. 333–338, 2003.

[62] P. J. Papakanellos and C. N. Capsalis, "Numerical Analysis of Cylindrical Dipole Antennas Using an Auxiliary Sources Model," *J. Electromagn. Waves Appl.*, vol. 17, no. 3, pp. 389–407, 2003.

[63] Ansoft Corporation. (2007, January) HFSS. [Online]. Available: http://www.ansoft.com/products.cfm

[64] CST - Computer Simulation Technology. (2007, January) CST Microwave Studio. [Online]. Available: http://www.cst.com/Content/Products/Products.aspx

[65] J. A. Dobrowolski, *Introduction To Computer Methods For Microwave Circuit Analysis And Design*, 2nd ed. John Wiley & Sons, Inc., New York, 1998.

[66] M. Manteghi and Y. Rahmat-Samii, "Multiport Characteristics of a Wide-Band Cavity Backed Annular Patch Antenna for Multipolarization Operations," *IEEE Trans. Antennas Propag.*, vol. 53, no. 1, pp. 466–474, 2005.

[67] E. Brookner and J. M. Howell, "Right Way to Calculate Reflector and Active-Phased-Array Antenna System Noise Temperature Taking into Account Antenna Mismatch," *IEEE Int. Symp. Phased Array Systems and Technology*, pp. 130–135, 2003.

[68] K. Nørgaard and U. V. Gothelf, *Inmarsat BGAN Land Vehicular Phased Array Antenna G/T Calculations*, Thrane & Thrane A/S, August 2004.

[69] A. K. Bhattacharyya, *Phased Array Antennas.* John Wiley & Sons, New York, 2006.

[70] B. L. Diamond, "Mutual Coupling Effects in Hybrid-Fed, Crossed-Dipole-Pair Arrays," *IEEE Antennas Propag. Soc. Int. Symp. Dig.*, pp. 157–163, 1965.

[71] A. J. Roscoe and R. A. Perrott, "Large Finite Array Analysis Using Infinite Array Data," *IEEE Trans.*

Antennas Propag., vol. 42, no. 7, pp. 983–992, 1994.

[72] D. M. Pozar and D. H. Schaubert, "Scan Blindness in Infinite Phased Arrays of Printed Dipoles," *IEEE Trans. Antennas Propag.*, vol. 32, no. 6, pp. 602–610, 1984.

[73] J. T. Aberle and D. M. Pozar, "Analysis of Infinite Arrays of One- and Two-Probe-Fed Circular Patches," *IEEE Trans. Antennas Propag.*, vol. 38, no. 4, pp. 421–432, 1990.

[74] ——, "Analysis of Infinite Arrays of Probe-Fed Rectangular Microstrip Patches Using a Rigorous Feed Model," *IEE Proc., Pt. H*, vol. 136, no. 2, pp. 110–119, 1989.

[75] C. L. Mak, Y. L. Chow, and K. M. Luk, "Finite Ground Plane Effects of a Microstrip Patch Antenna: a CAD Formula of Impedance Perturbation by Synthetic Asymptote and GTD," *IEE Proc. Microw. Antennas Propag.*, vol. 150, no. 1, pp. 11–17, 2003.

[76] J. Wettergren, P.-S. Kildahl, and K. Forooraghi, "Admittance of a Longitudinal Slot in a Finite Ground Plane," *IEEE Antennas Propag. Soc. Int. Symp. Dig.*, pp. 1608–1611, 1993.

[77] K. H. Awadalla and T. S. M. Maclean, "Input Impedance of a Monopole Antenna at the Center of a Finite Ground Plane," *IEEE Trans. Antennas Propag.*, vol. 26, no. 2, pp. 244–248, 1978.

[78] S. H. Zainud-Deen, K. H. Awadalla, and H. A. Sharshar, "Analysis of Normal Mode Helical Antenna on Finite Ground Plane," *IEEE Antennas Propag. Soc. Int. Symp. Dig.*, pp. 1879–1882, 1978.

[79] J. M. Johnson and Y. Rahmat-Samii, "Genetic Algorithms in Engineering Electromagnetics," *IEEE Antennas Propag. Mag.*, vol. 39, no. 4, pp. 7–21, 1997.

[80] M. Wall, *GAlib: A C++ Library of Genetic Algorithm Components, version 2.4*, Massachusetts Institute of Technology, August 1996.

[81] D. M. Pozar, "Input Impedance and Mutual Coupling of Rectangular Microstrip Antennas," *IEEE Trans. Antennas Propag.*, vol. 30, no. 6, pp. 1191–1196, 1982.

[82] R. Chair, A. A. Kishk, and K.-F. Lee, "Comparative Study on the Mutual Coupling Between Different Sized Cylindrical Dielectric Resonators Antennas and Circular Microstrip Patch Antennas," *IEEE Trans. Antennas Propag.*, vol. 53, no. 3, pp. 1011–1019, 2005.

[83] H. E. King, "Mutual Impedance of Unequal Length Antennas in Echelon," *IEEE Trans. Antennas Propag.*, vol. 5, no. 3, pp. 306–313, 1957.

[84] K. Y. Chow and K. W. Leung, "Mutual Coupling of Hemispherical Cavity-Backed Slot Antennas," *Microwave Opt. Technol. Lett.*, vol. 20, no. 5, pp. 304–306, 1999.

[85] G. H. Knittel, "Wide-Angle Impedance Matching of Phased-Array Antennas - a Survey of Theory and Practice," in *Phased Array Antennas*, A. A. Oliner and G. H. Knittel, Eds.   Artech House, Inc., Dedham, 1972, ch. 6, pp. 157–172.

[86] P. J. Papakanellos and C. N. Capsalis, "Estimation of the Coupling Between Closely Spaced Transmitters Using the Method of Auxiliary Sources," *J. Electromagn. Waves Appl.*, vol. 17, no. 5, pp. 785–805, 2003.

[87] D. Sievenpiper, *et al.*, "High-Impedance Electromagnetic Surfaces with a Forbidden Frequency Band," *IEEE Trans. Microwave Theory Tech.*, vol. 47, no. 11, pp. 2059–2074, 1999.

[88] R. E. Collin, *Field Theory of Guided Waves*, 2nd ed.   IEEE Press, Wiley Interscience, 1991.

[89] K. Sarabandi, M. D. Casciato, and I.-S. Koh, "Efficient Calculation of the Fields of a Dipole Radiating Above an Impedance Surface," *IEEE Trans. Antennas Propag.*, vol. 50, no. 9, pp. 1222–1235, 2002.

[90] R. F. Harrington, *Time-Harmonic Electromagnetic Fields*.   John Wiley & Sons Inc., New York, 2001.

[91] T. B. A. Senior and J. L. Volakis, *Approximate Boundary Conditions in Electromagnetics*.   The Institution of Electrical Engineers, London, 1995.

[92] D. M. Pozar, "Finite Phased Arrays of Rectangular Microstrip Patches," *IEEE Trans. Antennas Propag.*, vol. 34, no. 5, pp. 658–665, 1986.

[93] P.-S. Kildal, "Artificially Soft and Hard Surfaces in Electromagnetics," *IEEE Trans. Antennas Propag.*, vol. 38, no. 10, pp. 1537–1544, 1990.

[94] P.-S. Kildal, A. A. Kishk, and S. Maci, "Special Issue on Artificial Magnetic Conductors, Hard/Soft Surfaces, and Other Complex Surfaces," *IEEE Trans. Antennas Propag.*, vol. 53, no. 1, pp. 2–7, 1999.

[95] E. C. Dufort, "Design of Corrugated Plates for Phased Array Matching," *IEEE Trans. Antennas Propag.*, vol. 16, no. 1, pp. 37–46, 1968.

[96] P. W. Hannan and S. P. Litt, "Capacitive Gound Plane for Phased Array Antenna," *IEEE Antennas Propag. Soc. Int. Symp. Dig.*, pp. 115–123, 1968.

[97] R. B. Waterhouse and D. Novak, "Comparison of Performance of Artificial Magnetic Conductors at L-Band," *IEEE Antennas Propag. Soc. Int. Symp. Dig.*, vol. 1B, pp. 648–651, 2005.

[98] H. Xin, *et al.*, "Mutual Coupling Reduction of Low-Profile Monopole Antenna on High-Impedance Ground Plane," *IEE Electron. Lett.*, vol. 38, no. 16, pp. 849–850, 2002.

[99] Y. Fu and N. Yuan, "Elimination of Scan Blindness in Phased Array of Microstrip Patces Using Electromagnetic Bandgap Materials," *IEEE Antennas Wireless Propag. Lett.*, vol. 3, no. 1, pp. 63–65, 2004.

[100] D. Sievenpiper, J. Schaffner, and J. Navarro, "Axial Ratio Improvement in Aperture Antennas Using High-Impedance Ground Plane," *IEE Electron. Lett.*, vol. 38, no. 23, pp. 1411–1412, 2002.

[101] G. Zhang and N. Yuan, "Radiation Characteristics Improvement in Waveguide-Fed Slot Antennas with a High-Impedance Ground Plane (HIGP)," *Microwave Opt. Technol. Lett.*, vol. 45, no. 2, pp. 176–179, 2005.

[102] A. Clavin, "A Multimode Antenna Having Equal E- and H-Planes," *IEEE Trans. Antennas Propag.*, vol. 23, no. 9, pp. 735–737, 1975.

[103] R. S. Elliot, "On the Mutual Admittance Between Clavin Elements," *IEEE Trans. Antennas Propag.*, vol. 28, no. 6, pp. 864–870, 1980.

[104] K. Nishizawa, *et al.*, "Broadening Beamwidth of E-plane Radiation Pattern of a Dipole Antenna With Loaded Monopole Elements," *IEEE Antennas Propag. Soc. Int. Symp. Dig.*, vol. 4, pp. 3984–3987, 2004.

[105] C.-N. Hu, *et al.*, "Design of the Cross-Dipole Antenna with Near-Hemispherical Coverage in Finite-Element Phased Array by Using Genetic Algorithms," *IEEE Antennas Propag. Soc. Int. Symp. Dig.*, vol. 1, pp. 303–306, 2000.

[106] M. Scott, "A Printed Dipole for Wide-Scanning Array Applications," *Int. Conf. Antennas Propag.*, no. 480, pp. 37–40, 2001.

[107] J. S. Fu, *et al.*, "Compound Dipole With H-Plane Parasitic Posts For Phased Array Wide-Angle Wide-Band Scanning," *IEEE Antennas Propag. Soc. Int. Symp. Dig.*, vol. 1, pp. 22–26, 1999.

[108] J. A. MacDonald, D. M. McPherson, and M. J. Devine, "Axial Ratio Optimization of an Array of Crossed-Dipoles Using Phasing Posts," *IEEE Antennas Propag. Soc. Int. Symp. Dig.*, vol. 2, pp. 1252–1255, 1994.

[109] K. M. Lee and R.-S. Chu, "Analysis of Mutual Coupling Between an Infinite Phased Array of Horizontal Dipoles and Vertical Wires," *IEEE Trans. Antennas Propag.*, vol. 39, no. 5, pp. 591–599, 1991.

[110] P. Steyn, *et al.*, "Phased Array Antenna," Patent US 7.081.861 B2, 2006.

[111] R. B. Waterhouse, "The Use of Parasitic Elements to Remove Potential E-Plane Scan Blindness in High Dielectric Substrate Microstrip Patch Probe-Fed Phased Arrays," *IEEE Antennas Propag. Soc. Int. Symp. Dig.*, vol. 1, pp. 456–459, 1994.

[112] E. G. Magill and H. A. Wheeler, "Wide-Angle Impedance Matching of a Planar Array Antenna by a Dielectric Sheet," *IEEE Trans. Antennas Propag.*, vol. 14, no. 1, pp. 49–53, 1966.

[113] Q. Huang and X. Shi, "Depressing Mutual Coupling Between Patch Antennas Using Multi-Layer Dielectric Boards," *IEEE Antennas Propag. Soc. Int. Symp. Dig.*, vol. 1, pp. 622–625, 2003.

[114] P. W. Hannan, D. S. Lerner, and G. H. Knittel, "Impedance Matching a Phased Array Over Wide Scan Angles by Connecting Circuits," *IEEE Trans. Antennas Propag.*, vol. 13, no. 1, pp. 28–34, 1965.

[115] H. Morishita, K. Hirasawa, and K. Fujimoto, "Analysis of a Cavity-Backed Annular Slot Antenna with One Point Shorted," *IEEE Trans. Antennas Propag.*, vol. 39, no. 10, pp. 1472–1478, 1991.

[116] S. Shi, K. Hirasawa, and Z. N. Chen, "Circularly Polarized Cavity Backed Two-Element Rectangular Loop Slot Antenna," *IEICE Trans. Electron.*, vol. E82-C, no. 7, pp. 1217–1222, 2001.

[117] ——, "Circularly Polarized Rectangularly Bent Slot Antennas Backed by a Rectangular Cavity," *IEEE Trans. Antennas Propag.*, vol. 49, no. 11, pp. 1517–1524, 2001.

[118] Q. Li, Z. Shen, and X. Shan, "A New Microstrip-Fed Cavity-Backed Annular Slot Antenna," *IEEE Antennas Propag. Soc. Int. Symp. Dig.*, vol. 1, pp. 68–71, 2002.

[119] T. Kotani, *et al.*, "A Rectangular Cavity Backed Slot Antenna with Parasitic Slots," *IEEE Antennas Propag. Soc. Int. Symp. Dig.*, pp. 166–169, 2001.

[120] D. Sievenpiper, H.-P. Hsu, and R. M. Riley, "Low-Profile Cavity-Backed Crossed-Slot Antenna With a Single-Probe Feed Designed for 2.34-GHz Satellite Radio Applications," *IEEE Trans. Antennas Propag.*, vol. 52, no. 3, pp. 873–879, 2004.

[121] N. C. Karmakar, "Investigations Into a Cavity-Backed Circular-Patch Antenna," *IEEE Trans. Antennas Propag.*, vol. 50, no. 12, pp. 1706–1715, 2002.

[122] N. V. Larsen, "An L-Band Antenna for Circularly Polarized, Phased Arrays with Hemispherical Coverage," Master's thesis, Ørsted·DTU, Technical University of Denmark, Lyngby, Denmark, March 2004.

[123] F. Manshadi, "End-Loaded Crossed-Slot Radiating Elements," *IEEE Trans. Antennas Propag.*, vol. 39, no. 8, pp. 1237–1240, 1991.

[124] E. Jørgensen, B. K. Nielsen, and O. Breinbjerg, "A Cavity-Backed Crossed-Slot Antenna Element for an S-Band Circular Polarization Spherical Coverage Satellite Antenna System," *Proc. Int. Symp. Antennas Propag.*, vol. 1, pp. 361–364, 2000.

[125] U. K. Revankar and Harishchandra, "Printed Dipole Radiating Elements for Broadband and Wide Scan Angle Active Phased Array," *IEEE Antennas Propag. Soc. Int. Symp. Dig.*, vol. 4, pp. 796–799, 2001.

[126] C. J. Miller, "Dipole Phased Array with Capacitance Plate Elements to Compensate for Impedance Variations over the Scan Angle," *U.S. Patent*, no. 4.131.896, 1978.

[127] J.-P. Bayard, M. E. Cooley, and D. H. Schaubert, "Analysis of Infinite Array of Printed Dipoles on Dielectric Sheets Perpendicular to a Ground Plane," *IEEE Trans. Antennas Propag.*, vol. 39, no. 12, pp. 1722–1732, 1991.

[128] Z. Yumei, "A Printed Dipole for Wide-Scanning Array Applications," *Proc. 2001 CIE Int. Conf. Radar*, pp. 214–218, 2001.

[129] M. S. Gatti and D. J. Nybakken, "A Circularly Polarized Crossed Drooping Dipole Antenna," *IEEE Antennas Propag. Soc. Int. Symp. Dig.*, vol. 1, pp. 254–257, 1990.

[130] D.-C. Chang and J.-H. Chen, "2.3 GHz Antenna with both LHCP and LP for SDARS," *IEEE Antennas Propag. Soc. Int. Symp. Dig.*, vol. 3, pp. 874–877, 2003.

[131] E. B. Rodal, *et al.*, "Antenna with Curved Dipole Elements," *U.S. Patent*, no. 5.173.715, 1992.

[132] I. E. Timofeev and K. Q. Chau, "Crossed Dipole Antenna Element," *U.S. Patent*, no. 7.053.852 B2, 2006.

[133] B. J. Edward and D. F. Rees, "Microstrip Fed Printed Dipole with Integral Balun," *U.S. Patent*, no. 4.825.220, 1989.

[134] D. Allcock, "Crossed-Drooping Dipole Antenna," *U.S. Patent*, no. 4.686.536, 1987.

[135] Rogers Corporation, *Datasheet for RT/duroid® 5870*, 2006.

[136] Technical University of Denmark. (2007, January) DTU-ESA Spherical Near-Field Antenna Test Facility. [Online]. Available: http://www.oersted.dtu.dk/forskning/emi/afg/dtu_esa_facilitet.aspx

[137] R. Mongia, I. Bahl, and P. Bhartia, *RF and Microwave Coupled-Line Circuits*. Norwood: Artech House, 1999.

[138] A. Petosa, *et al.*, "Recent Advances in Dielectric-Resonator Antenna," *IEEE Antennas Propag. Mag.*, vol. 40, no. 3, pp. 35–48, 1998.

[139] S. A. Long, M. W. McAllister, and L. C. Shen, "The Resonant Cylindrical Dielectric Cavity Antenna," *IEEE Trans. Antennas Propag.*, vol. 31, no. 3, pp. 406–412, 1983.

[140] K. M. Luk and K. W. Leung, *Dielectric Resonator Antennas*. Research Studies Press Ltd., Baldock, England, 2003.

[141] A. A. Kishk, "Dielectric Resonator Antenna Elements for Array Applications," *IEEE Int. Symp. Phased Array Systems and Technology*, pp. 300–305, 2003.

[142] A. Petosa, *et al.*, "Low Profile Phased Array of Dielectric Resonator Antennas," *IEEE Int. Symp. Phased*

Array Systems and Technology, pp. 182–185, 1996.

[143] A. Petosa, A. Ittipiboon, and M. Cuhaci, "Array of Circularly Polarised Cross Dielectric Resonator Antennas," *IEE Electron. Lett.*, vol. 32, no. 19, pp. 1742–1743, 1996.

[144] S.-J. Yang, *et al.*, "Study on Sequential Feeding Networks for Subarrays of Circularly Polarized Elliptical Dielectric Resonator Antenna," *IEEE Trans. Antennas Propag.*, vol. 55, no. 2, pp. 321–333, 2007.

[145] Emerson & Cuming Microwave Products, *Datasheet for Eccostock HiK 500F*, 2006.

[146] C. Tucker, "Radiation Pattern Aberrations when Using a Vehicle as a Ground Plane," *Colloquium on Antenna Systems for Mobile Communications*, pp. 3.1–3.6, 1983.

[147] M. Daginnus, *et al.*, "SDARS - Antennas: Environmental Influences, Measurement, Vehicle Application Investigations and Field Experiences," *SAE Technical Paper Series*, no. 2002-01-120, 2002.

[148] R. Kronberger, A. Stephan, and M. Daginnus, "3D Antenna Measurement and Electromagnetic Simulation for Advanced Vehicle Antenna Development," *IEEE Antennas Propag. Soc. Int. Symp. Dig.*, pp. 342–345, 2001.

[149] K. Taguchi, *et al.*, "FDTD Large-Scale Parallel Supercomputing and its Application to the Analysis of Radiation Characteristics of an Antenna Mounted on a Vehicle," *Int. J. of RF and Microwave Computer-Aided Engineering*, vol. 14, no. 3, pp. 253–261, 2004.

[150] J. T. S. Sumantyo, *et al.*, "Numerical Analysis of Ground Plane Size Effects on Patch Array Antenna Characteristics for Mobile Satellite Communications," *Int. J. Numer. Model.*, vol. 18, pp. 95–106, 2005.

[151] V. Volski and G. A. E. Vandenbosch, "Efficient Physical Optics Approximation for the Calculation of Radiation Patterns of Planar Antennas Located on a Finite Ground Plane," *IEEE Trans. Antennas Propag.*, vol. 53, no. 1, pp. 460–465, 2005.

[152] J. Huang, "The Finite Ground Plane Effect on the Microstrip Antenna Radiation Pattern," *IEEE Trans. Antennas Propag.*, vol. 31, no. 4, pp. 649–653, 1983.

[153] S. Rengarajan, "Finite Ground Plane Effects on Planar Arrays of Microstrip Patch Elements," *IEEE Antennas Propag. Soc. Int. Symp. Dig.*, pp. 741–744, 1984.

[154] C. J. Reddy, *et al.*, "Radiation Characteristics of Cavity Backed Aperture Antennas in Finite Ground Plane Using the Hybrid FEM/MoM Technique and Geometrical Theory of Diffraction," *IEEE Trans. Antennas Propag.*, vol. 44, no. 10, pp. 1327–1333, 1996.

[155] R. E. Hodges and Y. Rahmat-Samii, "POHM Modelling of Complex Radiators on Curved Ground Plane," *IEEE Conf. on Electromagn. Field Computation*, pp. WOD3–WOD3, 1992.

[156] E. Jørgensen, "Communication Antennas for Small Satellites," Master's thesis, Department of Electromagnetic Systems, Technical University of Denmark, Lyngby, Denmark, March 2000.

[157] S. N. Pivnenko, *et al.*, "Pattern Diversity Antenna System for Small Satellites," *Proceedings of 25th ESA Antenna Workshop on Satellite Antenna Technology, ESTEC*, pp. 485–488, 2002.

[158] M. Haneishi, S. Yoshida, and N. Goto, "A Broadband Microstrip Array Composed of Single-Feed Type Circularly Polarized Microstrip Antennas," *IEEE Antennas Propag. Soc. Int. Symp. Dig.*, vol. 1, pp. 160–163, 1982.

[159] J. Huang, "C.P. Microstrip Array with Wide Axial Ratio Bandwidth and Single Feed L.P. Elements," *IEEE Antennas Propag. Soc. Int. Symp. Dig.*, vol. 2, pp. 705–708, 1985.

[160] T. Teshirogi, M. Tanaka, and W. Chujo, "Wideband Circularly Polarized Array Antenna with Sequential Rotations and Phase Shift of Elements," *Proc. Int. Symp. Antennas Propag.*, vol. 1, pp. 117–120, 1985.

[161] P. S. Hall, J. S. Dahele, and J. R. James, "Design Principles of Sequentially Fed, Wide Bandwidth, Circularly Polarised Microstrip Antennas," *IEE Proc., Pt. H*, vol. 136, no. 5, pp. 381–389, 1989.

[162] P. S. Hall, "Application of Sequential Feeding to Wide Bandwidth, Circularly Polarised Microstrip Patch Arrays," *IEE Proc., Pt. H*, vol. 136, no. 5, pp. 390–398, 1989.

[163] K. D. Palmer, J. H. Cloete, and J. J. van Tonder, "Bandwidth Improvement of Circular Polarised Arrays Using Sequential Rotation," *IEEE Antennas Propag. Soc. Int. Symp. Dig.*, pp. 135–138, 1992.

[164] M. N. Jazi and M. N. Azarmanesh, "Design and Implementation of Circularly Polarised Microstrip Antenna Array Using a New Serial Feed Sequentially Rotated Technique," *IEE Proc. Microw. Antennas*

Propag., vol. 153, no. 2, pp. 133–140, 2006.

[165] M. Haneishi and B. Wu, "Array Antenna Composed of Circularly Polarized Dielectric Resonator Antennas," *IEEE Antennas Propag. Soc. Int. Symp. Dig.*, vol. 1, pp. 252–255, 1999.

[166] A. A. Kishk, "Application of Rotated Sequential Feeding for Circular Polarization Bandwidth Enhancement of Planar Arrays with Single-Fed DRA Elements," *IEEE Antennas Propag. Soc. Int. Symp. Dig.*, vol. 1, pp. 664–667, 2003.

[167] T. Teshirogi, M. Tanaka, and N. Takahashi, "Phased Arrays Using Sequential Rotation and Phasing Techniques," *Proc. Int. Symp. Antennas Propag.*, vol. 1, pp. 149–152, 1996.

[168] Q. García-García, "Scanning Properties of Sequentially Rotated Linear Arrays of Circularly Polarized Patch Radiators," *Microwave Opt. Technol. Lett.*, vol. 30, no. 5, pp. 343–350, 2001.

[169] J. Huang, "A Technique for an Array to Generate Circular Polarization with Linearly Polarized Elements," *IEEE Trans. Antennas Propag.*, vol. 34, no. 9, pp. 1113–1124, 1986.

[170] L. Baggen, *et al.*, "Phased Array Using the Sequential Rotation Principle: Analysis of Coupling Effects," *IEEE Int. Symp. Phased Array Systems and Technology*, pp. 571–576, 2003.

[171] M. Tanaka, "Sequentially Rotated Array Consisting of Higher Order Mode Antenna Elements," *IEEE Antennas Propag. Soc. Int. Symp. Dig.*, vol. 3, pp. 1928–1931, 1996.

An L-band, Circularly Polarised, Dual-Feed, Cavity-Backed Annular Slot Antenna for Phased Array Applications

Niels Vesterdal Larsen and Olav Breinbjerg

AN L-BAND, CIRCULARLY POLARISED, DUAL-FEED, CAVITY-BACKED ANNULAR SLOT ANTENNA FOR PHASED ARRAY APPLICATIONS
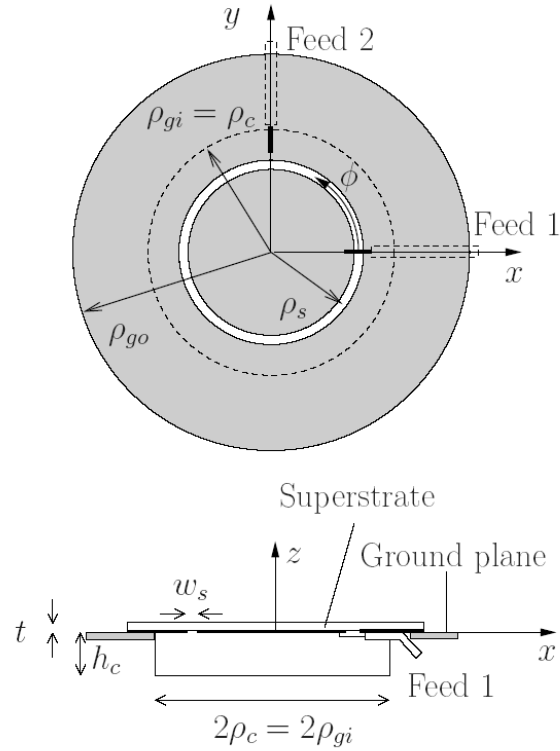
Niels Vesterdal Larsen and Olav Breinbjerg

Abstract: The results of a parametric study for the development of an L-band, circularly polarised, dual-feed, cavity-backed annular slot antenna is presented. The study included detailed numerical simulations and measurements on a prototype with different ground planes, to assess the antenna's applicability as an element in a small phased array antenna.

1 Introduction

This work documents the investigation of an antenna element for application in a small phased array antenna. The antenna array is intended for mobile terminals in a satellite communication system and must be suitable for mounting on vehicles such as cars and airplanes. In order to ensure minimal protrusion from the vehicle structure, the array and hence the elements must be low-profile. The antenna is intended for operation in the L-band around a centre frequency of 1.6GHz with circular polarisation. The requirement of wide-angle scanning calls for antenna elements with good hemispherical coverage.

Microstrip patch antennas have previously been used as elements in phased array applications [1–3]; however, due to the poor radiation near the horizon these are not well suited for wide-angle scanning applications. Other antennas such as drooping dipoles [4], helix antennas [5, 6] and dielectric resonator antennas [7] may yield better coverage but their height often conflicts with the low-profile requirement. Cavity-backed slot antennas are inherently low-profile and exhibit good hemispherical coverage. In particular, crossed-slot elements have been widely used, both for phased arrays [8] as well as a single element [9]. In the present work the cavity-backed annular slot antenna (CBAS) has been selected. It is possible to obtain circular polarisation with only a single feed by employing various perturbations to the slot [10] or by shorting the slot [11]. Such solutions, however, are usually associated with low axial ratio bandwidths. By utilising two feeds in phase quadrature, as is done in [12, 13] for other types of antennas, this problem is avoided - albeit at the expense of increased complexity of the feed network.

In this work, a dual feed CBAS antenna is investigated. Starting with extensive numerical computer simulations using the commercially available solver HFSS 9.2 from Ansoft [14], an element prototype has afterwards been constructed and measured at the DTU-ESA Spherical Near-Field Antenna Test Facility. Different ground planes were used to determine the influence of these on the wide-angle performance of the antenna.

Figure 1: Geometry of the CBAS antenna and the chosen design parameters. For simplicity the dielectric superstrate is not shown on the top view.

$$\rho_c = 40.0 \, \text{mm}, \quad h_c = 20.0 \, \text{mm}, \quad t = 0.79 \, \text{mm}$$
$$\rho_s = 32.0 \, \text{mm}, \quad w_s = 2.0 \, \text{mm}, \quad \epsilon_r = 3.38$$
$$R_{in} = 450 \, \Omega, \quad f_{res} = 1.59 \, \text{GHz}, \quad BW = 6 \, \%$$

2 Antenna Element

The CBAS antenna with a small circular ground plane is depicted in Figure 1. An annular slot with mean radius ρ_s and width w_s is etched in the lower copper layer of a copper-clad substrate with relative permittivity ϵ_r and thickness t. The top copper layer is removed leaving a dielectric superstrate on top of the slot. The annular slot is mounted concentrically on the ground plane which has the shape of a broad annular ring, the inner and outer radii of which are ρ_{gi} and ρ_{go}. This structure is backed by a circular metallic cavity with interior radius $\rho_c = \rho_{gi}$ and depth h_c which includes the ground plane (with thickness 2mm) as shown in Figure 1. The annular slot is excited by two coaxial cables, denoted feed 1 and feed 2, which are led through holes cut in the ground plane and cavity wall, respectively, and whose inner conductors are soldered to the copper-clad side of the superstrate inside the annular slot. Feed 2 is phased with a 90° lag with respect to feed 1 resulting in right-hand circular polarisation in the boresight direction, i.e., along the positive z-axis of Figure 1. Throughout this text the harmonic time

dependence $e^{j\omega t}$, with t and ω being the time and angular frequency, respectively, is assumed and suppressed.

3   Impedance Characteristics

The values of the aforementioned design parameters were chosen on basis of extensive numerical simulations using HFSS. The impedance properties are naturally greatly affected by variations in the design parameters and the computer simulations have led to the following observations on the qualitative behaviour of the resonance frequency and impedance bandwidth:

- The resonance frequency decreases for increasing values of the cavity radius ρ_c and height h_c as well as slot radius ρ_s, relative permittivity ϵ_r and thickness t of the superstrate. It increases for increasing values of the slot width.

- The impedance bandwidth increases for increasing values of ρ_c, h_c, and w_s but has been found to be independent on ρ_s. It decreases for increasing values of ϵ_r and t.

The ground plane size and shape were found to have only minor impact on the impedance properties. The selected values of the design parameters of the constructed prototype are summarised in Figure 1. In addition it is noted that the substrate used is of the type RO-4003 from Rogers. The input reflection coefficients, $\Gamma_{in,1}$ and $\Gamma_{in,2}$, at the two feeds are determined from the antenna scattering matrix and can be expressed as

$$\Gamma_{in,i} = \frac{Z_{in,i} - Z_0}{Z_{in,i} + Z_0}, \qquad i = 1, 2, \tag{1}$$

where Z_0 is the characteristic impedance of the feed line. The input impedances $Z_{in,i} = R_{in,i} + j X_{in,i}$, with $R_{in,i}, X_{in,i}$ being the input resistance and reactance, respectively, are given by

$$Z_{in,i} = \sum_{j=1}^{2} Z_{ij} \frac{I_j}{I_i}, \qquad i = 1, 2, \tag{2}$$

where the Z_{ij} are the self- or mutual impedances of the antenna. I_i is the terminal current at the i'th antenna feed point. This terminal current can be found from the matrix equation

$$\mathbf{I} = (\mathbf{V}^+ - \mathbf{V}^-)/Z_0, \tag{3}$$

where $\mathbf{V}^+$ and $\mathbf{V}^-$ are the incident and reflected voltage waves at the feed points, respectively, the latter of which follows from

$$\mathbf{V}^- = \overline{\overline{\mathbf{S}}}^A \mathbf{V}^+. \tag{4}$$

The self and mutual impedances are calculated directly from the measured antenna scattering matrix and are given by

$$\overline{\overline{\mathbf{Z}}} = Z_0 (\overline{\overline{\mathbf{U}}} - \overline{\overline{\mathbf{S}}}^A)^{-1} (\overline{\overline{\mathbf{U}}} + \overline{\overline{\mathbf{S}}}^A), \tag{5}$$

where $\overline{\overline{\mathbf{U}}}$ is the identity matrix. Lastly it is noted that the total terminal voltages are

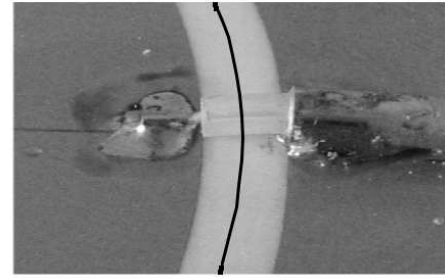$$\mathbf{V} = \mathbf{V}^+ + \mathbf{V}^-. \tag{6}$$

Figure 2: Feed point of the antenna. Top: physical feed, bottom: simulation model. The chosen reference plane is shown.

Thus the input impedances and reflection coefficients of the two ports can be found from the known antenna scattering matrix and incident voltage waves by straightforward application of equations (1)-(5), and the input impedances can be expressed as

$$Z_{in,i} =$$
$$Z_0 \frac{(1 + S_{ii}^A)(1 - S_{jj}^A) + S_{ij}^A S_{ji}^A + 2 S_{ij}^A \frac{V_j^+(1 - S_{jj}^A) - V_i^+ S_{ji}^A}{V_i^+(1 - S_{ii}^A) - V_j^+ S_{ij}^A}}{(1 - S_{ii}^A)(1 - S_{jj}^A) - S_{ij}^A S_{ji}^A}, \tag{7}$$

where $j = 3 - i, i = 1, 2$. This expression can be somewhat reduced by using the fact that $S_{12} = S_{21}$, however, it is noted that $S_{11} \neq S_{22}$, since the two ports do not face the same environment. The expressions in (7) can be further simplified by assuming perfect phase quadrature between the incident voltages waves, i.e.,

$$V_2^+ = -j V_1^+. \tag{8}$$

and this assumption will be employed in the following.

With the present type of feed the choice of the reference plane is not obvious. Indeed, some difference in the feed

point geometry exists between the simulation model and the physical antenna since an accurate modelling of the feed points is difficult. A close-up view of the feed point for both the simulation model and the physical antenna is shown in Figure 2. Here the reference plane is defined on the coaxial feed line where this intersects the annular slot as shown in the figure. In the simulation model the feed points are excited by applying the incident voltage waves $\mathbf{V}^+$ at wave ports defined at the end of the feed lines some distances d_1, d_2 from the respective reference planes. So for both the simulation model and the physical antenna the initially obtained scattering matrix $\overline{\overline{\mathbf{S}}}_0^A$ must be transformed through the operation

$$\overline{\overline{\mathbf{S}}}^A = \begin{bmatrix} e^{-j\beta_1 d_1} & 0 \\ 0 & e^{-j\beta_2 d_2} \end{bmatrix} \overline{\overline{\mathbf{S}}}_0^A \begin{bmatrix} e^{-j\beta_1 d_1} & 0 \\ 0 & e^{-j\beta_2 d_2} \end{bmatrix}, \quad (9)$$

where β_1, β_2 are the propagation constants of the two feed lines, in order that the S-parameters refer to the selected reference plane.
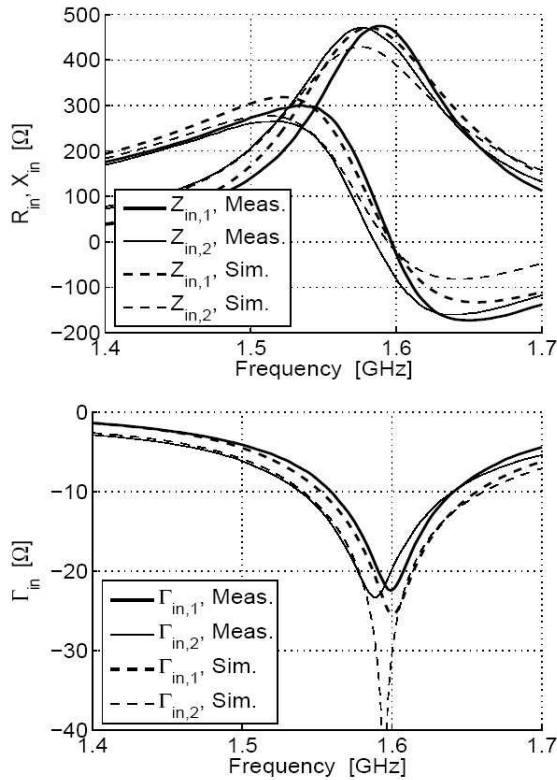

Figure 3: Input impedances $Z_{in} = R_{in} + jX_{in}$ and reflection coefficients Γ_{in} of the two input ports, assuming characteristic feed line impedances of 400Ω.

In Figure 3 the input impedances and reflection coefficients of the two ports are plotted under the ideal assumptions of (8) and a feed line characteristic impedance of $Z_0 = 400\Omega$. The input impedances are seen to be approximately 450Ω at the resonance frequency (defined at $X_{in} = 0$) for the simulation result, whereas they are slightly larger for the measurements. The resonance frequency is approximately

1.59GHz with a bandwidth of roughly 6% with respect to an input reflection coefficient $\Gamma_{in} < -10$dB. The results from the simulation and measurement are generally in good agreement although slight deviations are seen for port 2. This deviation of about 1% of the resonance frequency may be due to manufacturing inaccuracies in the feed point implementation as shown in Figure 2 or imperfections in the feed line due to bending of the coaxial cables. Additionally it is noted that for the measurement data even small uncertainties with respect to the dielectric constant and lengths of the feed lines may be a cause for inaccuracy when transforming the reference planes.

4 Radiation Characteristics for Different Ground Planes

The antenna element has been measured using 3 different ground planes attached behind the fixed ground plane shown in Figure 1. These changeable ground planes comprise a square ground plane with side lengths of 250mm, denoted GP 1, and two circular ground planes with diameters of 360mm and 1500mm, denoted GP 2 and GP 3, respectively. To facilitate measurements of the radiation patterns the CBAS element was fed using a quadrature hybrid.
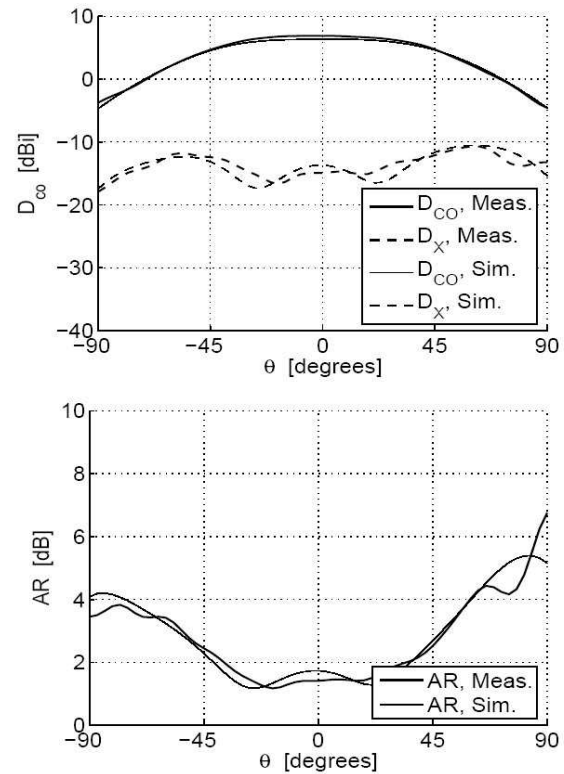

Figure 4: Directivity (left) and axial ratio (right) of the CBAS antenna as function of θ for GP 1, $\phi = 0°$. The frequency is 1.58GHz.

For the simulations of the radiation the CBAS element is fed by introducing two terminal voltages V_1, V_2, across the slot at its intersections with the coaxial feed lines. The aforementioned assumption of ideal phase quadrature be-
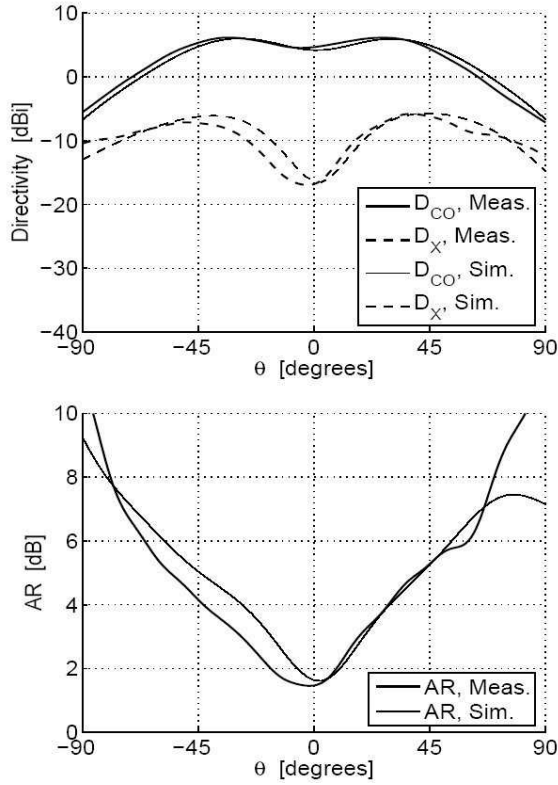
Figure 5: Directivity (top) and axial ratio (bottom) of the CBAS antenna as function of θ for GP 2, $\phi = 0^{\circ}$. The frequency is 1.58GHz.
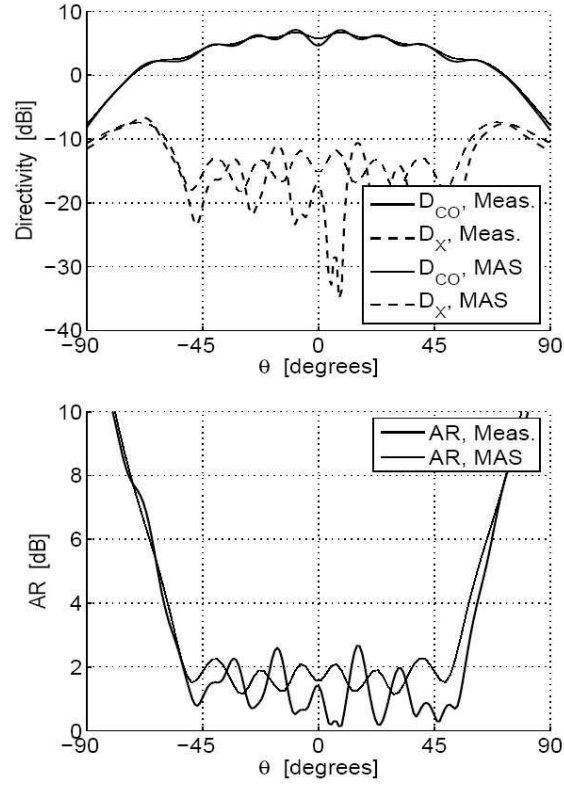

Figure 6: Directivity (top) and axial ratio (bottom) of the CBAS antenna as function of θ for GP 3, $\phi = 0^{\circ}$. The frequency is 1.58GHz.

tween the incident waves, given by (8), is still used and thus an ideal quadrature hybrid is assumed. By application of (4) and (6) the appropriate values of the terminal voltages are calculated. Thus the mutual coupling between the antenna feed points as well as the reflections at the terminals are taken into account and generally there is not ideal phase quadrature between the terminal voltages, i.e., $V_2 \neq -jV_1$.

For the ground plane cases GP 1-2 the simulations were carried out with HFSS but due to the large problem size in the case of ground plane GP 3 this was not possible with the available computer resources. To circumvent this problem a Method of Auxiliary Sources (MAS) [15, 16] code was developed. Presently, it suffices to mention that the problem is modelled as a scattering problem where the circular ground plane is illuminated by an infinitely thin magnetic ring current coinciding with the annular slot except for a small vertical displacement from the ground plane. The magnetic ring current is expressed as

$$\mathbf{M}(\phi) = -\hat{\boldsymbol{\phi}}\delta(z-h)\delta(\rho-\rho_s)(V_1\cos\phi + V_2\sin\phi), \quad (10)$$

where $h = 5$mm is selected and δ is the Dirac delta function. The azimuthal coordinate ϕ is defined with respect to the right-hand coordinate system of which the x- and y-axes are imposed on the antenna in Figure 1, i.e., $\phi = 0^{\circ}$ is along the x-axis.

In Figure 4-6 radiation patterns and the axial ratio in the θ-cut, $\phi = 0^{\circ}$, are shown for the 3 ground planes. Generally, the agreement between the measurement and simulation re-

sults is good for both the co- and cross-polar components as well as the axial ratio. This holds both for the GP 1-2 cases simulated with HFSS and for the GP 3 case simulated using MAS.

As expected the amount of ripples present in the radiation pattern increases with the ground plane size. Thus the half power beam width varies for the 3 ground planes but generally attains values around 100°. Similar variations occur for the axial ratio but for the large GP 3 ground plane case it is generally below 4 dB within $\pm 60^{\circ}$ from boresight.

The maximum co-polar directivity as well as the boresight axial ratio are plotted as function of frequency in Figure 7. The maximum directivity varies around 7dBi, most significantly for GP 3. The axial ratio is below 3dB in almost the entire frequency range, however, it is not lower than 1dB anywhere. This level implies that coupling between the feeds deteriorates the phase quadrature of the feed currents. It is further seen that the boresight axial ratio is slightly different for the for the 3 ground planes.

5   Conclusion

An L-band circularly polarised dual-feed cavity-backed annular slot antenna has been developed. The antenna was equipped with different ground planes and simulated using the commercially available programme HFSS. In order to simulate the influence of large ground planes a Method of Auxiliary Sources code was developed. The
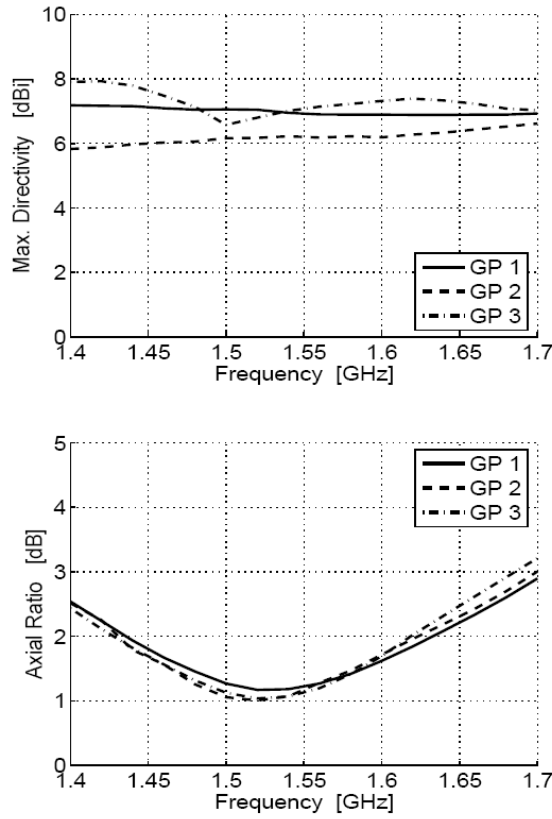
Figure 7: Maximum co-polar directivity (top) and axial ratio at boresight (bottom) measured for the three ground planes.

calculated results are in good agreement with the measurements. The antenna element has an impedance bandwidth of 6% around a resonance frequency of 1.59GHz. The input impedance is approximately 450Ω. Measurements of the antenna equipped with 3 different ground planes have been conducted at the DTU-ESA Spherical Near-Field Antenna Test Facility and have shown the occurrence of ripples in the radiation pattern. The maximum co-polar directivity is about 7dBi and the half power beam width around 100°. Both, however, vary slightly for different ground planes as well with frequency. The boresight axial ratio is below 3dB in almost the entire considered frequency band and has a minimum of 1.0dB at 1.52GHz. In order to improve the axial ratio, application of four feeds with sequential phase shifts of 90° may be considered, although this entails an increase in complexity. The wide-angle performance with respect to directivity and axial ratio suggests that the element may be well suited for application in a phased array. It is, however, noted that the coupling between two or more antennas of this type has not been addressed in this work. This is indeed of importance when assessing the amount of scan loss that will undoubtedly occur when used in a phased array.

Bibliography

[1] R. N. Simons, R. Q. Lee, and G. R. Lindamood, "A Seven Patch Hexagonal CP Subarray with CPW/Stripline Feed Network," *IEEE Antennas Propag. Soc. Int. Symp. Dig.*, vol. 2, pp. 592–595, 1991.

[2] L. C. Kretly, A. Cerqueira S. Jr., and A. Tavora A. S., "A Hexagonal Antenna Array Prototype for Adaptive System Application," *The 5th International Symposium on Wireless Personal Multimedia Communications*, vol. 2, pp. 757–761, 2002.

[3] C. H. Chen, W. C. Wong, and S. J. Hamada, "A Hexagonal Slot-Coupled CP Patch Array with an Integrated Filter," *IEEE Antennas Propag. Soc. Int. Symp. Dig.*, pp. 131–134, 1992.

[4] C.-N. Hu, *et al.*, "Design of the Cross-Dipole Antenna with Near-Hemispherical Coverage in Finite-Element Phased Array by Using Genetic Algorithms," *IEEE Antennas Propag. Soc. Int. Symp. Dig.*, vol. 1, pp. 303–306, 2000.

[5] H. T. Hui, *et al.*, "Design of a Small and Low-Profile 2×2 Hemispherical Helical Antenna Array for Mobile Satellite Communications," *IEEE Trans. Antennas Propag.*, vol. 52, no. 1, pp. 346–348, 2004.

[6] H. Nakano, *et al.*, "An Extremely Low-Profile Helical Array Antenna," *IEEE Antennas Propag. Soc. Int. Symp. Dig.*, pp. 702–705, 1990.

[7] A. Petosa, *et al.*, "Low Profile Phased Array of Dielectric Resonator Antennas," *IEEE Int. Symp. Phased Array Systems and Technology*, pp. 182–185, 1996.

[8] H. H. Chung, W. Foy, and S. Y. Peng, "Printed Crossed Slot Phased Array Antenna System for Mobile Satellite Communication," *IEEE Antennas Propag. Soc. Int. Symp. Dig.*, vol. 1, pp. 204–207, 1988.

[9] E. Jørgensen, B. K. Nielsen, and O. Breinbjerg, "A Cavity-Backed Crossed-Slot Antenna Element for an S-Band Circular Polarization Spherical Coverage Satellite Antenna System," *Proc. Int. Symp. Antennas Propag.*, vol. 1, pp. 361–364, 2000.

[10] M. K. Fries and R. Vahldieck, "Uniplanar Circularly Polarized Slot-Ring Antenna Architectures," *Radio Science*, vol. 38, no. 2, pp. 5.1–5.10, 2003.

[11] H. Morishita, K. Hirasawa, and K. Fujimoto, "Analysis of a Cavity-Backed Annular Slot Antenna with One Point Shorted," *IEEE Trans. Antennas Propag.*, vol. 39, no. 10, pp. 1472–1478, 1991.

[12] X. M. Qing and Y. W. M. Chia, "Circularly Polarised Circular Ring Slot Antenna Fed by Stripline Hybrid Coupler," *IEE Electron. Lett.*, vol. 35, no. 25, pp. 2154–2155, 1999.

[13] N. C. Karmakar, "Investigations Into a Cavity-Backed Circular-Patch Antenna," *IEEE Trans. Antennas Propag.*, vol. 50, no. 12, pp. 1706–1715, 2002.

[14] A. Corporation, *HFSS User's Manual v9.2*, 2004.

[15] D. I. Kaklamani and H. T. Anastassiu, "Aspects of the Method of Auxiliary Sources in Computational Electromagnetics," *IEEE Antennas Propag. Mag.*, vol. 44, no. 3, pp. 48–64, 2002.

[16] N. V. Larsen and O. Breinbjerg, "Modelling the Impact of Ground Planes on Antenna Radiation Using the Method of Auxiliary Sources," *IET Microw. Antennas Propag.*, vol. 1, no. 2, pp. 472–479, 2007.

Modelling the Impact of Ground Planes on Antenna Radiation Using the Method of Auxiliary Sources

Niels Vesterdal Larsen and Olav Breinbjerg

MODELLING THE IMPACT OF GROUND PLANES ON ANTENNA RADIATION USING THE METHOD OF AUXILIARY SOURCES

Niels Vesterdal Larsen and Olav Breinbjerg

Abstract: The Method of Auxiliary Sources is employed to model the impact of finite ground planes on the radiation from antennas. In many cases the computational cost of available commercial tools restricts the simulations to include only a small ground plane or, by use of the image principle, the infinitely large ground plane. The method proposed here makes use of results from such simulations to model large and moderate-sized finite ground planes. The method is applied to 3 different antenna test cases and a total of 5 different ground planes. Firstly it is validated through comparison with reference simulation results for the case of crossed Hertzian dipoles antennas. Later the method is applied to the cases of real antennas, a slot antenna and a printed dipole phased array, for which corresponding measurements have been conducted. The results obtained with the method agree well with the simulated and measured reference solutions and the method is thus found to be a useful tool in determining the impact of finite ground planes.

1 Introduction

When employing commercially available simulation tools in antenna design the computational cost often prohibits the inclusion of the antenna's surroundings, e.g., a large finite ground plane or a support structure. The commercial tools are often based on computationally expensive methods which are well suited for modelling of small detailed structures, e.g., the Method of Moments (MoM) in IE3D [1] or the Finite Element Method (FEM) in HFSS [2]. They may, however, become unattractive for large finite ground planes due to large computation time. In many cases antenna designs are thus based on the assumption of either an infinite or a small ground plane, and hence the impact on the antenna radiation of a large or moderate-sized ground plane is not known with good accuracy prior to actual fabrication and testing of the antenna.

Several methods have been applied to deal with the impact of finite ground planes and these are reported extensively in the literature. In particular, the physical optics or geometrical theory of diffraction techniques have found wide-spread employment, either based on approximate representations of the antenna itself or combined with MoM or FEM in hybrid techniques. A detailed list of references can be found in [3].

Due to its low computational cost the Method of Auxiliary Sources (MAS) represents another alternative to MoM and FEM. Indeed, for many large-scale problems the potential of MAS has been well documented, e.g., as shown in [4]

and its efficiency has been shown to be superior to that of MoM in many cases [5, 6]. In the present work the so-called standard MAS [7] is suggested as a means to analyse the impact of large finite ground planes on the radiation from antennas. The outset is taken in known antenna characteristics such as impedance, scattering parameters, currents on wires, or fields in apertures. These characteristics can be obtained from an analysis of an infinite ground plane case using a commercially available simulation tool. From these characteristics the antenna can be modelled by an impressed incident field whose interaction with the finite ground plane forms a scattering problem. Due to the low computational cost of MAS it becomes possible to investigate very large ground planes. In principle, the approach requires that the known antenna currents or apertures fields can be assumed to be unaffected by the introduction of the finite ground plane which, however, is a reasonable assumption for large and moderate-sized ground planes. In particular for low-profile antennas such as microstrip and slot antennas investigations [8, 9] have shown that the input impedance is unaffected by the ground plane size, even for small ground planes. For high-profile antennas such as monopole and helix antennas investigations in [10] and [11], however, conclude that some variation with the ground plane size may be expected for small ground planes.

In this work three very different antenna configurations are modelled. One with idealised Hertzian dipole (HD) antennas, where the incident field is known exactly, and two practical antenna cases where the incident field is inferred from known antenna characteristics. The three antenna cases are investigated with ground planes of different shapes and sizes and the obtained far-field results are compared with reference simulations and measurements.

2 The MAS Model

2.1 Mathematical Formulation

The mathematical formulation of the MAS solution takes outset in a scattering problem where an impedance scatterer with the surface impedance Z_s is surrounded by free space with intrinsic impedance Z_0. The scatterer is illuminated by a time-harmonic incident field $(\mathbf{E}^i, \mathbf{H}^i)$, with angular frequency ω and free-space wave number $k_0 = \frac{2\pi}{\lambda}$, where λ is the wavelength. The outward pointing unit normal vector of the scatterer surface B is denoted by $\hat{\mathbf{n}}$ and the time dependence $e^{j\omega t}$ is assumed and suppressed throughout the text. The standard impedance boundary condition (SIBC) [12] is assumed to hold on B and thus the total field

$$\mathbf{E} = \mathbf{E}^s + \mathbf{E}^i, \ \ \mathbf{H} = \mathbf{H}^s + \mathbf{H}^i, \tag{1}$$

being the sum of the incident field and the scattered field $(\mathbf{E}^s, \mathbf{H}^s)$ satisfies the relation

$$\hat{\mathbf{n}} \times \mathbf{E} = Z_s \hat{\mathbf{n}} \times (\hat{\mathbf{n}} \times \mathbf{H}). \tag{2}$$

To recover the scattered field, N auxiliary sources (AS) are placed inside the scatterer at positions $\mathbf{a}_n$ on the so-

called auxiliary surface A. This auxiliary surface is chosen conformal to the physical scatterer surface, B, into which it is receded by a distance d. On B, $M = N$ test points (TP) are located at positions $\mathbf{b}_m$ at which the boundary condition (2) is to be enforced. The auxiliary and scatterer surfaces with the AS and TP are shown in Figure 1. Local coordinate systems, with unit vectors $(\hat{\mathbf{a}}_n^x, \hat{\mathbf{a}}_n^y, \hat{\mathbf{a}}_n^z)$ and $(\hat{\mathbf{b}}_m^x, \hat{\mathbf{b}}_m^y, \hat{\mathbf{b}}_m^z)$, are associated with the n'th AS and the m'th TP, respectively.
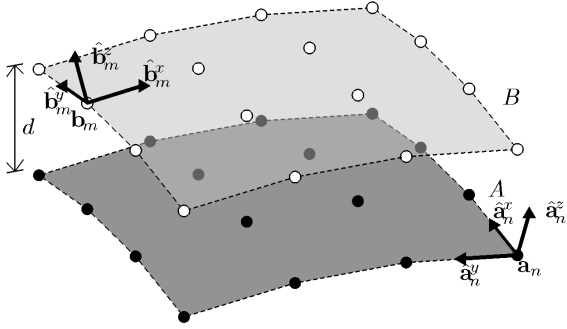

Figure 1: Sketch of a part of the ground plane surface B and auxiliary surface A. The auxiliary sources and test points are shown as black and white dots, respectively, together with examples of their associated coordinate systems.

The AS are chosen as pairs of crossed HD of either electric (EHD) or magnetic (MHD) type with independent excitations. The two crossed HD of the n'th AS are parallel to $\hat{\mathbf{a}}_n^x$ and $\hat{\mathbf{a}}_n^y$, respectively; $\hat{\mathbf{b}}_m^x$ and $\hat{\mathbf{b}}_m^y$ are tangential to B; and lastly $\hat{\mathbf{b}}_m^z$ coincides with the outward unit normal vector $\hat{\mathbf{n}}(\mathbf{b}_m)$ at the m'th TP, $\mathbf{b}_m$. Thus the positions of the AS and TP are related through $\mathbf{a}_n = \mathbf{b}_m - d\hat{\mathbf{n}}(\mathbf{b}_m)$, for $m = n$. The total field at the m'th TP is the sum of the incident field from the antenna and the radiated fields from the AS

$$\mathbf{E}(\mathbf{b}_m) = \mathbf{E}^i(\mathbf{b}_m) + \sum_{n=1}^{N} \left[C_n^x \mathbf{E}_n^{sx}(\mathbf{b}_m) + C_n^y \mathbf{E}_n^{sy}(\mathbf{b}_m) \right], \quad (3a)$$

$$\mathbf{H}(\mathbf{b}_m) = \mathbf{H}^i(\mathbf{b}_m) + \sum_{n=1}^{N} \left[C_n^x \mathbf{H}_n^{sx}(\mathbf{b}_m) + C_n^y \mathbf{H}_n^{sy}(\mathbf{b}_m) \right], \quad (3b)$$

where $(\mathbf{E}_n^s, \mathbf{H}_n^s)$ is the field radiated by the n'th AS and superscripts x and y refer to the $\hat{\mathbf{a}}_n^x$- and $\hat{\mathbf{a}}_n^y$-directed dipoles of the n'th AS. The MAS excitation coefficients C_n^x and C_n^y are to be determined through fulfilment of (2) in the M TP. This yields $2M$ equations with $2N$ unknowns for the two components of the boundary condition along $\hat{\mathbf{b}}_m^x$ and $\hat{\mathbf{b}}_m^y$ to be satisfied. For the m'th TP the two equations read

$$\sum_{n=1}^{N} \left[C_n^x (-E_{nm}^{sxy} + Z_s H_{nm}^{sxx}) + C_n^y (-E_{nm}^{syy} + Z_s H_{nm}^{syx}) \right]$$
$$= E_m^{iy} - Z_s H_m^{ix}, \quad (4a)$$

$$\sum_{n=1}^{N} \left[C_n^x (E_{nm}^{sxx} + Z_s H_{nm}^{sxy}) + C_n^y (E_{nm}^{syx} + Z_s H_{nm}^{syy}) \right]$$
$$= -E_m^{ix} - Z_s H_m^{iy}, \quad (4b)$$

where $E_{nm}^{sxy} = \hat{\mathbf{b}}_m^y \cdot \mathbf{E}_n^{sx}(\mathbf{b}_m)$, and similarly for the other field quantities. In matrix notation equations (4a-b) take the form

$$\begin{bmatrix} \overline{\overline{\mathbf{Z}}}_y^x & \overline{\overline{\mathbf{Z}}}_y^y \\ \overline{\overline{\mathbf{Z}}}_x^x & \overline{\overline{\mathbf{Z}}}_x^y \end{bmatrix} \begin{bmatrix} \mathbf{C}^x \\ \mathbf{C}^y \end{bmatrix} = \begin{bmatrix} \mathbf{V}_y \\ \mathbf{V}_x \end{bmatrix}, \quad (5)$$

from which the C_n^x, C_n^y can readily be determined. The elements of the matrix and vectors of (5) are

$$Z_{y,nm}^x = -E_{nm}^{sxy} + Z_s H_{nm}^{sxx}, \quad (6a)$$

$$Z_{y,nm}^y = -E_{nm}^{syy} + Z_s H_{nm}^{syx}, \quad (6b)$$

$$Z_{x,nm}^x = E_{nm}^{sxx} + Z_s H_{nm}^{sxy}, \quad (6c)$$

$$Z_{x,nm}^y = E_{nm}^{syx} + Z_s H_{nm}^{syy}, \quad (6d)$$

$$V_{y,m} = E_m^{iy} - Z_s H_m^{ix}, \quad (6e)$$

$$V_{x,m} = -E_m^{ix} - Z_s H_m^{iy}. \quad (6f)$$

Detailed expressions for these quantities are given in appendix A. The boundary condition error (BCE) is calculated in P points $\mathbf{d}_p$ distributed evenly on B between the TP. P is selected proportional to N, and the mean BCE is defined as

$$\text{Mean } BCE = \frac{1}{P} \sum_{p}^{P} |\hat{\mathbf{n}}(\mathbf{d}_p) \times \mathbf{E}(\mathbf{d}_p)$$
$$- Z_s \hat{\mathbf{n}}(\mathbf{d}_p) \times (\hat{\mathbf{n}}(\mathbf{d}_p) \times \mathbf{H}(\mathbf{d}_p))|. \quad (7)$$

It is noted that the absolute value of this error is not of particular importance but its variation with the number of AS is of interest when assessing the convergence of the solution.

2.2   Practical Aspects of Ground Plane Modelling

The MAS formulation is now applied to the problem of determining the impact of finite ground planes on the radiation from antennas. That is, the ground plane takes the role of the scatterer and the antenna is represented by the incident field. The MAS solution derived in section 2.1 allows for general impedance ground planes and thus the case of non-perfectly conducting ground planes or ground planes covered with thin layers of dielectric can be modelled. For the cases discussed in this text, however, the ground planes are assumed to be perfect electric conductors (PEC), i.e., $Z_s = 0$.

It is well known that the standard MAS formulation [7] is well suited for the modelling of smooth and closed structures. Thus curved surfaces of vehicles and air craft fuselages are examples of ground planes that can readily be modelled with this approach. However, the standard MAS does not lend itself well to modelling of thin structures or structures with sharp edges. Furthermore, in cases where the illuminating sources are very close to the ground plane the spatial variation of the incident field along the surface is particularly high and may thus be a cause for inaccuracy. Both of these potential problems can be solved by employing a localised MoM solution at the corners and near closely positioned sources as reported in [13, 14]. This will, however, be at the expense of increased complexity.

The case of a thin planar ground plane, which can be considered an open structure, is not easily modelled with the standard MAS. The so-called Modified MAS [15] is an alternative to the standard MAS and has been shown to be effective for thin structures, e.g., microstrip and dipole antennas. It has also been applied to a thin square plate, however, the nature of the problem restricts the solution's validity to a single half space [15].

For the standard MAS, the problem can be avoided by increasing the thickness and rounding the edges of the ground plane, such as suggested in [5], and the ground plane model thus essentially becomes a closed structure. In this work the emphasis is put on such thin planar ground planes with the purpose of showing that accurate results can be obtained with the standard MAS - even for this type of challenging structure.

In the model used here the thickness of the ground plane model, denoted t_{MAS}, is therefore larger than for the ground plane itself. The rounding of the ground planes edges makes these semicircular with a curvature radius of $t_{MAS}/2$. The size of the ground plane model is defined with respect to the flat part and thus the rounded edges constitute small additions to the overall ground plane size. In the case of closely positioned illuminating sources a patch of densely positioned AS is introduced in the vicinity below the illuminating sources and furthermore the distance between B and A is set to $d/2$ in this area. A sketch of a MAS ground plane model with rounded edges and with a dense patch of AS is shown in Figure 2.
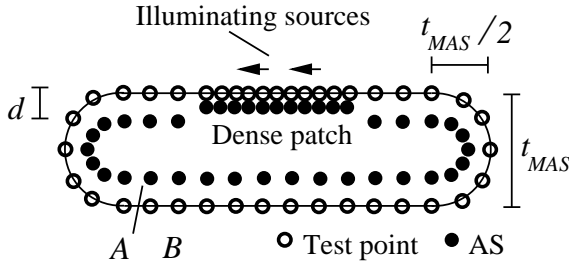

Figure 2: Cross-sectional view of a MAS ground plane with rounded edges and a dense patch of AS.

Due to the aforementioned limitation in the standard MAS, it is clear that there is a lower limit on the value of t_{MAS} that can be used in the model. Both the choice of t_{MAS}, and whether or not a dense patch is used, influence the BCE. This is discussed further in connection with a practical antenna case in section 3.2.

Since the model relies on known antenna characteristics some inaccuracy will occur if this characterisation is not accurate. This will for instance be the case if very small ground planes are modelled using antenna characteristics valid for an infinite ground plane. Also the rounding of the edges may, depending on t_{MAS}, result in an almost spherical shape for very small ground planes and constitutes a significant difference between the true and the modelled ground plane. Thus the model is not well suited for very small ground planes.

The MAS simulation results shown in this work have been carried out using MATLAB and the equations systems solved using its standard matrix inversion routine. Primarily a 2.8 GHz PC with 1 GB RAM, however in one case this RAM was not sufficient and a 750 MHz "Sun Fire 6800" computer with sufficient RAM was used. The CPU time used for the calculations is given in Table 1 where the investigated ground planes are described.

	Shape	Dim. [λ]	t_{MAS} [λ]	N	CPU time [s]
GP 1	Circ.	4 , D	0.375	2501	906 + 71.2
GP 2	Square	1.32, SL	0.25	743	66.0 + 2.53
GP 3	Circ.	1.90, D	0.375	756	67.4 + 2.59
GP 4*	Circ.	7.90, D	0.5	4821	25080 + 1835
GP 5	R. circ.	5.27, D	0.5	3026	1597 + 121

*Table 1: Description of the 5 different ground planes used in the 3 antenna configurations. The CPU time is divided into matrix "fill" + "solve" time. For the dimensions, D and SL indicate diameter and side length, respectively. The * indicates that the "Sun Fire 6800" computer was used.*

3 Antenna Cases

3.1 The Case of Ideal Antennas

Before applying the proposed method to practical antennas, two well-defined idealised test configurations are investigated, both with the ground plane GP 1 described in Table 1. In the first case, GP 1 is illuminated by crossed MHD excited in phase quadrature and positioned 0.03λ above the centre of the ground plane. In the second configuration crossed EHD positioned at a distance of 0.25λ above the ground plane are used. The co- and cross-polar directivities for these configurations are shown in Figure 3 and compared with reference solutions [16]. For the reference solutions thin ground planes with sharp edges have been used. As can be seen in Figure 3 the agreement between the two results is very good within a wide dynamic range and both the main-, side-, and back lobes are accurately recovered, however, some minor deviations are seen in the cross polarisation near the bore sight direction. It is noted that this is not a consequence of lack of convergence but is caused by the rounded corners used in the MAS model. Since the rounded edges are and inherent part of the model this can not be avoided.

This investigation shows that in the case where the antenna is accurately represented by an incident field the proposed method can accurately simulate the presence of the ground plane. It is further seen that even though the shape of the ground plane has been slightly changed, by rounding the edges and increasing the thickness, the resulting far field does not deviate significantly from that of the original ground plane.
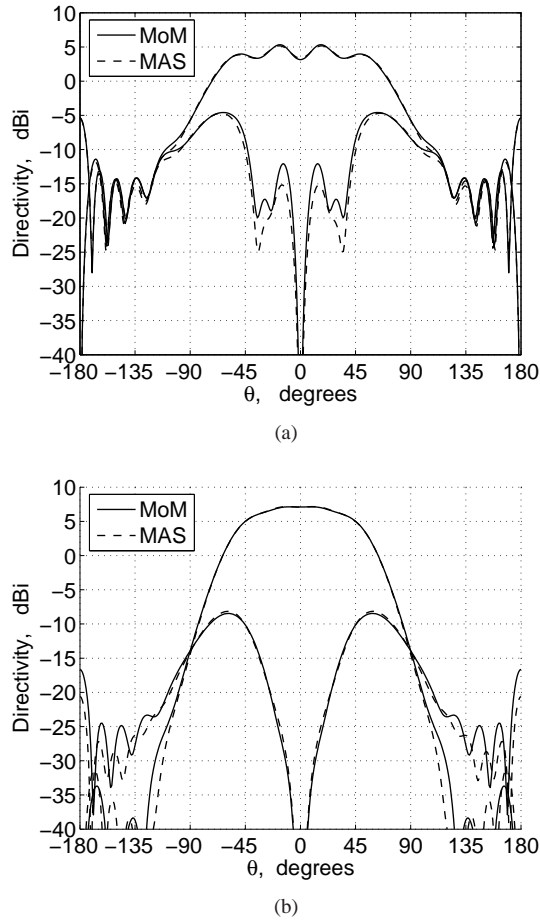
(a)

(b)

Figure 3: Directivity of a configuration with crossed HD in phased quadrature centred above GP 1. (a) MHD, 0.03λ above, (b) EHD, 0.25λ above.
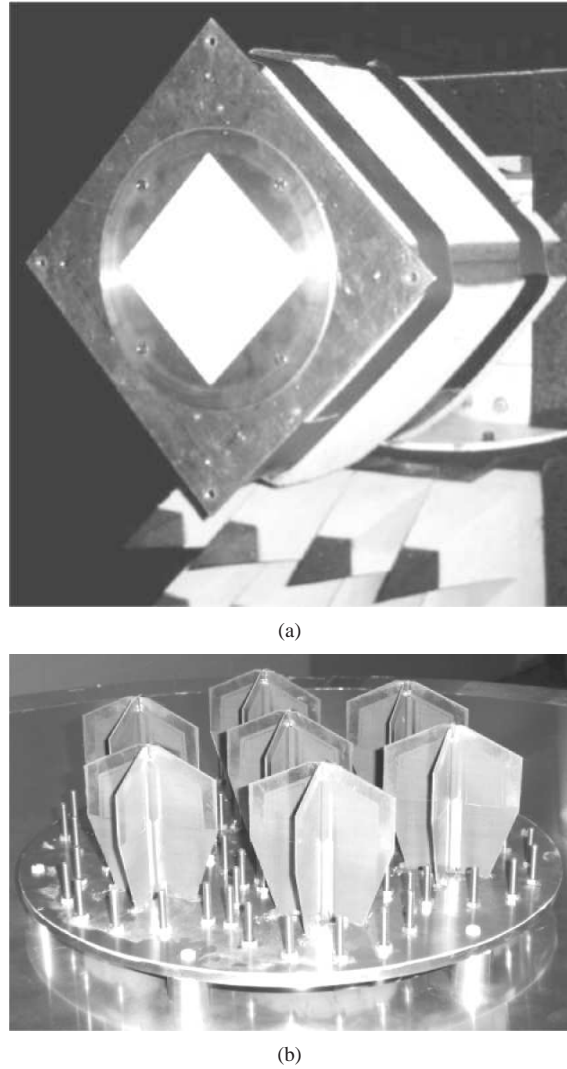

(a)

(b)

Figure 4: (a) The CBAS antenna mounted with GP 2. The white dielectric superstrate covers the slot. (b) The 7-element phased array raised above GP 5.

3.2 The Case of a Cavity-Backed Annular Slot Antenna

In this case a cavity-backed annular slot (CBAS) antenna is modelled, see the left-hand sides of Figure 4 and Figure 5. It is a circularly polarised dual-feed antenna fed at two points spaced 90° apart along the slot. The slot is etched in a copper-clad dielectric superstrate. The antenna is described in more detail in [17]. Based on the measured 2-port scattering matrix of this antenna the terminal voltages can be determined. The slot is modelled as a thin slot cut in a PEC ground plane and the dielectric superstrate is not included in the model. The slot field is represented by an infinitely thin magnetic ring current which is raised 0.05λ above the ground plane surface and subsequently discretised using $K = 64$ MHD.

The antenna model is now applied to the three different ground planes denoted GP 2-4 and described in Table 1. For reference, measurements have been conducted at the DTU-ESA Spherical Near-Field Antenna Test Facility at the Technical University of Denmark. The ground planes used in the measurements have a thickness of 0.01λ, whereas the selected values for t_{MAS} in the MAS models are larger, see Table 1. The measurement and simulation results are shown in Figure 6. Generally there is good agreement between the measured and simulated result both with respect to the co- and cross-polar components. Some deviations are seen between the levels of ripples in the patterns of GP 3-4 and are more pronounced than what can be attributed to the differences introduced by the rounding of the edges. The remaining deviations reflect the differences between the physical slot in the dielectric superstrate and the magnetic ring current approximation used to form the incident field in the MAS model.

For GP 3 the BCE (7) has been investigated for configurations with and without the dense patch for different values of t_{MAS}. The BCE as function of N is shown in Figure 7. It is seen that both with and without the dense patch it is notably larger for the thin ground planes (small t_{MAS}) than for the thicker ones. Also it is seen that with the dense patch the BCE continues its descent for large values of N which is not the case without the patch. Although the dense patch implies
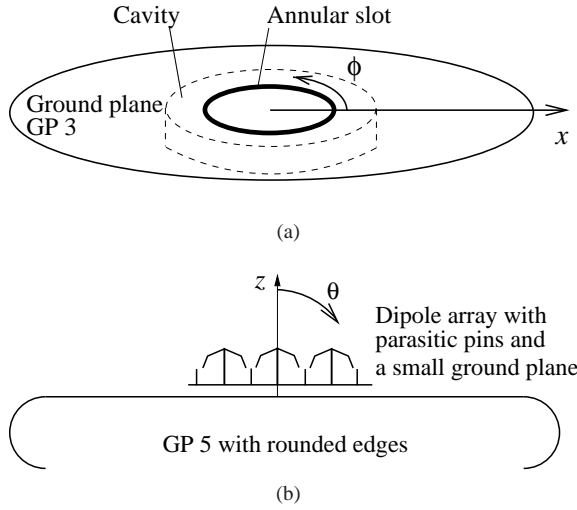
(a)

(b)

Figure 5: Sketches of the two antenna cases, mounted on GP 3 (a) and GP 5 (b), respectively.

an increase in N it is seen to yield a lower mean BCE for the same N - especially in the cases where $t_{MAS} = 0.375\lambda$ and $t_{MAS} = 0.5\lambda$.

The increase in the BCE for thin ground planes can be explained by the fact that the auxiliary and physical surfaces are forced to be closer to each other which has deleterious effects on the accuracy. The impact of the distance d on the BCE has previously been reported for 2-dimensional problems [18] and is has been shown that the condition number of the linear equation system grows with both d and N and for a certain threshold renders the numerically solution unstable. In [19] investigations have shown that barring the advent of numerical instability an optimum value of d, i.e., minimising the BCE, can be found and it depends on the distance between the scatterer surface and the illuminating source. In the present work $d \simeq t_{MAS}/4$ has been found to be a good value for d, however, it is noted that it depends on the amount of AS used.

In Figure 8 the radiation patterns obtained for different values of t_{MAS} and N are shown, all calculated using a dense patch. In Figure 8a, where $t_{MAS} = 0.375\lambda$, it is seen that no significant difference occurs between the solutions for $N = 756$ and $N = 1114$, however, for $N = 484$ some deviations occur in the cross-polar pattern and in the ripples of the main beam. In Figure 8b the three values of t_{MAS} are used and $N = 1232, 1152, 1305$, corresponding to the respective cases of minimum BCE in figure 7b. The difference between $t_{MAS} = 0.375\lambda, 0.5\lambda$ is seen to have little impact, however, the $t_{MAS} = 0.25\lambda$ case deviates slightly. Both the deviating cases, $t_{MAS} = 0.375\lambda, N = 484$, and $t_{MAS} = 0.25\lambda, N = 1232$, have approximately the same BCE, see figure 7b, whereas all the other have smaller BCE. This indicates that the relatively large BCE in these cases lead to deviations in the radiation patterns and that these deviation are not directly a consequence of the differences in the rounding of the ground plane edges.
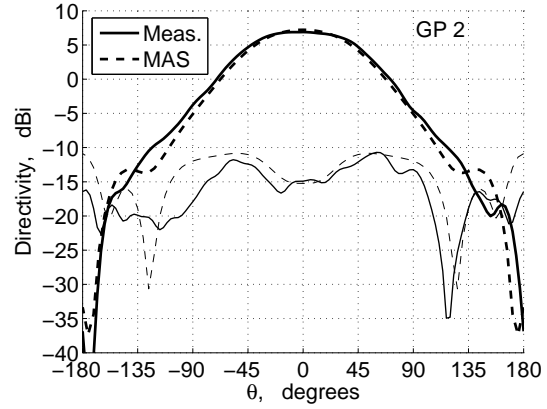

(a)
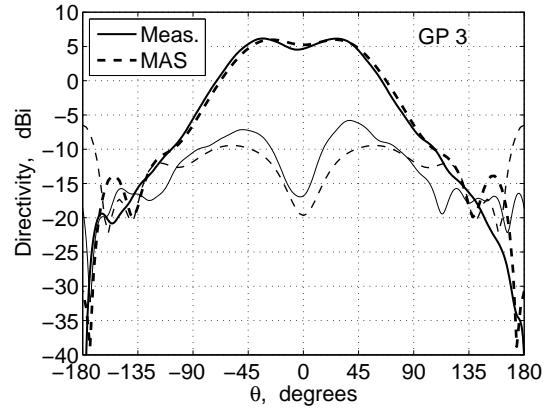
(b)
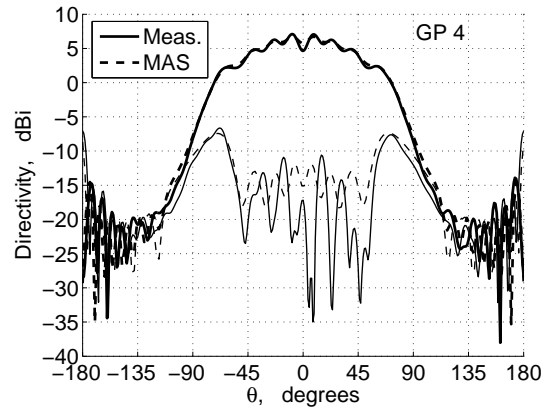
(c)

Figure 6: Directivity of the CBAS antenna mounted on the ground planes, GP 2-4. The frequency is 1.58 GHz, and $\phi = 0°$ in all cases.

3.3 The Case of a Dipole Phased Array

In this case the configuration is a small phased array antenna mounted 0.11λ above a conducting ground plane, see the right-hand sides of Figure 4 and Figure 5. The ground plane, which is denoted GP 5 and described in Table 1, has rounded edges and this enables a more accurate representation in the MAS model. The phased array antenna com-
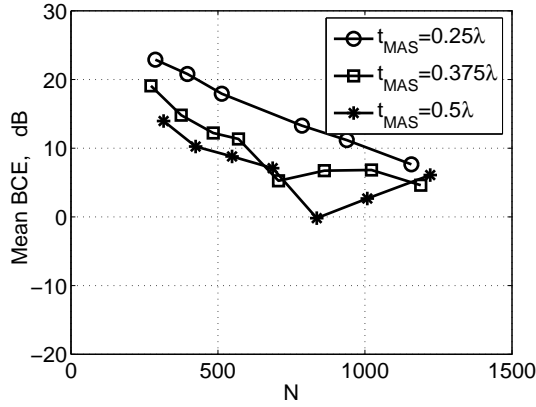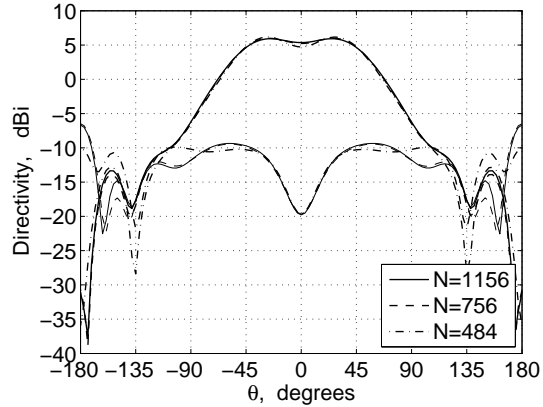
(a)
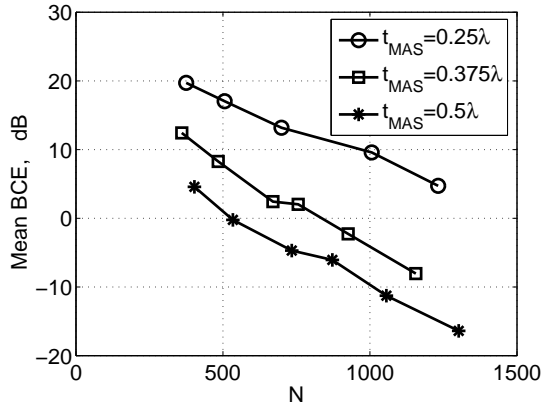
(b)

Figure 7: Mean BCE for GP 3 using 3 different values for t_{MAS}. (a) Without extra dense mesh. (b) With extra dense mesh.

(a)

(b)

Figure 8: Far field for the MAS model of GP 3. (a) $t_{MAS} = 0.375\lambda$ and 3 different values for N. (b) 3 different values for t_{MAS} with corresponding $N = 1232, 1152, 1305$, respectively.
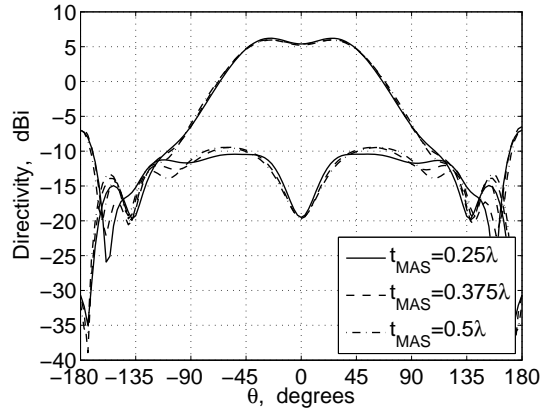
prises 7 circularly polarised crossed printed dipole elements, parasitic pins positioned between the elements, and a small ground plane with a diameter of 1.58λ. The elements are fed at four ports each, resulting in a total of 28 ports in the array. The case of interest in this investigation is when the array is mounted without electrical connection between its own small ground plane and GP 5.

The antenna array including its small ground plane is simulated using AWAS 2.0 [20] and all wires are assumed to be circular PEC wires in free space thus differing from the true printed dipoles. The small ground plane of the array is modelled as a wire grid structure and the whole configuration is positioned above an infinite ground plane. From this AWAS simulation all wire currents of the array are calculated. From samples of these wire currents the entire array, including the small ground plane, is modelled using $K \simeq 5000$ EHD.

In order to calculate the active element patterns [21] of the array mounted on GP 5, a modified version of (5) is used. The right-hand side of (5) is for this problem a $2N \times 28$ matrix with columns for each of the 28 ports. The solution for this system is also a $2N \times 28$ matrix holding the 28 sets of MAS excitation coefficients. From these coefficients, deter-

mining the scattered field, and the incident field itself, the 28 active element patterns can be formed. As described so far, the model does not take the non-ideal array and element feed networks into account and these may cause an increase of the cross polarisation as well as introduce small errors in the beam scanning. However, from measurements of the scattering parameters of the array and element feed networks these non-ideal, and more realistic, excitation coefficients have been calculated and these are used in the model.

Measurements of the printed dipole array mounted on GP 5 have been carried out and examples of the array far field patterns are shown in Figure 9 for two different scan angle settings. Both MAS simulations and measurements are shown. The agreement is reasonably good and it is noted that the impact of the finite ground plane on the shape of the main lobe is well recovered. With regard to the cross polar component some deviations are present. The cause for these deviations is most likely the differences between the actual array and the AWAS wire model from which the incident field is derived. Particularly the differences between the actual printed dipoles and the simulated PEC wires may cause this, however, also the AWAS wire-grid model of the small array ground plane may be a cause for inaccuracy.
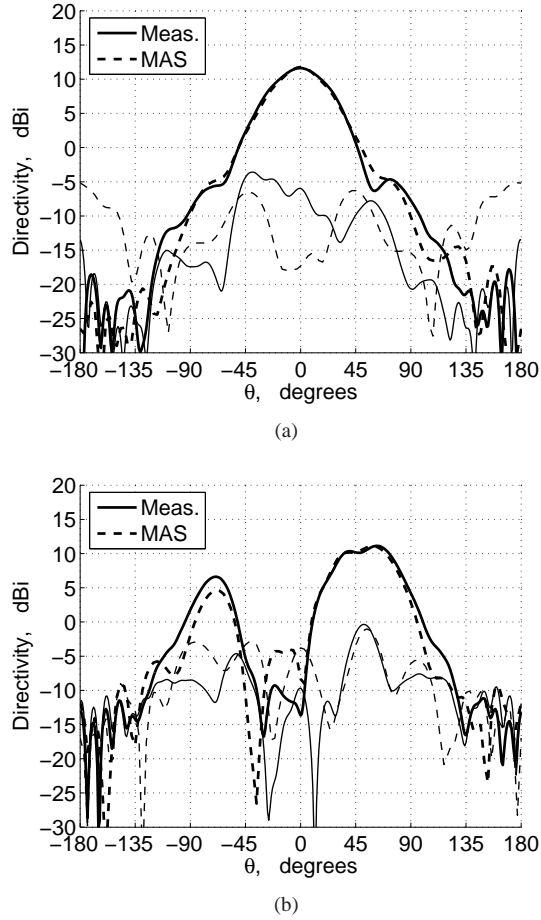
(a)

(b)

Figure 9: Directivity of the measured and simulated array mounted on GP 5 for a frequency of 1.6 GHz. The beam is scanned towards boresight (a), and 60° from boresight (b).

4   Conclusion

The Method of Auxiliary Sources has been applied for the modelling and analysis of the impact of large and moderate-sized finite ground planes on the radiation from antennas. An ideal antenna test case and two real antenna cases, a cavity-backed annular slot antenna, and a 7-element printed dipole phased array, have been included in the investigation. Both square and circular ground planes with widths of up to 7.90λ have been included. The results were compared to measurements and good agreement was found. The consequences of different modelling schemes for the ground planes were discussed and the implication on the boundary condition error and the radiation patterns were demonstrated. It was found that for thin ground plane models the error is generally larger. Also it was seen that the insertion of a patch of densely positioned auxiliary sources and test points serves to minimise the error. The impact on the radiation patterns was found to be small.

The proposed method has been shown to be capable of recovering reference solutions with very high accuracy in cases where the antenna can be represented accurately by an incident field. In cases where the antenna model is less accurate minor deviations occur. The method can thus be used favourably in combination with commercially available antenna simulation tools whose computational cost does not allow inclusion of large finite ground planes.

In this work the model has only been validated for PEC ground planes, although it allows for general impedance structures. Future work may demonstrate the validity for general impedance ground planes also.

A   Evaluation of the Auxiliary Source Fields at the Test Points

In order to express the field from the n'th AS in terms of the coordinate system of the m'th TP, a rotated version of the n'th AS coordinate system is introduced. It is rotated through the Euler angles $(\chi_0, \theta_0, \phi_0)$ [22], such that its rectangular unit vectors are parallel to those of the m'th TP coordinate system. The spherical unit vectors of this rotated coordinate system are denoted by $(\hat{\mathbf{w}}_{nm}^r, \hat{\mathbf{w}}_{nm}^\theta, \hat{\mathbf{w}}_{nm}^\phi)$ and the position of the m'th TP, described in this coordinate system, is denoted by $\mathbf{w}_{nm}$ with the rectangular- or spherical coordinates $(x_{nm}^w, y_{nm}^w, z_{nm}^w; r_{nm}^w, \theta_{nm}^w, \phi_{nm}^w)$. Expressed in terms of this coordinate system the electric field from the $\hat{\mathbf{a}}_n^x$ directed n'th AS evaluated at the m'th TP is

$$\begin{bmatrix} E_{nm}^{sxx} \\ E_{nm}^{sxy} \\ E_{nm}^{sxz} \end{bmatrix} = \overline{\overline{\mathbf{T}}}(\theta_{nm}^w, \phi_{nm}^w) \begin{bmatrix} \hat{\mathbf{w}}_r^r \cdot \mathbf{E}_n^x(\mathbf{w}_{nm}) \\ \hat{\mathbf{w}}_r^\theta \cdot \mathbf{E}_n^x(\mathbf{w}_{nm}) \\ \hat{\mathbf{w}}_r^\phi \cdot \mathbf{E}_n^x(\mathbf{w}_{nm}) \end{bmatrix}, \qquad (8)$$

and similarly for the magnetic field. Here

$$\overline{\overline{\mathbf{T}}}(\theta, \phi) = \begin{bmatrix} \sin\theta\cos\phi & \cos\theta\cos\phi & -\sin\phi \\ \sin\theta\sin\phi & \cos\theta\sin\phi & \cos\phi \\ \cos\theta & -\sin\theta & 0 \end{bmatrix}, \quad (9)$$

converts from spherical to rectangular coordinates. In the case where the AS are chosen as EHD the electric and magnetic fields from the $\hat{\mathbf{a}}_n^x$-directed dipole [1] are given by

$$\mathbf{E}_n^x(\mathbf{w}_{nm}) = E_0 \frac{e^{-jk_0 r_{nm}^w}}{k_0 r_{nm}^w}.$$

$$\left[\frac{2}{k_0 r_{nm}^w} \left[1 - \frac{j}{k_0 r_{nm}^w}\right] \hat{\mathbf{w}}_{nm}^r \left[f_1 \sin\theta_{nm}^w + f_3 \cos\theta_{nm}^w\right] - \right.$$

$$\left[j + \frac{1}{k_0 r_{nm}^w} - \frac{j}{(k_0 r_{nm}^w)^2}\right].$$

$$\left. \left[\hat{\mathbf{w}}_{nm}^\theta \left(\cos\theta_{nm}^w f_1 - f_3 \sin\theta_{nm}^w\right) - f_2 \hat{\mathbf{w}}_{nm}^\phi\right]\right], \qquad (10\text{a})$$

$$\mathbf{H}_n^x(\mathbf{w}_{nm}) = j\frac{E_0}{Z_0} \frac{e^{-jk_0 r_{nm}^w}}{k_0 r_{nm}^w} \left[1 - \frac{j}{k_0 r_{nm}^w}\right].$$

$$\left[-\hat{\mathbf{w}}_{nm}^\theta f_2 + \hat{\mathbf{w}}_{nm}^\phi \left[-f_1 \cos\theta_{nm}^w + f_3 \sin\theta_{nm}^w\right]\right], \quad (10\text{b})$$

---

[1]The fields from the $\hat{\mathbf{a}}_n^y$-directed dipole can be calculated in the same way by replacing ϕ_0 with $\phi_0 - \frac{\pi}{2}$ in (10c-e).

where $E_0 = 1\frac{\text{V}}{\text{m}}$ and

$$
\begin{aligned}
f_1 &= \cos\theta_0 \cos\phi_0 \cos(\chi_0 + \phi_{nm}^w) \\
&\quad - \sin\phi_0 \sin(\chi_0 + \phi_{nm}^w),
\end{aligned} \tag{10c}
$$

$$
\begin{aligned}
f_2 &= \sin\phi_0 \cos(\chi_0 + \phi_{nm}^w) \\
&\quad + \cos\theta_0 \cos\phi_0 \sin(\chi_0 + \phi_{nm}^w),
\end{aligned} \tag{10d}
$$

$$
f_3 = \sin\theta_0 \cos\phi_0. \tag{10e}
$$

The coordinates of $\mathbf{w}_{nm}$ are given by

$$
x_{nm}^w = \hat{\mathbf{b}}_m^x \cdot (\mathbf{b}_m - \mathbf{a}_n), \tag{11a}
$$

$$
y_{nm}^w = \hat{\mathbf{b}}_m^y \cdot (\mathbf{b}_m - \mathbf{a}_n), \tag{11b}
$$

$$
z_{nm}^w = \hat{\mathbf{b}}_m^z \cdot (\mathbf{b}_m - \mathbf{a}_n). \tag{11c}
$$

In the case where MHD are used as AS the corresponding fields can be found by application of the duality principle.

Bibliography

[1] Zeland Software, Inc. (2007, January) IE3D. [Online]. Available: http://www.zeland.com/ie3d.html

[2] Ansoft Corporation. (2007, January) HFSS. [Online]. Available: http://www.ansoft.com/products.cfm

[3] V. Volski and G. A. E. Vandenbosch, "Efficient Physical Optics Approximation for the Calculation of Radiation Patterns of Planar Antennas Located on a Finite Ground Plane," *IEEE Trans. Antennas Propag.*, vol. 53, no. 1, pp. 460–465, 2005.

[4] R. S. Zaridze, *et al.*, "Electromagnetic Analysis for Vehicle Antenna Development Using Method of Auxiliary Sources," *IEEE Antennas Propag. Soc. Int. Symp. Dig.*, pp. 185–188, 2003.

[5] H. T. Anastassiu, *et al.*, "Electromagnetic Scattering Analysis of Coated Conductors With Edges Using the Method of Auxiliary Sources (MAS) in Conjunction With the Standard Impedance Boundary Condition (SIBC)," *IEEE Trans. Antennas Propag.*, vol. 50, no. 1, pp. 59–66, 2002.

[6] G. K. Avdikos and H. T. Anastassiu, "Computational Cost Estimation and Comparison for Three Methods of Applied Electromagnetics (MoM, MAS, MMAS)," *IEEE Antennas Propag. Mag.*, vol. 47, no. 1, pp. 121–129, 2005.

[7] D. I. Kaklamani and H. T. Anastassiu, "Aspects of the Method of Auxiliary Sources in Computational Electromagnetics," *IEEE Antennas Propag. Mag.*, vol. 44, no. 3, pp. 48–64, 2002.

[8] C. L. Mak, Y. L. Chow, and K. M. Luk, "Finite Ground Plane Effects of a Microstrip Patch Antenna: a CAD Formula of Impedance Perturbation by Synthetic Asymptote and GTD," *IEE Proc. Microw. Antennas Propag.*, vol. 150, no. 1, pp. 11–17, 2003.

[9] J. Wettergren, P.-S. Kildahl, and K. Forooraghi, "Admittance of a Longitudinal Slot in a Finite Ground Plane," *IEEE Antennas Propag. Soc. Int. Symp. Dig.*, pp. 1608–1611, 1993.

[10] K. H. Awadalla and T. S. M. Maclean, "Input Impedance of a Monopole Antenna at the Center of a Finite Ground Plane," *IEEE Trans. Antennas Propag.*, vol. 26, no. 2, pp. 244–248, 1978.

[11] S. H. Zainud-Deen, K. H. Awadalla, and H. A. Sharshar, "Analysis of Normal Mode Helical Antenna on Finite Ground Plane," *IEEE Antennas Propag. Soc. Int. Symp. Dig.*, pp. 1879–1882, 1978.

[12] T. B. A. Senior and J. L. Volakis, *Approximate Boundary Conditions in Electromagnetics*. The Institution of Electrical Engineers, London, 1995.

[13] S. Eisler and Y. Leviatan, "Analysis of Electromagnetic Scattering From Metallic and Penetrable Cylinders with Edges Using Multifilament Current Model," *IEE Proc., Pt. H*, vol. 136, no. 6, pp. 431–438, 1989.

[14] N. V. Larsen and O. Breinbjerg, "A Hybrid MAS/MoM Technique for 2D Impedance Scatterers Illuminated by Closely Positioned Sources," *Microwave Opt. Technol. Lett.*, vol. 44, no. 2, pp. 112–114, 2005.

[15] F. Shubitidze, H. T. Anastassiu, and D. I. Kaklamani, "An Improved Accuracy Version of the Method of Auxiliary Sources for Computational Electromagnetics," *IEEE Antennas Propag. Mag.*, vol. 52, no. 1, pp. 302–309, 2004.

[16] E. Jørgensen, *et al.*, "Higher Order Hierarchical Legendre Basis Functions for Electromagnetic Modeling," *IEEE Trans. Antennas Propag.*, vol. 52, no. 11, pp. 2985–2995, 2004.

[17] N. V. Larsen and O. Breinbjerg, "An L-band, Circularly Polarised, Dual-Feed, Cavity-Backed Annular Slot Antenna for Phased Array Applications," *Microwave Opt. Technol. Lett.*, vol. 48, no. 5, pp. 873–878, 2006.

[18] H. T. Anastassiu, *et al.*, "Accuracy Analysis and Optimization of the Method of Auxiliary Sources (MAS) for Scattering by a Circular Cylinder," *IEEE Trans. Antennas Propag.*, vol. 52, no. 6, pp. 1541–1547, 2004.

[19] N. V. Larsen and O. Breinbjerg, "An Analytical Method of Auxiliary Sources Solution for Line Source Illumination of Impedance Cylinders," *Proc. Int. Conf. on Mathematical Methods Electromagnetic Theory*, pp. 25–29, 2004.

[20] A. R. Djordjević, *et al.*, *AWAS for Windows, Version 2.0, Analysis of Wire Antennas and Scatterers, Software and User Manual*. Artech House Inc., Boston, 2002.

[21] R. J. Mailloux, *Phased Array Antenna Handbook*. Artech House, Boston, 1994.

[22] J. E. Hansen, *Spherical Near-Field Antenna Measurements*. Peter Peregrinus Ltd., London, 1998.

PAPER 3

Analysis of Circularly Polarised Hemispheroidal Dielectric Resonator Antenna Phased Arrays Using the Method of Auxiliary Sources

Niels Vesterdal Larsen and Olav Breinbjerg

ANALYSIS OF CIRCULARLY POLARISED HEMISPHEROIDAL DIELECTRIC RESONATOR ANTENNA PHASED ARRAYS USING THE METHOD OF AUXILIARY SOURCES

Niels Vesterdal Larsen and Olav Breinbjerg

Abstract: The Method of Auxiliary Sources is employed to model and analyse probe-fed hemispheroidal dielectric resonator antennas and arrays. Circularly polarised antenna elements of different designs are analysed and impedance bandwidths of up to 14.7% are achieved. Selected element designs are subsequently employed in a 7-element phased array. The array performance is analysed with respect to scan loss and main beam directivity as function of scan angle and frequency, and the influence of element separation is investigated.

1 Introduction

The Dielectric Resonator Antenna (DRA) has attracted much attention in recent years due to its many favourable features such as low loss, compact size, structural simplicity, and simple feeding schemes. Various different shapes have been investigated, the most common being hemispherical, cylindrical, and rectangular shapes, e.g., [1–4].

In order to obtain a large bandwidth, a wide range of complex shapes have been used, common to which is the inclusion of an air gap inside the DRA [5–7]. Also multi-band operation has been achieved by using inhomogeneous dielectrics in the form of stacked DRAs or by enclosing one DRA in another [8, 9].

Circularly polarised DRAs have been designed using either single-feed or multiple-feed excitations. With a single feed, orthogonal modes can be excited in the DRA by applying parasitic patches [10] or by exciting the DRA asymmetrically [11]. These methods, however, are generally very narrow-band with respect to the axial ratio and therefore practical designs often make use of multiple feeds excited in phase quadrature, e.g., [12].

The compact size is an important factor when considering the DRA as a candidate for phased arrays. This allows smaller element separation compared with many other antenna types, and this is important for reducing scan loss [13]. Planar linearly polarised DRA phased arrays have previously been examined in [14, 15], and in [16] a circularly polarised phased array was developed. In [14] the influence of the mutual coupling between the elements on the radiation pattern was investigated. However, a detailed investigation of the array scan loss and its variation with element distance and frequency has not been reported for these designs.

Much theoretical work has been done in analysing hemispherical DRA elements where spherical wave expansion techniques (SWE) can be used to derive analytical solutions or be combined with numerical techniques such as the Method of Moments (MoM) to solve for currents on probes or fields in apertures that excite the DRA, e.g., [1, 2]. For more general shapes of DRAs or for DRA arrays, accurate modelling usually relies on numerical techniques, e.g., the Finite Element Method (FEM) or MoM. For arrays in particular, the computational cost of numerical analysis may be prohibitive with these methods.

The Method of Auxiliary Sources (MAS) is well known for its low computational cost and may thus be an alternative to MoM and FEM. Indeed, MAS has previously been employed in the analysis of dielectric antennas [17] where an infinite periodic waveguide array with protruding dielectric elements was investigated. In particular the simple and computationally cheap standard MAS [18] can be employed when the field varies smoothly along the boundaries and in this case simple Hertzian dipoles can be used as auxiliary sources. For configurations where the fields vary rapidly near the boundary, e.g., near edges or closely positioned illuminating sources, the MAS model can be augmented with localised Method of Moments patches [19, 20]. MAS has also been proven effective for thin-wire antennas where, by using sinusoidal dipoles as auxiliary sources, the impedance properties of dipole antennas have been evaluated accurately [21].

The purpose of this work is two-fold. Firstly, it is demonstrated that the simple standard MAS model can be employed for detailed and accurate analysis of small finite arrays of smooth hemispheroidal probe-fed DRAs positioned on an infinite, perfectly electrically conducting (PEC), ground plane. Secondly, the model is used to investigate and design a 7-element hexagonal phased array consisting of such DRA elements. The emphasis is put on circularly polarised elements fed in phase quadrature with four probes. A number of different element designs are first investigated and subsequently the 7-element phased array is analysed. Examples of array performance in terms of directivity and scan loss is presented and the dependence on element separation and scan angle is discussed. In order to validate the MAS model, the results are compared with results obtained using the software tool CST Microwave Studio (CST-MS) [22] and reference measurement from [23]. In the case of a single hemispherical DRA comparison is also made with SWE solutions. These validations are done for one- and two-element configurations, however, it was not practically possible to model an entire 7-element array with CST-MS with the available computer resources and this further illustrates the justification of developing this MAS model.

The text is organised as follows. The MAS model is presented in Section 2 and the element and array investigations are given in Section 3 and Section 4, respectively. The conclusions are drawn in Section 5 and additional mathematical details of the MAS model and the SWE solution are given in Appendix A and B, respectively.
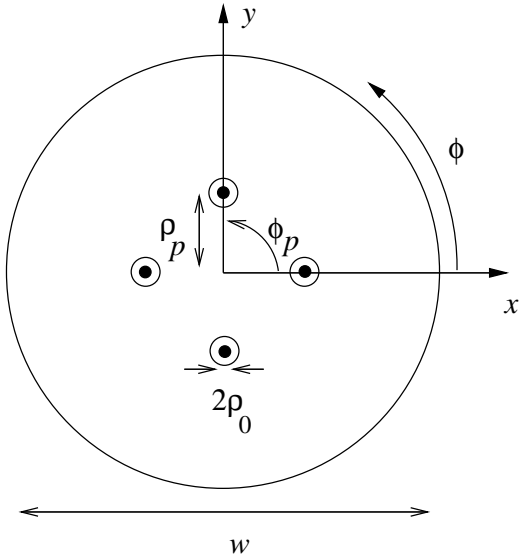
Figure 1: Cross-sectional views of the probe-fed hemispheroidal DRA with $P = 4$ probes. (a) (x, z)-plane. (b) (x, y)-plane.

2 MAS Models of the DRA Elements and Arrays

2.1 The DRA Element

The hemispheroidal DRA element is depicted in Figure 1 where also the coordinate system is defined. It is positioned on an infinite ground plane and is uniquely described by its height h and width w. It is fed by a number, P, of probes positioned inside the DRA. The position of the p'th probe in the (x, y)-plane is given by the circular cylindrical coordinates (ρ_p, ϕ_p) and the probe radius is denoted ρ_0.

The MAS model of a single DRA with one probe is shown in Figure 2a. The upper half space is divided into two regions, Region 0 outside the DRA and Region 1 inside with the boundary denoted B. The outward unit normal vector to B is denoted $\hat{\mathbf{n}}$. The permittivities and permeabilities of the two regions are (ϵ_0, μ_0) and $(\epsilon_1 = \epsilon_r \epsilon_0, \mu_1 = \mu_r \mu_0)$, respectively, where ϵ_r and μ_r are the relative permittivity and permeability of the DRA material. Thus the wave numbers and intrinsic impedances of the two regions are, respectively, $k_0 = \omega \sqrt{\epsilon_0 \mu_0}$, $Z_0 = \sqrt{\mu_0/\epsilon_0}$ and $k_1 = k_0 \sqrt{\epsilon_r \mu_r}$, $Z_1 = Z_0 \sqrt{\mu_r/\epsilon_r}$ with ω being the angular frequency. The to-
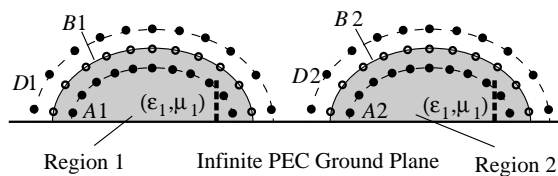

Figure 2: Cross section of the MAS model showing AS, TP and IS for a single-probe configuration. (a) A single DRA element. (b) Two DRA elements.

tal field in the two regions are denoted by $(\mathbf{E}_0, \mathbf{H}_0)$ and $(\mathbf{E}_1, \mathbf{H}_1)$. The probes are modelled as currents with sinusoidal shape with unknown amplitude and phase. This probe model is of course an approximation, however, as has been demonstrated in [21], MAS can be used to accurately recover impedance properties of wire antennas, e.g., such probes. Even with this approximate probe model the present MAS model yields useful results, as will be apparent.

The probes produce an incident field $(\mathbf{E}_1^{\text{inc}}, \mathbf{H}_1^{\text{inc}})$ in Region 1 inside the DRA, whose interaction with the DRA boundary B forms a scattering problem. In Region 1 the total field is thus the sum of the incident and the scattered field $(\mathbf{E}_1^{\text{scat}}, \mathbf{H}_1^{\text{scat}})$. The tangential components of the total field are continuous across B and thus,

$$\hat{\mathbf{n}} \times \mathbf{E}_0 = \hat{\mathbf{n}} \times (\mathbf{E}_1^{\text{inc}} + \mathbf{E}_1^{\text{scat}}), \tag{1a}$$

$$\hat{\mathbf{n}} \times \mathbf{H}_0 = \hat{\mathbf{n}} \times (\mathbf{H}_1^{\text{inc}} + \mathbf{H}_1^{\text{scat}}). \tag{1b}$$

In the MAS probe model the sinusoidal probe current is taken as

$$\mathbf{I}^{(p)}(z) = \hat{\mathbf{z}} I_0^{(p)} \frac{\sin k_1(l - z)}{\sin k_1 l}, \quad 0 \le z \le l, \tag{2}$$

where l is the probe length and $I_0^{(p)}$ is the complex excitation. The excitations will be calculated based on the scattering matrix of the DRA elements or arrays as detailed in Section 2.3.

In order to calculate the incident field the probe currents are discretised using Q so-called incidence sources (IS) for each probe. The IS are electric Hertzian dipoles and the position and dipole moment of the q'th IS of the p'th probe are denoted $\mathbf{r}_{pq} = (\rho_p, \phi_p, z_q)$ and $\mathbf{p}_q^{(p)} = \frac{l}{Q} \mathbf{I}^{(p)}(z_q)$ where

$z_q = ql/Q$, respectively. The IS are shown in Figure 2a and radiate in a homogeneous half space with the material parameters of Region 1, however, the thus produced incident field is confined to Region 1. The contribution to the incident field radiated by the q'th IS is denoted $\mathbf{E}_q^{\text{inc},(p)}$ and the incident field radiated by the p'th probe is then

$$\mathbf{E}^{\text{inc},(p)} = \sum_{q=1}^{Q} \mathbf{E}_q^{\text{inc},(p)}. \tag{3}$$

To recover the fields in both regions, two sets of auxiliary sources (AS) are positioned on so-called auxiliary surfaces denoted A and D and chosen conformal to B. The auxiliary surfaces are receded into and advanced outside B by the distances d_A and d_D, respectively, as indicated in Figure 2a. The AS on A and D radiate in homogenous half spaces with the material parameters of Region 0 and Region 1, respectively, and the radiated fields are confined to the respective regions. The AS are chosen as pairs of crossed Hertzian dipoles of either electric (EHD) or magnetic (MHD) type with independent excitations and the numbers of AS on A and D are equal and denoted by N. The positions of the AS are denoted by $\mathbf{a}_n$ and $\mathbf{d}_n$, respectively. On the scatterer surface B the boundary conditions (1a-b) are tested in $M = N$ test points (TP) at positions $\mathbf{b}_m$ and thus the positions of the AS and TP are related through

$$\mathbf{a}_n = \mathbf{b}_m - d_A \hat{\mathbf{n}}(\mathbf{b}_m), \quad m = n, \tag{4a}$$
$$\mathbf{d}_n = \mathbf{b}_m + d_D \hat{\mathbf{n}}(\mathbf{b}_m), \quad m = n. \tag{4b}$$

The total field on the two sides of the boundary B, evaluated at the m'th TP, $\mathbf{b}_m$, are

$$\begin{Bmatrix} \mathbf{E}(\mathbf{b}_m) \\ \mathbf{H}(\mathbf{b}_m) \end{Bmatrix} = \sum_{n=1}^{N} \sum_{t=1}^{2} C_{nt}^{A} \begin{Bmatrix} \mathbf{E}_{nt}^{A}(\mathbf{b}_m) \\ \mathbf{H}_{nt}^{A}(\mathbf{b}_m) \end{Bmatrix}, \quad \text{Region 0,} \tag{5a}$$

$$\begin{Bmatrix} \mathbf{E}(\mathbf{b}_m) \\ \mathbf{H}(\mathbf{b}_m) \end{Bmatrix} = \sum_{p=1}^{P} \begin{Bmatrix} \mathbf{E}^{\text{inc},(p)}(\mathbf{b}_m) \\ \mathbf{H}^{\text{inc},(p)}(\mathbf{b}_m) \end{Bmatrix}$$
$$+ \sum_{n=1}^{N} \sum_{t=1}^{2} C_{nt}^{D} \begin{Bmatrix} \mathbf{E}_{nt}^{D}(\mathbf{b}_m) \\ \mathbf{H}_{nt}^{D}(\mathbf{b}_m) \end{Bmatrix}, \quad \text{Region 1,} \tag{5b}$$

In (5a) $\mathbf{E}_{nt}^{A}$ and $\mathbf{H}_{nt}^{A}$ denote the electric and magnetic fields radiated by the t'th of the two crossed Hertzian dipoles of the n'th AS on the auxiliary surface A and similarly for $\mathbf{E}_{nt}^{D}$ and $\mathbf{H}_{nt}^{D}$ in (5b). These fields are weighted by the MAS excitation coefficients C_{nt}^{A} and C_{nt}^{D} which are to be determined through fulfilment of (1a-b) in the M TP. This yields $4M$ equations with $4N$ unknowns for the tangential components of the electric and magnetic fields at B. The presence of the infinite PEC ground plane is taken into account by employing image theory. It thus follows that the fields from the AS and IS can be found by removing the ground plane and adding the field from the corresponding image source below the ground plane. Thus the field from a single source above the infinite ground plane consists of two contributions, one from the AS directly and one from the image source, e.g.,

$$\mathbf{E}_{nt}^{A}(\mathbf{b}_m) = \mathbf{E}_{nt}^{A,\text{direct}}(\mathbf{b}_m) + \mathbf{E}_{nt}^{A,\text{image}}(\mathbf{b}_m). \tag{6}$$

Explicit expressions for the electric and magnetic fields, evaluated at the TP, are given in Appendix B.

In the case where there are more than one probe, i.e., $P > 1$, it is convenient to form P independent equation systems with individual sets of incident fields and corresponding solutions of the MAS excitation coefficients. The solutions of these systems may then be combined later in accordance with the actual excitations of the probes. In this way it is only necessary to invert the linear system matrix once. The linear system of equations thus established can be written as a matrix equation of the form

$$\begin{bmatrix} \overline{\overline{\mathbf{Z}}}_E^A & \overline{\overline{\mathbf{Z}}}_E^D \\ \overline{\overline{\mathbf{Z}}}_H^A & \overline{\overline{\mathbf{Z}}}_H^D \end{bmatrix} \begin{bmatrix} \overline{\overline{\mathbf{C}}}^A \\ \overline{\overline{\mathbf{C}}}^D \end{bmatrix} = \begin{bmatrix} \overline{\overline{\mathbf{V}}}_E \\ \overline{\overline{\mathbf{V}}}_H \end{bmatrix}. \tag{7}$$

The sub-matrices $\overline{\overline{\mathbf{Z}}}_E^A$, $\overline{\overline{\mathbf{Z}}}_E^D$, $\overline{\overline{\mathbf{Z}}}_H^A$, and $\overline{\overline{\mathbf{Z}}}_H^D$ have $2M \times 2N$ elements and hold two tangential components of the electric or magnetic fields of the 2 Hertzian dipoles of the N AS on the auxiliary surfaces A or D at the M TP. The right-hand side sub-matrices $\overline{\overline{\mathbf{V}}}_E$ and $\overline{\overline{\mathbf{V}}}_H$ have $2M \times P$ elements and their columns hold the incident electric and magnetic fields from the P probes. The MAS excitation coefficients in $\overline{\overline{\mathbf{C}}}^A$ and $\overline{\overline{\mathbf{C}}}^D$ are readily found by inversion of the left-hand side matrix and are similarly arranged in columns corresponding to the P sets of incident fields.

2.2 The DRA Array

The single-element formulation is now extended to the case of a planar array consisting of R DRAs. Thus the DRA boundaries, regions, auxiliary surfaces, AS, and TP are now referred to by an index from 1 to R.

In Figure 2b an example of a MAS configuration with $R = 2$ is shown. It is noted that the interaction between the AS and TP within each DRA element of the array is the same as in the single-element case. The interaction between the AS and IS of one DRA element and the TP of a neighbouring DRA elements must, however, now be included. Thus the field radiated by the AS on the external auxiliary surfaces, denoted by Dr, as well as the incident field radiated by the IS inside the r'th DRA are confined to Region r. Hence it is only the AS on the internal auxiliary surfaces, denoted by Ar, that contribute to the field in Region 0 and hence to the field at the boundaries of the other DRA elements. In total a $4RN$-dimensional linear system of equations results. In the case where the p'th probe is excited the total fields on the two sides of the boundary Br at the m'th TP of the r'th DRA, $\mathbf{b}_m^r$, is

$$\begin{Bmatrix} \mathbf{E}(\mathbf{b}_m^r) \\ \mathbf{H}(\mathbf{b}_m^r) \end{Bmatrix} = \sum_{s=1}^{R} \sum_{n=1}^{N} \sum_{t=1}^{2} C_{nt}^{As,(p)} \begin{Bmatrix} \mathbf{E}_{nt}^{As}(\mathbf{b}_m^r) \\ \mathbf{H}_{nt}^{As}(\mathbf{b}_m^r) \end{Bmatrix}, \tag{8a}$$

in Region 0, and

$$\begin{Bmatrix} \mathbf{E}(\mathbf{b}_m^r) \\ \mathbf{H}(\mathbf{b}_m^r) \end{Bmatrix} = \sum_{p=1}^{RP} \gamma_{pr} \begin{Bmatrix} \mathbf{E}^{\mathrm{inc},(p)}(\mathbf{b}_m^r) \\ \mathbf{H}^{\mathrm{inc},(p)}(\mathbf{b}_m^r) \end{Bmatrix}$$
$$+ \sum_{n=1}^{N} \sum_{t=1}^{2} C_{nt}^{Dr,(p)} \begin{Bmatrix} \mathbf{E}_{nt}^{Dr}(\mathbf{b}_m^r) \\ \mathbf{H}_{nt}^{Dr}(\mathbf{b}_m^r) \end{Bmatrix}, \qquad (8b)$$

in Region r. The factor γ_{pr} takes the value 1 if the p'th probe is located in the r'th Region and 0 otherwise. Thus for each element the summation over the RP probes only yields P contributions. Note that the sum in (8a) includes the interior AS of all the R DRAs whereas those of (8b) only include the IS and exterior AS associated with the r'th DRA. The corresponding matrix systems now becomes

$$\begin{bmatrix} \overline{\overline{\mathbf{Z}_1^1}} & \overline{\overline{\mathbf{Z}_1^2}} & \cdots & \overline{\overline{\mathbf{Z}_1^R}} \\ \overline{\overline{\mathbf{Z}_2^1}} & \overline{\overline{\mathbf{Z}_2^2}} & \cdots & \overline{\overline{\mathbf{Z}_2^R}} \\ \vdots & \vdots & \ddots & \vdots \\ \overline{\overline{\mathbf{Z}_R^1}} & \overline{\overline{\mathbf{Z}_R^2}} & \cdots & \overline{\overline{\mathbf{Z}_R^R}} \end{bmatrix} \begin{bmatrix} \overline{\overline{\mathbf{C}_1^1}} & \overline{\overline{\mathbf{C}_1^2}} & \cdots & \overline{\overline{\mathbf{C}_1^R}} \\ \overline{\overline{\mathbf{C}_2^1}} & \overline{\overline{\mathbf{C}_2^2}} & \cdots & \overline{\overline{\mathbf{C}_2^R}} \\ \vdots & \vdots & \ddots & \vdots \\ \overline{\overline{\mathbf{C}_R^1}} & \overline{\overline{\mathbf{C}_R^2}} & \cdots & \overline{\overline{\mathbf{C}_R^R}} \end{bmatrix}$$
$$= \begin{bmatrix} \overline{\overline{\mathbf{V}_1^1}} & \overline{\overline{\mathbf{0}}} & \cdots & \overline{\overline{\mathbf{0}}} \\ \overline{\overline{\mathbf{0}}} & \overline{\overline{\mathbf{V}_2^2}} & \cdots & \overline{\overline{\mathbf{0}}} \\ \vdots & \vdots & \ddots & \vdots \\ \overline{\overline{\mathbf{0}}} & \overline{\overline{\mathbf{0}}} & \cdots & \overline{\overline{\mathbf{V}_R^R}} \end{bmatrix}. \qquad (9)$$

The sub-matrices $\overline{\overline{\mathbf{V}_j^i}}$, $\overline{\overline{\mathbf{C}_j^i}}$, and $\overline{\overline{\mathbf{Z}_j^i}}$ in (9) are of the same size as the full matrices for the single-element case in (7). In particular it is noted that $\overline{\overline{\mathbf{Z}_j^i}}$ equals the left-hand side matrix in (7) for $i = j$. The P columns of $\overline{\overline{\mathbf{V}_j^i}}$ and $\overline{\overline{\mathbf{C}_j^i}}$ hold the incident fields and MAS coefficients associated with the j'th DRA corresponding to the case where the P probes of the i'th DRA are excited. Since the incident field is confined inside the respective DRA, the $\overline{\overline{\mathbf{V}_j^i}}$ are only non-zero for $i = j$. However, since the neighbouring DRA become excited due to the mutual coupling between the DRAs, the $\overline{\overline{\mathbf{C}_j^i}}$ are generally non-zero. The full $\overline{\overline{\mathbf{C}}}$ and $\overline{\overline{\mathbf{V}}}$ matrices have RP columns corresponding to each of the RP probes in the array.

2.3   Calculation of Impedances and Far Fields

The probe input ports are located at the probes' intersections with the ground plane. The self and mutual impedances of these ports are calculated using the reaction theorem [24]. In the present model, where the probe currents are discretised using Q IS, a discrete version of the reaction theorem is employed,

$$Z_{ij} = -\frac{1}{I_0^{(i)} I_0^{(j)}} \sum_{q=1}^{Q} \mathbf{E}^{(i)}(\mathbf{r}_{jq} + \hat{\boldsymbol{\rho}}\rho_0) \cdot \mathbf{p}_q^{(j)}, \qquad (10)$$

where $\mathbf{E}^{(i)}(\mathbf{r}_{jq} + \hat{\boldsymbol{\rho}}\rho_0)$ is the field sampled at the surface of the j'th probe when the i'th probe is excited. The electric

field is calculated as

$$\mathbf{E}^{(i)}(\mathbf{r}_{jq} + \hat{\boldsymbol{\rho}}\rho_0) = \sum_{r=1}^{R} \gamma_{jr} \Bigg[\gamma_{ir} \mathbf{E}^{\mathrm{inc},(i)}(\mathbf{r}_{jq} + \hat{\boldsymbol{\rho}}\rho_0)$$
$$+ \sum_{n=1}^{N} \sum_{t=1}^{2} C_{nt}^{Dr,(i)} \mathbf{E}_{nt}^{Dr}(\mathbf{r}_{jq} + \hat{\boldsymbol{\rho}}\rho_0) \Bigg]. \quad (11)$$

The factor $\gamma_{jr}\gamma_{ir}$, multiplied on the incident field, indicates that this only contributes directly to the coupling between probes located in the same region.

In the present model the probes are assumed to be excited with forward propagating voltage waves $\mathbf{V}^+$ and the input reflection coefficient $\Gamma_{in,p}$ and input impedance $Z_{in,p} = R_{in,p} + jX_{in,p}$ of the p'th port are calculated from

$$\Gamma_{in,p} = \frac{V_p^-}{V_p^+}, \qquad (12a)$$

$$Z_{in,p} = Z_0 \frac{1 + \Gamma_{in,p}}{1 - \Gamma_{in,p}}, \qquad (12b)$$

where $Z_0 = 50\,\Omega$ is the assumed characteristic impedance of the feed lines connected to the probe ports and the reflected voltage waves V_p^- are given by

$$\mathbf{V}^- = \overline{\overline{\mathbf{S}}}\mathbf{V}^+, \qquad (13a)$$

$$\overline{\overline{\mathbf{S}}} = (\overline{\overline{\mathbf{Z}}} + Z_0 \overline{\overline{\mathbf{U}}})^{-1} (\overline{\overline{\mathbf{Z}}} - Z_0 \overline{\overline{\mathbf{U}}}). \qquad (13b)$$

In (13b) $\overline{\overline{\mathbf{Z}}}$ is the impedance matrix with the elements given by (10) and $\overline{\overline{\mathbf{U}}}$ is the identity matrix. While the amplitudes of the probes currents were set to unity when calculating the probe impedances, the actual probe excitations, corresponding to a certain set of forward voltage wave excitations $\mathbf{V}^+$, can now be calculated using the obtained knowledge of the coupling between the probes.

The field outside the DRAs, i.e., in Region 0, is the sum of the contributions from the AS on the interior auxiliary surfaces, Ar. Thus the field in Region 0 due to a current on the p'th probe is

$$\mathbf{E}_0^{(p)}(\mathbf{r}) = \sum_{r=1}^{R} \sum_{n=1}^{N} \sum_{t=1}^{2} C_{nt}^{Ar,(p)} \mathbf{E}_{nt}^{Ar}(\mathbf{r}). \qquad (14)$$

From this expression and the knowledge of the element-to-element coupling the active element patterns (AEP) [13] of the array can be found as follows. When any of the probe ports are excited by a forward voltage wave non-zero currents will result on all the probes of the array due to the coupling between the probes and hence all DRA elements are excited. In the case where the p^*'th port is excited by a unit forward voltage wave the corresponding current of the p'th probe is

$$I_0^{(p,p^*)} = \frac{V_p^+ - V_p^-}{Z_0}, \; V_p^+ = \begin{cases} 1\mathrm{V}, & \text{for } p = p^* \\ 0, & \text{otherwise} \end{cases}, \quad (15)$$

where the V_p^- follow from (13a). Having calculated the currents on all probes the corresponding AEP can be established. For a unit forward voltage wave excitation of 1 V of

the p^*'th port the resulting AEP is

$$\mathbf{E}_{\text{AEP}}^{(p^*)}(\mathbf{r}) = \sum_{p=1}^{RP} W_{p,p^*} \mathbf{E}_0^{(p),far}(\mathbf{r}), \qquad (16)$$

where $\mathbf{E}_0^{(p),far}$ is the far field corresponding to $\mathbf{E}_0^{(p)}$ of (14) and $W_{p,p^*} = I_0^{(p,p^*)}/I_0^{(p)}$ are dimensionless weight factors. The array patterns for specific beam scanning follow straightforwardly by applying suitable weights $W_{p^*}^+(\theta_0, \phi_0)$ for the forward voltage waves exciting the ports, corresponding to the desired scan angles (θ_0, ϕ_0). Thus the array far field is

$$\mathbf{E}_{array}^{far}(\theta_0, \phi_0, \mathbf{r}) = \sum_{p^*=1}^{RP} W_{p^*}^+(\theta_0, \phi_0)\mathbf{E}_{\text{AEP}}^{(p^*)}(\mathbf{r}). \qquad (17)$$

3 Analysis of DRA Elements

The MAS model is now applied to the case of a single DRA element. The investigations presented here will concentrate on oblate hemispheroidal DRA elements, i.e., $w \geq 2h$. The elements are circularly polarised with $P = 4$ probes. The probe displacement ρ_p from the centre is chosen such that the probes are positioned as close as possible to the DRA edge and excite the fundamental broadside mode, [1]. The probe displacement ρ_p is the same for all probes but varies for different DRA designs. The probes are spaced equiangularly such that $\phi_p = 90^\circ(p - 1)$ and ideal phase quadrature is imposed for the forward voltage waves of the ports, i.e., $V_p^+ = (-j)^{p-1}$ V. The frequency interval of interest is L-band around 1.6GHz. 6 different designs, denoted Design 0-5, are considered and these are further described in Table 1 where also the number of AS on each auxiliary surface, N, is given. For all the designs, the probe height l has been selected such that $k_1 l = \frac{\pi}{2}$ at 1.6GHz, and a probe radius of $\rho_0 = 0.5$ mm and element height of $h = 2$cm are used throughout. Furthermore $\mu_r = 1$, and by varying w and ϵ_r, the resonance frequency f_{res}, defined at $X_{in} = 0$, can be tuned. Investigations, which are not shown here, indicate that the input impedance of the DRA elements, and in particular the centre element, is shifted to slightly higher frequencies when used in an array. For this reason the single-element designs presented have values of ϵ_r selected to obtain a resonance frequency somewhat lower than 1.6GHz as can also be seen from Table 1.

In order to check the convergence of the solution the relative changes $\Delta_Z^{\text{IS}}(Q_n), \Delta_Z^{\text{AS}}(N_n)$ of the input impedance, resulting from an increase in the number of IS and AS, are calculated. $\Delta_Z^{\text{IS}}(Q_n)$ is defined as

$$\Delta_Z^{\text{IS}}(Q_n) = \frac{|Z_{in}(Q_n) - Z_{in}(Q_{n-1})|}{|Z_{in}(Q_{n-1})|}, \qquad (18)$$

where $N = 223$ is kept constant. For $\Delta_Z^{\text{AS}}(N_n)$, which is defined in a similar way, $Q = 51$ is kept constant. The results are shown in Figure 3 for Design 1. As can be seen the change quickly becomes very small indicating convergence.

Design	h [mm]	w [mm]	ϵ_r	ρ_p [mm]	l [mm]	f_{res} [GHz]	BW [%]	N
0	20	40	22	13	10.0	1.54	2.7	165
1	20	50	18	15	11.0	1.49	4.0	223
2	20	60	15	18	12.1	1.49	6.5	223
3	20	70	13	21	13.0	1.49	8.1	223
4	20	80	12	23	13.5	1.48	12.9	297
5	20	90	11	24	14.1	1.49	14.7	297

Table 1: The 6 investigated designs of the hemispheroidal DRA element.

In the remaining investigations $Q = 71$ is used throughout. As a further validation the MAS model is compared with results obtained using CST-MS [22].
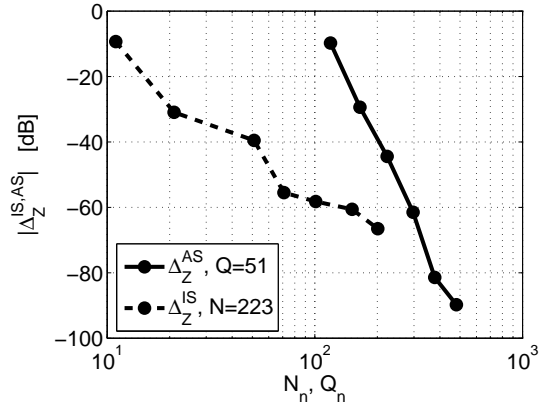

Figure 3: Convergence of the input impedance for increasing Q and N for Design 1.

Design 0, with $w = 2h$, is the special case of a hemispherical DRA. The probe-fed hemispherical DRA has been widely described in the literature and selected analytical solutions are reported in [1, 2]. An analytical solution, based on a spherical wave expansion (SWE), has been derived here, see Appendix A, and this serves as an additional means for testing the proposed MAS model. In Figure 4 the input impedance and directivity obtained for Design 0 are shown together with the corresponding SWE and CST-MS results. It is noted that the MAS probe model is employed for both the MAS and the SWE solutions but not for the CST-MS solution. In the CST-MS model the probes are modelled more accurately with coaxial cable feed ports which might not lead to the sinusoidal current distribution assumed in the MAS model. As can be seen the MAS and SWE results agree very well for both impedance and radiation results. This shows that the field both inside and outside the DRA are accurately recovered. When comparing the impedance results with the CST-MS solution it is seen that the approximate probe model used in the SWE and MAS models introduces some inaccuracy. Thus the resonance frequency is about 2% higher and the resistance at resonance is about 20% lower than for CST-MS. In the present case of Design
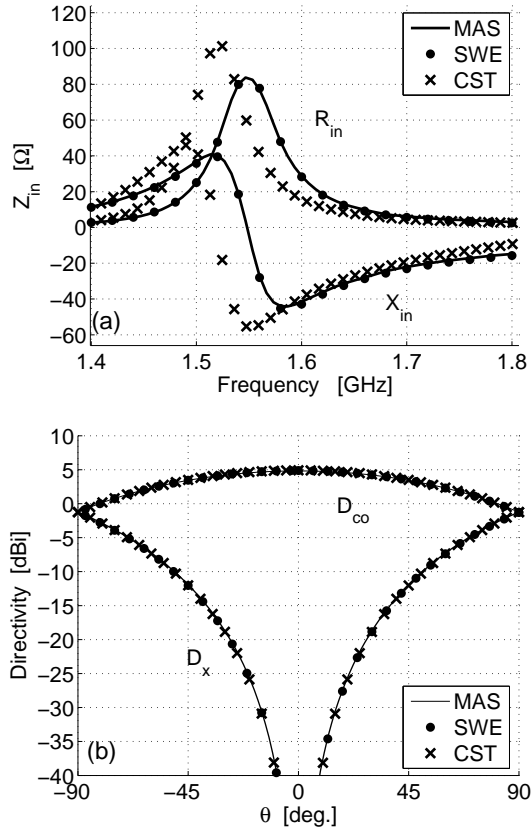
Figure 4: Comparison of the results for the hemispherical Design 0 calculated by MAS and the SWE solution. (a) Input impedance, Z_{in}. (b) Directivity for $f = 1.6GHz$.

0 MAS yields a resistance of about 80Ω while the CST-MS result is about 100Ω. For the radiation results, however, all 3 solutions agree well and the probe models have little impact on the result.

To calculate the impedance bandwidth the DRA input ports are matched with identical lossless open-circuit single-stub (OCSS) matching networks as shown in Figure 5. This matching network is designed to match the mean input reflection coefficient of the P probe ports

$$\Gamma_{in}^{E}(f_0) = \frac{1}{P} \sum_{p=1}^{P} \Gamma_{in,p}(f_0), \qquad (19)$$

where $\Gamma_{in,p}(f_0)$ is the input reflection coefficient, seen at the p'th probe input port of the unmatched DRA element, and is calculated from (12a) for a chosen design frequency f_0. The scattering matrix of the OCSS matching network can easily be determined and is

$$\overline{\overline{\mathbf{S}}}_{OCSS}(f) = \frac{1}{2 + j\tan(\beta d_1)} \times \\ \begin{bmatrix} -j\tan(\beta d_1) & 2e^{-j\beta d_2} \\ 2e^{-j\beta d_2} & -j\tan(\beta d_1)e^{-2j\beta d_2} \end{bmatrix}, \quad (20)$$

where d_1, d_2, and β are the lengths and phase constant of the transmission lines in the matching network. The proper
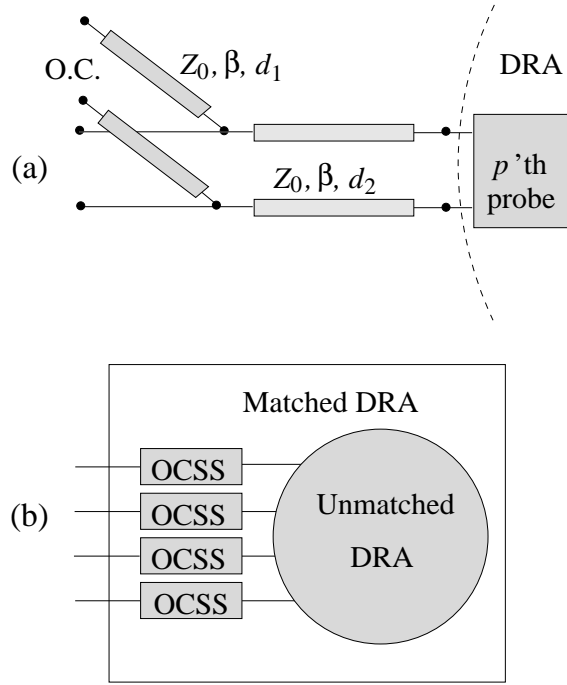

Figure 5: (a) OCSS matching network connected to a probe port. (b) A matched DRA with 4 probes and matching elements.

values of d_1 and d_2 depend on the reflection coefficient to be matched and the design frequency f_0 and expressions can be found in most text books on the topic, e.g., [25]. By combining the scattering parameters of the matching network $\overline{\overline{\mathbf{S}}}_{OCSS}$ with those of the array in (13b), e.g., as described in [26], the combined scattering matrix of the matched DRA element can be derived and the reflected voltages from this matched DRA can be calculated. The matching network is designed for $f_0 =$1.5GHz which is close to the element resonance frequencies f_{res} and the impedance bandwidth (BW) is defined with respect to $|\hat{\Gamma}_{in}^{E}(f)|^2 < -10$dB, where

$$|\hat{\Gamma}_{in}^{E}(f)|^2 = \frac{1}{P} \sum_{p=1}^{P} |\hat{\Gamma}_{in,p}(f)|^2, \qquad (21)$$

and $\hat{\Gamma}_{in,p}(f)$ is the input reflection coefficient seen at the input port of the OCSS matching network connected to the p'th probe.

The impedance bandwidths and resonance frequencies obtained with the MAS model are listed in Table 1 for all the designs. The impedance results for Design 1, 3, and 5 are shown in Figure 6 and compared with the corresponding CST-MS results. The deviations between the resonance frequencies and impedance values obtained by the two solutions are still approximately 2% higher and 20% lower, respectively for the MAS solutions. The impact of increasing w and decreasing ϵ_r on the bandwidth is clearly seen and thus the obtained impedance bandwidths range from 2.7% to 14.7% around 1.5GHz. It is also seen that the impedances become smaller as the permittivity is decreased. For Design 1 and 5 examples of radiation patterns for 3 frequencies
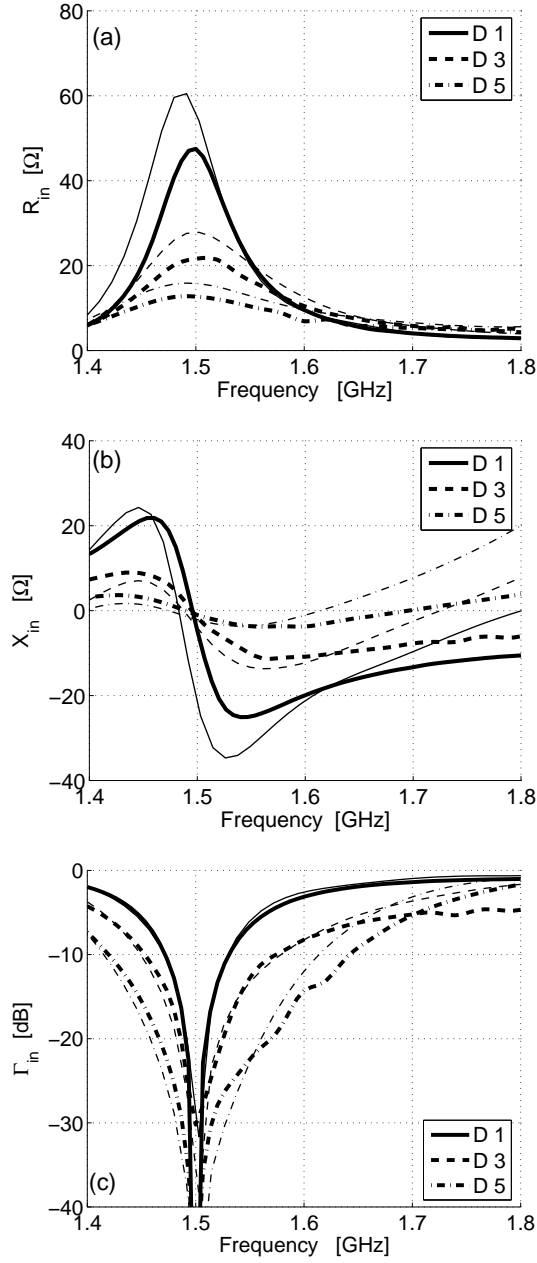
Figure 6: Impedance results for probe 1 of Design 1, 3, and 5 for the MAS (thick lines) and CST-MS (thin lines) solutions. (a) Input resistance, $R_{in,1}$. (b) Input reactance, $X_{in,1}$. (c) Reflection coefficient, $\hat{\Gamma}^E_{in}(f)$ after matching with the OCSS matching network designed with $f_0 = 1.5$ GHz.

Figure 7: Directivity for DRA elements calculated with the MAS model. Both DRAs are matched for $f_0 = 1.5GHz$. (a) Design 1, MAS. (b) Design 5.

4 Analysis of DRA Arrays

In this section the MAS model is applied to a 7-element phased array where the identical elements are positioned in a hexagonal lattice and are separated by the distance d as shown in Figure 8. The hexagonal lattice is advantageous compared to the rectangular lattice for phased array applications since wider element separations can be used before the scan angle dependent effects of grating lobes and impedance mismatch become too severe [13]. Also the hexagonal lattice improves the rotational symmetry of the radiation pattern compared to the rectangular one.

However, before applying the MAS model to the entire 7-element array the MAS and CST-MS results are compared for a simple 2-element configuration. In this way the MAS model can be validated for the case where more than one element is present. With reference to Figure 8 the investigated 2-element configuration corresponds to the case where only elements 1 and 2 are present. The elements are displaced by $d = 9$cm. In Figure 9a-b the mutual impedances of port 1 (i.e., $p = 1$) in element 1 and ports 1, 2, and 3 in element 2 are shown as function of frequency. In Figure 9c the directivity resulting from an excitation of port 1 of element 2 is shown. Again it is seen that the radiation results

are shown in Figure 7. It is seen that the radiation patterns are quite similar. This illustrates the fact that the shape of the DRA does not influence the radiation very much since it is the same fundamental broadside mode that is excited. It should be noted that the high level of cross polarisation near the horizon is a consequence of the infinite ground plane used in the model and would not appear to the same extent for a finite ground plane.
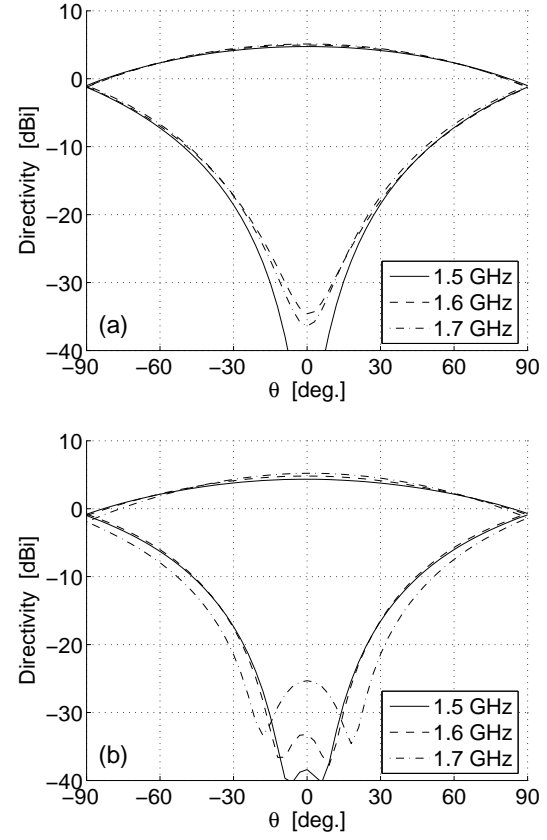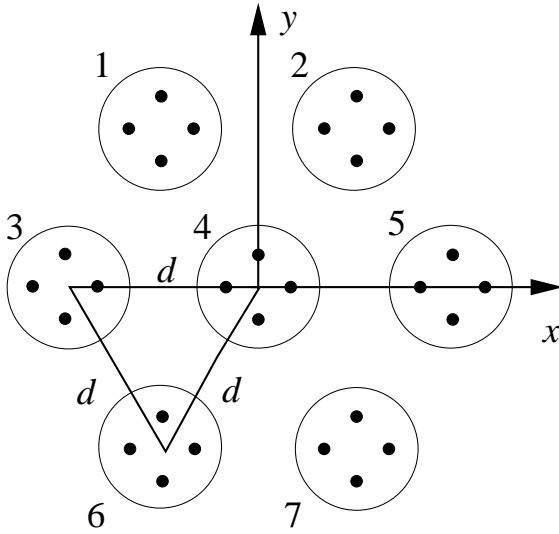
Figure 8: Top view of the DRA array with element numbering.

are accurately recovered by the MAS model. However, due to the approximate probe model, the mutual impedances are somewhat lower than predicted by CST-MS.

To further validate the method reference results from [23] of the mutual coupling between two single-probe hemispherical DRA elements is reproduced. The DRA elements have the parameters $w = 2h = 50.8$mm, $\epsilon_r = 9.5$, $l = 6.5$mm, $\rho_p = 6.4$mm, and $\rho_0 = 0.5$mm. The measurements were performed at a frequency of 3.84GHz. In Figure 10 the MAS results are compared with the measured reference results. It is seen that the agreement is very good with only minor deviations in the E-plane for a separation of about one wavelength.

Having validated the MAS model the analysis of the phased array is now resumed. The elements of the array are matched with OCSS matching networks, designed for $f_0 = 1.6$GHz. The choice of which reflection coefficient to match is, however, less obvious for several reasons. Firstly, the presence of neighbouring elements have direct impact on the self and mutual impedances of the probe ports. Secondly, the coupling between the elements cause scan-dependent variation in the input impedances and, lastly, the frequency dependence of the impedances should be considered.

In order to ensure that the employed matching network does not favour a specific scan direction it has been chosen not to include the element-to-element coupling when designing the matching network. Therefore R mean reflection coefficients $\Gamma_{in,r}^{\mathrm{E}}$ are calculated, one for each of the unmatched DRA elements, in the same way as in (19). These reflection coefficients vary somewhat from element to element and therefore an average between the elements is used. Furthermore, the frequency variation is taken into account by averaging the $\Gamma_{in,r}^{\mathrm{E}}$ over frequency. The OCSS matching networks for the array are thus designed to match the
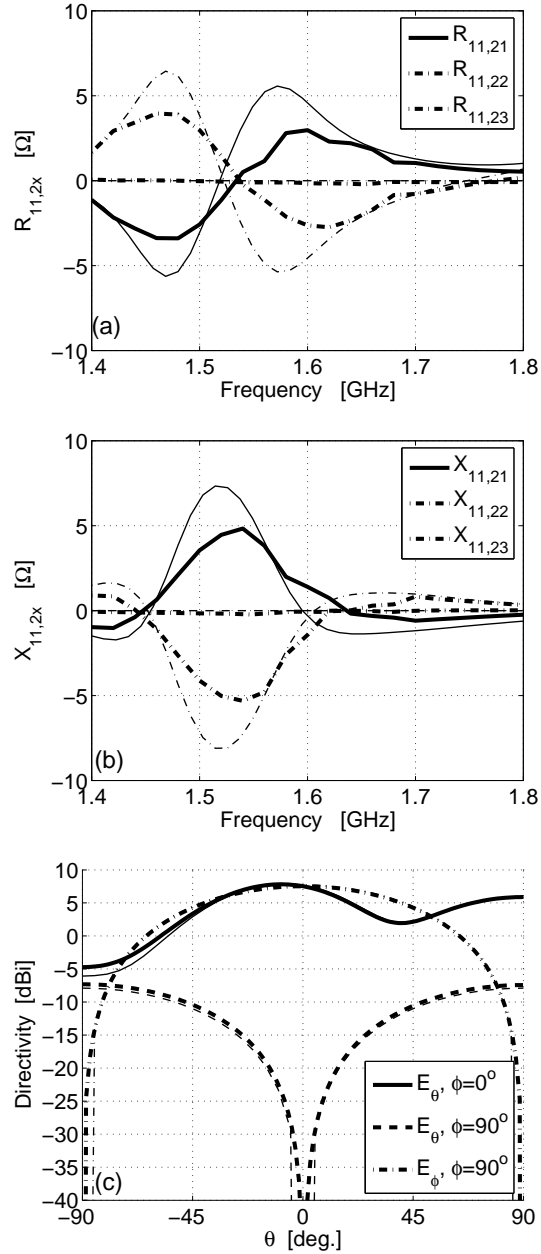

Figure 9: Results for 2-element configuration calculated by MAS (thick lines) and CST-MS (thin lines). The double indices refer to element number and probe number as indicated in figures 1 and 8. (a) Mutual resistance. (b) Mutual reactance. (c) Radiation pattern when port 1 of element 1 is excited.

reflection coefficient

$$\Gamma_{in}^{\mathrm{A}} = \frac{1}{f_2 - f_1} \frac{1}{R} \int_{f=f_1}^{f_2} \sum_{r=1}^{R} \Gamma_{in,r}^{\mathrm{E}}(f)df, \qquad (22)$$

where $f_1 = 1.52$GHz and $f_2 = 1.66$GHz. In a manner similar to the single element case, the reflection coefficients $\hat{\Gamma}_{in,p}(\theta_0, \phi_0, f)$ seen at the input port of the OCSS matching networks are calculated.

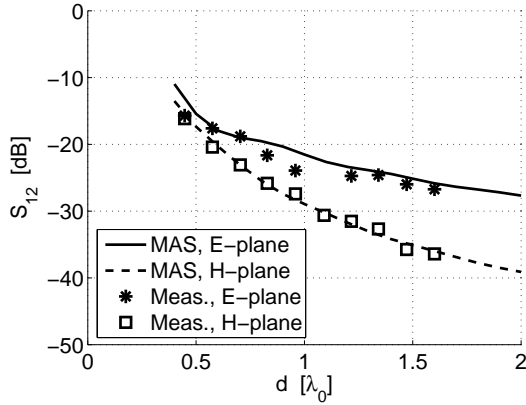The definition of the scan loss used in this work only in-

Figure 10: Mutual coupling in the E and H plane between two single-probe hemispherical DRA elements, as function of element separation d in free-space wavelengths, λ_0. The calculated MAS results are compared with measurements from [23].

cludes the effects of impedance mismatch and although the main beam directivity also varies with scan angle this is not included in the scan loss but treated separately. The scan loss is thus defined as

$$SL(\theta_0, \phi_0, f) = \frac{1}{1 - |\hat{\Gamma}_{in}^{A}(\theta_0, \phi_0, f)|^2}, \qquad (23)$$

where $|\hat{\Gamma}_{in}^{A}(\theta_0, \phi_0, f)|^2$ is defined similar to (21), with P being replaced with RP. Examples of the calculated scan loss is shown in Figure 11 for a DRA array with Design 1 and 3 elements. The element separation is $d = 9$cm in both cases, which equals $0.48\lambda_0$ at $f = 1.6$GHz. The shown results are the worst case for all azimuthal scan angles ϕ_0 as function of θ_0 and frequency. The impact of the element bandwidth is evident since the broadband Design 3 has low scan loss for a larger frequency interval than the narrow-band Design 1. Also the impact of scanning the beam towards large θ_0 angles is clear and the scan loss generally increases with θ_0. For $f = 1.6$GHz the increase is from about 0.25dB for $\theta_0 \leq 25°$ to about 1dB for $\theta_0 \simeq 75°$ for the two cases.

In Figure 12 the variation of the scan loss and main beam directivity with scan angle is shown for Design 1 and 3, the former with two different values of the element separation, $d = 7$cm ($0.37\lambda_0$ at $f = 1.6$GHz) and $d = 9$cm. The general tendency of increasing scan loss for increasing θ_0 is seen in all cases but the impact of the element separation is particularly noteworthy. For Design 1, with closely spaced elements, a relatively low scan loss is obtained for the two extreme frequencies 1.5GHz and 1.7GHz, whereas significantly higher scan loss results for the larger separation. With respect to the main beam directivity, it is seen that it is more uniform with respect to scan angle for the small separation than for large. This illustrates the positive impact on both scan loss and directivity due to closely positioned elements. In the case of Design 3 the element width, $w = 7$cm, precludes such close element separation and $d = 9$cm is used. With respect to the main beam directivity, however, the large variation with θ_0 persists and even deteriorates.
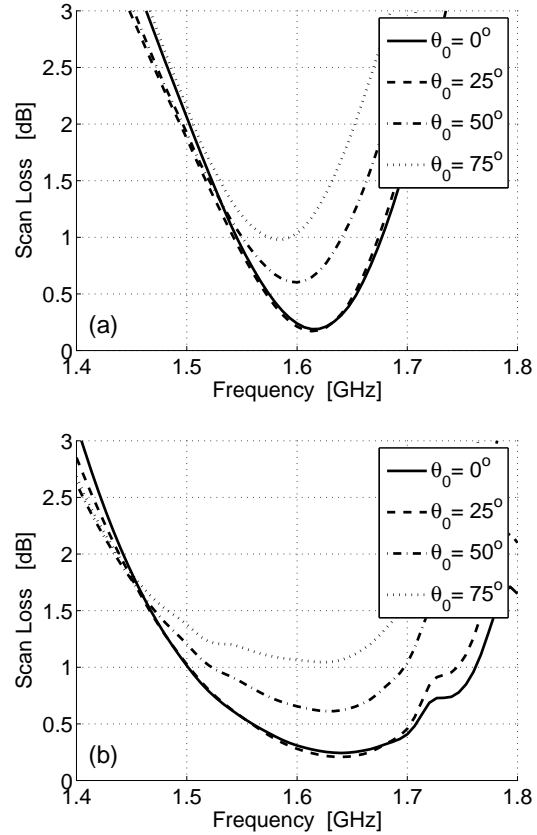

Figure 11: Resulting scan loss of the hemispheroidal DRA array when matched with the OCSS matching network. (a) Design 1. (b) Design 3.

5 Conclusion

The Method of Auxiliary Sources (MAS) has been applied for the modelling and analysis of circularly polarised probe-fed hemispheroidal dielectric resonator antenna (DRA) elements and phased arrays. The MAS solutions were compared with the simulation tool CST Microwave Studio (CST-MS), measured reference results, and in the case of a hemispherical DRA also with a spherical wave expansion (SWE) solution. The agreement is excellent as far as the radiation results are concerned, however, the MAS probe model implies a slight deviation of about 2% in the obtained resonance frequencies and the resistances at resonance are about 20% smaller for MAS than the CST-MS results. For the SWE solution, where the same probe model is used, the impedance results agree excellently. This demonstrates that MAS can be used to effectively analyse even complicated antennas with high accuracy.

Investigations were carried out for different element designs where the DRA height was kept at 2cm and the element width and permittivity were varied to maintain a resonance frequency somewhat below 1.6GHz. The resulting impedance bandwidths ranged between 2.7% for the hemispherical case to 14.7% for a 9cm wide DRA.

Two designs were subsequently selected for use in a 7-

element hexagonal phased array. The impact of the element impedance bandwidths and separation on the resulting scan loss and main beam directivity were investigated as function of frequency and scan angles. As expected the wide DRA elements yielded the lowest scan loss due to their inherently large bandwidth. It was, however, demonstrated that lowering the element separation, which is possible for the small elements, has a positive impact on the array bandwidth and serves to lower the scan loss. Furthermore, the main beam directivity was more uniform with respect to scan angle for the smaller element separation.

The present analysis has been carried out assuming an infinite ground plane beneath the DRA. This limitation may, however, be overcome by including a finite ground plane in the MAS model as proposed in [27].

A   Analytical Results for Hemispherical DRA

The hemispherical DRA on an infinite ground plane can be modelled as a dielectric sphere in free space with all current sources being augmented by appropriate image sources below the ground plane. For this dielectric sphere the dyadic Green's function $\vec{\vec{G}}^E(\mathbf{r}, \mathbf{r}')$ for the electric field has been derived and can be expressed as an SWE. The electric field everywhere then follows from

$$\mathbf{E}(\mathbf{r}) = \int_V \vec{\vec{G}}^E(\mathbf{r}, \mathbf{r}') \cdot \mathbf{J}(\mathbf{r}') dV', \qquad (24)$$

where $\mathbf{J}(\mathbf{r}')$ is the current source inside the DRA including the image source. The dyadic Green's function can be expressed as

$$\vec{\vec{G}}^E(\mathbf{r}, \mathbf{r}') = k_1^2 Z_1 \sum_{s=1}^{2} \sum_{n=1}^{\infty} \sum_{m=-n}^{n} \vec{g}_{smn}^E(\mathbf{r}, \mathbf{r}'), \qquad (25)$$

where

$$\vec{g}_{smn}^E = (-1)^m \left[\mathbf{F}_{s,-m,n}^{(4)}(k_1, \mathbf{r}') + A_{sn} \mathbf{F}_{s,-m,n}^{(1)}(k_1, \mathbf{r}') \right]$$
$$\mathbf{F}_{smn}^{(1)}(k_0, \mathbf{r}), \quad r < r', \qquad (26a)$$

$$\vec{g}_{smn}^E = (-1)^m \mathbf{F}_{s,-m,n}^{(1)}(k_1, \mathbf{r}') \left[A_{sn} \mathbf{F}_{smn}^{(1)}(k_1, \mathbf{r}) + \mathbf{F}_{smn}^{(4)}(k_1, \mathbf{r}) \right], \quad a > r > r', \qquad (26b)$$

$$\vec{g}_{smn}^E = (-1)^m B_{sn} \mathbf{F}_{s,-m,n}^{(1)}(k_1, \mathbf{r}') \mathbf{F}_{smn}^{(4)}(k_0, \mathbf{r}), \quad r > a. \qquad (26c)$$

The $\mathbf{F}_{smn}^{(1,4)}$ are spherical vector wave functions, a is the radius of the dielectric sphere, and

$$A_{sn} = -\frac{1}{\Delta_{sn}} \left[R_{sn}^{(4)}(k_1 a) R_{3-s,n}^{(4)}(k_0 a) \right.$$
$$\left. - \frac{k_1 \mu_0}{k_0 \mu_1} R_{3-s,n}^{(4)}(k_1 a) R_{sn}^{(4)}(k_0 a) \right], \qquad (27a)$$

$$B_{sn} = \frac{j(-1)^{s+1}}{\Delta_{sn}}, \qquad (27b)$$

$$\Delta_{sn} = R_{sn}^{(1)}(k_1 a) R_{3-s,n}^{(4)}(k_0 a)$$
$$- \frac{k_1 \mu_0}{k_0 \mu_1} R_{3-s,n}^{(1)}(k_1 a) R_{sn}^{(4)}(k_0 a). \qquad (27c)$$

The functions $\mathbf{F}_{smn}^{(1,4)}$ and $R_{sn}^{(1,4)}$ used in (26a-c) and (27a-c) are all defined in [28]. In the case where EHD are used to model the probe currents the integral in (24) simplifies to a summation.

B   Auxiliary Source Fields at Test Points

Presently, only the AS on A are considered. The same principle applies for the AS on D. The unit vectors of the local coordinate systems of the n'th AS on A and the m'th TP are denoted by $(\hat{\mathbf{a}}_n^x, \hat{\mathbf{a}}_n^y, \hat{\mathbf{a}}_n^z)$ and $(\hat{\mathbf{b}}_n^x, \hat{\mathbf{b}}_n^y, \hat{\mathbf{b}}_n^z)$, respectively. Thus the two orthogonal Hertzian dipoles of the n'th AS coincide with $\hat{\mathbf{a}}_n^x$ for $t = 1$ in (5), and $\hat{\mathbf{a}}_n^y$ for $t = 2$, and $\hat{\mathbf{b}}_n^z$ coincides with $\hat{\mathbf{n}}(\mathbf{b}_m)$. In order to express the field from the n'th AS in terms of the coordinate system of the m'th TP, a rotated version of the n'th AS coordinate system is introduced. It is rotated through the Euler angles $(\chi_0, \theta_0, \phi_0)$ [28], such that its rectangular unit vectors, denoted by $(\hat{\mathbf{v}}_{nm}^x, \hat{\mathbf{v}}_{nm}^y, \hat{\mathbf{v}}_{nm}^z)$, are parallel to $(\hat{\mathbf{b}}_n^x, \hat{\mathbf{b}}_n^y, \hat{\mathbf{b}}_n^z)$. The corresponding spherical unit vectors are denoted by $(\hat{\mathbf{v}}_{nm}^r, \hat{\mathbf{v}}_{nm}^\theta, \hat{\mathbf{v}}_{nm}^\phi)$ and the position of the m'th TP, described in this coordinate system, is denoted by $\mathbf{v}_{nm}$ with the rectangular- and spherical coordinates $(x_{nm}^v, y_{nm}^v, z_{nm}^v; r_{nm}^v, \theta_{nm}^v, \phi_{nm}^v)$. Expressed in this coordinate system the electric field from, e.g., the t'th Hertzian dipole of the n'th AS on the interior auxiliary surface, A, evaluated at the m'th TP, $\mathbf{b}_m$, on B is

$$\begin{bmatrix} \hat{\mathbf{b}}_m^x \cdot \mathbf{E}_{nt}^A(\mathbf{b}_m) \\ \hat{\mathbf{b}}_m^y \cdot \mathbf{E}_{nt}^A(\mathbf{b}_m) \\ \hat{\mathbf{b}}_m^z \cdot \mathbf{E}_{nt}^A(\mathbf{b}_m) \end{bmatrix}$$
$$= \vec{\vec{T}}(\theta_{nm}^v, \phi_{nm}^v) \begin{bmatrix} \hat{\mathbf{v}}_{nm}^r \cdot \mathbf{E}_{nt}^A(\mathbf{v}_{nm}) \\ \hat{\mathbf{v}}_{nm}^\theta \cdot \mathbf{E}_{nt}^A(\mathbf{v}_{nm}) \\ \hat{\mathbf{v}}_{nm}^\phi \cdot \mathbf{E}_{nt}^A(\mathbf{v}_{nm}) \end{bmatrix}, \quad (28)$$

and similarly for the magnetic field. Here

$$\vec{\vec{T}}(\theta, \phi) = \begin{bmatrix} \sin\theta\cos\phi & \cos\theta\cos\phi & -\sin\phi \\ \sin\theta\sin\phi & \cos\theta\sin\phi & \cos\phi \\ \cos\theta & -\sin\theta & 0 \end{bmatrix}, \quad (29)$$

converts from spherical to rectangular coordinates. In the case where the AS are chosen as EHD the direct electric and
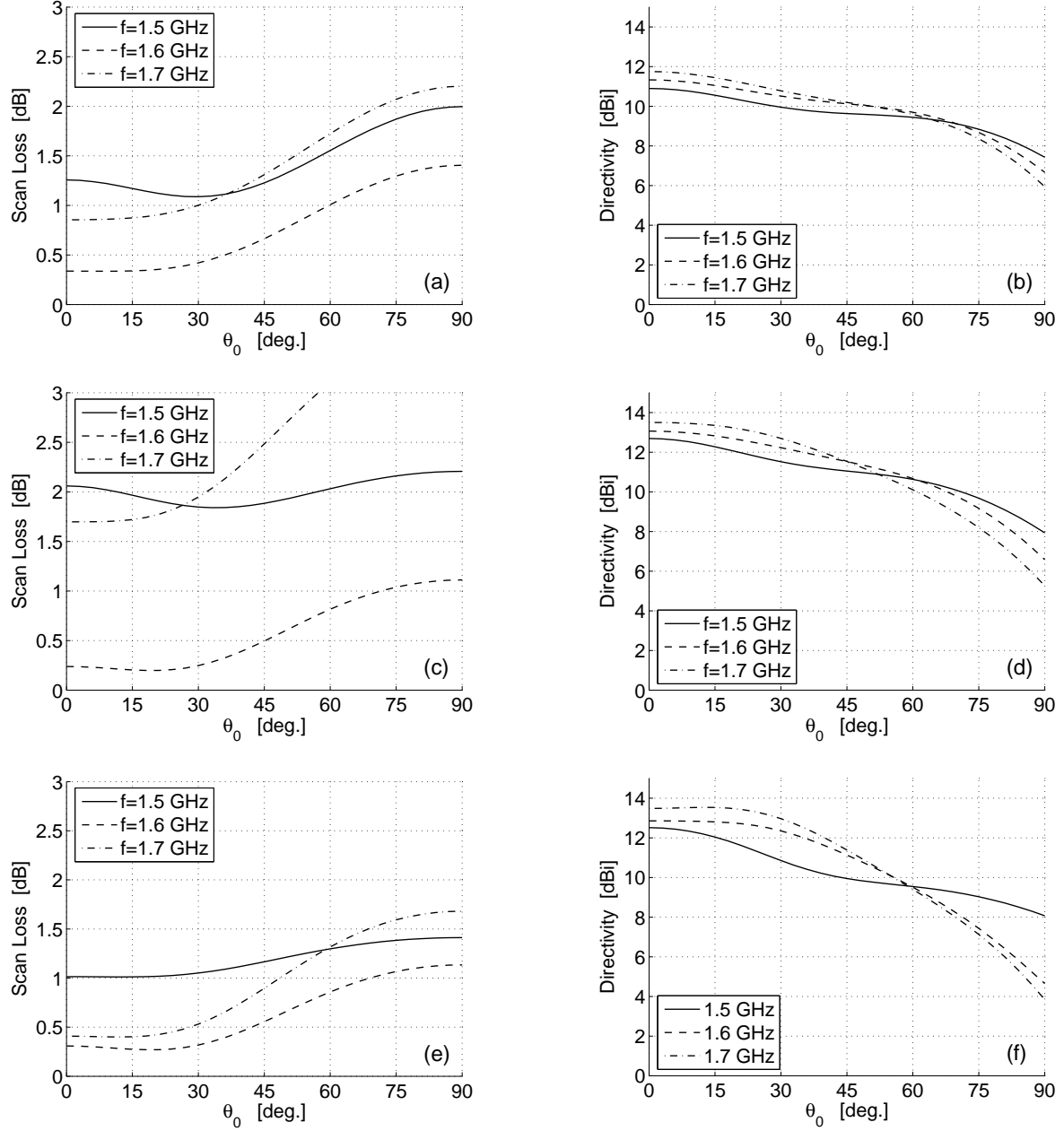
Figure 12: Resulting scan loss and main beam co-polar directivity of the hemispheroidal DRA array for Design 1 and 3. (a)-(b) Design 1 with $d = 7cm$. (c)-(d) Design 1 with $d = 9cm$. (e)-(f) Design 3 with $d = 9cm$.

magnetic fields are given by

$$\mathbf{E}_{nt}^{A,\text{direct}}(\mathbf{v}_{nm}) = E_0 \frac{e^{-jk_0 r_{nm}^v}}{k_0 r_{nm}^v}\cdot$$

$$\left[\frac{2}{k_0 r_{nm}^v}\left[1 - \frac{j}{k_0 r_{nm}^v}\right]\hat{\mathbf{v}}_{nm}^r \left[f_1 \sin\theta_{nm}^v + f_3 \cos\theta_{nm}^v\right] - \right.$$

$$\left[j + \frac{1}{k_0 r_{nm}^v} - \frac{j}{(k_0 r_{nm}^v)^2}\right]\cdot$$

$$\left.\left[\hat{\mathbf{v}}_{nm}^\theta \left(\cos\theta_{nm}^v f_1 - f_3\sin\theta_{nm}^v\right) - f_2\hat{\mathbf{v}}_{nm}^\phi\right]\right], \tag{30a}$$

$$\mathbf{H}_{nt}^{A,\text{direct}}(\mathbf{v}_{nm}) = j\frac{E_0}{Z_0}\frac{e^{-jk_0 r_{nm}^v}}{k_0 r_{nm}^v}\left[1 - \frac{j}{k_0 r_{nm}^v}\right]\cdot$$

$$\left[\hat{\mathbf{v}}_{nm}^\phi \left[f_3\sin\theta_{nm}^v - f_1\cos\theta_{nm}^v\right] - \hat{\mathbf{v}}_{nm}^\theta f_2\right], \tag{30b}$$

where $E_0 = 1\frac{\text{V}}{\text{m}}$. For $t = 1$,

$$f_1 = \cos\theta_0\cos\phi_0\cos(\chi_0 + \phi_{nm}^v) - \\ \sin\phi_0\sin(\chi_0 + \phi_{nm}^v), \tag{30c}$$

$$f_2 = \sin\phi_0\cos(\chi_0 + \phi_{nm}^v) + \\ \cos\theta_0\cos\phi_0\sin(\chi_0 + \phi_{nm}^v), \tag{30d}$$

$$f_3 = \sin\theta_0\cos\phi_0. \tag{30e}$$

and for $t = 2$, ϕ_0 should be replaced with $\phi_0 - \frac{\pi}{2}$ in (30c-e). The coordinates of $\mathbf{v}_{nm}$ are given by

$$x_{nm}^v = \hat{\mathbf{b}}_m^x \cdot (\mathbf{b}_m - \mathbf{a}_n), \tag{31a}$$

$$y_{nm}^v = \hat{\mathbf{b}}_m^y \cdot (\mathbf{b}_m - \mathbf{a}_n), \tag{31b}$$

$$z_{nm}^v = \hat{\mathbf{b}}_m^z \cdot (\mathbf{b}_m - \mathbf{a}_n). \tag{31c}$$

In the case where MHD are used as AS the corresponding fields can be found by application of the duality principle. The direct field from (30a-b) should be augmented by the field from the image source beneath the infinite ground plane. This image source field can be calculated in the same way as the direct field by using the image position

$$\mathbf{a}_n^{\mathbf{i}} = \mathbf{a}_n - 2\hat{\mathbf{z}}(\hat{\mathbf{z}}\cdot\mathbf{a}_n), \tag{32a}$$

where $\hat{\mathbf{z}}$ is perpendicular to the infinite ground plane, and local unit vectors

$$(\hat{\mathbf{a}}_n^{\mathbf{i}x}, \hat{\mathbf{a}}_n^{\mathbf{i}y}, \hat{\mathbf{a}}_n^{\mathbf{i}z}) = \alpha(-\hat{\mathbf{a}}_n^x, -\hat{\mathbf{a}}_n^y, \hat{\mathbf{a}}_n^z), \tag{32b}$$

where $\alpha = 1$ and $\alpha = -1$ should be chosen for the EHD and MHD AS, respectively, in order to be in accordance with the "+" of (6). For the AS on the exterior auxiliary surface, D, the k_0 and Z_0 in (30a-b) should be replaced by k_1 and Z_1.

Bibliography

[1] K. W. Leung, *et al.*, "Theory and Experiment of a Coaxial Probe Fed Hemispherical Dielectric Resonator Antenna," *IEEE Trans. Antennas Propag.*, vol. 41, no. 10, pp. 1390–1398, 1993.

[2] Z. N. Chen, *et al.*, "Electromagnetic Scattering from the Probe-Fed Dielectric Resonator Antenna," *IEEE Antennas Propag. Soc. Int. Symp. Dig.*, vol. 2, pp. 1410–1413, 1996.

[3] S. A. Long, M. W. McAllister, and L. C. Shen, "The Resonant Cylindrical Dielectric Cavity Antenna," *IEEE Trans. Antennas Propag.*, vol. 31, no. 3, pp. 406–412, 1983.

[4] M. Cooper, *et al.*, "Investigation of Dielectric Resonator Antennas for L-Band Communications," *Symposium on Antenna Technology and Applied Electromagnetics*, pp. 167–170, 1996.

[5] A. Ittipiboon, *et al.*, "An Investigation of a Novel Broadband Dielectric Resonator Antenna," *IEEE Antennas Propag. Soc. Int. Symp. Dig.*, vol. 3, pp. 2038–2041, 1996.

[6] K.-L. Wong, N.-C. Chen, and H.-T. Chen, "Analysis of an Hemispherical Dielectric Resonator Antenna with an Air Gap," *IEEE Microwave and Guided Wave Letters*, vol. 3, no. 9, pp. 355–357, 1993.

[7] A. A. Kishk, R. Chair, and K. F. Lee, "Broadband Dielectric Resonator Antennas Excited by L-Shaped Probe," *IEEE Trans. Antennas Propag.*, vol. 54, no. 8, pp. 2182–2189, 2006.

[8] A. A. Kishk, *et al.*, "Numerical Analysis of Stacked Dielectric Resonator Antennas Excited by a Coaxial Probe for Wideband Applications," *IEEE Trans. Antennas Propag.*, vol. 51, no. 8, pp. 1996–2006, 2003.

[9] A. A. Kishk, A. W. Glisson, and G. P. Junker, "Bandwidth Enhancement for Split Cylindrial Dielectric Resonator Antennas," vol. 33, pp. 97–118, 2001.

[10] K. W. Leung and H. K. Ng, "Theory and Experiment of Circularly Polarized Dielectric Resonator Antenna With a Parasitic Patch," *IEEE Trans. Antennas Propag.*, vol. 51, no. 3, pp. 405–411, 2003.

[11] M. B. Oliver, *et al.*, "Circularly Polarised Rectangular Dielectric Resonator Antenna," *IEE Electron. Lett.*, vol. 31, no. 6, pp. 418–419, 1995.

[12] G. Drossos, Z. Wu, and L. E. Davis, "Circular Polarised Cylindrical Dielectric Resonator Antenna," *IEE Electron. Lett.*, vol. 32, no. 4, pp. 281–283, 1996.

[13] R. J. Mailloux, *Phased Array Antenna Handbook*. Artech House, Boston, 1994.

[14] A. A. Kishk, "Dielectric Resonator Antenna Elements for Array Applications," *IEEE Int. Symp. Phased Array Systems and Technology*, pp. 300–305, 2003.

[15] A. Petosa, *et al.*, "Low Profile Phased Array of Dielectric Resonator Antennas," *IEEE Int. Symp. Phased Array Systems and Technology*, pp. 182–185, 1996.

[16] A. Petosa, A. Ittipiboon, and M. Cuhaci, "Array of Circularly Polarised Cross Dielectric Resonator Antennas," *IEE Electron. Lett.*, vol. 32, no. 19, pp. 1742–1743, 1996.

[17] S. P. Skobelev, "Algorithm of the Method of Auxiliary

Sources for Analysis of Arrays of Circular Waveguides with Protruding Dielectric Rods," *IEEE Int. Symp. Phased Array Systems and Technology*, pp. 333–338, 2003.

[18] D. I. Kaklamani and H. T. Anastassiu, "Aspects of the Method of Auxiliary Sources in Computational Electromagnetics," *IEEE Antennas Propag. Mag.*, vol. 44, no. 3, pp. 48–64, 2002.

[19] S. Eisler and Y. Leviatan, "Analysis of Electromagnetic Scattering From Metallic and Penetrable Cylinders with Edges Using Multifilament Current Model," *IEE Proc., Pt. H*, vol. 136, no. 6, pp. 431–438, 1989.

[20] N. V. Larsen and O. Breinbjerg, "A Hybrid MAS/MoM Technique for 2D Impedance Scatterers Illuminated by Closely Positioned Sources," *Microwave Opt. Technol. Lett.*, vol. 44, no. 2, pp. 112–114, 2005.

[21] P. J. Papakanellos and C. N. Capsalis, "Numerical Analysis of Cylindrical Dipole Antennas Using an Auxiliary Sources Model," *J. Electromagn. Waves Appl.*, vol. 17, no. 3, pp. 389–407, 2003.

[22] CST - Computer Simulation Technology. (2007, January) CST Microwave Studio. [Online]. Available: http://www.cst.com/Content/Products/Products.aspx

[23] K. M. Luk, W. K. Leung, and K. W. Leung, "Mutual Impedance of Hemispherical Dielectric Resonator Antenna," *IEEE Trans. Antennas Propag.*, vol. 42, no. 12, pp. 1652–1654, 1994.

[24] R. F. Harrington, *Time-Harmonic Electromagnetic Fields*. John Wiley & Sons Inc., New York, 2001.

[25] D. M. Pozar, *Microwave Engineering*, 2nd ed. John Wiley & Sons, Inc., 1998.

[26] J. A. Dobrowolski, *Introduction To Computer Methods For Microwave Circuit Analysis And Design*, 2nd ed. John Wiley & Sons, Inc., New York, 1998.

[27] N. V. Larsen and O. Breinbjerg, "Modelling the Impact of Ground Planes on Antenna Radiation Using the Method of Auxiliary Sources," *IET Microw. Antennas Propag.*, vol. 1, no. 2, pp. 472–479, 2007.

[28] J. E. Hansen, *Spherical Near-Field Antenna Measurements*. Peter Peregrinus Ltd., London, 1998.

PAPER 4

Two-Stage MAS Technique for Analysis of DRA Elements and Arrays on Finite Ground Planes

Niels Vesterdal Larsen and Olav Breinbjerg

Bibliographical details

[J4] N.V. Larsen and O. Breinbjerg, "A Two-Stage MAS Technique for Analysing DRA Elements and Arrays on Finite Ground Planes", accepted for publication in *Electronic Letters*[†], May, 2007.

[†][J4] later appeared in *Electronic Letters*, Vol. 43, No. 12, 2007, pp. 657-659.

TWO-STAGE MAS TECHNIQUE FOR ANALYSIS OF DRA ELEMENTS AND ARRAYS ON FINITE GROUND PLANES

Niels Vesterdal Larsen and Olav Breinbjerg

Abstract: A two-stage Method of Auxiliary Sources (MAS) technique is proposed for analysis of dielectric resonator antenna (DRA) elements and arrays on finite ground planes (FGPs). The problem is solved by first analysing the DRA on an infinite ground plane (IGP) and then using this solution to model the FGP problem.

1 Introduction

The impact of an FGP on antenna radiation is an important issue when assessing antenna performance. The MAS has previously been employed to this end [1] for large and moderate-sized FGPs in cases where the antenna characteristics are available, e.g., currents on wire antennas or fields in the apertures of slot antennas. Such characteristics can be obtained from an antenna analysis with the large or moderate-sized FGP being replaced by a small FGP or the IGP. These simplified configurations can typically be modelled without the excessive computational cost that would occur for large-FGP configurations. In [1] a cavity-backed slot antenna and a dipole phased array positioned on a small FGP and the IGP, respectively, were thus readily modelled using commercially available software and subsequently the results were used to take the FGP into account.

The wide-beam pattern of the DRA is also greatly impacted by an FGP [2], however, the DRA is not easily characterised in terms of wire currents or aperture fields. The MAS has previously been employed for hemispheroidal DRA elements and small arrays [3], as well as for infinite arrays of general smooth DRAs [4]. These investigations have relied on assuming an IGP which can be taken into account simply using image sources. In the present work a two-stage MAS technique is proposed for the analysis of hemispheroidal DRA elements and small arrays positioned on large or moderate-sized FGPs. With this technique the total problem is split into two stages, where firstly, the DRA is investigated in detail for the IGP case and, secondly, the influence of the FGP is addressed.

2 The Two-Stage MAS Technique

The two-stage MAS technique is based on a first-stage analysis of the DRA element or array positioned on an IGP, as detailed in [3], and a second-stage analysis of the impact of the FGP as detailed in [1]. The two MAS models of the FGP and the DRA, respectively, have previously been validated and compared with measurements and reference simulation tools [1, 3], and presently they are combined. The DRA elements shown in Figure 1a-b are probe-fed and have height h, width w, and relative permittivity and permeabil-
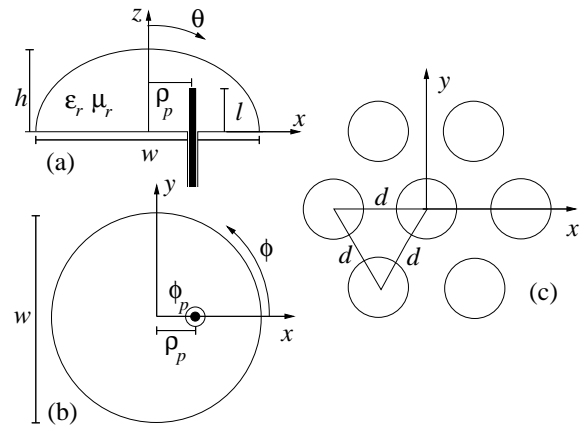

Figure 1: Probe-fed hemispheroidal DRA and array. (a) Cross section of single-probe DRA. (b) Top view of single-probe DRA. (c) Top view of 7-element hexagonal DRA array.

ity ϵ_r and μ_r, respectively. The probe height is denoted by l, and its intersection with the (x, y)-plane by the cylindrical coordinates ρ_p and ϕ_p. The probe current is assumed to be sinusoidal and the FGP to be perfectly electrically conducting (PEC). The DRA surface above the FGP is denoted by B and the surface of the FGP by C.

The MAS model of the first-stage analysis is shown in Figure 2a. The probe current is modelled as an assembly of discrete incidence sources (ISs) which radiate the incident field inside the DRA. The ISs are Hertzian dipoles with excitations equalling samples of the assumed sinusoidal probe current. The total field, being the sum of incident and scattered fields, must obey the boundary conditions at B, i.e., continuous tangential electric and magnetic fields across B, as well as vanishing tangential electric field on the surface of the IGP. To this end the scattered fields outside and inside the DRA are expanded in sums of contributions from N_{DRA} auxiliary sources (ASs) each consisting of 2 crossed Hertzian dipoles with independent excitations. The ASs are positioned on auxiliary surfaces conformal to B inside and outside B, respectively, separated by the distance d_{DRA}. The boundary condition at the IGP is taken into account by augmenting all ISs and ASs with image sources below the IGP. By enforcing the boundary condition in $M_{DRA} = N_{DRA}$ test points (TPs) on B a linear system of equations is formed from which the excitation coefficients of the ASs are found. The mathematical details of this first-stage model are given in [3].

The second stage takes outset in the assumption that the fields at the DRA surface B are not affected by replacing the IGP with the FGP, which is a reasonable assumption for large and moderate-sized FGP. In [1] the aperture field of a slot antenna is approximated by an equivalent magnetic line current on a ground plane. In a similar way the DRA can, with respect to the region exterior to it, be represented by equivalent electric or magnetic currents. The interior AS from the first-stage IGP model can be considered as discrete representations of these currents and hence they rep-
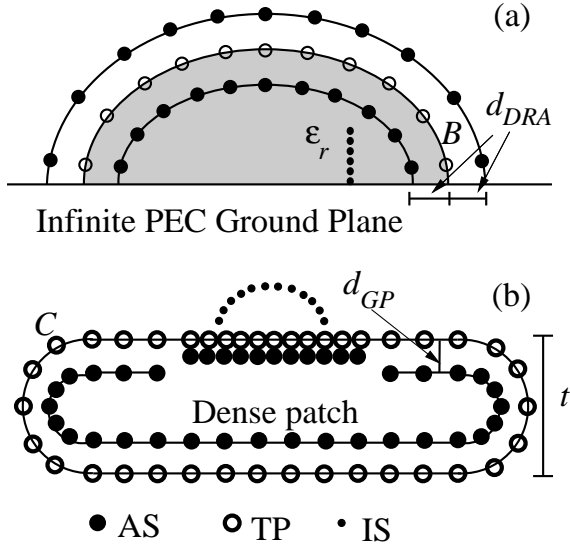
Figure 2: Cross sections of the MAS model of the probe-fed hemi-spheroidal DRA on an FGP. (a) First-stage model. (b) Second-stage model.

resent the DRA. Thus the AS excitation coefficients from the first-stage problem can be used to derive the incident field of the new second-stage problem. This problem consists of an impenetrable PEC FGP illuminated by the DRA, or more specifically, the ASs inside B from the first-stage problem. The corresponding MAS model is shown in Figure 2b. The FGP has a finite thickness t and rounded edges for the reasons explained in [1]. The scattered field of the second-stage problem is again expanded as contributions of N_{GP} ASs, however, since the FGP is impenetrable, ASs are only needed inside the FGP. They are thus positioned on an auxiliary surface inside C, separated by the distance d_{GP}. In the immediate vicinity of the ISs, which now represent the DRA, an extra dense patch of ASs and TPs is employed and here the distance to C is $d_{GP}/2$. $M_{GP} = N_{GP}$ TPs are positioned on C in which the boundary condition is enforced and a second linear equation system is formed. The mathematical details of the second-stage model are given in [1].

3 Example of a DRA Array

A circularly polarised DRA array is analysed. It consists of 7 elements arranged in a hexagonal lattice with element separations of $d = 0.37\lambda$, where λ is the free-space wavelength. The array is shown in Figure 1c and has previously been analysed in [3] for the IGP case. The elements are fed by 4 probes each, positioned at $\rho_p = 0.08\lambda$, $\phi_p = 0^\circ, 90^\circ, 180^\circ, 270^\circ$, and excited in phase quadrature. The further physical characteristics are: $w = 0.267\lambda$, $h = 0.107\lambda$, $l = 0.059\lambda$, and $\epsilon_r = 18$, $\mu_r = 1$. The MAS model of the array consists of $N_{DRA} = 446$ ASs per DRA element and $d_{DRA} = 0.03\lambda$. The array is positioned on a circular FGP with diameter of 5.33λ. The MAS model of the FGP has $t = 0.5\lambda$, $d_{GP} = 0.15\lambda$, and about $N_{GP} = 4000$ ASs
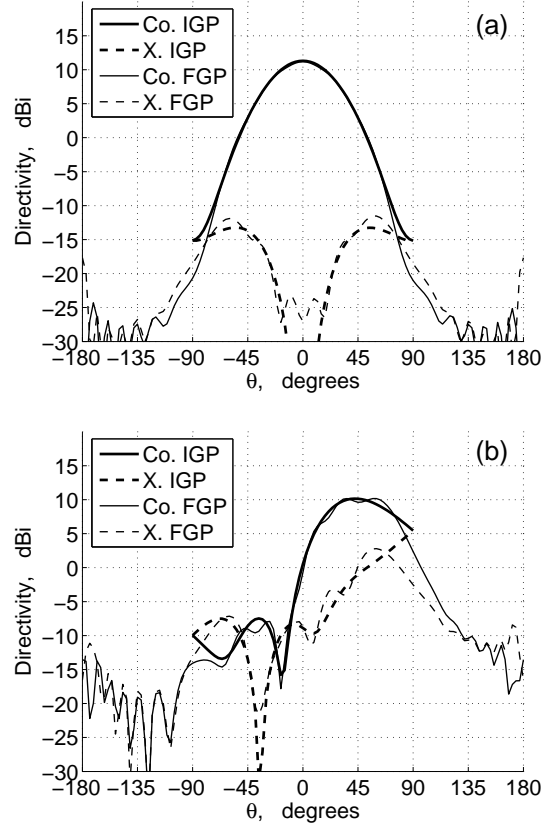

Figure 3: Co- and cross-polar (Co. and X.) radiation patterns of the 7-element DRA array for the IGP and FGP cases shown in the $\phi = 90^\circ$ plane. (a) Scanned to bore sight. (b) Scanned towards $\theta_0 = 60^\circ$, $\phi = 90^\circ$.

including a dense patch of ASs below the area occupied by the DRA array.

The obtained radiation patterns for the IGP and FGP cases are shown in Figure 3a-b for the two cases of bore-sight scanning and scanning at 60° off bore sight, respectively. With the FGP model, information of the back radiation is now available as opposed to the IGP case. In the bore-sight scanning case the cross-polar component is seen to be slightly larger for the FGP case and simultaneously the main beam is narrower. This can be explained by diffraction at the FGP edges which also causes ripples in the patterns, especially seen in the 60° scanning case.

In conclusion, a simple and computationally cheap MAS model has been established. It is based on two MAS models, which have previously been validated individually in [1, 3]. The combined method has been applied to the complex problem of a DRA array on a 5.33λ diameter FGP and the influence of the FGP has been demonstrated.

Bibliography

[1] N. V. Larsen and O. Breinbjerg, "Modelling the Impact of Ground Planes on Antenna Radiation Using the

Method of Auxiliary Sources," *IET Microw. Antennas Propag.*, vol. 1, no. 2, pp. 472–479, 2007.

[2] A. Petosa, *et al.*, "Recent Advances in Dielectric-Resonator Antenna," *IEEE Antennas Propag. Mag.*, vol. 40, no. 3, pp. 35–48, 1998.

[3] N. V. Larsen and O. Breinbjerg, "Analysis of Circularly Polarised Hemispheroidal Dielectric Resonator Antenna Phased Arrays using the Method of Auxiliary Sources," *Accepted for publication in IEEE Trans. Antennas Propag.*, 2007.

[4] S. P. Skobelev, "Algorithm of the Method of Auxiliary Sources for Analysis of Arrays of Circular Waveguides with Protruding Dielectric Rods," *IEEE Int. Symp. Phased Array Systems and Technology*, pp. 333–338, 2003.

PAPER 5

Single-Feed Circularly Polarised Hemi-Ellipsoidal Dielectric Resonator Antenna

Niels Vesterdal Larsen and Olav Breinbjerg

Bibliographical details

[J5] N.V. Larsen and O. Breinbjerg, "Single-Feed Circularly Polarised Hemi-Ellipsoidal Dielectric Resonator Antenna", May, 2007.

SINGLE-FEED CIRCULARLY POLARISED HEMI-ELLIPSOIDAL DIELECTRIC RESONATOR ANTENNA

Niels Vesterdal Larsen and Olav Breinbjerg

Abstract: A hemi-ellipsoidal dielectric resonator antenna (DRA) fed by a single probe is analysed. By exciting two orthogonal modes in phase quadrature circular polarisation is obtained. The obtained axial ratio (AR) and impedance bandwidths are 1.7% and 11.4%, respectively, at L-band around 1.6GHz.

1 Introduction

The DRA [1] has long been acknowledged as a low-loss and compact antenna which lends itself well to several feeding schemes. Single-feed circularly polarised DRAs can be realised in a number of ways, common to which is the excitation of orthogonal modes in the DRA. This can be accomplished by introducing various types of asymmetries in the antenna. The use of parasitic structures such as a metallic patch at the DRA surface [2] or uneven-lengths slots in the ground plane [3] allow circular polarisation for a circular symmetric DRA. Other shapes such as rectangular [4], elliptic cylindrical [5], or hemi-ellipsoidal [6] may yield circular polarisation when the feed is positioned asymmetrically with respect to the DRA. In [6] an investigation is given of a hemi-ellipsoidal DRA fed by a crossed aperture in the ground plane. In the present work a single probe is employed to obtain the circular polarisation. The DRA is modelled under the assumption that it is positioned on an infinite ground plane, and it is investigated using the Method of Auxiliary Sources (MAS) model presented in [7].

2 Antenna Model

The hemi-ellipsoidal DRA is depicted in Figure 1. The DRA shape is characterised by the 3 semi-axes a, b, and c, parallel to the x-, y-, and z-coordinate axes, respectively. The relative permittivity of the DRA is denoted ϵ_r and the relative permeability equals 1. The relationship between the semi-axes are defined by $a = c\sqrt{\rho}$, $b = c/\sqrt{\rho}$, where $\rho \in]0, 1]$ is the ratio between the two lateral semi-axes a and b. Thus $\rho = 1$ corresponds to the case of a hemispherical DRA. The DRA is fed by a single probe, with height l, positioned at a point along the diagonal of the enclosing rectangle as shown in Figure 1b. By positioning the probe along this diagonal, it is possible to excite two orthogonal broadside modes, however, in order to achieve circular polarisation these modes must ideally be $90°$ out of phase. The investigation of the optimum lateral dimensions takes outset in the hemispherical ($\rho = 1$) baseline configuration. The baseline configuration is linearly polarised since the two modes are equally strong and in-phase. By varying ρ this relationship changes and an optimum value of ρ can be found in
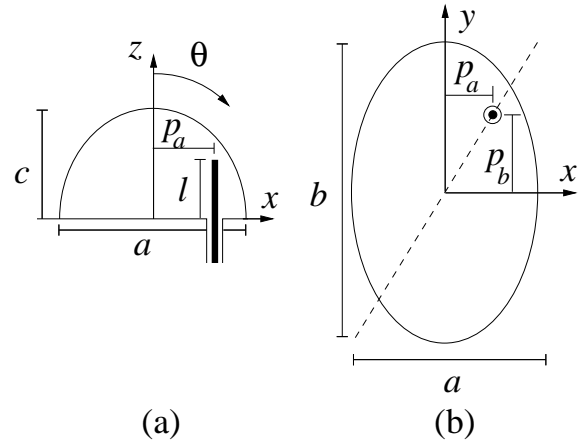

Figure 1: The probe-fed hemi-ellipsoidal DRA. (a) Cross section. (b) Top view.

which, as best as possible, the modes are equally strongly excited and $90°$ out of phase, yielding low bore-sight AR and thus circular polarisation. The configuration is analysed using a MAS model. This model is described in detail in [7] and will not be discussed further here.

3 Example and Results

The specific example shown herein is that of a DRA with $c = 20.0$mm and $\epsilon_r = 21$. This corresponds to the relative permittivity of Lithium Ferrite which is a well-known material used for DRA [1]. The probe height is $l = 10.2$mm and its position is given by $p_a = 0.65a/\sqrt{2}$, $p_b = 0.65b/\sqrt{2}$. For the baseline configuration the resonance frequency, defined as zero input reactance $X_{in} = 0$, has been found and is $f_{res} = 1.58$GHz. The input impedance $Z_{in} = R_{in} + jX_{in}$ and input reflection coefficient Γ_{in} of this configuration are shown with full lines in Figure 2a,b. Subsequently the baseline configuration was altered by varying ρ between 0.6 and 0.9 for a fixed frequency of $f = 1.59$GHz. The obtained bore-sight AR as function of ρ is shown in Figure 2c. As can be seen, the minimum occurs for $\rho = 0.78$ where a value of 0.4dB is obtained. Thus for the fixed height of $c = 20.0$mm the optimal lateral dimensions of the DRA are $2a = 35.4$mm and $2b = 45.2$mm, respectively. The optimal value of $\rho = 0.78$ is somewhat different from that obtained in [5] of 0.67 for the elliptic cylindrical probe-fed DRA.

This optimised DRA configuration is investigated as function of frequency and the resulting bore-sight AR is shown in Figure 2d. It is seen to be below 3dB within 27MHz with a minimum at $f = 1.59$GHz, corresponding to 1.7%. In Figure 2a,b Z_{in} and Γ_{in} for $\rho = 0.78$ are shown with broken lines. Comparison with the baseline configuration (full lines) shows that the circularly polarised DRA has a slightly lower impedance as well as a lower resonance frequency of $f_{res} = 1.55$GHz. The impedance bandwidths, defined as $|\Gamma_{in}| < -10$dB, are calculated with the baseline and circularly polarised DRA being matched at their respective
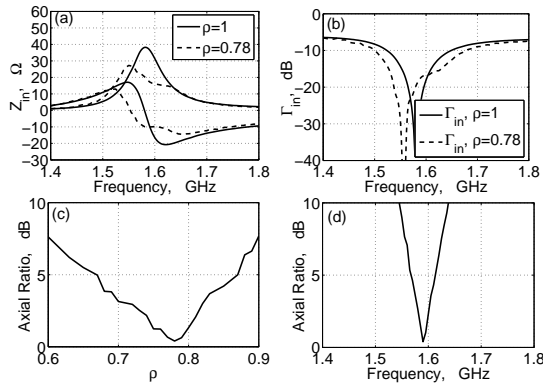
Figure 2: Impedance and polarisation results for the hemispherical and hemi-ellipsoidal DRA. (a) Input impedance. (b) Input reflection coefficient. (c) Axial ratio as function of ρ for $f = 1.59GHz$. (d) Axial ratio as function of frequency for $\rho = 0.78$.

resonance frequencies. The circularly polarised DRA has an impedance bandwidth of 11.4% which is larger than that of the baseline DRA which has 7.9%. In Figure 3a,b the radiation patterns and AR of the circularly polarised DRA are plotted as function of observation angle for $f = 1.59$GHz. It is seen that the radiation patterns are very similar in the two planes with a small difference in the cross-polar component. At bore-sight the co-polar directivity is 4.9dBi.

In conclusion, the probe-fed hemi-ellipsoidal DRA has been investigated using a MAS model and an optimum set of dimensions has been found which yields circular polarisation. The obtained AR bandwidth is 1.7% and the impedance bandwidth is 11.4%.

Bibliography

[1] K. M. Luk and K. W. Leung, *Dielectric Resonator Antennas*. Research Studies Press Ltd., Baldock, England, 2003.

[2] K. W. Leung and H. K. Ng, "Theory and Experiment of Circularly Polarized Dielectric Resonator Antenna With a Parasitic Patch," *IEEE Trans. Antennas Propag.*, vol. 51, no. 3, pp. 405–411, 2003.

[3] C.-Y. Huang, J.-Y. Wu, and K.-L. Wong, "Crossed-Slot-Coupled Microstrip Antenna and Dielectric Resonator Antenna for Circular Polarization," *IEEE Trans. Antennas Propag.*, vol. 47, no. 4, pp. 605–609, 1999.

[4] M. B. Oliver, *et al.*, "Circularly Polarised Rectangular Dielectric Resonator Antenna," *IEE Electron. Lett.*, vol. 31, no. 6, pp. 418–419, 1995.

[5] A. A. Kishk, "An Elliptic Dielectric Resonator Antenna Designed for Circular Polarization with Single Feed," *Microwave Opt. Technol. Lett.*, vol. 37, no. 6, pp. 454–456, 2003.

[6] B. Li and K. W. Leng, "On the Circularly Polarised Hemi-Ellipsoidal Dielectric Resonator Antenna," *Microwave Opt. Technol. Lett.*, vol. 48, no. 9, pp. 1763–1766, 2006.
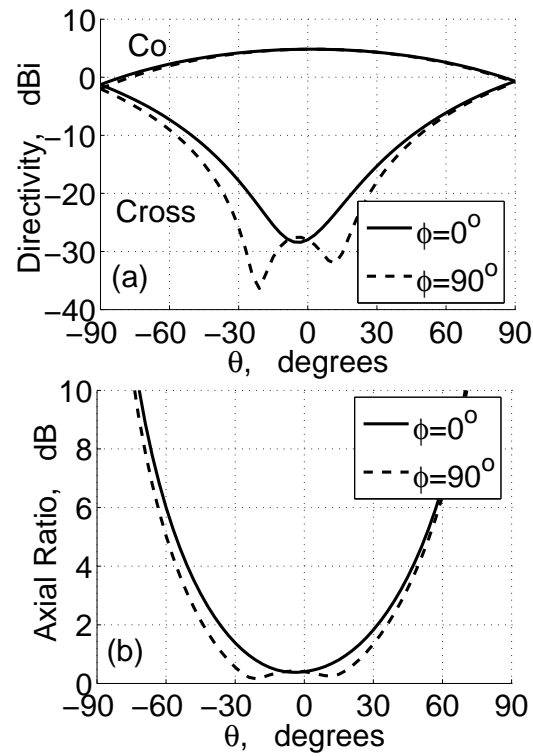
Figure 3: Radiation results as function of observation angle for the hemi-ellipsoidal DRA for $f = 1.59GHz$. (a) Co- and cross-polar radiation pattern. (b) Axial ratio.

[7] N. V. Larsen and O. Breinbjerg, "Analysis of Circularly Polarised Hemispheroidal Dielectric Resonator Antenna Phased Arrays using the Method of Auxiliary Sources," *Accepted for publication in IEEE Trans. Antennas Propag.*, 2007.

A Spherical Wave Expansion Model of Sequentially Rotated Phased Arrays with Arbitrary Elements

Niels Vesterdal Larsen and Olav Breinbjerg

Status

Submitted: May 2007
Accepted: July 2007 (after completion of thesis)
Published: December 2007 (after completion of thesis)

Bibliographical details

[J6] N.V. Larsen and O. Breinbjerg, "A Spherical Wave Expansion Model of Sequentially Rotated Phased Arrays with Arbitrary Elements", in submission[‡], May, 2007.

A SPHERICAL WAVE EXPANSION MODEL OF SEQUENTIALLY ROTATED PHASED ARRAYS WITH ARBITRARY ELEMENTS

Niels Vesterdal Larsen and Olav Breinbjerg

Abstract: An analytical model of sequentially rotated phased arrays with arbitrary antenna elements is presented. It is applied to different arrays and the improvements of axial ratio bandwidth and co-polar directivity are investigated. It is compared to a numerical Method of Auxiliary Sources model to ascertain the accuracy and limitations.

1 Introduction

The sequential rotation (SR) is a well-known technique for improving the circular polarisation (CP) purity of an antenna array. The CP purity of conventional arrays is impaired by the lack of CP purity of the antenna elements and their mutual coupling, leading to a high axial ratio (AR) and a narrow AR bandwidth. Early applications of the SR include [1, 2] and theoretical descriptions of the technique have been presented in [3, 4]. It is thus well known that the CP purity of a sequentially rotated array, in the absence of mutual coupling, is independent of the polarisation of the antenna elements. The SR has primarily been used with fixed-beam arrays where significant improvement of the AR can be obtained. Fixed-beam applications include microstrip antennas [1, 3–6] and dielectric resonator antennas [7, 8]. The SR has also been employed for phased arrays, however, to a lesser extent. In [9, 10] sequentially rotated linear phased arrays of circularly polarised elements are investigated theoretically and experimentally, and in [2, 11–13] planar microstrip phased arrays are addressed.

In this work the far field from sequentially rotated phased arrays (SRPAs) is derived on basis of a general spherical wave expansion (SWE) of the antenna element far field. This model assumes that the elements patterns are identical and that the mutual coupling between the array elements is negligible or symmetric. It is applied to a crossed dipole antenna model for which the SWE coefficients are calculated.

For typical phased array applications, the elements are electrically small. This implies that they can be accurately represented with only a few SWE modes. The analytical nature of the SWE model gives a qualitative insight into how the different modes of the antenna element far fields contribute to the SRPA far field, and further, how this is affected by the various choices of the SRPA design.

In order to establish the validity and limitations of the SWE model it is compared with a full-wave analysis based on a Method of Auxiliary Sources (MAS) model [14]. The two models are thus employed to assess the improvement of the main beam co-polar CP directivity and AR as function of frequency and scan angle.

2 Field Expression for Sequentially Rotated Phased Arrays

In this section the far field from an SRPA is derived and expressed as an SWE. In this model the antenna elements patterns are assumed to be identical. Thus the array far field is the sum of identical but rotated element far fields which are weighted with excitations in accordance with the desired scan angles and employment of SR. The derivation thus takes outset in the far field of an isolated antenna element. Throughout this text the harmonic time dependence $e^{j\omega t}$ is assumed and suppressed.

2.1 The Isolated Antenna Element

For an arbitrary antenna the electric far field $\mathbf{E}^f(\theta, \phi)$ of the field $\mathbf{E}(r, \theta, \phi)$ can be written as an SWE [15]

$$\mathbf{E}^f(\theta, \phi) = \lim_{r \to \infty} \frac{k_0 r \sqrt{4\pi}}{e^{-jk_0 r}} \mathbf{E}(r, \theta, \phi)$$

$$= k_0 \sqrt{Z_0} \sum_{s=1}^{2} \sum_{n=1}^{N} \sum_{m=-n}^{n} Q_{smn} \mathbf{K}_{smn}(\theta, \phi), \quad (1)$$

where the Q_{smn} are expansion coefficients and $\mathbf{K}_{smn}$ are far-field pattern functions

$$\begin{Bmatrix} \mathbf{K}_{1mn} \\ \mathbf{K}_{2mn} \end{Bmatrix} = \frac{j^n \sqrt{2}}{\sqrt{n(n+1)}} \left(\frac{-m}{|m|} \right)^m e^{-jm\phi}.$$

$$\left[\frac{m\overline{P}_n^{|m|}(\cos\theta)}{\sin\theta} \begin{Bmatrix} \hat{\boldsymbol{\theta}} \\ -j\hat{\boldsymbol{\phi}} \end{Bmatrix} + \frac{d\overline{P}_n^{|m|}(\cos\theta)}{d\theta} \begin{Bmatrix} -j\hat{\boldsymbol{\phi}} \\ \hat{\boldsymbol{\theta}} \end{Bmatrix} \right]. \quad (2)$$

Here, $\overline{P}_n^{|m|}$ is the normalised associated Legendre function of degree n and order $|m|$ [15] and Z_0 and k_0 are the free-space intrinsic impedance and wave number, respectively. In principle an infinite number of radial n-modes must be included in (1), however, in practice the sum is truncated at mode N. The right- and left-hand circularly polarisation (RHCP and LHCP) field components are

$$\begin{Bmatrix} E_{RHCP}^f \\ E_{RHCP}^f \end{Bmatrix} = \frac{1}{\sqrt{2}} \left(\hat{\boldsymbol{\theta}} \cdot \mathbf{E}^f(\theta, \phi) \pm j\hat{\boldsymbol{\phi}} \cdot \mathbf{E}^f(\theta, \phi) \right)$$

$$= k_0 \sqrt{Z_0} \sum_{n=1}^{N} \sum_{m=-n}^{n} \frac{j^n e^{-jm\phi}}{\sqrt{n(n+1)}} \left(\frac{-m}{|m|} \right)^m$$

$$(Q_{1mn} \pm Q_{2mn}) \left[\frac{d\overline{P}_n^{|m|}(\cos\theta)}{d\theta} \pm \frac{m\overline{P}_n^{|m|}(\cos\theta)}{\sin\theta} \right], \quad (3)$$

where the $+$ and $-$ in $\pm$ refer to the RH and LH cases, respectively. From, [15],

$$\left. \frac{d\overline{P}_n^{|m|}(\cos\theta)}{d\theta} \right|_{\theta=0} = \left. \frac{\overline{P}_n^{|m|}(\cos\theta)}{\sin\theta} \right|_{\theta=0}$$

$$= \begin{cases} n(n+1)/2, & |m| = 1, \\ 0, & |m| \neq 1, \end{cases} \quad (4)$$

so it follows that for $\theta = 0^\circ$ only the $m = 1$ mode can contribute to the RHCP component, and only the $m = -1$ mode to the LHCP component.

2.2 Sequentially Rotated Phased Array

The SRPA is depicted in Figure 1 with the elements being numbered from 1 to K. The elements are located in the (x, y)-plane, but their positions are otherwise arbitrary. The positions are denoted by the displacement d_k and angle ϕ_k. In accordance with the SR principle, the elements are physically rotated by the angles

$$\phi_{pk} = \frac{\pi P}{|m_0| K}(k - 1), \tag{5}$$

and furthermore, a phase shift is introduced in the element excitations

$$\phi_{ek} = -m_0 \phi_{pk}. \tag{6}$$

The integer m_0 is a parameter that can be chosen and, depending on the sign of m_0, the phase shift ϕ_{ek} implies either a sequential phase lead ($m_0 < 0$) or a sequential phase lag ($m_0 > 0$). As will become evident after equation (12) below, m_0 denotes that azimuth mode m of the element pattern that is enhanced by the SR relative to the others, e.g., $m_0 = 1$ favours the $m = 1$ mode, resulting in RHCP as seen from (3) and (4). P is another parameter that can be chosen and it is related to the rotation angle of the last K'th element. If $|m_0| = 1$, $P = 1$ implies that ϕ_{pk} is less than π, while $P = 2$ implies that ϕ_{pk} is larger than but less than 2π, etc. The conventional phased array (CPA), with elements having the same orientation, can thus be described by $P = 0$, while the cases $P = 1$ and $P = 2$ are two different implementations of SRPA. In this work the P in (5) is chosen to be restricted to $2P \leq K|m_0|$.

elements are rotated incrementally as implied by (5) there is no loss of generality since the positions of the elements can still be chosen freely. However, as will become evident later the SRPA is influenced by the choice of these positions. A few examples of SR schemes are given in Figure 2a-d. It is clear that for the SRPAs in Figure 2b,c, all elements see exactly the same environment. This is, however, not the case for the SRPA's of Figure 2a,d. For later reference the arrays in Figure 2b,c will be classified as symmetric SRPA and those of Figure 2a,d as asymmetric SRPA.
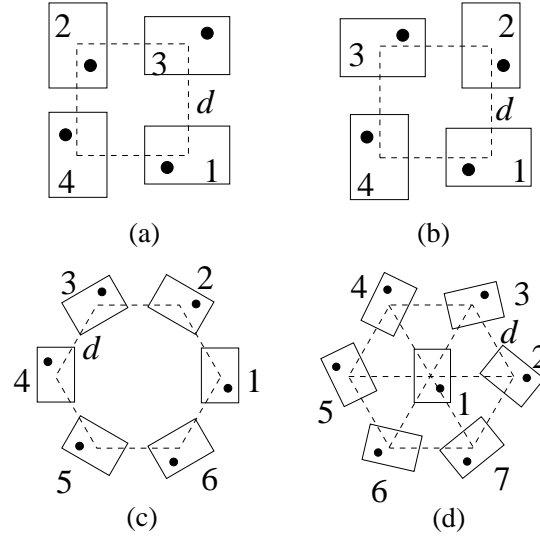
Figure 2: Examples of SR applications. (a)-(b) $K = 4$, $P/|m_0| = 2$ with different ϕ_k. (c) $K = 6$, $P/|m_0| = 2$. (d) $K = 7$, $P/|m_0| = 2$.

As in shown in Figure 1, the element excitations include a phase shift ψ_k to obtain a certain main beam scan angle (θ_0, ϕ_0), in addition to the sequential phase shift in (6). These phase shifts will typically be designed for a particular design frequency f_0 and will not be exact at other frequencies. In order to incorporate this practical aspect the following frequency-dependent models are employed

$$\phi_{ek} = -m_0 \phi_{pk} \frac{f}{f_0}, \tag{7}$$

$$\psi_k = k_0 \frac{f_0}{f} d_k \sin \theta_0 \cos(\phi_0 - \phi_k). \tag{8}$$

In (7), the factor $\frac{f}{f_0}$ models the frequency variation which would occur if the phase shifts were realised using fixed-length transmission lines. In (8), $\frac{f_0}{f}$ signifies that the beam scanning is implemented for the design frequency f_0 and thus the ψ_k are not frequency dependent.

When the k'th element is rotated by the angle ϕ_{pk} its far field (3) is changed such that the azimuth angle ϕ in (3) is exchanged with $\phi - \phi_{pk}$. In total, the field radiated by the
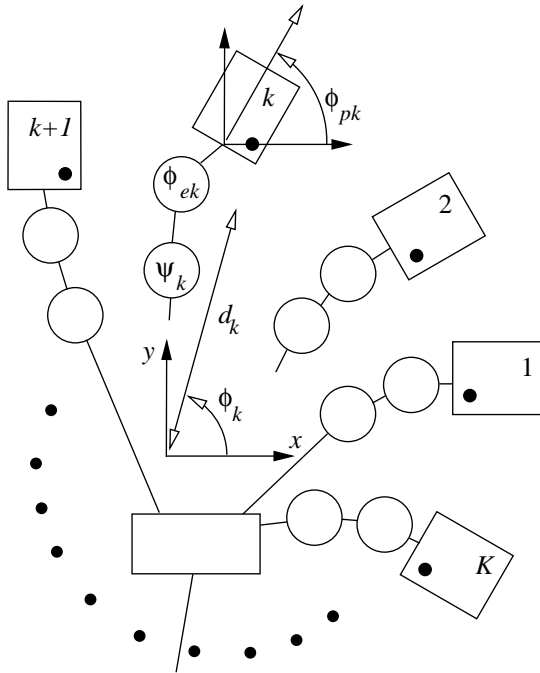

Figure 1: Sequential rotation principle.

It is noted that the SR in principle only concerns the rotation, but not the positions, of the elements. Even though the

SRPA can thus be expressed as

$$\mathbf{E}^f = k_0\sqrt{2Z_0}\sum_{k=1}^{K}C_k^{SR}C_k^{scan}C_k^{disp}\sum_{n=1}^{N}\sum_{m=-n}^{n}\frac{j^n}{\sqrt{n(n+1)}}$$

$$\left(\frac{-m}{|m|}\right)^m e^{-jm(\phi-\phi_{pk})}\left[\frac{m\overline{P}_n^{|m|}(\cos\theta)}{\sin\theta}[\hat{\boldsymbol{\theta}}Q_{1mn}-j\hat{\boldsymbol{\phi}}Q_{2mn}]\right.$$

$$\left.+\frac{d\overline{P}_n^{|m|}(\cos\theta)}{d\theta}[-j\hat{\boldsymbol{\phi}}Q_{1mn}+\hat{\boldsymbol{\theta}}Q_{2mn}]\right], \quad (9)$$

where the factors

$$C_k^{SR} = e^{j\phi_{ek}}, \qquad (10a)$$

$$C_k^{scan} = e^{j\psi_k}, \qquad (10b)$$

$$C_k^{disp} = e^{-jk_0 d_k \sin\theta\cos(\phi-\phi_k)}, \qquad (10c)$$

account for the SR, beam scanning, and element displacement. The LHCP and RHCP components of the SRPA are

$$\begin{Bmatrix}E_{RHCP}^f\\E_{RHCP}^f\end{Bmatrix} = k_0\sqrt{Z_0}\sum_{k=1}^{K}C_k^{SR}C_k^{scan}C_k^{disp}\sum_{n=1}^{N}\sum_{m=-n}^{n}$$

$$\frac{j^n}{\sqrt{n(n+1)}}\left(\frac{-m}{|m|}\right)^m e^{-jm(\phi-\phi_{pk})}(Q_{1mn}\pm Q_{2mn})$$

$$\left[\frac{d\overline{P}_n^{|m|}(\cos\theta)}{d\theta}\pm\frac{m\overline{P}_n^{|m|}(\cos\theta)}{\sin\theta}\right]. \quad (11)$$

In summary, this expression gives the RHCP and LHCP components of an SRPA consisting of arbitrary antenna elements with the SWE coefficients Q_{smn}. It is based on the assumption that the active element patterns (AEP) are identical and that mutual coupling can be neglected. The expression is valid for general element positions, scan angles, and type of SR which are governed by the factors C_k^{SR}, C_k^{scan}, and C_k^{disp} in (10a-c). It is very useful in understanding how the SR works as it shows how the SR influences the different spherical modes of the element pattern. It is noted that the expression takes into account the error in the phase excitation away from the design frequency.

In the following the focus will be on the main beam of the array far field, i.e., $(\theta,\phi)=(\theta_0,\phi_0)$, where $C_k^{scan}C_k^{disp}=1$ at the design frequency $f=f_0$. This enables a simplification of (11) and, by interchanging the k and n summations, the factor

$$\sum_{k=1}^{K}C_k^{SR}e^{jm\phi_{pk}} = \sum_{k=1}^{K}e^{j\frac{\pi P(m-m_0)(k-1)}{|m_0|K}}. \quad (12)$$

appears. For $m=m_0+q2K|m_0|/P$, where q is an arbitrary integer, this sum attains its maximum value K. Thus the $m=m_0$ mode in (11) is favoured and, depending on the choice of P, the remaining azimuth modes will be more or less dampened compared to this mode. In particular for $P=2$ all other modes vanish since the sum in (12) equals zero when $m\neq m_0+qK|m_0|$. In this case the main beam field

expressions simplify to

$$\begin{Bmatrix}E_{RHCP}^f\\E_{RHCP}^f\end{Bmatrix} = k_0\sqrt{Z_0}\sum_{n=1}^{N}\frac{j^n e^{-jm_0\phi_0}}{\sqrt{n(n+1)}}\left(\frac{-m_0}{|m_0|}\right)^{m_0}$$

$$(Q_{1m_0n}\pm Q_{2m_0n})\left[\frac{d\overline{P}_n^{|m_0|}(\cos\theta_0)}{d\theta_0}\pm\frac{m_0\overline{P}_n^{|m_0|}(\cos\theta_0)}{\sin\theta_0}\right], \quad (13)$$

where the azimuth modes $m=m_0+qK|m_0|$ have been omitted, assuming that such higher-order modes are not present in the element patterns. Since the $m=-1$ mode corresponds to LHCP and $m=1$ to RHCP it follows that the choices of phase lead ($m_0=-1$) and phase lag ($m_0=1$), see (6), result in LHCP and RHCP radiation, respectively at the $\theta=0°$ direction for $\theta_0=0°$. Although the undesired azimuth modes (except for multiples of $K|m_0|$) may be removed from the main beam this does not generally mean that the main beam cross-polar component is removed, or correspondingly, that the main beam AR is 0dB. This only happens if the main beam is scanned to $\theta_0=0°$ since the azimuth modes $m_0=\pm1$ are only purely CP in that direction.

If instead of $P=2$, it is chosen that $P=1$, the SR may still ensure perfect AR for $\theta_0=0°$. For instance, if $m_0=1$, the $m=-1$ mode will still vanish, however, the remaining azimuth modes generally do not vanish. Since the element positions have not been specified in any way, it is clear that the results given so far are independent of the element positions. Thus for all the examples of Figure 2, the SR will in principle ensure an AR of 0dB at $\theta=0°$.

2.3 Influence of Neighbouring Elements and Mutual Coupling

In the discussions and theoretical derivations given above, the mutual coupling between the elements has been disregarded. In any real application the mutual coupling will influence the SRPA performance and the results of the preceding section will be modified. It is, however, still possible to foresee some of the impact of the neighbouring elements. If the elements are fed with forward propagating voltage waves V_k^+, the resulting feed currents $\mathbf{I}$ become

$$\mathbf{I} = \frac{1}{Z_c}(\overline{\overline{\mathbf{U}}} - \overline{\overline{\mathbf{S}}}_A)\mathbf{V}^+, \quad (14)$$

where $\overline{\overline{\mathbf{S}}}_A$ is the array scattering matrix, $\overline{\overline{\mathbf{U}}}$ is the identity matrix and Z_c is the characteristic impedance of the feed lines. If the SRPA is symmetric, as discussed in Section 2.2, it is clear that the coupling between any two antennas, say i and j, is the same as the coupling between other two antennas, $i+1$ and $j+1$. Thus the $\overline{\overline{\mathbf{S}}}_A$ will be a symmetric Toeplitz matrix. In the case of $\theta_0=0°$, the only difference between the K feed signals is the electric phase shifts ϕ_{ek} and thus $V_{k+1}^+/V_k^+=e^{j\phi_{e1}}$. If further ϕ_{ek} is given by the ideal expression (6) and $P=2$ it also holds that $V_1^+/V_K^+=e^{j\phi_{e1}}$. In this case it can be shown that the resulting feed currents $\mathbf{I}$ calculated via (14) will be proportional to $\mathbf{V}^+$ and no relative error will be introduced in spite of the mutual

coupling. In the specific case of the SRPA in Figure 2b, $\overline{\overline{\mathbf{S}}}_A$ simplifies to

$$\overline{\overline{\mathbf{S}}}_A = \begin{bmatrix} S_{11} & S_{12} & S_{13} & S_{12} \\ S_{12} & S_{11} & S_{12} & S_{13} \\ S_{13} & S_{12} & S_{11} & S_{12} \\ S_{12} & S_{13} & S_{12} & S_{11} \end{bmatrix}, \quad (15)$$

and the feed currents become

$$\mathbf{I} = \frac{1 - S_{11} + S_{13}}{Z_c} \mathbf{V}^+. \quad (16)$$

With respect to the AEP it is obvious that they will be slightly different from that of the isolated element due to the influence of the neighbouring elements. However, when the SRPA is symmetric the assumption of identical AEP still holds. Thus in such cases, even though the neighbouring elements influence the radiation, the SR ensures that the main beam AR is unity when the beam is scanned towards $\theta = 0^\circ$, and that it is generally improved for other scan angles.

In the case of an asymmetric SRPA, the AEP are not identical. Furthermore, the current excitations, e.g., (16), will not occur if either, the SRPA is asymmetric, the phase shifts ϕ_{ek} are imperfect, e.g., due to the frequency variation, or the main beam is scanned away from $\theta = 0^\circ$. In such cases the non-identical AEP and mutual coupling will have detrimental effects on the performance of the SRPA.

3   Examples with a Generic Antenna Element

In the following the SWE model given by (11) is employed for the analysis of small SRPA consisting of crossed dipole antenna (CDA) elements with known isolated element patterns. In order to compare with the more realistic case, where the mutual coupling is included and non-identical AEP are taken into account, the same SRPA is also modelled with a MAS model of the entire SRPA. The MAS model is based on that derived in [14].

3.1   SWE and MAS Models of the CDA Array

A single CDA element is depicted in Figure 3. The dipoles are parallel to the x- and y-axes, respectively, which is indicated with subscripts x and y in the following. The two dipoles have lengths $L = 75.0$mm, widths $w = 2.0$mm, and are positioned above an infinite ground plane at a height $h = 47.0$mm. The CDA elements are used in the two SRPAs shown in Figure 2b,d, where the element separation is $d = 112.5$mm. The dipoles are fed by voltage generators positioned between the dipole arms. Depending on the excitations, different qualities of CP elements can be simulated. Presently, narrow-band AR elements will be investigated. To this end the forward voltage waves of the dipoles are defined to be frequency dependent such that

$$V_{x,0}^+ = e^{-\left(\alpha \frac{|f - f_0|}{f_0} + \beta\right)}, \quad (17a)$$

$$V_{y,0}^+ = -j, \quad (17b)$$

where α and β are positive constants and f_0 is the design frequency. These element excitations imply a minimum AR at f_0, and for increasing α and β the AR becomes more narrow-band and the minimum AR increases, respectively. Presently, $\alpha = 16$, $\beta = 0.1$, and $f_0 = 1.6$GHz are chosen which imply a 3dB AR bandwidth at $\theta = 0^\circ$ of about 3.1% and a minimum AR of 0.87dB at 1.6GHz.
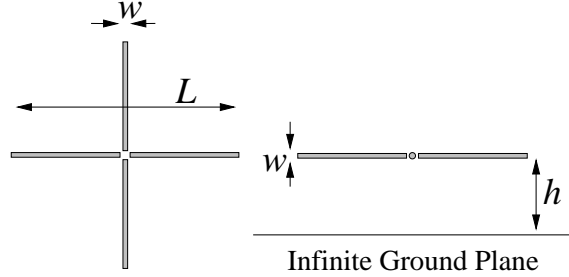

Figure 3: Crossed dipole antenna element.

For the SWE model the Q_{smn} can be calculated from, [15]

$$Q_{smn} = k_0 \sqrt{Z_0} (-1)^{m+1} \int_V \mathbf{F}_{s,-m,n}^{(1)}(\mathbf{r}') \cdot \mathbf{J}(\mathbf{r}') dV', \quad (18)$$

where $\mathbf{F}_{s,-m,n}^{(1)}$ is a spherical vector wave function defined in [15] and $\mathbf{J}$ is the current on the dipoles of the CDA. The normalised power spectra as function of mode numbers n and m, defined as

$$P_{rad}^{(n)} = \sum_{s=1}^{2} \sum_{m=-n}^{n} |Q_{smn}|^2 / \sum_{s=1}^{2} \sum_{n=1}^{N} \sum_{m=-n}^{n} |Q_{smn}|^2, \quad (19a)$$

$$P_{rad}^{(m)} = \sum_{s=1}^{2} \sum_{n=1}^{N} |Q_{smn}|^2 / \sum_{s=1}^{2} \sum_{n=1}^{N} \sum_{m=-n}^{n} |Q_{smn}|^2, \quad (19b)$$

are plotted for the isolated CDA element at 1.6GHz in Figure 4. It is seen that $P_{rad}^{(n)}$ is at a level of -50dB for $n = 5$. From the $P_{rad}^{(m)}$ plot the RHCP is clearly indicated by the fact that the $m = -1$ mode is very low compared to the $m = 1$ mode. Also for $|m| > 3$, $P_{rad}^{(m)}$ is below -50dB. This illustrates that the CDA element can be described with only a few modes, and further, that the omission of the $m = m_0 + qK|m_0|$ modes in (13) is justified.

For the SWE model the SRPA far field is now calculated by (9) and (10a-c). The SWE model thus includes the narrow-band CP purity of the single element, mutual coupling between the two dipoles of the CDA element, and frequency variation in the SR phase factors ϕ_{ek}. It does, however, not include the mutual coupling between elements in the array. For the full-wave MAS model the entire SRPA is included and for this model the excitations of the k'th element are given by

$$V_{x,k}^+ = V_{x,0}^+ C_k^{SR} C_k^{scan}, \quad (20)$$

and similarly for $V_{y,k}^+$. In addition to the effects included in the SWE model the MAS model also includes the mutual coupling and the possibly different AEP.
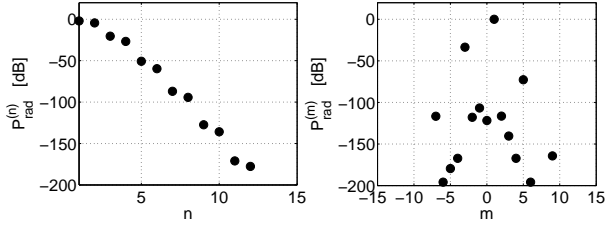
Figure 4: Normalised power spectra $P_{rad}^{(n)}$ and $P_{rad}^{(m)}$ for the isolated CDA at 1.6GHz.

4 Results for SWE and MAS Models

In Figure 5 the main beam AR is shown for a CPA, i.e., $P = 0$, for scan angles of $\theta_0 = 0^o$ and $\theta_0 = 45^o$. The worst case, among all azimuth scan angles ϕ_0, are shown for different polar scan angles θ_0 and as function of frequency. For the SWE model the results are independent of the array shape and therefore only a single result is shown for the SWE. However, some differences are evident from the MAS model when the array is scanned away from $\theta = 0^o$. Thus for the MAS models of the 4- and 7-element CPAs the AR is about 1.5dB and 2.5dB higher, respectively, than the corresponding SWE models, and this reflects the impact of the mutual coupling. In Figure 6 the corresponding results for the 4- and 7-element SRPAs are shown together with the directivities for both the CPAs and SRPAs. For the 4-element array, in the left-hand side of Figure 6, it is seen that the SR has resulted in a significant improvement of the AR. The SWE and MAS results agree reasonably well and both yield an AR of 0dB at $\theta_0 = 0^o$ and $f = f_0$. This illustrates that for the symmetric SRPA (Figure 2b) the SR works perfectly in spite of the mutual coupling. It is further seen that for frequencies other than the design frequency f_0, the frequency variation in (7) gives rise to an AR larger than 0dB in the $\theta = 0^o$ direction.
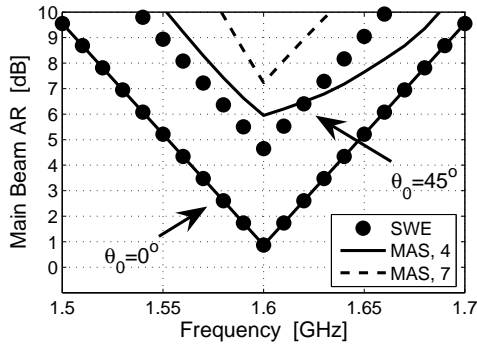

Figure 5: Worst case AR of a CDA, CPA $(P = 0)$ as function of frequency for $\theta_0 = 0^o$ and $\theta_0 = 45^o$.

The main beam co-polar directivity is in general maximum near f_0 and decreases for frequencies away from f_0. For the CPA $(P = 0)$, this decrease is a consequence of the poor CP purity for these frequencies, evident from the high

AR in Figure 5. However, for the SRPA $(P = 2)$ case the AR remains low and can not explain the decrease in the main beam co-polar directivity. The decrease should instead be explained by an overall increase in the cross-polar radiation away from the main beam. This is well known to occur for linearly polarised antennas [11] used in sequentially rotated arrays. The SWE and MAS results are slightly different and thus the SR seems to improve the main beam co-polar directivity slightly when the SWE results are considered, while the MAS results indicate the opposite behaviour. This is believed to be caused by the mutual coupling included in the MAS model. It is thus found that the SR improves the main beam AR but not necessarily the main beam directivity.
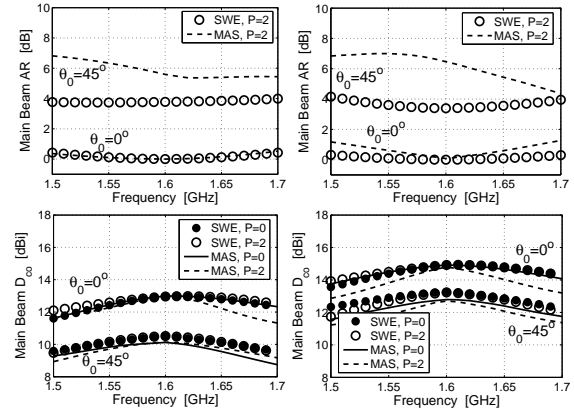

Figure 6: Worst case AR (top) and directivity (bottom) as function of frequency for 4-element (left) and 7-element (right) CDA, SRPAs for $\theta_0 = 0^o$ and $\theta_0 = 45^o$.

In the right-hand side of Figure 6 the corresponding results for the 7-element arrays are shown. As far as the SWE results are concerned the observed behaviour is quite similar to the 4-element case, except for the obvious increase in directivity. Thus the fact that the 7-element SRPA is asymmetric can not be observed from the SWE results and the SR seems to be working flawlessly. However, from the MAS results the effects of the mutual coupling become evident. The most obvious difference is that the main beam AR is larger than 0dB at $\theta_0 = 0^o$ and $f = f_0$. This illustrates that the asymmetric array topology precludes an ideal performance of the SR because of non-identical AEP and non-Toeplitz scattering matrix. This lack of symmetry generally implies larger deviation between the SWE and MAS results as can be seen in the figure.

Examples of radiation patterns are shown in Figure 7 for $P = 0, P = 2$ and for $\theta_0 = 0^o, \theta_0 = 45^o$. The frequency is 1.58GHz at which the AR of the isolated element is about 2.8dB, see Figure 5. The observations made from Figure 6 are also evident here, and the difference in the cross-polar components is particularly noteworthy. As expected it is very low for the 4-element symmetric SRPA for both the SWE and MAS models when $\theta_0 = 0^o$, whereas for the 7-element asymmetric SRPA this is only the case for the SWE solution. For the $\theta_0 = 45^o$ case the cross-polar directivity is
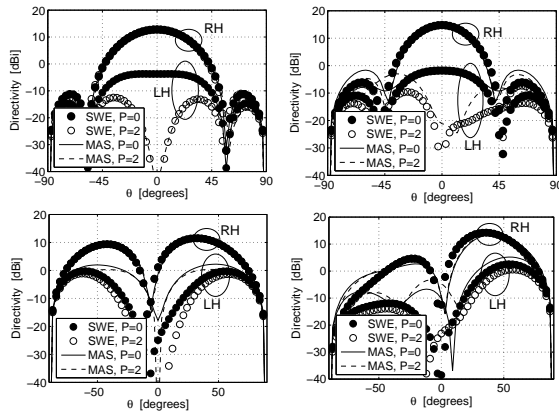
clearly seen to decrease due to the SR.

Figure 7: Co- and cross-polar directivity for $\theta_0 = 0^\circ$ (top) and $\theta_0 = 45^\circ$ (bottom) for the 4-element (left) and 7-element (right) CDA, SRPAs.

5   Conclusion

An analytical spherical wave expansion (SWE) model has been derived for sequentially rotated phased arrays (SR-PAs). It takes outset in known SWE of an isolated antenna element and can thus be used for general elements. It is demonstrated that application of sequential rotation (SR) removes the unwanted azimuth modes from the main beam, and thus improves the circular polarisation.

The approximate SWE is compared with a full-wave Method of Auxiliary Sources (MAS) model which includes the mutual coupling and non-identical active element patterns (AEP). Both from the SWE and the MAS models it is found that the axial ratio (AR) of the main beam is improved also when it is scanned away from $\theta_0 = 0^\circ$. However, it is also found that the main beam co-polar directivity is not necessarily improved by the SR.

When the mutual coupling and the non-identical AEP are included it is found that the improvements of the AR, predicted by the SWE, are only ideally obtainable when the SR-PAs are rotationally symmetric. Furthermore, the improvements of the AR, predicted by the SWE, are generally found to be slightly optimistic compared with the situations where the mutual coupling and true AEP are taken into account.

Bibliography

[1] M. Haneishi, S. Yoshida, and N. Goto, "A Broadband Microstrip Array Composed of Single-Feed Type Circularly Polarized Microstrip Antennas," *IEEE Antennas Propag. Soc. Int. Symp. Dig.*, vol. 1, pp. 160–163, 1982.

[2] J. Huang, "C.P. Microstrip Array with Wide Axial Ratio Bandwidth and Single Feed L.P. Elements," *IEEE Antennas Propag. Soc. Int. Symp. Dig.*, vol. 2, pp. 705–708, 1985.

[3] T. Teshirogi, M. Tanaka, and W. Chujo, "Wideband Circularly Polarized Array Antenna with Sequential Rotations and Phase Shift of Elements," *Proc. Int. Symp. Antennas Propag.*, vol. 1, pp. 117–120, 1985.

[4] P. S. Hall, J. S. Dahele, and J. R. James, "Design Principles of Sequentially Fed, Wide Bandwidth, Circularly Polarised Microstrip Antennas," *IEE Proc., Pt. H*, vol. 136, no. 5, pp. 381–389, 1989.

[5] K. D. Palmer, J. H. Cloete, and J. J. van Tonder, "Bandwidth Improvement of Circular Polarised Arrays Using Sequential Rotation," *IEEE Antennas Propag. Soc. Int. Symp. Dig.*, pp. 135–138, 1992.

[6] M. N. Jazi and M. N. Azarmanesh, "Design and Implementation of Circularly Polarised Microstrip Antenna Array Using a New Serial Feed Sequentially Rotated Technique," *IEE Proc. Microw. Antennas Propag.*, vol. 153, no. 2, pp. 133–140, 2006.

[7] M. Haneishi and B. Wu, "Array Antenna Composed of Circularly Polarized Dielectric Resonator Antennas," *IEEE Antennas Propag. Soc. Int. Symp. Dig.*, vol. 1, pp. 252–255, 1999.

[8] A. A. Kishk, "Application of Rotated Sequential Feeding for Circular Polarization Bandwidth Enhancement of Planar Arrays with Single-Fed DRA Elements," *IEEE Antennas Propag. Soc. Int. Symp. Dig.*, vol. 1, pp. 664–667, 2003.

[9] T. Teshirogi, M. Tanaka, and N. Takahashi, "Phased Arrays Using Sequential Rotation and Phasing Techniques," *Proc. Int. Symp. Antennas Propag.*, vol. 1, pp. 149–152, 1996.

[10] Q. García-García, "Scanning Properties of Sequentially Rotated Linear Arrays of Circularly Polarized Patch Radiators," *Microwave Opt. Technol. Lett.*, vol. 30, no. 5, pp. 343–350, 2001.

[11] J. Huang, "A Technique for an Array to Generate Circular Polarization with Linearly Polarized Elements," *IEEE Trans. Antennas Propag.*, vol. 34, no. 9, pp. 1113–1124, 1986.

[12] L. Baggen, *et al.*, "Phased Array Using the Sequential Rotation Principle: Analysis of Coupling Effects," *IEEE Int. Symp. Phased Array Systems and Technology*, pp. 571–576, 2003.

[13] M. Tanaka, "Sequentially Rotated Array Consisting of Higher Order Mode Antenna Elements," *IEEE Antennas Propag. Soc. Int. Symp. Dig.*, vol. 3, pp. 1928–1931, 1996.

[14] P. J. Papakanellos and C. N. Capsalis, "Numerical Analysis of Cylindrical Dipole Antennas Using an Auxiliary Sources Model," *J. Electromagn. Waves Appl.*, vol. 17, no. 3, pp. 389–407, 2003.

[15] J. E. Hansen, *Spherical Near-Field Antenna Measurements*. Peter Peregrinus Ltd., London, 1998.